CHEMICAL REVIEWS

pubs.acs.org/CR

Review

Interatomic and Intermolecular Coulombic Decay

Till Jahnke,* Uwe Hergenhahn, Bernd Winter, Reinhard Dörner, Ulrike Frühling, Philipp V. Demekhin, Kirill Gokhberg, Lorenz S. Cederbaum, Arno Ehresmann, André Knie, and Andreas Dreuw*

Cite This: *Chem. Rev.* 2020, 120, 11295−11369

Read Online

ACCESS | Metrics & More | Article Recommendations

ABSTRACT: Interatomic or intermolecular Coulombic decay (ICD) is a nonlocal electronic decay mechanism occurring in weakly bound matter. In an ICD process, energy released by electronic relaxation of an excited atom or molecule leads to ionization of a neighboring one via Coulombic electron interactions. ICD has been predicted theoretically in the mid nineties of the last century, and its existence has been confirmed experimentally approximately ten years later. Since then, a number of fundamental and applied aspects have been studied in this quickly growing field of research. This review provides an introduction to ICD and draws the connection to related energy transfer and ionization processes. The theoretical approaches for the description of ICD as well as the experimental techniques developed and employed for its investigation are described. The existing body of literature on experimental and theoretical studies of ICD processes in different atomic and molecular systems is reviewed.

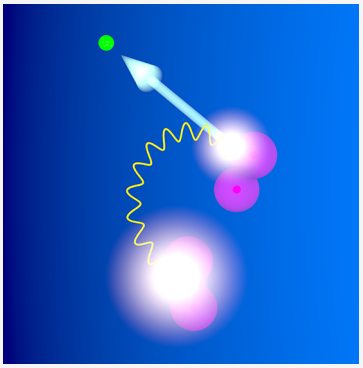

CONTENTS

Received: February 7, 2020
Published: October 9, 2020

https://dx.doi.org/10.1021/acs.chemrev.0c00106
Chem. Rev. 2020, 120, 11295−11369

1. INTRODUCTION

In 1997, Cederbaum and co-workers realized a novel type of electronic decay mechanism to be present in weakly bound matter.[1] In their seminal theoretical work, they showed a new set of doubly ionized states to emerge in small HF and H_2O clusters, which is energetically not accessible in the corresponding monomers. These are, for example, dicationic states with two outer-shell vacancies located at two different monomers of the loosely bound compound, resulting in two monocations instead of one dication. While the double ionization of the initially excited monomer is energetically not feasible due to the strong Coulomb repulsion of the charges, the ionization of a neighboring molecule is energetically feasible. They realized, furthermore, that these doubly ionized states are generated extremely efficiently upon inner-valence ionization of the cluster. They termed this process interatomic (or intermolecular) Coulombic decay (ICD).

Figure 1 (taken from ref 2) depicts a schematic of the overall process in a cluster consisting of two atoms. After removing an inner-valence electron from one of the atoms of the dimer, the ionized atom de-excites when an outer-shell electron fills the vacancy. The energy released in this transition is transferred to the neighboring atom and induces its ionization. After ICD, the cluster fragments rapidly in a Coulomb explosion because the two singly positively charged atoms repel each other.

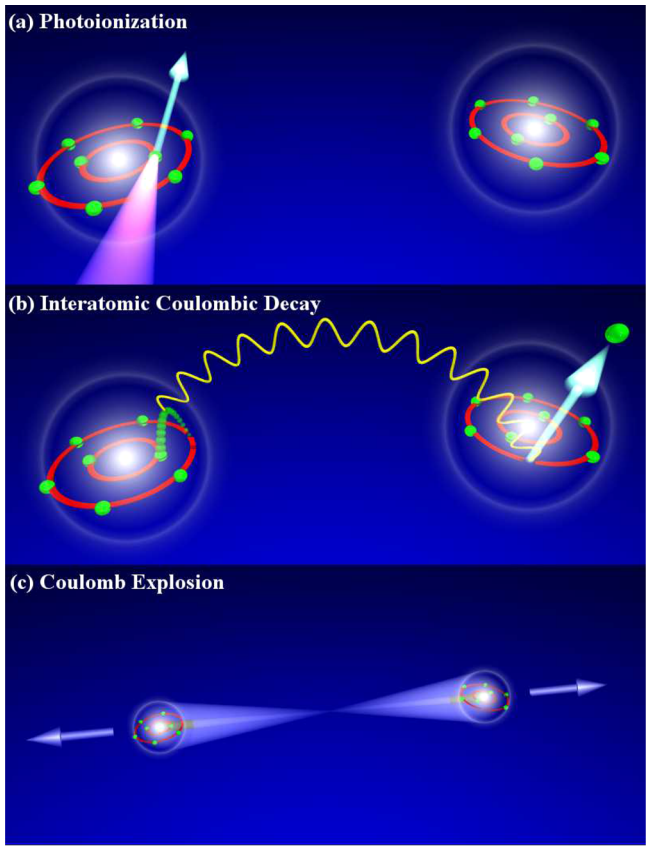

Figure 1. Schematic of a prototypical ICD process in a dimer. (a) An inner-valence electron of one of the atoms is removed by means of photoionization. (b) As ICD takes places, an outer-valence electron fills the inner-valence vacancy. The energy gained in this transition is transferred to the neighboring atom, which is ionized as a consequence. (c) The doubly charged dimer fragments in a Coulomb explosion. Reprinted with permission from ref 2. Copyright 2004 APS.

After the theoretical prediction, it took almost ten years before the existence of ICD was demonstrated experimentally. First evidence for this novel decay route was found by Marburger et al.,[3] and an unequivocal experimental signature for its occurrence in loosely bound matter was provided by Jahnke et al. shortly thereafter by measuring the ICD electron and the two ionic fragments after Coulomb explosion in coincidence.[2] Öhrwall and co-workers demonstrated the predicted high efficiency of ICD in pioneering work by measuring the line width of the inner-valence photoelectron.[4] A reason why ICD has not been recognized in experiments earlier could be the low kinetic energy of typical ICD electrons. In experiments on clusters in the gas phase, a strong low energy electron background (due to inelastic scattering) is a common feature, masking possible ICD electrons.

Conceptually, ICD is described in the same way as Auger decay, a local autoionization decay in which both final state

https://dx.doi.org/10.1021/acs.chemrev.0c00106
Chem. Rev. 2020, 120, 11295−11369

vacancies reside at the initially ionized site. In both processes, an inner-shell vacancy is coupled to and decays into the continuum of states, which comprise two outer-shell vacancies and a freely moving electron.[5] According to Fermi's Golden Rule, the leading coupling element mediating electronic decay is proportional to the square of the electron−electron Coulomb matrix element, given in the molecular orbital representation as[1,6]

$$V_{kio_1o_2} = \iint \phi_k^*(\vec{r}_1)\phi_i^*(\vec{r}_2)\frac{e^2}{|\vec{r}_2 - \vec{r}_2|}\phi_{o_1}(\vec{r}_1)\phi_{o_2}(\vec{r}_2)\,\mathrm{d}\vec{r}_1\,\mathrm{d}\vec{r}_2 \quad (1)$$

where ϕ_k is the orbital of the outgoing electron, ϕ_i is the orbital corresponding to the initial inner-valence vacancy, and ϕ_{o_1} and ϕ_{o_2} are the orbitals representing the final outer-valence vacancies, which are located on the same atom in the case of Auger decay and one on each atom in the case of ICD. Because of the antisymmetry of the electronic wave function, two terms of the type $V_{kio_1o_2}$ contribute to the overall decay rate, which is in first-order perturbation theory, thus proportional to[7]

$$\left|V_{ki[o_1o_2]}\right|^2 = \left|V_{kio_1o_2} - V_{kio_2o_1}\right|^2 \quad (2)$$

While these two contributions do not have an immediate intuitive meaning in the case of a conventional Auger decay, they directly relate to two different physical decay mechanisms in case of ICD because the participating electrons can each be assigned to a specific monomer. The first term $V_{kio_1o_2}$ corresponds to the direct mechanism shown in Figure 2a. Here the inner-valence vacancy is filled by an electron from the same monomer. The energy is then transferred to the neighboring monomer by a classical Coulomb interaction, which is of dipole−dipole type and can thus be seen as a virtual photon transfer leading to the ionization of that neighbor. This contribution has been named direct term in the literature. The second contribution $V_{kio_2o_1}$ relates to a markedly different decay mechanism, which is shown in Figure 2b. In that case, the inner-valence vacancy is filled by an outer-valence electron from the neighboring atom. The energy gathered from this transition is used to release an outer-valence electron from the initially ionized atom. In line with this physical picture and the exchange-nature of the coupling element, this contribution has been named the exchange term.

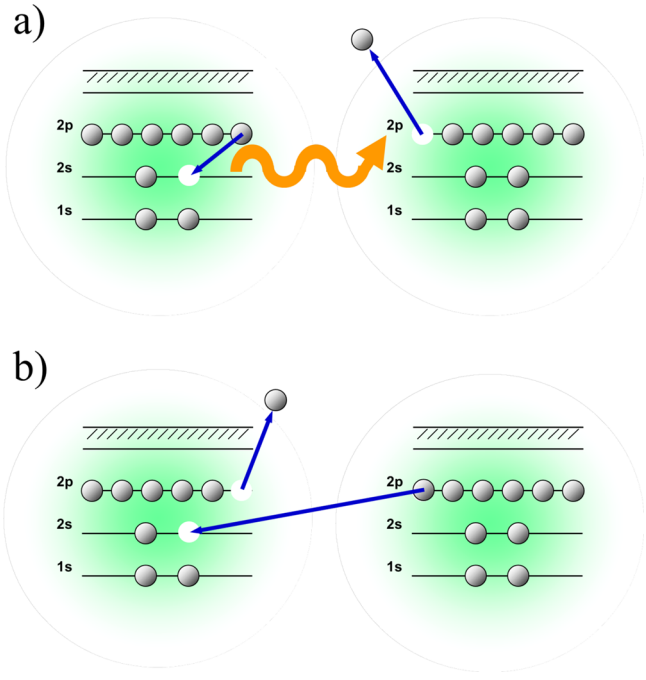

Figure 2. Physical pictures behind the two different contributions to the ICD matrix element (ICD occurring after inner-valence ionization of a neon dimer as an example). (a) Direct term, (b) exchange term. Figure adapted with permission from ref 8. Copyright 2007 APS.

The initial and the final state of the direct and the exchange contribution are obviously identical. However, the two contributions differ in their efficiency. In addition, they depend differently on the internuclear distance R of the two involved monomers. Because the leading term of the direct contribution consists of a dipole−dipole interaction, the corresponding direct ICD rate scales with $1/R^6$ just as expected for an interaction of that kind.[9] In contrast, the exchange term depends on orbital overlap, which is required for electron exchange to happen, and thus the exchange ICD rate decays exponentially with R. Therefore, the direct contribution dominates clearly over the exchange contribution at larger distances. Additionally, different selection rules apply for the two contributions. The direct term only contributes significantly for dipole-allowed transitions. The exchange term does not have this restriction, and only the spin state of the transferred electron needs to match the filled vacancy. By making use of these selection rules, the two contributions to ICD have been separately investigated employing normal and conjugate shakeup ionization of neon dimers[8] (see Section 5.1.1).

Up to now, five major topical review articles on ICD have appeared, which focus on different aspects. The reviews by Hergenhahn[10,11] cover early experimental research. The research of the maturing field has been summarized by Jahnke.[12] An early summary on theoretical aspects of ICD has been provided by Santra and Cederbaum in 2002,[7] and in 2011, Averbukh et al. reviewed more recent theoretical research on ICD.[13] In addition, in 2009, Dias gave a very brief review on the topic,[14] two short reviews on coincident particle detection in the gas phase covered several experiments on ICD as well,[15,16] and a review[17] and a book[18] on core-level spectroscopy of free clusters discuss ICD with respect to this topic. Time domain-aspects of ICD were reviewed in a short article by Frühling et al. in 2015.[19]

Since the early days of ICD, more than 300 articles on different facets of this process and its related phenomena have been published. The present review contains a comprehensive summary of that research. The layout of this article is as follows. The next section will assume a broader perspective on electronic decay processes. The main traits of the ICD process and of various related processes, common features, and differences will be described. We will also connect ICD to nonlocal energy transfer processes examined in other disciplines. Detailed information on computational approaches to model ICD in all its different aspects is presented in Section 3. This section describes various approaches for calculating the electronic structure of transient metastable states in molecules as well as methods for theoretical description of nuclear dynamics accompanying electronic decay of such states. Section 4 deals with different experimental schemes that have been used to investigate ICD. This section covers examples of electron spectroscopy, ion spectroscopy and the

https://dx.doi.org/10.1021/acs.chemrev.0c00106
Chem. Rev. 2020, 120, 11295−11369

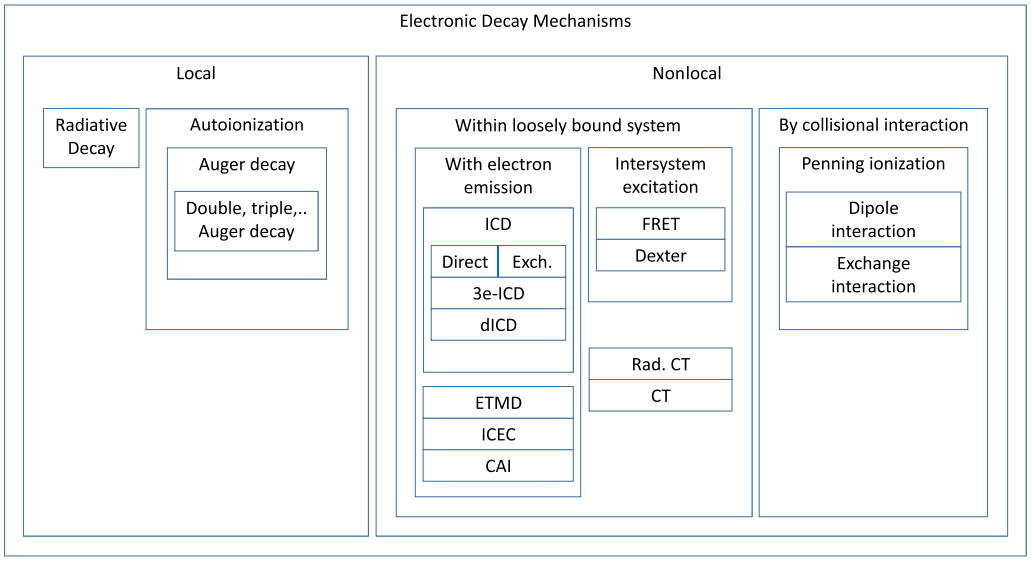

Figure 3. Schematic overview of nonradiative electronic decay processes and their relation. An inner box depicts a subcategory of its surrounding outer box. Abbreviations: **I**nteratomic/**I**ntermolecular **C**oulombic **D**ecay; **Exch**ange (see Section 1); Three electron-ICD (**3e-ICD**) (see Section 5.1.8); double-ICD (**dICD**) (see Section 5.1.8); **E**lectron **T**ransfer **M**ediated **D**ecay (see Section 2.1); **I**nteratomic/**I**ntermolecular **C**oulombic **E**lectron **C**apture (see Section 2.2); **C**ollective **A**uto**I**onization (see Section 5.7); **F**örster **R**esonant **E**nergy **T**ransfer (see Section 2.5); **Dexter** (electron exchange) energy transfer (see Section 2.5); (**Rad**iative) **C**harge **T**ransfer (see Section 2.4).

coincident measurement of electrons and ions, and methods to investigate ICD and its features by employing photon detection and time-resolving techniques. Section 5 incorporates an extensive description of works on ICD divided into the following categories: fundamental investigations, ICD in clusters of different sizes, liquids, biological systems and quantum dots, and cases where ICD and the emitted ICD electron have been employed as a tool for investigations on topics other than ICD. The article closes with a section on future perspectives.

The content of this review is composed of the results of a coordinated research program carried out jointly by the authors, but nevertheless, we aim to cover the field of ICD in full.

2. GENERAL PERSPECTIVE ON ELECTRONIC DECAY PROCESSES

Auger decay has been discovered independently in 1922 and 1925 by Meitner and Auger.[20,21] Since then, many more electronic decay processes have been found, which are driven by electron/electron−Coulomb interaction. Figure 3 provides an overview of these processes and schematically depicts their interrelation. They can be distinguished depending on whether the process occurs locally within an atomic or molecular entity or nonlocally by involving adjacent spatially separated entities. The latter nonlocal mechanisms can be further divided into cases in which the electronic decay process occurs during a collision or within a loosely bound but otherwise stationary molecular environment. The mechanisms displayed in Figure 3 are either covered in specific subsections (as indicated in the figure caption) or described within this section. ICD and ICD-like mechanisms are typically considered as nonlocal decay processes occurring in weakly bound, structurally stable systems. Please note that Auger decay and Penning ionization exhibit a similarly rich substructure as ICD, which is, however, omitted due to the focus of this review.

During the past decade, several other nonlocal de-excitation mechanisms with similar features as ICD have been proposed and studied in experiment and theory. These are presented in the following subsections. Furthermore, it has been realized that in principle in any setting in which nonlocal de-excitation by electron emission is energetically possible, it is the dominating decay channel as it outpaces radiative decay channels. ICD is typically several orders of magnitude more efficient than fluorescence. Comparing nonlocal to local nonradiative decay channels, nonlocal channels dominate in situations in which a local de-excitation is energetically not possible. In the case of inner-valence ionization of neon clusters, for example, the overall energy of the system is not sufficient for a local Auger decay leading to a dicationic Ne ion. Thus, besides fluorescence only ICD is energetically possible, resulting in two cationic Ne ions. In general situations, ICD does of course compete with open local channels. In a molecular environment with several spatially close neighbors, usually a manifold of ICD channels are open, which decreases the ICD lifetime drastically. This has been predicted, for example, for endohedral fullerenes,[22] in which the ICD lifetime has been calculated to be as short as a few femtoseconds. Thus, nonlocal IC-decay involving the fullerene cage is then able to outpace a local Auger decay of the encaged species.

In line with these findings it has been stated that "ICD is everywhere"[23] accounting for the fact that even when more than two species need to be involved in a nonlocal de-excitation process via electron emission, this pathway will commonly occur in nature due to omnipresent molecular environments.

As pointed out before, nonlocal decay phenomena other than ICD (or its related processes) have been examined, as well, and some of them are well established in their respective disciplines. Connections will be made where appropriate, and these aspects will be discussed in the final subsection of this section, that is, Related Mechanisms from Other Disciplines.

https://dx.doi.org/10.1021/acs.chemrev.0c00106
Chem. Rev. 2020, 120, 11295−11369

2.1. Electron Transfer Mediated Decay

Akin to ICD, also electron transfer mediated decay (ETMD) is triggered by an initial vacancy in an, for example, inner-valence or core level. This vacancy is filled by an electron transfer from a neighboring atom or molecule (just as in the case of exchange ICD). Other than in ICD, however, the released energy is transferred either to the donor itself or to another neighboring species and used to ionize it (see Figure 4). To

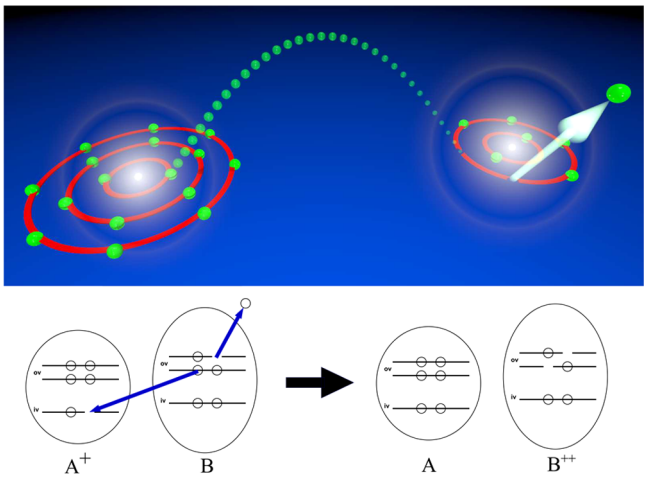

Figure 4. Scheme of ETMD(2): A vacancy in the left atom is filled by an electron of the right atom of a dimer. The energy that is released by this transition is used to emit an electron from the right atom. Bottom: Energy-level representation of the process, depicting the involved inner-valence (iv) and outer-valence (ov) states. Atom A is neutralized after ETMD(2), and atom B is doubly charged (right). The figure has been taken from ref 12.

distinguish the variants of this process involving two versus three entities, they are abbreviated as ETMD(2)[24] and ETMD(3),[25] respectively. Conceptually, ETMD predominantly occurs in heteronuclear systems, as only these can provide energy levels that are adequate for the process, as illustrated in the bottom part of Figure 4. The system's energy levels need to be such that the transition of an electron from atom B to atom A releases an energy sufficiently high to ionize atom B. Accordingly, a first experimental confirmation of ETMD has been provided by Förstel et al. by examining ArKr heteroclusters[26] as proposed in preceding theoretical work.[27] However, at the same time, Sakai and co-workers demonstrated the occurrence of ETMD in a homonuclear system as they observed a corresponding spectroscopic fingerprint in triply charged Ar_2.[28] Because of the asymmetric charge distribution, the energy levels are shifted such that ETMD is possible in homonuclear matter as well.

Two earlier experiments showed already possible evidence of ETMD, but the observed features could not be clearly separated from those of competing processes.[29,30] In 2017, ETMD was finally observed in a liquid.[31] Recent works[32,33] revealed new variants of both ETMD(2) and ETMD(3). They showed[32] ETMD to be a very efficient pathway for neutralization of singly charged and more generally of multiply charged ions produced, for example, in Auger processes. The relevance of ETMD-like processes was theoretically predicted also in situations, in which at the same time local and ICD-like channels are open.[25,34] In all ETMD processes, an additional slow electron is produced, which may trigger interatomic (or intermolecular) Coulombic electron capture (ICEC), which is introduced in the following subsection.

2.2. Interatomic and Intermolecular Coulombic Electron Capture

Electron capture by isolated neutral or ionic atoms can only proceed by photorecombination, that is, the atom captures a free electron by emitting a photon which carries away the excess energy. In molecules, the excess energy is usually redistributed over internal vibrational degrees of freedom creating hot electron-attached molecules. In the presence of a chemical environment, it was shown for atoms, however, that a competing nonlocal nonradiative electron capture process can take place due to long-range Coulombic interactions of the electrons. In this interatomic (intermolecular) process, the excess energy is, in analogy to ICD, transferred to a neighboring entity and ionizes it. The first prediction of this interatomic (or intermolecular) Coulombic electron capture (ICEC) was presented in 2009 by Gokhberg et al.[35] The ICEC process is schematically visualized in Figure 5. An incoming

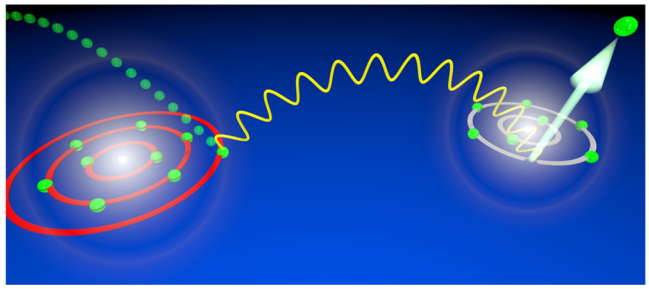

Figure 5. Scheme of interatomic Coulombic electron capture (ICEC). An electron is captured from the continuum into the left atom of a dimer. The energy released in the capture process is employed to free an electron from the right atom.

electron of low kinetic energy is captured by an atom or molecule, and a neighboring atom or molecule releases an electron. As an example, a Mg^{2+} metal ion surrounded by H_2O ligands can be considered. The excess energy released after capture of a free electron at the metal center is sufficient to ionize one of the neighboring H_2O molecules,[35] leading to the reaction:

$$e^- + Mg^{2+}(H_2O)_N \rightarrow Mg^{+}H_2O^{+}(H_2O)_{N-1} + e^-_{ISEC} \quad (3)$$

Coulomb explosion of the two cations in the final state offers a good opportunity to detect the process experimentally.

The ICEC cross-sections were originally derived analytically in the limit of large separation between participating species.[35,36] Similar to the asymptotic expression for the ICD width (see eq 12), the analytic ICEC cross-sections are computed using the electronic properties of the isolated monomers and typically represent lower bounds of the true cross-sections. Calculations for a number of systems demonstrated that ICEC strongly dominates photorecombination in atoms for the capture of slow electrons (<10 eV), even though the distance between the monomers can be as much as a few nanometers. Accurate ICEC cross-sections computed by *ab initio* R-matrix methods reproduce the asymptotic expression at large monomer separations while producing significantly larger values at shorter separations.[37]

Müller et al. proposed and investigated a variant of ICEC,[38−41] in which the capture of an electron on one atomic

https://dx.doi.org/10.1021/acs.chemrev.0c00106
Chem. Rev. 2020, 120, 11295−11369

center leads to the electronic excitation of a neighboring center and subsequent emission of a photon, not of an electron. This two-center dielectronic recombination (2CDR) is a resonant process, acting as an efficient electron capture mechanism in dilute atomic gases. As an example, the reaction

$$\begin{aligned} e^- + H^+ + He^+(1s) \\ \rightarrow H(1s) + He^+(2p_m) \\ \rightarrow H(1s) + He^+(1s) + h\nu \end{aligned} \quad (4)$$

was considered.[38] The two-center process becomes dominant at electron kinetic energies for which the transferred energy matches the He^+ 1s → 2p-resonance condition. In the inverse process to eq 4, a photon resonantly excites an atom or molecule, the "antenna", in a weakly bound complex. Subsequent energy transfer leads to autoionization of a neighboring site. An example for this 'two-center resonant photoionization' is shown in the section on ICD in rare gas clusters, Section 5.2.2.

ICEC was studied theoretically for a number of small clusters that consist of atoms or small molecules. The choice of systems was dictated by the availability of experimental quantities needed to evaluate the asymptotic expressions, or by the computational effort in case of *ab initio* calculations. Notwithstanding the limited number of computed cross-sections, it is clear already now that ICEC is an important electron capture process in weakly bound atomic or molecular environments. In particular, it might be important in solutions or large clusters, since similar to ICD, its efficiency increases with the number of neighbors.[35,42] Since ICEC is a general process, it is not confined solely to atomic and molecular systems. Recently, it was demonstrated by further theoretical work that ICEC is also operative in semiconductor quantum dots (QDs).[43−46] ICEC can take place whenever there are at least two microscopic objects that can accommodate electrons. In 2017, ICEC was finally observed in experiments involving slow highly charged ions impinging a graphene foil. Wilhelm et al. demonstrated that the key to the effective neutralization of the highly charged ion during the passage of the foil is an ICD-like process, that is, ICEC.[47,48] Later work by the same group pointed out the occurrence of a splash of low energy electrons due to ICD and ICEC and emphasized the relevance of ICD and ICEC for ion-induced radiation damage in cells and genes.[49] We will describe these processes in more detail in Section 5.7.5.

2.3. Collective Autoionization

With the advent of free-electron laser light sources,[50] VUV and X-ray light pulses with unprecedented intensity became available. In 2010, Kuleff et al. suggested a novel scheme of ICD, which becomes possible when clusters are irradiated with light pulses in such an intensity regime.[51] Because of the large number of photons present within a very short period of time, several atoms in the same cluster may be excited simultaneously. Upon de-excitation of one of these atoms, the excess energy can be used to ionize one or many other excited atoms (Figure 6a). Müller and Voitkiv investigated other aspects of this process in further theoretical investigations.[52]

Groundbreaking experiments on He droplets showed the existence of the collective ICD mechanism suggested above, but found, at sufficient intensity, that the actual relaxation of the multiply excited clusters prominently involves further de-excitation routes, shown in Figure 6.[53] These were summarized

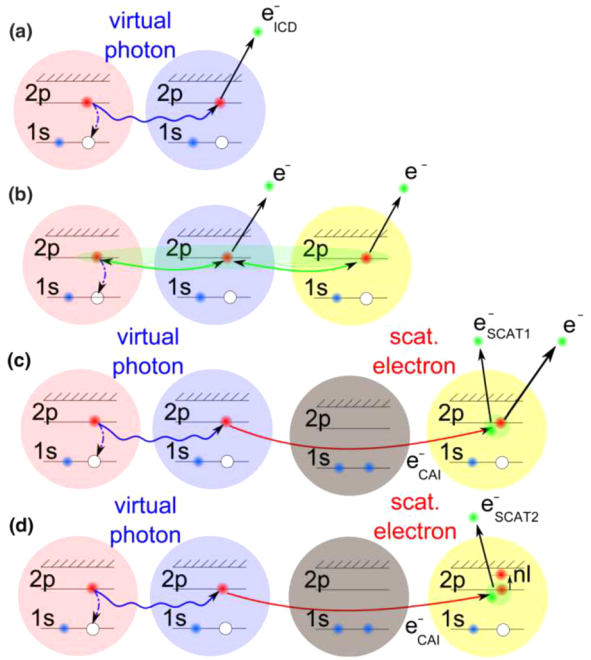

Figure 6. ICD and ICD-like processes after simultaneous excitation of several atoms in a cluster by absorption of multiple photons. See text for details. Reprinted with permission from ref 53. Copyright 2014 APS.

as "collective autoionization". Unlike ICD involving only one excited atom, an ICD-like collective autoionization process may incorporate several excited atoms at the same time, as shown in Figure 6b−d, which may or may not rely on scattering of the ICD electron. Further work on collective autoionization is covered in Section 5.7.

2.4. Radiative Charge Transfer

In weakly bound systems like rare gas clusters, ETMD occurs when an electron is transferred from an environmental atom to an ion, and the released energy is used to expel another electron, either of the donor atom (ETMD(2)) or of another atom in proximity to the ion (ETMD(3)). The latter process has been observed, for example, in heterogeneous NeKr clusters, where a 4*p*-electron of a Kr atom has been transferred to a Ne($2p^{-2}$) dication to fill one of the two vacancies. The released energy is subsequently used to emit a 4*p* electron from yet another neutral Kr atom.[54] This relaxation path is energetically forbidden if the dication resides within a homogeneous environment. Here the released energy due to the transfer of an electron from a neutral atom to the doubly charged ion is not sufficient for further ionization of the same species. Therefore, the surplus energy will be released by emission of a photon as the final state with two delocalized charges is still energetically favored compared to the one-site dicationic state. This process, in which an electron is transferred and a photon is emitted, was termed radiative charge transfer (RCT). It is a well-studied process emerging, for example, in transient molecules created by collisions.[55,56] In ICD-related research, its occurrence has been indirectly concluded in electron−ion coincidence studies on Ne and Ar dimers where the sum kinetic energy of the measured particles did not yield the expected total energy.[57−60] Only recently has RCT been observed directly via a measurement of the spectral characteristic of the emitted photon by dispersed fluorescence spectroscopy[61] and, later, in a photon−electron coincidence

https://dx.doi.org/10.1021/acs.chemrev.0c00106
Chem. Rev. 2020, 120, 11295−11369

experiment.[62] An example of an RCT process is described in the section on ICD in rare gas clusters, Section 5.2.2.

2.5. Related Mechanisms from Other Disciplines

In a most general view, interatomic/intermolecular Coulombic decay describes a nonlocal ionization process in which the energy required for ionization is not deposited at the ionized species itself but at a loosely bound neighbor. The energy is transferred from the excited neighbor to the eventually ionized species by one of the mechanisms depicted in Figure 2a and b. This is, of course, similar to many other energy transfer, electron transfer, or ionization processes known in the literature, closely related ones are Förster[63] or Dexter Resonance energy transfer,[64] photoinduced electron transfer,[65,66] and the assumedly most closely related one, Penning ionization.[67] It is thus fruitful to have a closer look at these and to highlight analogies and differences to ICD.

Förster resonant energy transfer (FRET) was first described in 1948,[63] and more modern reviews can be found in refs 68 and 69. It consists of an energy transfer between two entities, for example, molecules in a solution or pigments in a protein, separated by some distance typically much larger than the sum of the van der Waals radii. One of them is initially (locally) electronically excited, typically by an optical transition. The excited state may, instead of decaying by fluorescence, transfer its energy to another center with an identical energy level spacing via a dipole−dipole interaction or (in other terms) by virtual photon exchange. As a result, the other entity is excited into a bound electronically excited state (with typically large transition dipole moment for FRET to be efficient). Similar to ICD, FRET is thus often observed by quenching radiative decay of the initially excited entity. The rate for Förster resonant energy transfer depends on the distance R between the two entities by R^{-6}, which is, not surprisingly, identical to the rate dependence of direct ICD as given in the asymptotic limit by eq 12. Dexter energy transfer[64] is closely related to the energy transfer step in exchange ICD, as two electrons are exchanged between the two involved entities. One electron of the energy accepting moiety fills the hole of the initially excited one, and one electron of the latter is excited into a valence state of the former, in analogy to Figure 2b. The Dexter transfer rate decays exponentially with the distance and is thus only significant at short intermolecular distances. For FRET or Dexter transfer to occur, two transitions between discrete energy levels are involved. Thus, these have to be in resonance, for example, degenerate to ensure energy conservation. To generate the degeneracy of the levels of the two participating (molecular) entities, typically nuclear dynamics need to be involved, yielding the comparably long time scales of these nonlocal decay mechanisms. Such resonance requirements are intrinsically fulfilled in case of ICD because the energy accepting molecule is ionized and the emitted electron can take up the matching amount of kinetic energy to ensure the resonance condition. ICD processes can thus be expected to be much more efficient than FRET or Dexter energy transfer.

A process, which is usually treated within the framework of FRET theory, is photoinitiated electron transfer (PI-ET).[65,66] In most PI-ET processes, a molecule or pigment is directly photoionized, and the electron is transferred to a neighboring electron-accepting molecule. In some cases, however, a specific molecule, a so-called antenna molecule, is first electronically excited, its energy transferred to a neighboring atom, and an electron is transferred to a third electron-accepting partner. This is, for example, the case in photolyases, which are described in more detail in Section 5.4. For clarity, we will refer to these processes as FRET-ET to distinguish them from PI-ET by direct photoionization of the electron donating molecule. Whether such a process is a FRET-ET process, that is, a transition between two bound states, or an ICD process, that is, a transition between a bound electronically excited and a continuum state, depends to some extent on the perspective. If the electron donating molecule treated individually and the outgoing electron seen as a free electron, then beyond any doubt, it is a so-called resonant ICD process, which refers to the ionization of a neighboring molecule by an initially excited neutral one, which is not initially also ionized. However, if the electron donating and accepting molecules are treated as one entity and the electron-transfer state is electronically stable, the process can be seen as a FRET-ET. Hence, the distinction between FRET-ET and resonant ICD hinges upon the character of the transferred electron, is it bound or is it free? Or in other words, is the electron while being transferred still coupled to its donating molecule or already coupled to the accepting one? This certainly depends on the distance between donating and accepting moiety, and the larger is their distance, the larger is the free character of the electron. Hence, at short distances and in the case of electronically coupled donating and accepting moieties such a process corresponds certainly more to a FRET-ET, and at larger distances to a resonant ICD process. One possible measure is thus the distance between them or the transition dipole moment of the final ET state, which in the case of nonoverlapping donating and accepting wave functions is strictly zero. However, the transition between FRET-ET and resonant ICD is certainly smooth.

Penning ionization,[67] named after Frans Penning, is another related ionization mechanism, which occurs, for example, in collisional processes of electronically excited He atoms (mostly in a metastable triplet state) and other atoms or molecules in their ground-state.[70] The nonexcited entity is ionized during an ultrashort collision event:

$$\mathrm{He}^* + \mathrm{A} \rightarrow \mathrm{He} + \mathrm{A}^+ + e^- \tag{5}$$

While this reaction looks conceptually similar to an ICD process, Penning ionization is different from ICD because it occurs during a collision and not within a loosely bound (i.e., static) molecular complex or cluster of atoms. The collision process sets strict limits to the energy transfer rate due to the ultrashort lifetime of the intermediate collision complex during which the transfer has to occur. Because of this short interaction time, Penning ionization almost exclusively occurs via the exchange mechanism depicted in Figure 2b, which relies on orbital overlap and thus becomes very efficient at small internuclear distances R. An energy transfer via dipole−dipole interaction (i.e., virtual photon exchange, see Figure 2a, scaling, as mentioned before, with R^{-6}) by quadrupole interaction (scaling with R^{-8}) or even by spin−orbit interaction (scaling with R^{-10}) is too slow for such collision events. Accordingly, the overall Penning ionization rate has been observed experimentally to decay exponentially with the distance R between the colliding species. In ICD, on the contrary, the rate is practically exclusively determined by the direct mechanism due to the typically already large distances between the monomers at the equilibrium geometries of the static complexes or clusters. As a consequence, the ICD rate decays only with R^{-6}, and thus, ICD is a long-range effect as

https://dx.doi.org/10.1021/acs.chemrev.0c00106
Chem. Rev. 2020, 120, 11295−11369

FRET. Summarizing, Penning ionization is dominated by an electron-exchange type mechanism occurring in collision processes, while ICD is mostly a virtual-photon-exchange type mechanism occurring in weakly bound, static molecular complexes and atomic clusters.

3. THEORETICAL APPROACHES

The electronic states decaying by ICD belong to the class of metastable states known as electronic resonances. Electronic resonances are ubiquitous in physical chemistry and always appear whenever free electrons are present. Apart from ICD, electronic resonances are also central to processes such as autoionization,[71] the Auger effect,[72] and electron-activated chemical reactions,[73,74] all of which involve free electrons. In ICD, the final states of an electronically decayed chemical system, comprising the electron-detached system and the free electron, lie in the electronic continuum above the ionization potential of the initial system and are thus described by continuum eigenfunctions of the electronic Hamiltonian. Around certain discrete energies, E_r, in the spectrum of the final continuum states, an unbound electron has a large probability to be found localized at some atom or molecule of the chemical system, while at larger distances its wave function oscillates like the one of a free particle.[75] This peculiar behavior of the eigenfunction, which combines the features both of a bound and continuum wave function, indicates the presence of a resonance, and exciting atoms or molecules close to a resonance energy E_r populates metastable electronic states, or electronic resonances, which decay within some characteristic lifetime τ by emitting an electron. As will become clear from the discussion below, the resonances are not eigenstates of the electronic Hamiltonian, so that a system in a resonance state does not have a well-defined energy. Instead, the resonances are characterized by their position E_r and the energy width

$$\Gamma = 1/\tau \tag{6}$$

that is inversely proportional to the lifetime (atomic units $\hbar = m_e = e = 1$ are used throughout).

The particular structure of the continuum eigenfunctions close to resonance energies inspired different ways of viewing the resonances and resulted in the development of two prominent computational approaches to calculate their energies and widths.[75] In the Fano−Feshbach approach, which we discuss in Section 3.1, the resonance is described as a bound state embedded in and interacting with the electronic continuum. Initial excitation populates this bound state, which then leaks out into the continuum at a characteristic rate. In the second approach, which is described in Section 3.2, resonance states are calculated as discrete eigenstates of some non-Hermitian Hamiltonian with complex eigenenergies $E = E_r - i\Gamma/2$. Since the eigenenergies have a negative imaginary part, such states decay in time and color, and the imaginary part corresponds to the half of the energy width in eq 6. Both approaches have been actively used for computing energies and lifetimes of ICD states, which usually serve as input for simulations of experimental spectra, for example, ICD electron spectra and kinetic energy release (KER) spectra. In the following, we review these two major theories for the description of resonance states and the respective computational methods, which are based on them. In the last section, Section 3.3, we discuss the simulation of nuclear dynamics on complex resonance potential energy surfaces and numerical computation of ICD spectra.

3.1. Fano−Feshbach Theory of Resonances and Resulting Computational Approaches

The idea of a resonance as a bound state embedded in the electronic continuum was most clearly enunciated in the papers by U. Fano[71] and H. Feshbach.[76,77] At energy E close to a resonance energy E_r, the continuum solution Ψ_E of the electronic Schrödinger equation

$$\hat{H}\Psi_E = E\Psi_E \tag{7}$$

is assumed to be given in the following form:

$$\Psi_E = a(E)\Phi + \sum_\beta \int \mathrm{d}E b_\beta(E)\chi_{\beta\varepsilon_e} \tag{8}$$

where Φ is a bound-like part of the resonance, and $\chi_{\beta\varepsilon_e}$ is a wave function that describes an unbound electron moving away with kinetic energy ε_e and leaving the remaining system in the electronic state β. The integration over E and summation over β in eq 8 are carried over all continuum electronic states $\chi_{\beta\varepsilon_e}$. To construct Φ and $\chi_{\beta\varepsilon_e}$, subspaces of the energetically forbidden and allowed final states are defined, which comprise square integrable and continuum wave functions, respectively, together with the corresponding projectors Q and P. Projection of $\hat{H}$ on these subspaces of forbidden and allowed final states and solution of the two corresponding eigenvalue problems

$$\hat{H}_{QQ}\Phi = E_\Phi\Phi,\ \hat{H}_{PP}\chi_{\beta\varepsilon_e} = E\chi_{\beta\varepsilon_e} \tag{9}$$

subject to the conditions

$$\langle\Phi|\Phi\rangle = 1,\ \langle\chi_{\beta'\varepsilon_e'}|\chi_{\beta\varepsilon_e}\rangle = \delta_{\beta,\beta'}\delta(\varepsilon_e - \varepsilon_e'),\ P \times Q = 0 \tag{10}$$

yields Φ and $\chi_{\beta\varepsilon_e}$. Inserting the ansatz of eq 8 into the Schrödinger eq (eq 7) one solves for $a(E)$ to obtain

$$|a(E)|^2 = \frac{1}{2\pi}\frac{\Gamma(E)}{(E - E_\Phi - \Delta(E))^2 + \Gamma(E)^2/4},$$
$$\Delta(E) = \sum_\beta P\int_0^\infty \mathrm{d}\varepsilon_e \frac{|\langle\chi_{\beta\varepsilon_e}|\hat{H}_{PQ}|\Phi\rangle|^2}{E - E_\beta - \varepsilon_e},$$
$$\Gamma(E) = 2\pi\sum_\beta |\langle\chi_{\beta\varepsilon_e}|\hat{H}_{PQ}|\Phi\rangle|^2 \tag{11}$$

From eq 11, it can be recognized that a previously bound state shifts by $\Delta(E)$ and acquires a finite energetic width $\Gamma(E)$, when the interaction with the continuum is switched on, that is, when the coupling element between the wave functions of the outgoing electron and the bound state $\langle\chi_{\beta\varepsilon_e}|\hat{H}_{PQ}|\Phi\rangle$ is nonzero. For narrow resonances, to which class the ICD states belong, one assumes that neither $\Delta(E)$ nor $\Gamma(E)$ vary much around E_Φ, and they can be replaced by their values at E_Φ:[71] $\Delta \approx \Delta(E_\Phi)$ and $\Gamma \approx \Gamma(E_\Phi)$. In practical applications of the Fano−Feshbach theory to ICD, $\Delta(E)$ is usually not computed since it constitutes only a small correction to the energy of the ICD state comparable to numerical errors of its *ab initio* computation.

For numerical computations of decay widths via the Fano−Feshbach theory, one needs to choose an appropriate

https://dx.doi.org/10.1021/acs.chemrev.0c00106
Chem. Rev. 2020, 120, 11295−11369

approximation level for the electronic Hamiltonian and to select the corresponding N-electron wave functions spanning the P- and Q-subspaces of the allowed and forbidden final states. In the most straightforward approach, which goes back to the first calculation of Auger decay rates,[78] the N-electron bound-like and continuum states have been represented by Slater determinants constructed from a suitable Hartree−Fock reference state, and $\hat{H}$ is thus given as a part of a configuration interaction (CI) matrix. This method has later also been applied to compute ICD lifetimes of the inner-valence 2s hole of Ne in Ne_n clusters,[79] NeAr,[24] Ne-alkaline earth,[9] and in Ne@C_{60}[80] as well as to calculate resonant ICD rates in NeMg and Ne_2.[81,82] In the ICD literature, it is referred to as the Wigner−Weisskopf method. In an improved variant of this method, called Fano-CI,[83] the final states $\chi_{\beta\varepsilon_e}$ are not represented only as one single Slater determinant but as a linear combination of the latter.

The Wigner−Weisskopf method is computationally efficient and easy to implemen;, however, it possesses several fundamental drawbacks: (i) it is incapable of accurately describing decaying states with an electron in a valence orbital, (ii) it underestimates the polarization of the neighboring entity when the decaying state is ionic, and (iii) it lacks orbital relaxation in the final state. This usually leads to a severe underestimation of Γ, in particular, for ICD processes with highly polarizable neighboring atoms or molecules. These deficiencies of the Wigner−Weisskopf method are generally remedied by using correlated decaying and final states within the Fano−Feshbach theory.

While any post Hartree−Fock method is generally suitable, the propagator based algebraic diagrammatic construction (ADC) approach has been widely used to compute ICD widths (see Section 5). ADC(n) schemes provide representations of many-body quantities, such as of the polarization propagator,[84,85] of the one-particle Green's function,[86,87] or of the two-particle propagator,[88] which give direct access to excitation energies and single and the double ionization potentials, respectively. ADC(n) schemes are generally correct to n-th order in perturbation theory for the primary particle-hole, hole or two-hole states, and unlike configuration interaction (CI) methods, they are size-consistent and the computed properties are size-intensive, which is an important property particularly for studying weakly bound systems. In addition, ADC(n) schemes are computationally more efficient than the corresponding coupled cluster schemes of the same formal correct order of perturbation schemes; however, the efficiency gain sometimes comes at the prize of lower accuracy.[89,90] Importantly, the ADC secular matrix is just an electronic Hamiltonian represented in the basis of some specific correlated, intermediate states that can be explicitly constructed.[91−94] This so-called intermediate state representation (ISR) provides direct access to excited states wave functions and thus excited states properties.[95,96] More importantly, exploiting the ISR allows for the implementation of efficient Fano-ADC methods for computing more accurate electronic decay widths of neutral[97−99] as well as of singly[100] and doubly ionized states.[101]

The construction of meaningful P- and Q-subspaces within Fano theory for an N-electron state requires the grouping of the ISR basis states of the respective configuration classes, for example, within ionization ISR-ADC of the one-hole (1h) and two-hole-one-particle (2h1p) states, into allowed and forbidden decay channels. The most general way is to first compute the final $(N-1)$-electron states and then to find the energetically allowed states, that is, open channels, which then define the P-subspace of the N-electron ADC-ISR states. The corresponding orthogonal complement of P forms the Q-subspace (see refs 102 and 103 for details). Alternatively, the different spatial localization of electronic holes in the decaying and final states can be used as selection criterion, resulting in a more straightforward and less cumbersome construction of P- and Q-subspaces. This approach has been particularly useful in the computation of ICD widths in rare gas clusters, in which the atoms interact only weakly and the valence orbitals, which accommodate the holes in the final state, retain their atomic character (see, e.g., refs 98, 100, 101, 104). In clusters that exhibit inversion symmetry, this spatial selection criterion becomes impractical, since the valence orbitals are delocalized by symmetry, and one needs to enforce the localization of the occupied molecular orbitals prior to the selection.[22,82]

A meaningful representation of the electronic continuum in the ICD final states is another important aspect of the numerical implementation of Fano−Feshbach approaches. Most naturally, proper one-electron continuum functions can be used for the construction of the final states $\chi_{\beta\varepsilon_e}$.[105,106] Unlike square-integrable bound state functions, continuum functions do not vanish at large distances and can thus not be normalized to unity but instead to the δ-function in energy. Such functions have been used for ICD width calculations in diatomic clusters in the framework of the Wigner−Weisskopf theory. In addition to the correct treatment of the electronic continuum, proper continuum functions also provide angular distributions of ICD electrons.[107] Efficient implementations of post-HF methods are however usually based on square-integrable Gaussian-type functions, which produce only a discrete pseudocontinuum exhibiting the wrong normalization. Nevertheless, these states can be used to compute accurate bound-to-continuum transition moments, for which the long-range behavior of the continuum wave function is irrelevant.[108] Fano-ADC implementation used to compute ICD widths typically apply the Stieltjes imaging technique to obtain correctly normalized decay widths $\Gamma(E)$. The Stieltjes imaging procedure provides approximations to continuum properties, such as for instance $\Gamma(E)$, by computing it from its N first spectral moments calculated within the original square integrable pseudospectrum.[109−114] To avoid the otherwise required full diagonalization of H_{PP}, the matrix representation of $\hat{H}$ in the subspace of the allowed final states, within the computation of the full pseudocontinuum spectrum, the iterative block Lanczos procedure[115] is employed.[98,99] In larger clusters, the computational effort of a full Fano-ADC calculation can further be strongly reduced by combining the Fano-ADC method with the diatomics-in-molecules technique without seriously impairing the accuracy.[116] The application of Stieltjes imaging can generally be avoided by employing the so-called R-matrix method, which uses properly normalized continuum orbitals in constructing scattering wave functions.[117] Alternatively, discrete pseudocontinuum wave functions can be used without renormalization to describe electronic decay in multiply ionized clusters in which the emission of ICD electrons is frustrated by the cluster charge.[118]

Starting with the expression for Γ in eq 11, one can derive a useful analytical formula valid for a system consisting of two monomers (i.e., a rare gas dimer) at large separations between

https://dx.doi.org/10.1021/acs.chemrev.0c00106
Chem. Rev. 2020, 120, 11295−11369

the initially excited species and its neighbor. At such separations, the de-excitation and the ionization occur on almost isolated species and are coupled by the electron repulsion term, which can be written in the form of a multipole expansion. For the dipole allowed de-excitation step, in other words, direct ICD, one obtains

$$\Gamma = C(E)\frac{f^{(A)}\sigma_{ph}^{(B)}}{R^6}\Bigg|_{E=\Delta E} \tag{12}$$

where $f^{(A)}$ and ΔE are the oscillator strength and the energy of the transition on the species A, respectively, $\sigma_{ph}^{(B)}$ is the photoionization cross-section of species B, R is the distance between A and B, and the prefactor $C(E)$ depends on the transition energy and the symmetries of the initial and final states.[9,119] To obtain the total decay width, one should sum over all ICD final states. In the case of more than one neighbor, and assuming that they interact weakly among themselves, one should sum the expression in eq 12 over all neighbors. The asymptotic formula works well at large R; however, it tends to underestimate the width at smaller R due to the neglect of the exchange part of the coupling element.[9] This is very similar to the relations obtained for FRET and Dexter energy transfer between two bound species as previously described in Section 2.5. A similar approach has been used in ref 120 to obtain the ICD rate in a system consisting of two spatially separated chromophores within a protein, in which the Coulomb coupled transition electron densities have been integrated. The $1/R^6$ dependence is characteristic for energy transfer processes via dipole−dipole interaction as leading term; however, it needs to be corrected in the case of large excitation energies or in the presence of polarizable media due to additional quantum electrodynamic effects, usually leading to a considerable increase of the ICD width.[121]

In the Fano−Feshbach theory, the resonance energy, or its position, is given by $E_r \approx E_\Phi + \Delta(E_\Phi)$, and since the correction $\Delta(E)$ is generally very small, it is usually omitted. However, restricting the Hamiltonian to the Q-subspace in computations of these energies reduces their accuracy due to the poor description of electron correlation between the electrons of different species. This results in a reduced accuracy of the respective potential energy surfaces, which leads to lower binding energies of the ICD states of rare gas clusters (i.e., shallower minima of the respective PESs).

When accurate potential energy surfaces of ICD states are needed, they can be computed by any post-HF method, for example, ADC or equation-of-motion coupled cluster EOM-CC, which are capable of obtaining highly excited electronic states.[122,123] Generally, the underlying atomic Gaussian basis sets need to be carefully chosen, and it is a particularly challenging task in the calculation of resonances. Increasing the number of basis functions not only improves the description of electron correlation in the decaying state but also increases the density of the final pseudocontinuum states among which the decaying state lies. When the pseudocontinuum becomes too dense, multiple crossings and interactions with the decaying state make it practically impossible to extract the potential energy surfaces of interest, while the energies of the electronically stable initial and final states of an ICD process can still be calculated in a straightforward way by standard post-HF *ab initio* methods.

In the case of rare gas dimers, estimates of ICD electron and KER spectra can be also be obtained by simple mathematical modeling of the decaying and final states potential energy curves (PECs). At asymptotic distances their energies are just equal to the sum of the energies of the corresponding atomic states. At shorter distances the bound state PECs are just lines of constant energy, while it is represented by a k/R curve, if the PEC is repulsive. This simplified approach has been shown to yield accurate results when ICD proceeds faster than the nuclear dynamics in the decaying state, so that the decay occurs mostly at the equilibrium geometry of the dimer.[124,125]

When heavy atoms are involved in ICD processes, for example, as in clusters containing heavy atoms, relativistic effects are expected to impact both ICD electron spectra and ICD rates. These effects can be included in the computation via, for example, scalar relativistic corrections and spin−orbit couplings. At a higher level of sophistication, four-component relativistic ADC methods have been developed for ionized,[126,127] doubly ionized,[128] and excited[129] electronic states. A corresponding fully relativistic Fano−Feshbach method[130] made the study of relativistic effects in ICD possible. Computed low energy electron spectra of HI and LiI dimers,[131] and of rare gas clusters,[27,132,133] demonstrated the importance of taking relativistic effects into account. For example, their inclusion leads to the overlap of the ICD and ETMD peaks in the electron spectra of XeAr clusters.[133] The most dramatic impact of relativistic effects was demonstrated in PtF_6^{2-} (ref 134) and XeKr clusters,[135] in which the energy of the final states has been lowered due to relativistic effects opening electronic decay channels, which were closed in nonrelativistic calculations.

3.2. Analytic Continuation into the Complex Energy Plane

Resonance states have been shown by Siegert[136] to be computationally accessible by solving eq 7 when specific boundary conditions for its solutions are imposed. If one demands the wave function to comprise only an outgoing electronic wave packet and no incoming one, the Hamiltonian becomes non-Hermitian and possesses states with complex energies $E = E_r - i\Gamma/2$, which can be identified as resonances. Such Siegert states look like bound states in the vicinity of the decaying system; however, the wave function exponentially diverges farther away from it.[75] Although this idiosyncratic behavior of Siegert states makes them formally unsuitable for numerical calculations, this behavior can be practically corrected by applying several related mathematical techniques.

A first technique, called complex coordinate rotation or complex scaling, consists in replacing the real coordinates of electrons r_i by scaled coordinates $r_i \exp(i\theta)$.[137,138] The non-Hermitian Hamiltonian obtained under this transformation was rigorously shown to possess the same energy eigenvalues for the bound and resonance states as the original unscaled Hamiltonian. Most notably, the complex rotation angle θ can be chosen to make divergent Siegert wave functions square-integrable and, therefore, amenable to numerical calculation. The same effect can also be achieved by using complex one-particle basis functions[139] or by introducing complex potentials into the electronic Hamiltonian.[140,141]

Within the complex absorbing potential (CAP) technique, one solves for the complex eigenvalues of the following Hamiltonian

$$\hat{H}(\eta) = \hat{H} - i\eta\hat{W} \tag{13}$$

https://dx.doi.org/10.1021/acs.chemrev.0c00106
Chem. Rev. 2020, 120, 11295−11369

in which $\hat{W}$ is some positive real potential, and the positive real parameter η determines the CAP strength. In practical applications, $\hat{W}$ is selected to not perturb the bound electrons of the decaying system but to efficiently absorb the outgoing electronic wave function to avoid its reflection by the CAP. Different possible choices of CAPs are discussed in ref 142, which can readily be incorporated into *ab initio* electronic structure methods and applied to calculate atomic and molecular electronic resonances.[7,143−146] For the calculation of the complex resonance energies, one needs to compute so-called $E(\eta)$ trajectories and to identify their stabilization points in the complex energy plane, whose real and imaginary parts correspond to the resonance position and its width. Therefore, $H(\eta)$ needs to be diagonalized for many different values of η, which is the computational bottleneck of this procedure and which can be circumvented by several approaches. In principle, the complex Hamiltonian (eq 13) can be projected onto a small subspace of real eigenstates of $\hat{H}$ with energies close to the energy of the resonance,[147] resulting in much smaller matrices and thus much faster diagonalization. Filter diagonalization of the Hamiltonian matrix has been suggested as an efficient way to obtain the required subspace.[143,148] Alternatively to the subspace projection, one may use iterative diagonalization techniques such as complex Davidson or Lanczos methods,[7,149] which converge fast to the resonance and leave out superfluous continuum states.

The complex energies of ICD resonance states have been computed by a number of CAP-based techniques. The CAP-CI method has been employed to obtain energies and widths of ICD states in $(HF)_n$[150] and Ne_2[143,151−153] following single or double ionization of one monomer. The derivation of the ISR representation for ADC methods made it possible to include one-particle operators and potentials like $\hat{W}$ into the Hamiltonian matrix and enabled the development of CAP-ADC methods.[7,144] The latter have been applied to investigate ICD states in resonantly excited molecule−atom complexes,[154] and inner-valence ionized Ne clusters.[144] The more recently developed CAP/EOMCC method[145] has been applied for computing energies of inner-valence ionized ICD states in small rare gas[155] and hydrogen bonded clusters.[156,157] While one great advantage of CAP-based methods is their ability to compute both the corrected resonance energies and resonance widths directly, their major disadvantage lies in their enormous computational costs entailed in the required multiple diagonalizations of complex-symmetric Hamiltonian matrices needed to locate the resonance energy and width in the complex plane.

Unfortunately, the accurate CAP-based and Fano−Feshbach approaches are computationally very demanding and currently not applicable to large molecules with more than just a few atoms. Still, an approximate yet applicable approach to estimate the energy and width of an electronically metastable state is provided by the so-called stabilization method.[158−160] The gist of the stabilization method is to smoothly increase the size of the one-particle basis set used to solve electronic Schrödinger equation by adding more and more diffuse basis functions. As a result, the continuum states as well as the resonances are described better and better, and their energies decrease. Since continuum states are diffuse, their energies vary strongly with the basis set size. However, the energy of a resonance state is known to stabilize at some value and remain nearly constant for a broad range of basis set sizes. This "stable" energy is to be identified as the vertical excitation energy of the resonance state. There are also a number of techniques[158,161] that allow extraction of the resonance width from the stabilization graphs, that is, the plot of all energy eigenvalues of the electronic Hamiltonian as a function of the basis set size. These were used to determine the ICD resonances of a reduced flavine adenine dinucleotide ($FADH^-$) in photolyases[120] reviewed in Section 5.4, and in semiconductor quantum dots,[162] which are the topic of Section 5.5. In a related approach, the complex potential energy curves of ICD states in LiHe were computed by Landau et al.[163] via analytic continuation of stabilization graph into the complex plane.

3.3. Nuclear Dynamics and ICD Spectra

The important observables of ICD are the ICD electron and KER spectra. They can be obtained independently by theoretical computation or experimental measurement and as such provide a link between theoretical predictions and experimental observation. Their accurate computation requires taking the motion of the nuclei into account. The required nuclear Schrödinger equation can be obtained by generalizing the Born−Oppenheimer approximation to the case of electronic resonances[164] (see also eqs 14a and 14b). The observable quantities are obtained by propagating the nuclear wave packet on the potential energy surfaces (PESs) of the decaying and final electronic states. The respective PES, $V(R)$, and the ICD widths, $\Gamma(R)$, which serve as input to the nuclear dynamics calculations, are obtained as functions of nuclear coordinates by electronic structure methods described in the preceding sections. The full theory of the nuclear dynamics accompanying electronic decay processes, including broad-band and narrow-band excitation or ionization, as well as possible nonadiabatic couplings between several overlapping decaying states, has been developed in refs 165−170.

Here, the theory is reviewed for the case of electronic decay of a singly ionized electronic state $|d\rangle$ of a molecule into the electronic continuum associated with one final doubly ionized electronic state $|f\rangle$. For simplicity, the decaying state is assumed to be populated via a weak-field broad-band ionization of a neutral molecule in its ground vibronic state $|v_0\rangle$. In this case, the ionization occurs instantaneously at $t = 0$, and the time evolution of the system in the initial state can be replaced by initial conditions[167] (see below). The nuclear dynamics accompanying the electronic decay $|d\rangle \rightarrow |f\rangle + e^-$ can now be described in terms of the wave packets $|\Psi_d(R, t)\rangle$ and $|\Psi_f(\varepsilon_e, R, t)\rangle$ propagating, respectively, on the PESs of the decaying and final electronic states. The wave packets satisfy the following system of coupled differential equations:[167,169]

$$i|\dot{\Psi}_d(R, t)\rangle = \left(\hat{H}_d(R) - \frac{i}{2}\Gamma(R)\right)|\Psi_d(R, t)\rangle \tag{14a}$$

$$i|\dot{\Psi}_f(\varepsilon_e, R, t)\rangle = W_{fd}(R)|\Psi_d(R, t)\rangle + (\hat{H}_f(R) + \varepsilon_e)|\Psi_f(\varepsilon_e, R, t)\rangle \tag{14b}$$

Here, all active nuclear degrees of freedom are denoted by the coordinate R. The Hamiltonian operators for the nuclear motion in the initial and final electronic states $\hat{H}(R)=\hat{T}_R+V(R)$ consist of the nuclear kinetic energy $\hat{T}_R$ and the precomputed potential energy surface $V(R)$. The transition matrix element describing electronic decay is defined as $W_{fd} = \langle f|\hat{H}^{ee}|d\rangle$, and the local approximation[171,172] has already been applied to decouple eq 14b for different kinetic energies ε_e of the emitted

https://dx.doi.org/10.1021/acs.chemrev.0c00106
Chem. Rev. 2020, 120, 11295−11369

electron from eq 14a. Hence, the total decay width of the initial state $|d\rangle$ is given by $\Gamma(R) = 2\pi\sum_f |W_{fd}(R)|^2$. To start integrating eq 14a, the following initial conditions should be used:

$$|\Psi_d(R, 0)\rangle = |v_0\rangle \quad \text{and} \quad |\Psi_f(\varepsilon_e, R, 0)\rangle = 0 \tag{15}$$

These conditions assume an instantaneous vertical transition of the nuclear wave packet from the neutral ground vibronic state $|v_0\rangle$ onto the PES of the singly ionized decaying electronic state $|d\rangle$.

The nuclear wave packets $|\Psi_d(R, t)\rangle$ and $|\Psi_f(\varepsilon_e, R, t)\rangle$ contain all necessary information about the time-evolution of relevant observables. For instance, the autocorrelation function

$$P_d(t) = \langle\Psi_d(R, 0)|\Psi_d(R, t)\rangle \tag{16}$$

defines the survival probability of the decaying electronic state $|d\rangle$ such that $P_d(\infty) = 0$ after the decay is completed. It also gives access to the time-dependent absorption spectrum for monitoring the production of the decaying state. For broad-band ionization of a molecule, it is given by[165,166,169]

$$\sigma_{abs}(\omega) \approx Re\left(\int_0^\infty e^{i\omega t} P_d(t)\, dt\right) \tag{17}$$

The time-evolution of the spectrum of the emitted electrons during decay is given by the norm of the final wave packet:

$$\sigma_{el}(\varepsilon_e, t) = \langle\Psi_f(\varepsilon_e, R, t)|\Psi_f(\varepsilon_e, R, t)\rangle \tag{18}$$

In the case of only one final electronic state $|f\rangle$, the electronic spectrum at the end of the decay is normalized to the initial population of the decaying state via $\int\sigma_{el}(\varepsilon_e, \infty)\, d\varepsilon_e = P_d(0)$. Typically, an inner-valence ionized system, which undergoes ICD, fragments additionally in a Coulomb explosion of the final doubly ionized electronic state $|f\rangle$. In this case, the KER spectrum, that is, the distribution probability over the kinetic energy ε_n of all dissociation fragments in the center-of-mass frame, is given by the projections of the final wave packet onto a set of the continuous vibrational wave functions $|v_f\rangle$ via[173,174]

$$\sigma_{\text{ker}}(\varepsilon_n, t) = \int |\langle v_f|\Psi_f(\varepsilon_e, R, t)\rangle|^2\, d\varepsilon_e \tag{19}$$

Here, $|v_f\rangle$ are the vibrational eigenstates of the Hamiltonian $\hat{H}_f(R)$ with the energy $E_f = V_f(\infty) + \varepsilon_n$. The final KER spectrum is also normalized to the initial population of the decaying state according to $\int\sigma_{KER}(\varepsilon_n, \infty)d\varepsilon_n = P_d(0)$.

To treat nuclear dynamics within time-dependent wave packet propagation theory, one has to solve coupled time-dependent Schrödinger equations (eqs 14a and 14b) in a multidimensional coordinate space R. For this purpose, very efficient numerical algorithms have been developed and coded in Heidelberg, resulting in a powerful tool for the theoretical study of nuclear dynamics of molecules. A very efficient method for accurate simulations of quantum dynamics in molecular systems is multi-configuration time-dependent hartree (MCTDH),[175−177] allowing researchers to determine the quantum motion of nuclei evolving on several coupled potential energy surfaces.[178] An alternative and fully equivalent approach[179] to access the time-evolution of relevant observables is to describe nuclear dynamics, accompanying electronic decay in molecules, in terms of stationary vibrational eigenstates of the initial decaying $|d\rangle$ and final $|f\rangle$ electronic state PESs. For the case of a broad-band ionization of a neutral molecule from its ground vibronic state $|v_0\rangle$, time-evolution of the coincidence decay spectrum $\sigma(\varepsilon_e, \varepsilon_n, t)$ is given by[180]

$$\sigma(\varepsilon_e, \varepsilon_n, t) = \left|\sum_{v_d} \frac{\langle v_f|W_{fd}|v_d\rangle\langle v_d|v_0\rangle}{\varepsilon_e + V_f(\infty) + \varepsilon_n - E_{v_d} + \frac{i}{2}\Gamma_{v_d}} \left(1 - e^{-i\{\varepsilon_e + V_f + \varepsilon_n - E_{v_d} - \frac{i}{2}\Gamma_{v_d}\}t}\right)\right|^2 \tag{20}$$

This equation can be obtained within non-Hermitian quantum scattering theory.[152,179,181] The main difference between eq 20 and the Kramers−Heisenberg formula lies in the theoretical description of the resonances. In particular, vibrational states $|v_d\rangle$ in eq 20 are the so-called right-handed eigenstates (see ref 182 for details) of the total non-Hermitian Hamiltonian $\hat{\mathcal{H}}_d(R) = \hat{H}_d(R) - \frac{i}{2}\Gamma_d(R)$ from eq 14a. Accordingly, those decaying vibronic states have complex energies of $E_{v_d} - \frac{i}{2}\Gamma_{v_d}$, with the energy positions given by E_{v_d} and individual decay widths by Γ_{v_d}. The coincident spectrum (eq 20) provides direct access to the spectrum of electrons emitted via the decay and to the respective KER spectrum:

$$\sigma_{el}(\varepsilon_e, t) = \int\sigma(\varepsilon_e, \varepsilon_n, t)\, d\varepsilon_n \tag{21a}$$

$$\sigma_{\text{ker}}(\varepsilon_n, t) = \int\sigma(\varepsilon_e, \varepsilon_n, t)\, d\varepsilon_e \tag{21b}$$

As was mentioned above, these equations yield electron and KER spectra, which are absolutely equivalent[179] to those obtained via eqs 18 and 19 within the time-dependent theory for nuclear wave packet propagation.

The very first calculations of an ICD electron spectrum have been made for the decay of the inner-valence ionized states of Ne dimers.[151,152] The underlying nuclear dynamics was treated in those calculations within the non-Hermitian quantum scattering theory, and the final ICD electron spectra were obtained via eqs 20 and 21a at $t = \infty$. The theoretical spectra reported in refs 151 and 152 exhibited clear signatures of the nodal structure of the decaying vibronic states $|v_d\rangle$. Soon,[183] these theoretical predictions were confirmed by time-dependent nuclear dynamics simulations, in which the final ICD electron spectrum is given by eq 18 at $t = \infty$. Owing to an incorrect fit of the asymptotic behavior of the PESs[151] used, the calculations of refs 151, 152, and 183 resulted in the appearance of a nodal structure in the computed ICD electron spectra. Nevertheless, the theoretical predictions of refs 151, 152, and 183 triggered corresponding experimental effort.[2] The expected nodal structure in the ICD electron spectra of the inner-valence ionized Ne dimers was not observed in those experiments, and this was immediately confirmed theoretically in ref 184 with quantum dynamics simulations using the correct PESs. The latter approach was also used in ref 185 to compute ICD electron spectra of decaying NeAr, and those theoretical spectra were successfully verified in later experiments.[186]

The theoretical description of nuclear dynamics in terms of time-evolution of vibrational eigenstates via eqs 20, 21a, and 21b is especially efficient if the propagation of nuclear wave packets cannot be managed owing to a very slow or ultralong-range decay. A prominent example of such extreme quantum systems is the He dimer,[187−190] in which ICD takes place at a large internuclear separation of a few hundred of angstroms

https://dx.doi.org/10.1021/acs.chemrev.0c00106
Chem. Rev. 2020, 120, 11295−11369

and during long times up to pico or even micro seconds. ICD in He_2 is explicitly driven by the nuclear motion,[180,189,191] which is prominently manifested in the decay spectra by the nodal structure of vibronic resonance states.[187] Contrary to nuclear wave packet propagation theory, this approach allows visualization of the role of individual vibronic resonances. Moreover, it is especially suitable if more specific (differential or partial) observables need to be accessed, like, for example, laboratory or molecular frame angular emission distribution of ICD electrons in He_2,[188] HeNe,[107] and Ne_2.[192]

The full theory for nuclear dynamics accompanying electronic cascades and multimechanism decay processes in molecules was developed in ref 193. This theory was further adopted to Auger-ICD cascades[153,194] and successfully applied to interpret experimental ICD electron spectra after Ne K-shell ionization of Ne_2[195] and NeAr.[124,196] In these theoretical studies, it was assumed that the broad-band inner-shell ionization as well as the subsequent one-site atomic Auger decay of the created inner-shell vacancy are instantaneous processes. This allows one to decouple nuclear dynamics in the ICD transition step from that in the ionization and Auger decay steps, and to replace the latter dynamics by the initial condition which assumes a vertical transformation of the nuclear wave packet from the neutral ground state onto the PESs of the initial ICD states. Under this assumption, a very good agreement between the computed and measured electron spectrum of ICD after Auger decay in Ne dimers has been achieved.[195] A comprehensive theoretical study of ICD after Ne K-LL Auger decay in NeAr, performed in refs 124 and 196, allowed for a calibration of *ab initio* ICD widths to slow down the decay and enable nuclear dynamics, whose fingerprints were present in the experimental KER spectra.[196] Ref 197 extended the time-dependent theory for nuclear wave packet propagation to account for the recoil of nuclei by fast photo- or Auger electrons and interpreted a huge effect of recoil on the underlying nuclear dynamics and resulting ICD electron spectra of Ne_2 observed in the coincident experiment.[198] The time-dependent theory for nuclear wave packet dynamics was also applied in refs 199 and 200 to compute electron and KER spectra of ICD after resonant Auger decay in Ar_2 and ArKr, and theoretical predictions of those works on Ar dimers were later verified in independent experiments.[201,202]

Obviously, an accurate theoretical description of nuclear dynamics is key to a successful interpretation of experimental ICD spectra. For instance, recent time-resolved studies of ICD, which allowed to experimentally deduce the decay lifetime in Ne_2,[203,204] to reconstruct the R−dependent absolute decay widths in Ar_2,[201] and to measure the time-evolution of the KER spectrum and the survival probability of decaying states in He_2,[205] relied on explicit theoretical treatment of the underlying nuclear dynamics. In addition, nuclear dynamics calculations of the respective KER spectrum enabled researchers to uncover a three-electron ICD of inner-valence doubly ionized states in NeAr.[23] Wave packet nuclear dynamics calculations also helped researchers to understand an enhancement of the ICD and other nonlocal processes during relaxation of inner-shell ionized liquid water, which is caused by ultrafast proton transfer from the core-ionized water to neighboring water molecules.[34] Moreover, reliable theoretical prediction of ICD spectra must be based on accurate nuclear dynamic calculations. For instance, recent theoretical studies[206,207] proposed new methods to investigate ICD processes by multiphoton absorption schemes, which are much more efficient than traditional single-photon absorption schemes. Because of strong nonadiabatic effects evoked by intense laser fields,[208−210] coupled nuclear vibrational and rotational motions in Ne dimers were explicitly treated in these calculations with the MCTDH method.[175−177] Later on, these theoretical predictions were successfully verified in experiments[211,212] with free-electron lasers (FELs). Finally, explicit nonadiabatic wave packet propagation on coupled PESs, performed in ref 213, demonstrated a capability of ultrafast ICD to quench molecular photodissociation in CO·Mg complexes.

Unfortunately, for large systems, a full quantum mechanical treatment of nuclear dynamics is not feasible, owing to many relevant degrees of freedom involved. In such cases, ICD spectra can be estimated with the help of (semi)classical methods or simple physical considerations. For instance, a classical trajectory method was used in ref 214 to interpret the measured ICD spectrum of water dimers[215] by utilizing the Hessian-based integrator built in the Gaussian 03 package.[216,217] Another semiclassical approach, which treats electron dynamics quantum mechanically and nuclear dynamics by classical trajectories with a surface hopping method, was introduced in ref 218 and applied to estimate the KER spectrum of ICD in He dimers. In ref 219, quasi-classical molecular dynamics simulations based on a solution of Newton equations enabled researchers to identify ICD and a related process in large Ar and ArKr clusters irradiated by intense near-infrared laser pulses. The ICD electron spectra after O K-shell Auger decay in water dimers,[220] and inner-valence ionization of small biochemically relevant hydrogen-bonded systems[221] were roughly estimated by a normalized convolution of spectral envelopes of the initial and final ICD states. Alternatively, the spectrum of ICD electrons of inner-valence ionized benzene dimers[222] was estimated via weighted spectroscopic amplitudes, which were represented by Gaussian functions to approximately model vibrational broadening of the electron transition lines. Very similar approaches of introducing vibrational broadening to electron transition lines were utilized to estimate ICD electron spectra after Ar 3*s*-ionization of small ArXe clusters[223] and electron spectra of ICD and related nonlocal processes during relaxation of core-ionized LiOH molecules[224] and small (de)protonated ammonia clusters.[225,226]

Concluding this section, we would like to mention a few relevant theoretical studies of electron dynamics accompanying ICD processes. Owing to the complexity or specificity of the system or process under consideration, the electron dynamics simulations mentioned below were performed by excluding the accompanying nuclear dynamics (i.e., at a frozen geometry of the system). Different theoretical methods for the description of electron dynamics were applied. For instance: (i) expansion of an electron wave packet in terms of electronic eigenstates to trace time evolution of ICD in NeAr dimers;[227] (ii) solution of the rate equations for few-level systems to model relaxation of large multiply excited Ne clusters[51,228] and to investigate nanoplasma formation in small multiply ionized Xe clusters;[229] (iii) solution of the system of coupled equations for population amplitudes to study two-photon double excitation of Ne dimers[212] and multicenter resonantly enhanced photoionization of model systems.[230−233] Finally, a more sophisticated MCTDH method for Fermions, which was adopted to propagate two-electron wave packets in coupled potential

https://dx.doi.org/10.1021/acs.chemrev.0c00106
Chem. Rev. 2020, 120, 11295−11369

wells, was used in refs 162 and 234−237 to study real-time evolution of ICD in model system of two quantum dots.

4. EXPERIMENTAL METHODS

In the study of ICD, a variety of techniques from the portfolio of experimental atomic and molecular physics, or physical chemistry were used. Here we aim to present them in a comprehensive form. Figure 7 collects the main elements involved in ICD experiments.

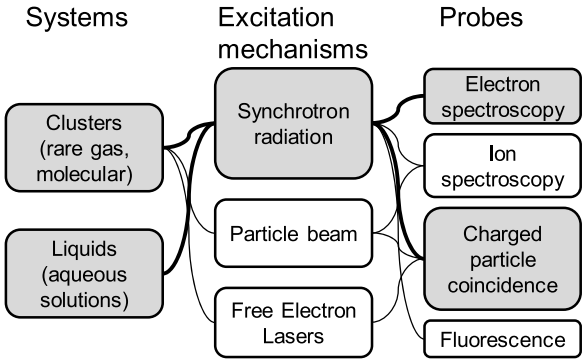

Figure 7. Systems, excitation mechanisms, and detection methods (probes) that were used in the study of ICD. Shaded boxes, connected by thick lines, highlight the elements that were used most frequently.

Systems: The notion of ICD assumes a weak bonding between entities making up a larger system. Examples found in nature are hydrogen-bonded liquids, most obviously water, and experiments on ICD in aqueous solutions have indeed been carried out. A different, equally attractive experimental environment is offered by clusters, composed of two to roughly millions of atoms or molecules. Clusters may exhibit hydrogen or van der Waals bonds, or metallic bonds, depending on their constituents. Only the two former types are of interest here. Weakly bonded clusters are conveniently produced by means of a supersonic expansion of gas into a vacuum, which leads to a cooling of the relative motion of atoms or molecules, respectively, and by that to the formation of a cluster jet.[238] A lot of our knowledge on ICD results from experiments on the two mentioned types of aggregation states, clusters, and aqueous solutions including neat liquid water.

Excitation Mechanisms: Interatomic and intermolecular Coulombic decay proceed from an excited state of some atom or molecule in a weakly coupled bath of other atoms or molecules. The amount of energy stored in the excited state must exceed the ionization potential of the system. Most studies in this review address ICD of excited cationic states created in some ionization process starting from a system in its neutral ground state. Including this primary process, roughly twice the ionization energy of the neutral system must be deposited into a single site to initiate ICD. In most studies presented below, single photon absorption of short wavelength electromagnetic radiation or impact of a charged particle beam were used as an excitation source. Further details are given in the next subsection (Section 4.1). Modifications to the ICD process due to absorption of multiple photons within the ICD lifetime will also be discussed (Section 5.7.1). ICD in anionic systems, which would require less excitation energy per event, so far was only studied theoretically, and could be an important future perspective.[120,239,240]

Detection Methods: Some experimental signatures of ICD are sketched in Figure 8. The excitation mechanism, the first

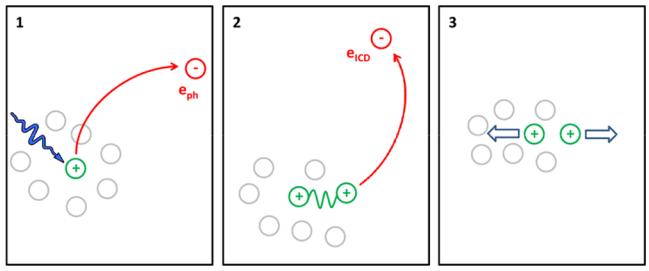

Figure 8. Experimental signatures of ICD. Left panel: ICD leads to a lifetime broadening of the excited state. This can be observed in the energy domain when the excited state is produced, for example, by photoionization or -excitation. Middle panel: Most obviously, the ICD electron can be observed directly. Right panel: The pair of ions created by ICD undergoes a Coulomb explosion. Detection of the final state ions also provides a strong indication for ICD. Experiments using these three characteristics have all been successfully performed in the past.

step, is drawn as a photoionization process here, but ICD occurs also after other types of excitation, as long as they deposit a sufficient amount of electronic energy in the system. In the IC decay, a secondary electron in the continuum is produced; two cations, often on neighboring sites, are left behind. Direct detection of the secondary electron has been shown in a lot of experiments. The Coulomb repulsion in the final state leads to a nuclear dynamics (in most cases a violent fragmentation), which also is a clear indicator for the occurrence of ICD. The lifetime of the ionized excited state is finite due to its decay by ICD. According to the energy-time uncertainty relation, a broadening of the excited state in the energy domain is therefore induced. In the absence of other (fast) decay channels, and if the excited state is produced by photoionization, this width can be directly read as a Lorentzian broadening of the respective photoelectron line. Additionally to the mechanisms shown in the figure, after resonant ICD, the final state may also be detected by its fluorescence decay.

In the following we will first review the excitation schemes used for a controlled creation of states that may decay by ICD and after that will describe experimental methods to observe the decay. The preparation of systems, for example, creation of clusters and liquid microjets, will be discussed in conjunction with the respective results in Section 5.

4.1. Excitation Mechanisms

An overview of excitation mechanisms that were used in ICD experiments so far is given in Table 1. The wide range of

Table 1. Excitation Mechanisms Used in the Study of ICD[a]

name	primary energy (eV)	pulse duration	repetition rate (Hz)
synchrotron radiation	30−1000	10−100 ps | cw	$1-5 \times 10^6$
free-electron laser	20−60	10−100 fs	1−800
electron beam	50−3000	1.5−40 ns	$50-170 \times 10^3$
proton or ion beam	10^5-10^7 range	pulsed | cw	$2-12 \times 10^6$

[a]"cw" (continuous wave) is entered for sources that have no time structure, or a time structure that has not been used in the experiment.

https://dx.doi.org/10.1021/acs.chemrev.0c00106
Chem. Rev. 2020, 120, 11295−11369

sources shows the universality of the ICD phenomenon. Some remarks on details of the table are in order. Many experiments were carried out using pulsed light or particle sources. With the exception of a few experiments carried out at free-electron lasers (covered in Section 5.7), this is not related to the temporal properties of the decay itself, or the time evolution of the decaying state. A pulsed source was rather used to enable time-of-flight measurements of the charged particles produced in the excitation and decay processes as seen, for example, in Figures 1 and 7. Details are explained below. For direct time-resolved experiments on ICD, photon sources using high harmonic generation of optical or IR lasers would also be attractive, but no such experiments have been reported, so far, to the best of our knowledge.

The first experimental studies of ICD used synchrotron radiation to prepare inner-valence hole states of Ne clusters by photoionization.[2,3] The production of synchrotron radiation makes use of the fact that the electromagnetic emission of accelerated charged particles becomes strongly directional and blue-shifted for electrons at relativistic velocities. This mechanism can be used as a source of focused electromagnetic radiation with a tunable wavelength, which covers the range from the visible to hard X-rays (not within a single experimental station, though). Current synchrotron radiation sources are based on storage rings for relativistic electrons or positrons that are optimized for the purpose of radiation production. The physics of synchrotron radiation production has been reviewed, for example, in ref 241. The temporal properties of synchrotron radiation pulses are of importance for many experimental schemes used in the investigation of ICD. They are determined by the electron or positron beam producing the radiation. This beam consists of individual packets, with a typical temporal width of few tens of ps in the laboratory system.[242]

Although the intensity available at synchrotron radiation sources revolutionized X-ray physics, it is by far not sufficient to carry out multiphoton experiments. Research on ICD-like decays involving multiple excited states, such as collective ICD,[51] has mostly used sources of much higher peak intensity. The same is true for pump−probe experiments since two photons must be absorbed by the same system. For illustration, we can compare the intensity of photon pulses used in the seminal experiments on ICD of the Ne dimer by Jahnke et al. (electron−ion−ion coincidence spectroscopy) and by Schnorr et al. (pump−probe).[2,203] A suitable metric for a comparison must be chosen, which depends on the type of experiment which is performed. For plain detection of spectra, often photon flux (photons/time unit) or spectral flux (photons/(time unit × spectral bandwidth)) is most important. Any experiment using time-of-flight detection of particles also strongly benefits from a high pulse rate of the source, even more so when coincidence detection of several particles is required. Multiphoton or pump−probe experiments most crucially depend on the peak intensity (photons/(pulse duration × spot size)). To quote some numbers, in the experiment on ICD in the Ne dimer schematically shown in Figure 1, photons from the U125−1/SGM beamline of the synchrotron radiation source BESSY were used, at a (time-averaged) flux of 2×10^{12}/s. In a time-resolved measurement of the same process at the free-electron laser FLASH, further detailed in Section 4.6.2, the time-averaged flux was not so different (4×10^{12}/s). When normalizing to peak flux however we arrive at a figure of 8×10^{22}/s during a 60 fs pulse, focused to a 10 μm spot for the FEL experiment, compared to 2.5×10^{16}/s in a 80 μm spot for the BESSY experiment. Figures are approximate only and provided for illustration.[2,203,243,244]

Experiments carried out on ICD by particle impact often used pulsed electron guns and particle accelerators, as described in the original publications.[59,245−250] Different than for excitation by photons, in experiments using particle impact the energy transfer by the projectile is not well-defined. Observation of the ICD final state (see Figure 8) and sometimes the use of ingenious multiparticle coincidence detection schemes nevertheless led to successful experiments.

4.2. Electron Spectroscopy

Electron spectroscopy is a technique widespread in applied physics and chemistry since the discovery of chemical shifts in core-level photoelectron lines. In this review the term "electron spectroscopy" refers to the detection of the energy of emitted photoelectrons and of second-order electrons, the latter resulting from Auger decay, ICD, and other autoionization processes. To account for both contributions, the technique is often referred to as photoemission (PE), not to be confused with photon emission (the emission of photons).

Most instruments for electron spectroscopy use static electric fields in an electrode arragement of some form to deflect electrons according to their kinetic energy E_{kin}, such that only those within a certain energy band reach a detector. Electrostatic electron spectrometers are mature, and a choice of instruments is available commercially (see Figure 9). Most

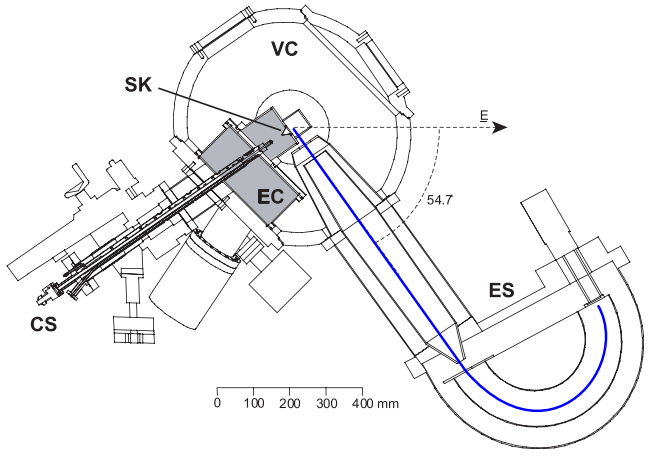

Figure 9. Cross-section through an apparatus including a molecular jet source for production of rare gas clusters ("CS"), and an expansion chamber ("EC"), separated from the main vacuum chamber "VC" by a skimmer "SK". Synchrotron radiation coming out of the drawing plane produces electrons that are collected in an electron spectrometer "ES" consisting of a straight transfer lens, a hemispherical dispersive section and a detector. An electron trajectory is drawn in blue color. Reproduced from ref 251, with the permission of AIP Publishing.

of these are hemispherical electron analyzers, which have superseded over other shapes due to an advantageous combination of good energy resolution and flexibility in apparatus design.[252] The latter results from the easy inclusion of a transfer lens between sample and the dispersive hemispherical section, which makes it straightforward to transport electrons to the detector and at the same time fulfill other spatial constraints from target beams, probe beams, etc. The pioneering experiment showing first evidence of ICD in

https://dx.doi.org/10.1021/acs.chemrev.0c00106
Chem. Rev. 2020, 120, 11295−11369

neon clusters,[3] for example, relied on electron spectroscopy of this kind.

Some properties of hemispherical analyzers are important in conjunction with experiments on ICD:

- Good energy resolution can be achieved even for electrons with kinetic energies in the hundreds of eV range. Such energies are typical for radiationless de-excitation of core levels, in which ICD competes with Auger decay, as seen in liquid solutions (Section 5.3).
- High pressures in the vacuum chamber can be accommodated by an efficient design of the transfer lens. Electron spectroscopy from a liquid microjet, with typical pressures in the 10^{-3} mbar range,[253] has been accomplished in this way and even mbar pressures are possible today.[254]
- Recording low kinetic energy electrons (below ∼5 eV) with a hemispherical electron analyzer requires very good shielding of residual magnetic fields and meticulous control of stray electric fields. In that respect, spectrometers using magnetic guiding fields are much more robust. Few experiments on inner-valence ICD have been done with hemispherical analyzers for this reason, for example, detecting electrons down to 1.2 eV.[255]
- The transfer lens of a hemispherical analyzer projects electrons from the source point onto a slit limiting the angular acceptance into the hemisphere. Typical figures for the accepted solid angle are below 1% (of 4π sR). This is not a severe limitation for experiments on bulk matter or a liquid jet because the intensity of the excitation source can be increased to a point at which sufficient count rates are achieved nevertheless. However, when it comes to coincidence detection, a small solid angle is a major drawback.

Other types of electron spectrometers in the context of ICD have mostly been used in coincidence experiments and will be presented in Section 4.4.

4.3. Ion Spectroscopy

The Coulomb explosion shown in the right-most panel of Figure 8 suggests the detection of energetic ions as a promising signature for ICD. Such experiments have indeed been done, and have used a hemispherical analyzer with reversed polarity of the fields, compared to an electron instrument, or energy filters built from electrostatic grids. Early experiments on resonant ICD have used ion spectroscopic approaches for their investigations.[256,257] An unhindered Coulomb explosion, however, takes only place in a dimer, and the analysis of ion energies as an indication for ICD is mostly limited to these species. In larger clusters collisions, fragmentation into complexes that include neutrals, and postdecay nuclear dynamics all lead to a blurring of the sought-for ion signal.[258,259] Pure spectroscopy of energetic ions is capable to detect ICD only in some favorable cases and has mostly been superseded by powerful coincidence methods, which will be described in the next section.

4.4. Coincidence Techniques

Compelling experiments on ICD and related phenomena have been carried out by detecting several charged particles produced in the same event, ideally from the excitation process and the ICD, in coincidence. A large collection solid angle for detecting the particles is a practical requirement for these experiments. For research on ICD, spectrometers with various electric and magnetic field configurations and geometries were used to spatially project charged particles emitted into a large angular range toward one or two detectors.

Mostly three techniques were used, namely projection by strong electric fields ("velocity map imaging", VMI[260,261]), collection and guiding of electrons by strong, anisotropic magnetic fields ("magnetic bottle" time-of-flight spectrometer)[262,263] and projection of the particles by weak magnetic and electric fields ('Cold Target Recoil Ion Momentum Spectroscopy', COLTRIMS, with the respective instrument also being called "reaction microscope"[264−266]). The former two have been used as efficient spectrometers for noncoincident electron spectroscopy and in coincidence experiments. Electrons and ions from the same event can be recorded by COLTRIMS and by VMI spectrometers extended by an ion time-of-flight section.

4.4.1. Velocity Map Imaging Spectrometer. This technique is based on a projection of charged particles by strong electric fields, applied via a stack of annular electrodes.[260] Different than in a COLTRIMS spectrometer, no magnetic field is used. VMI can in principle be applied to electrons as well as energetic ions (depending on the magnitude of the fields), but use of VMI as an electron spectrometer is far more widespread than its use for heavier particles, and we will restrict the discussion to electrons here.

In a VMI spectrometer (Figure 10), free electrons from a reaction are accelerated strongly in the electric field created by

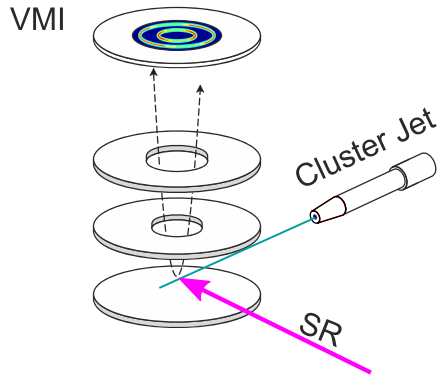

Figure 10. Sketch of an electron/ion spectrometer using the velocity map imaging (VMI) principle. Charged particles produced by the interaction of a photon beam (here from synchrotron radiation SR) with a cluster jet are projected upward by static electric fields produced between the ring-shaped electrodes. Depending on the polarity of the field, either electrons or ions can be projected.

a circular, solid electrode and an annular electrode enclosing the interaction reaction at both side. The electrodes are aligned along a rotational axis perpendicular to both the cluster jet and the ionizing radiation. Electron trajectories produced such are reminiscent to those of an object falling freely in a gravitational field. From the image of all electrons recorded by a spatially resolving detector, the initial momentum space distribution (and thus the electron energy distribution) can be inferred using mathematical inversion methods.[267] Time-of-flight information is not necessary in this step, that is a VMI is suitable for work with excitation sources independent of their time structure. Importantly, however, the inversion is restricted to an image-to-image transform, that is, a VMI cannot correlate momenta of electrons from individual events to those of other

https://dx.doi.org/10.1021/acs.chemrev.0c00106
Chem. Rev. 2020, 120, 11295−11369

particles, different to a COLTRIMS spectrometer (Section 4.4.3). Practically, VMI electron spectrometers are highly effective as the full solid angle around the reaction region is covered. A kinetic electron energy resolution $\Delta E_{kin}/E_{kin}$ of approximately 1/20 has been achieved in practice.[268,269] In a powerful extension of the original VMI technique, an electron VMI was coupled to a linear ion time-of-flight spectrometer pointing in the opposite direction of the interaction region, which allows to record electron spectra filtered by fragment mass.[268]

Works on ICD and ETMD that have used VMI electron spectroscopy are covered in refs 53, 228, 258, 261, and 269−274.

4.4.2. Magnetic Bottle Time-of-Flight Spectrometer. When an electron moves in a magnetic field, the magnetic moment μ of the cyclotron motion around the field lines is an invariant. With

$$\mu = \frac{p_\perp^{\,2}}{2m_e B} = \frac{E_{kin,\perp}}{B} \tag{22}$$

and quantities with subset $\perp$ referring only to the motion perpendicular to the magnetic field line, it can be seen that this is of consequence for the particle dynamics. This is because the conservation of μ even holds for motion along a spatially varying field $B(z)$, as long as the magnetic field gradient is slowly ("adiabatically") varying. If an electron is created in a region of high magnetic field that is adiabatically decreasing along the electron trajectory, energy conservation requires that almost all energy of motion perpendicular to the magnetic field is converted into kinetic energy parallel to the magnetic field. At the end of a straight section featuring an adiabatic magnetic field decrease (a factor of $B_i/B_f \approx 100$ is realistically achievable), almost all kinetic energy is converted into linear motion parallel to a weak field line. In a second section of the instrument, featuring a constant field, this can be used to build up substantial differences in time-of-flight, from which the initial kinetic energy can be determined. The time-of-flight differences, which electrons having same total kinetic energy, but different direction, encounter in the region of varying magnetic field can be made small compared to the total time-of-flight. The apparatus can therefore be used as an electron energy spectrometer. A sketch of some magnetic field lines and the ensuing electron trajectories is shown in Figure 11a.

The first electron spectrometer employing this principle was realized by Kruit and Read;[262] these authors also covered the electron-optical principles sketched above with rigor. For research on ICD, magnetic bottle spectrometers are of interest in particular because they allow to record electron−electron coincidence spectra over an energy range extending most COLTRIMS setups and with an energy resolution similar to a VMI ($\Delta E_{kin}/E_{kin}$ of approximately 1/20).[275] Typically, this has been used to filter the contributions of ICD or ETMD to a signal of slow electrons produced also by inelastic scattering.[276] An instrument employed in several studies discussed below is described in ref 275 (Figure 11b).

Experiments on ICD using a magnetic bottle spectrometer are described in refs 26, 31, 223, 263, and 276−286.

4.4.3. Cold Target Recoil Ion Momentum Spectroscopy. By Cold Target Recoil Ion Momentum Spectroscopy (COLTRIMS)[264,266] (also known as reaction microscope[265] or vector correlation[287,288]), the momentum vectors and charge states of several charged particles from the reaction of a single

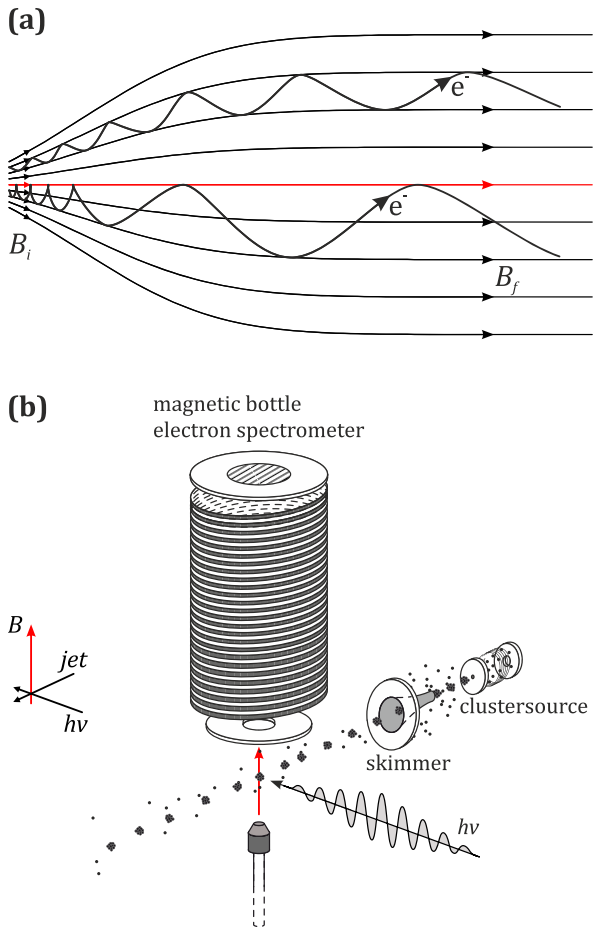

Figure 11. Magnetic bottle time-of-flight spectrometer. (a) Magnetic field distribution and some electron trajectories, (b) sketch of a cluster electron spectroscopy experiment using a magnetic bottle spectrometer with a magnetic field pointing vertically upward. The central magnetic field line is indicated by red color in both panels.

atom or molecule with an ionizing projectile (e.g., a photon, electron or ion) are measured in coincidence. At the heart of a COLTRIMS setup is a supersonic gas jet, which provides a well-localized and internally cold beam of atoms, molecules, or clusters in an ultrahigh vacuum surrounding. This target beam is crossed at right angle with the projectile beam generating a small interaction region of typically less than 1 mm^3. An electric field is used to guide charged reaction products toward two large area position- and time-sensitive micro channel plate detectors (the detectors are typically equipped with a multihit capable delay-line position readout[289,290]). Often a homogeneous magnetic field is superimposed parallel to the electric field to confine the electrons inside the spectrometer volume on a cyclotron motion.[291] Figure 12 shows a sketch of the detection geometry. The electric field of the spectrometer is generated by several ring-shaped electrodes. The homogeneous magnetic confinement field is typically produced by large Helmhotz coils, which are not situated inside the vacuum chamber.

The projectile beam is pulsed to provide a start signal for a time-of-flight measurement of the electrons and ions. The position and time of impact on the detector are recorded for each individual particle, and this information is stored in a listmode-file. To ensure that the detected particles result from the same atom or molecules, the target density and ionization

https://dx.doi.org/10.1021/acs.chemrev.0c00106
Chem. Rev. 2020, 120, 11295−11369

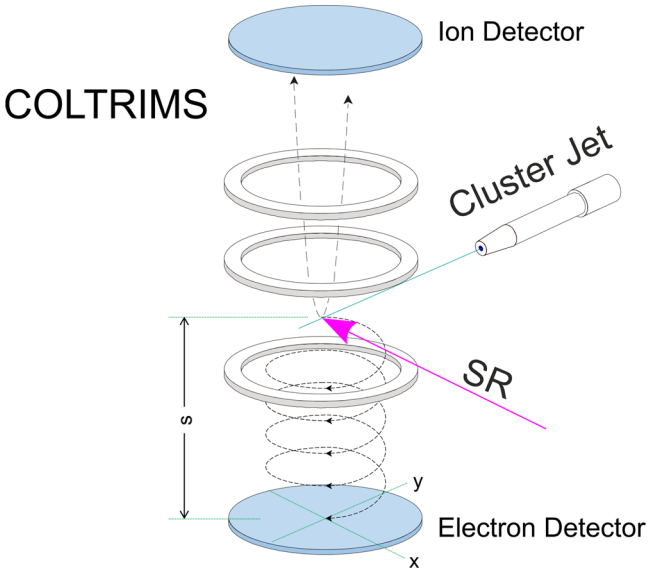

Figure 12. Sketch of a COLTRIMS reaction microscope. A supersonic gas jet is intersected by, for example, a monochromatized photon beam from a synchrotron radiation source (SR). Charged particles created in the interaction region are guided by electric and magnetic fields toward two position- and time-sensitive detectors. Here, the ions are deflected to the upper detector, while the electrons are imaged on the bottom detector after performing a cyclotron motion (due to the magnetic field) inside the spectrometer volume. By measuring the flight times along the spectrometer (for example, the distance s for electrons) and the positions of impact (x, y) on the detectors, the particles' momenta can be deduced. The three white rings symbolize electrodes, employed for generating the electric extraction fields.

rate is adjusted such that the reaction rate is much below one per projectile pulse. From the positions of impact and the times-of-flight the initial momenta, of all particles are obtained in an offline analysis. For electrons, this provides, for example, their kinetic energy and the their emission angle in the laboratory frame of reference. For fragment ions from a molecule, one obtains the kinetic energy release (KER) and the fragmentation direction. In many cases (and in particular in ICD related experiments), the internuclear distance of the atoms of the molecule prior to fragmentation can be inferred from the KER.[292,293] For more complex molecules also the molecular structure can be deduced from the ionic fragmentation pattern.[294] Often the fragmentation is so rapid that the molecular ion has no time to rotate and thus the measured fragment direction coincides with the orientation of the molecule at the instant of ionization.[295] There are two important features of COLTRIMS reaction microscopes in the context of ICD. First, the energies of the ions and electron are measured in coincidence. This can be used to identify ICD and to resolve the IC-decaying state. It can also be used to obtain the single event decay time (see Section 4.6.3). Second, the photoelectron and ICD electron direction can be transformed to the molecular frame of reference (see Section 5.1.4).

Early experiments on ICD using the COLTRIMS technique can be found, for example, in refs 2, 8, 15, 16, 29, 57, 58, 60, 187−189, 198, 215, and 296−303; later work in refs 23, 28, 196, 203, 205, 245, 247, 248, and 304−315; and most recent work in refs 54, 107, 192, 201, 249, 250, 259, and 316−324

4.5. Photon Spectroscopy and Electron−Photon Coincidence Techniques

A general overview of the experimental techniques used in synchrotron radiation based photon spectroscopy is given in ref 325. Briefly, the typical setup consists of a supersonic cluster source for generation of the clusters, an interaction chamber for ultrahigh vacuum synchrotron radiation experiments, a focusing grating spectrometer for dispersion, and a position-sensitive detector for wavelength resolved detection of the emitted photons. The sample generation, the interaction chamber, and the synchrotron radiation are similar to the electron detection techniques and are omitted here. Two main components are very distinct from the electron spectroscopy: the focusing grating and the detectors. A generalized grating setup is depicted in Figure 13.

A spherical grating is used to minimize the number of optical elements. It focuses the light from the entrance slit onto the detector and disperses wavelengths simultaneously. The groove density, blaze, and coating of the grating must be optimized for each experiment. Thereby, the light transmission and resolution can be chosen, respectively, for the given experimental requirements. Because of the low target density and often low cross-sections of the investigated processes, it is

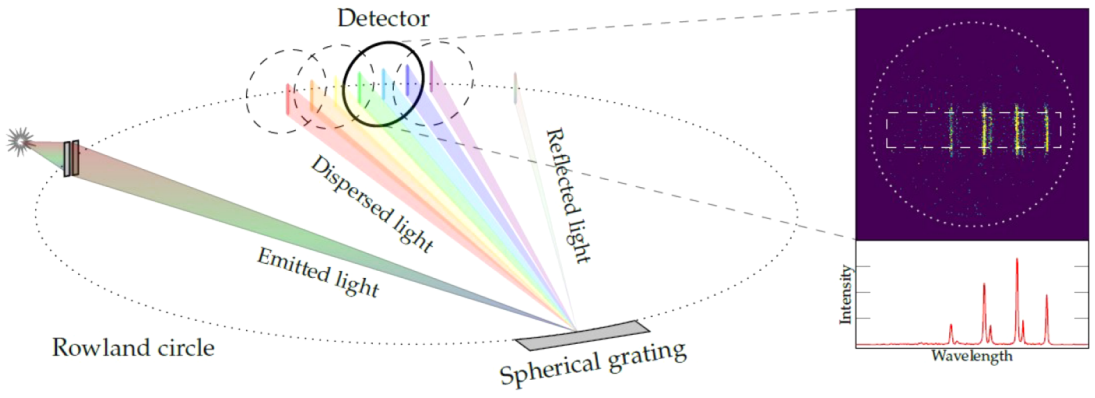

Figure 13. Illustration of the combination of a photon spectrometer with position-sensitive detection. Light emitted in a source volume enters the spectrometer through an entrance slit and is dispersed by a spherical grating. In reality, the detector is fixed in space and the grating is moved to project different spectral ranges onto the detector. The inset shows an exemplary detector image, from which the emission spectrum is obtained by integrating the signal within a region of interest (dashed rectangle) over the vertical coordinate. Figure and caption reprinted from ref 325, used under CC BY.

https://dx.doi.org/10.1021/acs.chemrev.0c00106
Chem. Rev. 2020, 120, 11295−11369

necessary to maximize the efficiency of the photon detection. On the one hand, the single optical element reduces losses due to low reflectance in the deep UV; on the other hand, MCP-based single-photon-counting position-sensitive detectors are used. They enable the simultaneous recording of large spectral intervals with high quantum efficiency and are quasi noise free. Depending on the wavelength of the photons, they are either converted into electrons directly in the first MCP or within an additional photocathode. This photocathode (or a coating of the first MCP) is critically enhancing the quantum efficiency of the detector. The photoelectron emitted in the first step is then amplified by two to three MCPs by up to seven orders of magnitude. The resulting electron cloud is then detected on a position-sensitive anode. Thereby, the temporal and spatial (later converted to wavelength) information can be recorded. The very low noise (few counts per second over the full detector area) allows the recording of very low intensity spectra. This is important for ICD-related investigations with low density samples. Other detection methods, for example, CCD or CMOS, with few dark counts per seconds per pixel, are not suitable for such experiments, regardless of their many beneficial attributes.

To increase this ultrahigh sensitivity even further, it is possible to utilize temporal information for each individual event. In combination with an electron spectrometer, the coincidence of photons and electrons can discriminate relevant events from background and thereby increase the signal-to-noise level even further. In ref 326, a setup for such experiments is described in detail. Briefly, the main challenge for photon−electron coincidences is the typically much lower collection efficiency of the photon detection. While electrons can be guided by electric and magnetic fields, photons can only be collected by means of optics. For the photons typically occurring in noble gas ICD experiments, that is, with deep UV wavelengths, no window materials are available. Hence, the maximization of the collection solid angle is purely by reflective optics. A combination of several parabolic surfaces enclosing the interaction volume increases the collectable solid angle by orders of magnitude and allows thereby the recording of electron−photon coincidences with a magnetic bottle spectrometer. Figure 14 illustrates the different light paths collected by the device presented in ref 326.

The first results on ICD were reported only recently in ref 62 and show the quasi background free capabilities of electron−photon coincidence measurements. The main finding is depicted in Figure 15. The figure illustrates remarkably how sensitive the combination of electron and photon detection can be. Since these investigations have only started recently, one can only speculate on the large variety of future applications, within the ICD context and in other fields.

Early experiments related to ICD using photon emission spectroscopy can be found, for example, in refs 327 and 328, later work in refs 280 and 329, and most recent work in refs 61, 62, 282, and 285.

4.6. Time-Resolving Techniques

The dynamics of ICD are in many systems very complex, and ICD typically deviates from a simple exponential decay. The decay rate strongly depends on the internuclear distance of the decay partners and the time frame in which ICD occurs is often similar to that of nuclear motion initiated by the excitation (see Section 3.3). This leads to a strong coupling of the electronic decay and nuclear dynamics. Several exciting

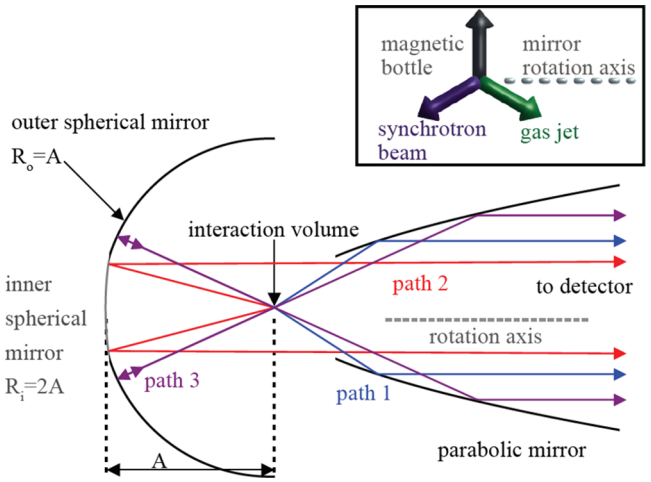

Figure 14. Sketch of the basic rotational symmetric mirror system. The rotation axis is indicated by a gray dashed line. In the direction of the detector, a parabolic mirror guides the photons onto it is active area (path 1, blue). On the opposite side of the detector, two spherical mirrors reflect photons toward the detector. The radius of the inner spherical mirror R_i is twice its distance to the interaction volume A and photons are reflected in a collimated beam to the detector. The radius of the outer mirror R_o is equal to the distance to the interaction volume A and therefore reflects the photons back into the interaction volume (path 3, violet). From here on, the path coincides with photons of path 1. Reproduced from ref 326 with the permission of AIP publishing. The caption has been taken from ref 326.

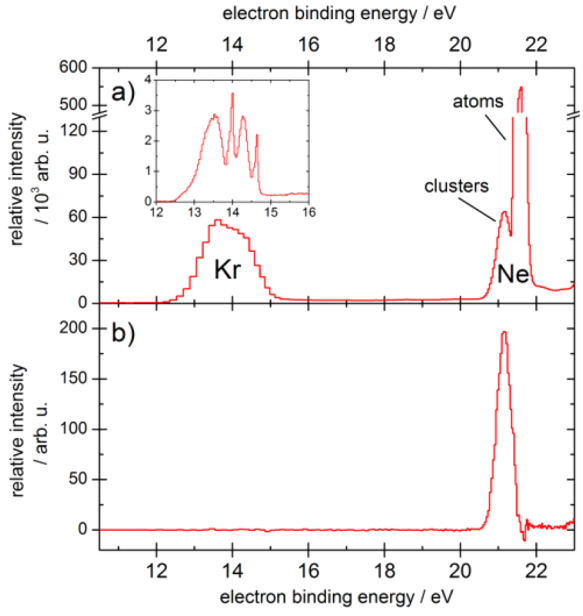

Figure 15. Valence electron spectrum of a NeKr cluster jet, ionized at a photon energy of 23 eV. (a) The total electron spectrum shows three distinct features attributed to electrons from Kr and Ne atoms and clusters. In a high-resolution spectrum of the Kr feature (see inset), two 4*p* fine structure components from Kr atoms and the corresponding cluster signals can be identified. (b) Electron spectrum filtered for true electron-photon coincidences. Reprinted with permission from ref 62. Copyright (2019) American Physical Society. The caption has been taken from ref 62.

experiments using very different approaches to investigate these complex processes in the time domain have been

https://dx.doi.org/10.1021/acs.chemrev.0c00106
Chem. Rev. 2020, 120, 11295−11369

performed during the past decade. They range from spectroscopic measurements where narrow-band excitation energies or high resolution photoelectron spectroscopy are used to measure the lifetime broadening of excited states, over pump−probe experiments to novel techniques where the emission times of electrons are mapped onto modulations of electron energies. Here a short summary of time-resolving techniques used for studies of ICD is given. A short review on this topic has been given in ref 19.

4.6.1. Traditional Approaches. Time and energy are fundamentally interweaved as conjugate properties. Accordingly, spectroscopic measurements of line widths have been employed since decades to obtain information on lifetimes of decaying states. A typical approach is to use high resolution photoelectron energy measurement techniques (see Section 4.2) to resolve the exact photoelectron line shape sufficiently well. With typical decay times in the range of 10 fs to 1 ps, the line widths pertaining to states decaying by ICD are typically within a regime that is resolvable with today's measurement techniques. A downside of this approach is that for a strict analysis of the lifetimes, the exact line shape has to be known. Typically, a Lorentzian profile is assumed, which is characteristic to a strictly exponential decay. While this approximation is for convalently bound molecules (and bound decaying states), in many cases sufficiently valid (known as the so-called constant resonance width Γ approximation[330,331]), it can be problematic in case of ICD due to its nonexponential decay behavior (see Section 5.1.1).

4.6.2. Time-Resolved Measurements Employing Pump−Probe Schemes. Modern time-resolved experiments often rely on the pump−probe approach. The idea of such experiments is to use a short light pulse to excite a system, and another, time-delayed light-pulse to probe it. By scanning the time delay between pump and probe pulses, the dynamics after the excitation can be traced. The temporal evolution of the measured signal consists of a convolution of the excited state dynamics and the pulse duration of the pump and probe pulses. Thus, light pulses that are short compared to the time scale of the investigated dynamics are necessary. A very prominent field relying on such measurement schemes is, for example, Femtochemistry.[332] While the latter research mainly uses strong femtosecond laser light, free-electron lasers (FELs) provide such short light pulses at higher photon energies. FELs are relatively new light sources[50,333] with pulse durations in the femtosecond regime and XUV photon fluxes sufficient to study ICD in a pump−probe scheme. In pioneering time-resolved work, Schnorr et al.[203,204] determined the average decay width of ICD in neon dimers after Ne 2*s*-ionization in an XUV-pump/XUV-probe experiment performed at the free-electron laser in Hamburg (FLASH[50]). More recently, Takanashi and co-workers used XUV-pump and UV-probe pulses to perform a time-resolved study of ICD in doubly excited neon dimers,[212] and a further pump−probe experiment was reported in early 2019.[334] All these studies are covered in Section 5.1.2 in more detail.

4.6.3. Time-Resolved Measurements Employing Post Collision Interaction. To investigate the nonexponential IC-decay behavior in real time in an experiment, Trinter and co-workers developed a novel experimental scheme to access the lifetime of individual atoms or molecules.[205] In their experiment, the energy exchange between the photoelectron and the ICD electron is used to map electron emission times onto electron kinetic energies. Whenever a photoelectron emission is followed by emission of a secondary electron with higher kinetic energy, an energy exchange between the two electrons will occur. This effect is commonly termed 'post collision interaction' (PCI).[335] It has been studied extensively during the past decades in the energy domain. Its implications in the time domain have been investigated more recently.[336,337] Trinter et al. employed PCI for the first time as a tool to measure ultrafast nuclear dynamics. PCI can be understood intuitively as follows: after ionization, the photoelectron emerges from a singly charged ion in a $1/R$ Coulomb potential. As soon as the fast secondary electron is emitted and overtakes the slower photoelectron, the photoelectron will suddenly be exposed to the $2/R$ Coulomb potential of the now doubly charged ion. Thus, the photoelectron will be decelerated, while the secondary electron will be accelerated.[338] In this classical picture, the kinetic energy of the photoelectron after PCI is given by

$$E_{PCI} = E_p - \frac{1}{R_p} = E_p - \frac{\nu_{ICD} - \nu_p}{\nu_p \nu_{ICD} t_{ICD}} \tag{23}$$

where E_p is the initial photoelectron energy, R_p the radius to which the photoelectron has traveled prior to the decay, ν_p and ν_{ICD} are the velocities of the photo- and ICD electron, respectively, and t_{ICD} is the ICD electron emission time. Accordingly, the ICD electron emission time is mapped onto the kinetic energy of the photoelectron. The conversion from deceleration energy to decay time is strongly nonlinear and Figure 16a shows the relation for different initial photoelectron

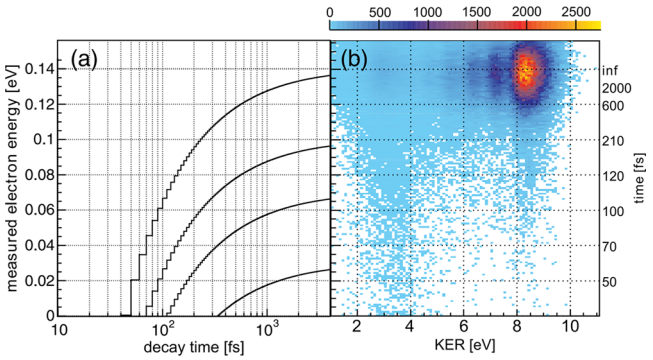

Figure 16. (a) Dependence of the shift in electron energy and the decay time. The plot depicts on the *y* axis the energy a measured electron will have if the decay happens after a certain time (shown on the *x* axis). The behavior is plotted for different initial photoelectron energies. From bottom to top: 30, 70, 100, 140 meV. (b) Electron energies and kinetic energy releases measured in coincidence. Reprinted with permission from ref 205. Copyright 2013 APS.

kinetic energies. By measuring other observables of interest (as, for example ion kinetic energies[205]) in coincidence with the electron kinetic energy, the temporal evolution of these observables can be accessed. Figure 16b shows the temporal evolution of the kinetic energy release after shakeup-induced ICD in He_2 obtained with the PCI-streaking approach.

4.6.4. Time-Resolved Measurements Employing Light-Field Streaking Approaches. In the aforementioned experiment by Trinter et al., the PCI-effect was used for a time-dependent modulation of the measured electron energies. This idea, to map emission times onto electron kinetic energies, is closely related to the concept of the light-field streaking technique, in which systems are excited by ultrashort XUV

https://dx.doi.org/10.1021/acs.chemrev.0c00106
Chem. Rev. 2020, 120, 11295−11369

pulses and a superimposed long-wavelength field is used to modulate (streak) the energies of emitted electrons.[339,340] Light-field streaking was first used in attosecond-physics where attosecond XUV pulses and near-infrared streaking fields were employed to measure, among others, Auger lifetimes[341] and photoelectron emission times in solids[342] and atoms.[343] For these experiments, the oscillation periods of the streaking light-field should be longer than the process under study. By using streaking fields in the THz-regime with oscillation periods of a few hundred fs, this concept can be adapted to investigate processes with lifetimes of a few to a few hundred fs.[344] Several research groups have proposed to employ this approach for time-resolved ICD measurements either using HHG-sources or FELs.[345]

5. SYSTEMS AND APPLICATIONS

In the previous sections, ICD as a process has been introduced, and the theoretical and experimental approaches to study this mechanism have been presented. This section will now provide a comprehensive summary of the theoretical and experimental research that has been performed on ICD and its related processes. In the first subsection, studies on fundamental properties of ICD are covered, followed by subsections on the observation of ICD in various systems, such as small and large clusters, liquids, and biological systems. The section closes with subsections on theoretical studies of ICD in quantum dots, applications of ICD, and works on related phenomena.

5.1. Fundamental Investigations

In this section, we present work on ICD and related processes that cover the fundamental aspects of the decay process itself, as, for example, its decay time dependencies, its features in the time domain, and its efficiency in general.

5.1.1. On the ICD Rate and Its Dependencies. The average lifetime of states decaying by ICD depends strongly on the extent of the system, its constituents, and the amount of direct neighbors available to the excited atom or molecule. A general trend is, however, that ICD is typically slower than local Auger decay but faster than a fluorescence decay of the same system. Already in 2001 Santra et al. predicted that the efficiency of ICD depends on the amount of atoms in the close proximity of the excited particle and thus on the amount of open decay channels.[79] While ICD lifetimes of 85 fs were obtained in modeling of neon dimers, the lifetime of an excited central atom in Ne_{13} was calculated to be as short as 3 fs. Accordingly, follow-up studies demonstrated, that ICD is able to outpace local Auger decay in endohedral fullerene as, for example, $Ne@C_{60}$ (ref 80, see Section 5.2.4). Later, Fasshauer et al. pointed out in theoretical investigations that, to correctly describe ICD, not only the nearest neighbors but also coordination shells at larger distance need to be considered.[281,346]

In experiments, several systems have been investigated with respect to decay times. Pioneering work by Öhrwall and co-workers found very short lifetimes of large neon clusters upon 2*s* ionization employing sychrotron radiation. By examining the width of the 2s-photoline, they concluded that the lifetime of an excited neon atom in the bulk of a neon cluster with an average size $\langle N \rangle \approx 900$ is approximately 6 fs, while atoms at the surface have a lifetime of approximately 30 fs. The same technique was applied somewhat later to the 2*s* spectra of Na^+, Mg^{2+}, and Al^{3+} cations solvated in water.[347] As all outer-valence electrons of the respective atomic species are solvated, the local Auger channel is closed and the $2s^{-1}$ states may only decay by ICD involving a neighboring water molecule. Lifetimes between 1 and 3 fs have been found for this process (see also Section 5.3.5). Similar studies on sodium dimers have been performed by Rander et al. in 2007.[348]

An analysis of the lifetime broadening is also applicable to the decay time of resonant ICD routes as shown by Trinter et al. Inspired by theoretical work on resonant ICD,[230] these authors examined the lifetime of excited helium atoms in HeNe dimers for different vibronic states.[305] In the experiment, a narrow-band excitation energy was chosen, and its energy was scanned across the $He(1s3p)^1P^0$ resonance. After the excitation, the system can decay by transferring the energy to the neon atom and ionizing it, leading to production of bound $HeNe^+$ ions. It was found that the mechanism of resonantly exciting the He atom followed by ICD is, just as predicted,[230] extremely efficient and leads to a large enhancement of $HeNe^+$ ion creation compared to the off-resonance case where the Ne atoms are ionized directly. The $HeNe^+$-yield in dependence on the excitation energy showed multiple peaks corresponding to different vibronic states of the HeNe dimers. From the widths of these peaks, the authors were able to obtain the excitation lifetimes and found a strong increase from 160 to 1100 fs with increasing vibrational levels. This can be explained by an increase of the mean internuclear distance for higher vibrational levels. A detailed theoretical investigation of the process as been performed by Jabbari et al.[104] Employing a pump−probe scheme, Schnorr et al. extracted a mean lifetime of 150 ± 50 fs of the 2*s*-ionized neon dimer. Studies on midsize water clusters extracted lifetimes in the range of 12 to 51 fs[284] for inner-valence ionized states.

All studies on the mean decay time suggest that ICD occurs in many cases on the same time-scale as nuclear motion of the decaying system. As the internuclear distance between the site donating energy (the site that was excited initially) and the energy acceptor is a key parameter for the efficiency of ICD, it is obvious that any nuclear motion occurring after the excitation can have a dramatic effect on decay rates. This is a recurring motif in many studies on ICD; some illustrative examples will be reviewed here. In HeNe mixed dimers, it has been, for example, observed that the nuclear motion even drives the decay, as some of the decaying states are energetically closed at small internuclear distance and open as the dimer is elongated during its vibration.[191] The decay rate of the $^2\Sigma^+(Ne^+(2p^{-2}3s) - He(1s^2))$-state shows a corresponding oscillatory feature during its depletion. Furthermore, ICD is expected to occur in many cases over a large range of internuclear distances due to the motion of the nuclei. In comparably simple systems, such as rare gas dimers, this behavior can cause distinct features in the final kinetic energy release distribution, as in such systems the kinetic energy release reflects the internuclear distance at the instant of the decay.

Pioneering theoretical investigations of the nuclear wave packet dynamics during the decay[151,152,183] predicted a fingerprint of the nodal structures of the vibrational wave function of the $Ne_2(2s^{-1})$-IC-decaying states to be observable in the KER. The corresponding experiment[2] did not show these features, and it turned out that, despite the assumptions being conceptually correct, they are lacking in later theoretical work performed with more refined potential energy curves as well.[184] The KER distribution was confirmed independently in further experiments, for example, in investigations using

https://dx.doi.org/10.1021/acs.chemrev.0c00106
Chem. Rev. 2020, 120, 11295−11369

electron impact ionization.[249] The prediction that vibrational nodes in the potential curve of the decaying state are visible in the kinetic energy release was later confirmed in studies of shakeup induced ICD in helium dimers by Havermeier and co-workers.[187] The corresponding distribution is shown in Figure 17. Because of the large difference in the mean internuclear distance of the neutral and the singly ionized dimer, the excitation leading finally to ICD populates mainly high-lying vibrational states. In ref 180, it has been shown that the kinetic energy release distribution observed in ref 187 can be reproduced by incorporating these vibrational states and weighting their contribution by $1/R^6$. Thus, the observed nodal structure can indeed be associated with nuclear motion and the features of the decaying vibrational wave packet. A nodal structure imprinted on the KER spectrum was also predicted and experimentally found for the Ne 2*s*-ionized state of the NeAr dimer.[185,186] Further detail on other excited states of that system is also available.[318]

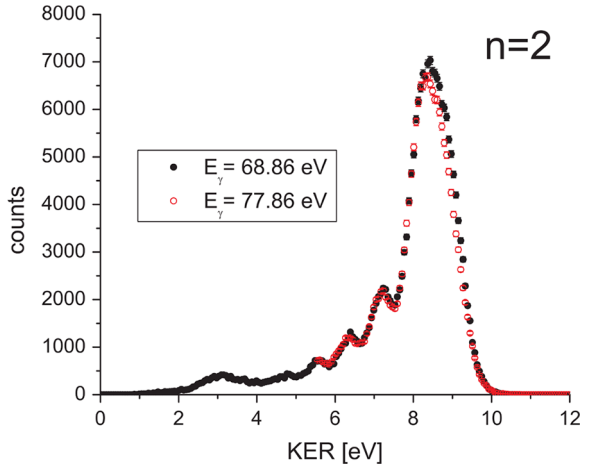

Figure 17. Kinetic energy release distribution of the He^+/He^+-breakup caused by shakeup induced ICD in He_2 employing two different photon energies for the excitation. Reprinted with permission from ref 187. Copyright 2010 APS.

The strong effect of the nuclear motion of the IC-decaying state on the efficiency of the process has further obvious implications. In descriptions of molecular Auger processes, the dependence of the decay rate Γ on the internuclear distance of the atoms forming the molecule is often neglected employing the above-mentioned 'constant (resonance width) Γ approximation'.[349−351] Only within this approximation (which is sufficiently good in most cases when describing covalently bound systems), a molecular Auger decay is strictly exponential as in the atomic case. With the aforementioned properties of ICD, it is understandable that this approximation will most likely fail in case of ICD. Accordingly, ICD became a prototype process for demonstrating nonexponential decay behavior and an experimental investigation[205] of that behavior was finally possible employing the PCI-streaking technique described in Section 4.6, where, for example, Figure 20 depicts the nonexponential decrease of the decaying state over time.

As can be seen from eq 20, the magnitude and dependence of the ICD rate on *R* are crucial parameters for a proper prediction of the kinetic energy release or the ICD electron spectra. The rate's value at Franck−Condon region relative to vibrational frequencies in the ICD state, as well as its behavior at shorter distances, makes a strong impact on the spectra's shape. To obtain the rate as the function of *R*, a number of theoretical methods were developed, which we discuss in detail in Section 3. They range from simple analytical formulas for energy transfer,[9,119,120] which give lower bounds for the rates, to accurate numerical *ab initio* methods based on different models of metastable electronic states.[99−101,144,154] A detailed comparison of these spectra obtained in an experiment to results obtained from theoretical predictions was used in work by Ouchi et al. to optimize the $\Gamma(R)$ of the modeling. A single decay channel of NeAr dimers was examined and the KER of the transition $Ne(^{2+}(2s^{-1}2p^{-1}{}^1P)Ar$ to $Ne^{2+}(2p^{-2}{}^1D)-Ar^+(3p^{-1}))$ was used such that by adapting $\Gamma(R)$ the theoretical results matched the distribution obtained in the experiment.[196] Rist and co-workers[201] examined experimentally shakeup-induced ICD of Ar_2 and identified a decay channel which turned out to be suitable for a direct extraction of $\Gamma(R)$ from the measured data without the need of any theoretical modeling. Although the extraction procedure treated the decay incoherently, the coherent treatment by full theoretical modeling yielded matching results.

Another interesting aspect of the *R*-dependence has been demonstrated by Jahnke et al. in 2007.[8] As explained in the Introduction, the direct and the exchange-contribution to ICD have a conceptually different behavior in *R*. By measuring the kinetic energy release and employing the reflection approximation the internuclear distances at which events of ICD occur after inner-valence shakeup ionization of neon dimers have been determined in an experiment. As Figure 18 depicts, two sets of shakeup states occur which differ by their mean internuclear distance at which they decay. Shake-up states of even parity (main line and states labeled D, E) may decay to the final Ne^+ state (which is of odd parity) by a dipole-allowed transition. These states decay therefore at large internuclear

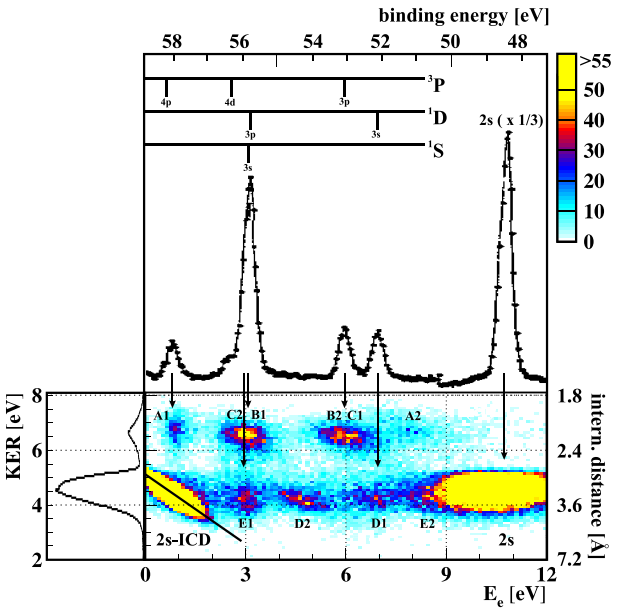

Figure 18. Coincidence map of kinetic energy release and electron kinetic energy after ionization of neon dimers using photons of $h\nu$ = 58.8 eV energy. The shakeup states observed in the electron energy spectrum form two sets that differ by their mean internuclear distance at which they decay. States of even parity decay at large, odd parity-states at shorter internuclear distances. Reprinted with permission from ref 8. Copyright 2007 APS.

https://dx.doi.org/10.1021/acs.chemrev.0c00106
Chem. Rev. 2020, 120, 11295−11369

distances and have been attributed to the direct ICD term. Shake-up states of odd parity (states labeled A-C) cannot perform such a dipole transition. These states may decay, however, by electron exchange, that is, due to the exchange term of ICD. As this decay route is dependent on orbital overlap, it occurs at much smaller internuclear distances. Similar findings with respect to the spin of the involved electrons were shown in 2008 by Ueda et al. in experiments on Ar/Kr mixtures.[300] They concluded that spin-conserved ICD is significantly stronger than spin-flip ICD.

5.1.2. Studies on the Temporal Evolution of ICD. The intriguing dynamics occurring during the IC decay suggested that tracing the nuclei and the electrons involved in space and time is an interesting goal for fundamental research on ICD. The latter, that is, observing the temporal evolution of the electrons and holes has been performed in theoretical work by Kuleff and Cederbaum in 2007.[227] They calculated, employing a fully *ab inito* approach, in real time the electron relaxation dynamics occurring during ICD after Ne 2*s*-ionization of NeAr dimers. Figure 19 shows the time-dependent hole occupation of the initial Ne(2*s*) hole, and the Ne(2*p*) and Ar(3*p*) holes generated during the decay.

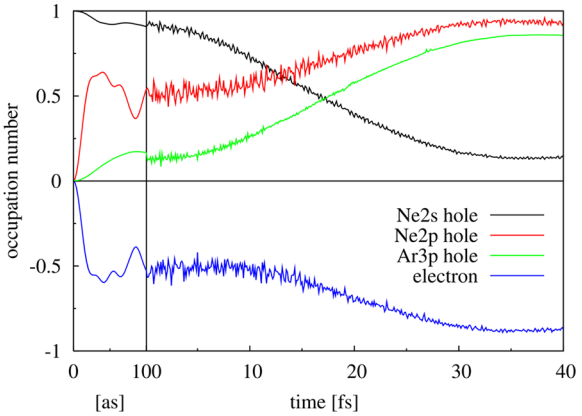

Figure 19. Hole occupation density of NeAr after Ne(2*s*) ionization in dependence of time. The initial vacancy (Ne(2*s*)) is filled while the two other holes (Ne(2*p*) and Ar(3*p*)) open during ICD. The blue line corresponds to the emitted ICD electron density (depicted in terms of an electron hole). Reprinted with permission from ref 227. Copyright 2007 APS.

On the side of experiments, the electron dynamics could, so far, not be traced, but the dynamics of the nuclei have been subject to time-resolved studies. In pioneering time-resolved work Schnorr et al.[203,204] determined the average decay width of ICD in neon dimers after Ne 2*s*-ionization in an XUV-pump/XUV-probe experiment performed at the free-electron laser in Hamburg (FLASH[50]). In the experiment, XUV-light pulses of approximately 60 fs duration (fwhm) were reflected and focused by a split multilayer mirror setup, which produced two photon beams of equal photon energy, but with an adjustable time delay in between them. A COLTRIMS reaction microscope was employed to measure the vector momenta of all created ions in coincidence. The pump pulse was used to create a 2*s* inner-valence vacancy in one of the Ne atoms of the dimers. After the ionization, nuclear motion sets in and the Ne_2^+ ion will contract since the equilibrium internuclear distance is smaller for the ionic state than for the initial dimer groundstate. Eventually, the system will undergo ICD leading to a $Ne^+(2p^{-1}) + Ne^+(2p^{-1})$ final state and finally the dimer fragments in a Coulomb explosion. The kinetic energy release (KER) of the reaction depends on the internuclear distance at the instant of the ICD. The probe pulse can now further ionize one of the Ne^+ ions, resulting in a triply charged $Ne^{2+} + Ne^+$ state. If the probe pulse ionizes the ionic dimer before ICD occurs, a $Ne^+ + Ne^+$ or $Ne^{2+} + Ne$ pair is created instead. Thus, the ICD-lifetime can be estimated by measuring the yield of $Ne^{2+} + Ne^+$ as a function of pump–probe delay. The KER of the $Ne^{2+} + Ne^+$ ion pairs (the ICD case) was found to decrease with increasing delay. This can be understood since the KER depends on the internuclear distance of the two Ne^+ ions at the arrival time of the probe pulse, which removes an additional electron and thus alters the potential energy curves involved. To determine the mean ICD-lifetime from the time-dependent KER measurements, the authors performed classical simulations of the nuclear motion assuming an exponential decay with a constant (i.e., *R*-independent) lifetime. From this, a lifetime of (150 ± 50) fs was inferred that compares well to theoretical calculations.[7] A more detailed theoretical study of the nuclear dynamics using a wave packet-approach has been published recently.[352] Just recently, Schmid et al. performed a similar pump–probe experiment to trace charge transfers in argon dimers employing strong IR-light as a probe.[324]

In an experiment, Takanashi and co-workers used XUV-pump and UV-probe pulses to perform a time-resolved study of ICD in doubly excited neon dimers.[212] This has been a new class of ICD processes that was predicted by Kuleff and co-workers in 2010.[51] Here, the de-excitation of one of the excited atoms leads to the ionization of the other. Employing the extremely intense XUV pulses available at the italian FEL FERMI,[333] the authors were able to create the following doubly excited states by two photon absorption:

$$Ne_2 + 2\hbar\omega_{XUV} \rightarrow [Ne^*(2p^{-1}3s)]_2 \quad (24)$$

ICD then leads predominantly to stable, bound dimer states:

$$[Ne^*(2p^{-1}3s)]_2 \rightarrow Ne^+(2p^{-1})Ne + e_{ICD}^- \quad (25)$$

The ion yield was measured with time-of-flight spectrometers. By adding a UV probe pulse with a photon energy just sufficient to ionize a 3*s* electron of an excited atom, it was possible to obtain the ICD lifetime. When the pump and probe pulses arrive at the target simultaneously the number of Ne_2^+ ions is strongly reduced because the excited states are ionized before ICD happens. In this case, the UV ionization leads to a dissociation of the dimers:

$$[Ne^*(2p^{-1}3s)]_2 + \omega_{UV} \rightarrow Ne^+(2p^{-1}) + Ne^*(2p^{-1}3s) + e^- \quad (26)$$

When the time delay of the probe pulse is increased, the number of stable Ne_2^+ ions (see eq 26) increases again, with the slope of this increase reflecting the ICD lifetime. From this, the authors were able to extract a lifetime of 390(−130/+450) fs for the long-lived $^1\Pi_g$ and $^1\Delta_g$ doubly excited states. The experimental resolution was not sufficient to determine the lifetime of the short-lived $^1\Sigma^+_g$ states, but an upper limit of 150 fs was given.

A further pump–probe experiment was reported in early 2019.[334] Fukuzawa et al. triggered the electronic decay of diiodomethane molecules (CH_2I_2) using XUV-light from an X-ray free-electron laser (SACLA, Japan[353]) and examined the

https://dx.doi.org/10.1021/acs.chemrev.0c00106
Chem. Rev. 2020, 120, 11295−11369

transient states using a near-infrared femtosecond laser for probing. Two different sets of states were observed. Short-lived states (~20 fs), which finally yielded highly charged molecular fragments, were identified to occur after molecular Auger decay, while long-lived states (~100 fs) decay via ICD between the two iodine atoms during the breakup of the molecule.

The experiments described above relied on the assumption of an exponential decay and thereby determined average ICD lifetimes. Trinter and co-workers pursued a novel experimental approach, so-called PCI-streaking, which allowed for the first time to study the complex decay behavior influenced by nuclear dynamics and measure the nonexponential decay behavior predicted for ICD.[205] The concept of PCI-streaking is explained in Section 4.6.4 in detail. The target system chosen for a first time-resolved measurement of that kind was the helium dimer, investigating ICD after ionization and simultaneous excitation by 65.5 eV synchrotron radiation. As excited dimers relax via ICD, the resulting ions undergo a Coulomb explosion, whereby the final kinetic energy release (KER) depends on the internuclear distance R at the instant of ICD. Within the reflection approximation,[354] it is given by $KER = 1/R$. The photoelectron energies and ion momenta were measured in coincidence using a COLTRIMS setup. Figure 16b in Section 4.6.3 shows the coincidence map of the ICD electron emission times (obtained from the photoelectron energies) and the KER of the ions. It is clearly visible that the KER strongly depends on the emission time of the ICD electron. For short decay times, the internuclear distance is large leading to low KER values. For longer decay times, the ionic dimer has time to contract and a strong feature at $KER \approx 8.5$ eV (corresponding to the inner turning point of the vibrational motion of the ionized dimer) appears. For even longer decay times, finally, a vibrational structure forms in the KER distribution. Plotted in Figure 20 is the norm of the decaying state versus time obtained from the measurement and from calculations by Sisourat et al.[180] Both the measured and calculated decay rates are clearly nonexponential. The deviations observed between the theoretical and experimental values are assumed to be due to the limited accuracy of the decay rates entering the nuclear dynamics simulations.

5.1.3. Efficiency of the ICD Process. Several other relaxation processes may compete with ICD. As mentioned before, fluorescence decay is a viable route for de-excitation of any state which can undergo ICD. In most cases, however, the decay rate of ICD is larger and strong quenching of ICD by fluorescence has been reported only for huge systems, such as the helium dimer.[180,187] There, approximately 50% of the excited dimers relax by means of photon emission. In contrast, experiments on neon clusters[255,279] found an efficiency close to 100% for ICD in case of Ne(2s)-ionization. For mixed rare gas systems, efficiencies of (or close to) 100%, within the experimental uncertainty, were also found for excited states that may decay by ICD and ETMD, or solely by ETMD.[223,283]

Other mechanisms yielding a suppression of ICD are connected to the nuclear motion during the decay. While ICD of inner-valence states has been observed in water dimers[215] and larger water clusters,[263] detailed studies on its efficiency found it only in the range of 10% to 45% in clusters of $\langle N \rangle = 2-250$. It turned out that this is a result of proton migration, which leads the system into configurations in which the ICD channel is closed.[284] The picture changes once again when core ionization-induced ICD in aqueous systems is considered (Section 5.3). Excitation energies are now so large

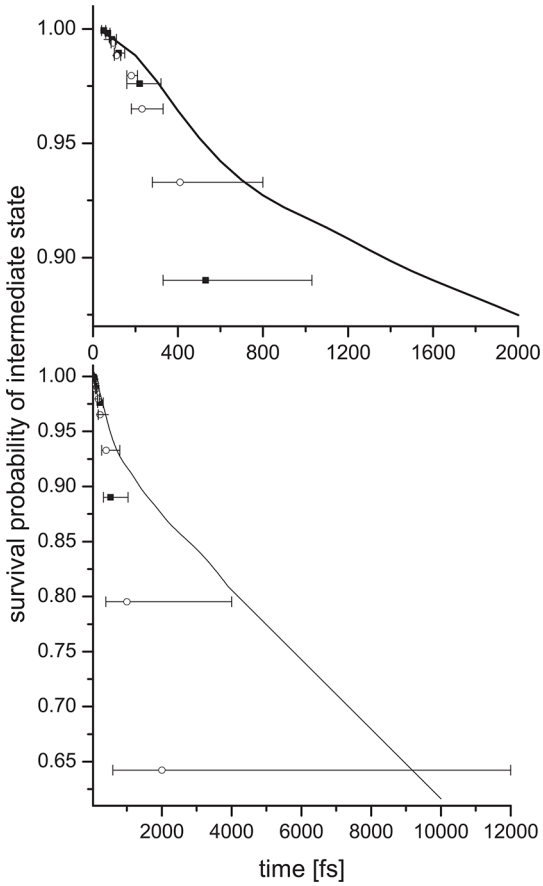

Figure 20. Norm of the intermediate excited state prior to ICD for two different time ranges. Reprinted with permission from ref 205. Copyright 2013 APS.

that the ICD channel never closes, but it now competes with local Auger decay.

The interplay between photodissociation and ICD was also studied theoretically in atom−molecule clusters. Kopelke et al. demonstrated that photoexciting the CO molecule in the CO−Mg cluster to a predissociating state opens up competition between ICD and nuclear dynamics.[213] It was found that for lower lying vibrational states of the decaying state, whose predissociation rate is less than the ICD rate, the dissociation is quenched by electronic decay and the cluster remains intact. Populating higher lying vibrational states, whose predissociaion rate exceeds that of ICD, leads to the dissociation of CO and a breakup of the cluster. Jabbari et al. investigated whether ICD might quench direct photodissociation, which proceeds on the time scale of <10 fs, which is at least an order of magnitude shorter than predissociation lifetimes.[355] Indeed, they showed that ICD in H_2O-Cl^- cluster can quench photodissociation of H_2O excited states to its lowest electronic state. Importantly, the quenching is assisted by the cage effect in the cluster which hinders the dissociation. The cage effect should become pronounced in larger molecular clusters or solutions, where it should lead to the increase in ICD efficiency. Overall, despite the presence of competing decay channels, in many cases, a significant proportion of decays by ICD and/or ETMD was nevertheless observed or inferred from theoretical studies.

We now would like to elaborate a bit on the experimental method for quantifying the branching ratio α_{ICD} of the ICD

https://dx.doi.org/10.1021/acs.chemrev.0c00106
Chem. Rev. 2020, 120, 11295−11369

channels. Different to the first studies on ICD in refs 3, 4, 255, and 356, later works used electron−electron coincidence spectroscopy to filter out a background of inelastically scattered electrons, which inevitably occurs when larger clusters are studied. This technique allows to extract α_{ICD}, as illustrated in Figure 21. For an ICD process with a branching ratio of unity (all excited states relax via ICD), recorded with a perfect spectrometer, the number of coincident e_{ph}, e_{ICD} pairs detected would equal the number of primary photoelectrons pertaining to the ICD initial state, recorded without any discrimination. In an actual experiment on a cluster jet, some correction factors have to be taken into account leading to

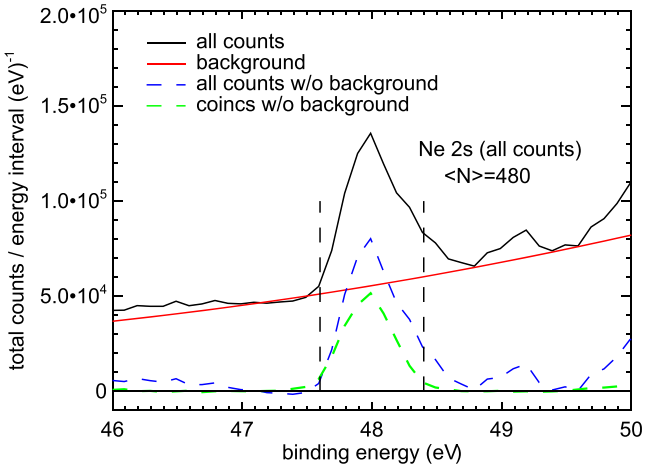

Figure 21. Ne 2*s* photoelectron spectrum from <*N*> = 480 Ne clusters recorded with a magnetic bottle time-of-flight spectrometer at a photon energy of 52 eV. The bulk and surface component cannot be resolved at the chosen spectrometer settings. The black trace shows the energy spectrum of all electrons that were recorded, the blue dashed trace is the same spectrum after a background due to inelastic scattering (red solid trace) has been subtracted. The green dashed trace shows the contributions of those 2*s* photoelectrons e_{ph} that were recorded in coincidence with an ICD electron e_{ICD}. An area comparison of the two dashed traces in the region between vertical bars allows to quantitatively determine the efficiency of ICD of the $2s^{-1}$ state, yielding a value of 0.99(11). See text for details. Reprinted from ref 279, with permission from Elsevier.

$$\alpha_{ICD} = \frac{P(e_{ph}, e_{ICD})}{p(e_{ph})} \frac{1}{c\gamma(e_{ICD})} \quad (27)$$

Here, P and p pertain to the coincident and noncoincident (undiscriminated) event rates, e refers to the kinetic energy of the respective electron, c denotes the degree of condensation in the cluster jet (number density of clustered atoms or molecules, divided by total number density), and γ is the detection efficiency of the spectrometer. In Figure 21, the green and blue traces refer to $P(e_{ph}, e_{ICD})$ and $p(e_{ph})$. Using this formalism, indeed an efficiency of unity could be shown for Ne $2s^{-1}$ ICD in Ne clusters, as surmised from earlier results (Figure 30).[279]

Another example to which the same method was applied is the Ar $3s^{-1}$-decay in larger ArKr clusters (<*N*> > 1000). According to calculations, in this system, only the ETMD(3) channel is energetically viable.[27,283] The efficiency analysis nevertheless led to values consistent with unity, within the experimental error. This is particularly interesting since even this complex interaction of three sites leads to decay rates that outpace fluorescence. Further detail on ETMD in ArKr and ArXe is shown below.

General experimental results on water clusters will be shown in Section 5.2.5. Results on the efficiency of ICD, however, are covered here. A detailed study on ICD of the $2a_1$ inner-valence vacancy in water clusters has been published.[284] This orbital is mostly derived from the oxygen 2*s* and in this respect is similar to the rare gas examples detailed above. Its binding energy of 32 eV is somewhat lower, however.[357] The molecular nature of the constituents, and the differences between hydrogen and van der Waals bonds nevertheless lead to a qualitatively deviating behavior of the ICD efficiency in water compared to rare gas clusters. By inspecting the experimental data (Figure 22),[284] one immediately sees that values are far below unity, confirming earlier reasoning in a theoretical study.[358] Further on, a significant isotope effect in the efficiency was found. At a cluster size <*N*> of approximately 60−90, α_{ICD} was found to be 0.07(1) larger for D_2O than H_2O-clusters. Both the low values and the isotope effect point to a role of nuclear dynamics in the relaxation of the excited state. Different than the van der Waals bonds in rare gas clusters, hydrogen bonds are directed and may give rise to proton dynamics. This aspect is of huge importance for ICD in liquids and will be covered in detail in Section 5.3. Water clusters of the sizes covered here, and formed in a supersonic expansion, are, however, solid and have the structure of amorphous ice, possibly with a crystalline core for the largest clusters in our expansion.[359] Nevertheless, calculations of the nuclear dynamics have found that internal conversion after proton transfer is an important competing channel with ICD.

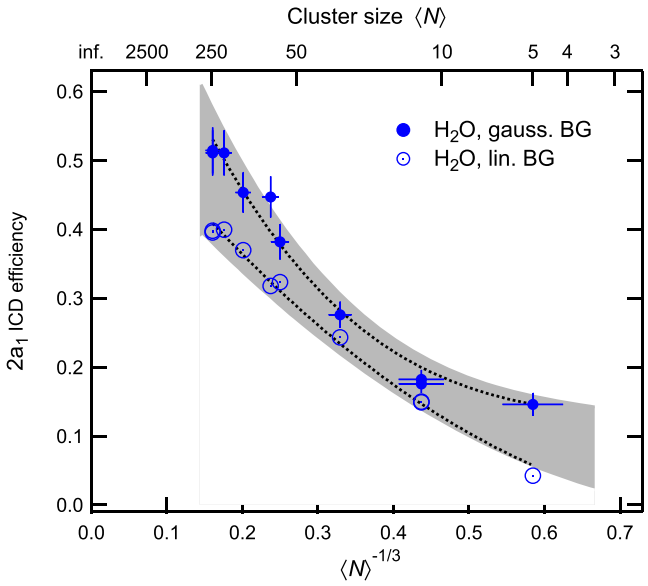

Figure 22. Experimental results for the ICD branching ratio α_{ICD} of the inner-valence ($2a_1$) ionized state in water clusters of different mean size, recorded as a function of mean cluster size <*N*> (top axis) or inverse cluster radius, ~ $<N>^{-1/3}$ (bottom axis). Data were recorded at a photon energy of 62 eV. A significant isotope effect in the efficiency was also found (see text). Several models for quantifying the background shown in Figure 21 were used (two sets of symbols). The parameter region compatible with the measurements is highlighted by gray shading. Figure adapted from ref 284, used under CC BY. See original publication for details.

https://dx.doi.org/10.1021/acs.chemrev.0c00106
Chem. Rev. 2020, 120, 11295−11369

The interdependence between ICD and proton transfer was investigated by calculations on the water dimer, as a prototypical system. Results for the potential energy curves of the relevant singly and doubly ionized states are shown in Figure 23.[284] The one pertaining to the singly ionized state

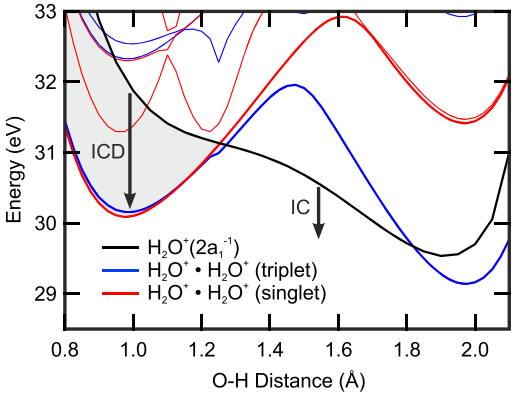

Figure 23. Calculated potential energy curves for singly and doubly ionized states of the water dimer. Energies are shown along the proton transfer coordinate, that is, the O−H distance in the proton donor. Gray shading highlights the parameter range in which ICD is energetically allowed; arrows indicate relaxation via ICD or internal conversion (IC), respectively. Absolute energies were calculated relative to the minimum of the electronic ground state of a water dimer. Figure adapted from ref 284, used under CC BY.

(black) has a negative slope at the ground state O−H equilibrium distance of 0.97 Å. By that, the system may relax by a proton transfer away from the ionized site. This is a common motif in ionized water. Interestingly, the curve of the singly ionized state has a crossing with the various potential curves of the doubly ionized states at a proton distance of approximately 1.3 Å. After proton transfer has proceeded that far, ICD is no longer energetically possible, and consequentially the system has to relax by other mechanisms. The final state after proton transfer consists of an excited $OH^\bullet$ radical and an H_3O^+ ion. A Mulliken population analysis shows that the positive hole is completely localized on the donor water after creation of the $2a_1$-ionized state. After completion of the proton transfer, the positive charge is mostly localized on the H_3O moiety (+0.83e). This system will most probably relax by further nuclear reactions, firstly hydrogen dissociation from the $OH^\bullet$. Combining the measured ICD efficiency with calculated values of the speed of nuclear dynamics, the ICD lifetime in the smallest set of clusters shown in Figure 22 was estimated in-between 12 and 52 fs.

The dependence of the efficiency on cluster size present in Figure 22 also deserves an explanation. Several factors may contribute to this observation. First, in larger clusters all states decrease in energy due to better polarization shielding. However, the doubly ionized states will lower by a larger amount than the singly ionized initial state. The amount of energy available to ICD is thus higher, and the ICD channel stays open over a longer time. A shift in the ICD energy with increasing cluster size is indeed present in the data, and will be shown below (Section 5.2.5). Calculated potential curves further underpin that this mechanism occurs.[284] Two other effects may also play a role. In calculations for rare gas clusters, the ICD rate was found to increase dramatically with the number of nearest neighbors.[79] A lesser effect is expected in water, as even in a dense water network every molecule is fourfold coordinated at most. Nevertheless, the average number of water bonds will increase over a wide range of cluster sizes, and the same should hold for the ICD rate. Finally, the hydrogen bond length is known to be slightly smaller in liquid water compared to small clusters. If the average bond length decreases also as a function of cluster size, this again will contribute to an increase in the ICD rate. The relative importance of these three factors, however, has not been quantified yet.[284]

Detailed results on the coexistence of Auger decay, ICD, and nuclear dynamics after core level ionization of water will be presented below (Section 5.3.2).

5.1.4. ICD Electron Angular Emission Distributions.

When escaping the system, ICD electrons (which are in most cases of low kinetic energy) acquire detailed information on the system's electronic structure, the system's Coulomb potential and geometry and on the dynamics of the process. In general, angular distributions of emitted electrons, which are very sensitive to an interplay of the emitted partial continuum waves, provide an access to important complementary information on the process, as compared to, for example, total cross-sections. The most complete information can be extracted from so-called molecular frame angular distributions (MFADs). These are angular emission patterns relative to, for example, the molecular axis when investigating diatomic systems (see, e.g., 360−363 for reviews). As most experiments on ICD have been performed in the gas phase, it is necessary to gather information on the spatial orientation of the examined dimer or cluster. Experimentally, this information is in most cases obtained by measuring the emission directions of the fragments of the Coulomb exploding or dissociating system in coincidence. From these emission directions, the system's orientation in the laboratory frame can be deduced and the emission direction of electrons (measured in coincidence, as well) can be transformed into the molecular frame by inspecting the relative emission angles of the detected particles. MFADs of ICD electrons were studied experimentally and theoretically, for example, for Ne dimers,[58,192,298,304] HeNe,[107] and helium dimers.[188,321]

Jahnke and co-workers[298] were the first to present MFADs of ICD electrons emitted from neon dimers after inner-valence ionization. The experimental distributions showed slight variations for different electron energies, which might be associated with the influence of the underlying nuclear dynamics. These experimental data were later interpreted theoretically in ref 192 within the frozen-core Hartree−Fock approximation. In subsequent experimental work by Kreidi et al.,[58] a COLTRIMS setup was used to investigate ICD after Ne(1s) ionization and subsequent one-site Auger decay of Ne_2. The MFADs of the photo- and ICD electrons showed asymmetric features, which imply localization of the K-vacancy created at one of the two atomic sites of the Ne_2 and an emission of the ICD electron from the opposite site (see Section 5.6.2 for details). The measured angular distributions of ICD electrons after Auger decay were interpreted theoretically in ref 304 within the relaxed-core Hartree−Fock approximation. Those calculations supported the implied core-hole localization and illustrated sharp variation of the angular distributions of the ICD electrons as a function of internuclear distance (i.e., of the kinetic energy of the ICD electron).

Havermeier et al. reported a strong variation of the measured angular distributions of ICD electrons emitted

https://dx.doi.org/10.1021/acs.chemrev.0c00106
Chem. Rev. 2020, 120, 11295−11369

from helium dimers as a function of the KER, that is, of the internuclear distance at the instance of the decay.[188] This strong dependence of the MFADs was qualitatively explained by a strongly simplified model, which implied a coherent superposition of two spherical electron waves emitted from two helium atoms and accounts for the symmetry of the electronic states involved in the transition. Subsequent *ab initio* calculations of these ICD electron MFADs[321] relate the observed variations to electronic properties of the process. In ref 107, angle resolved RICD spectra of HeNe were studied experimentally and theoretically. Two different decay channels, populating bound $HeNe^+$ and fragmenting He + Ne^+ ionic states, were identified experimentally. Here, the angular distributions enabled to uncover an origin of the fragmentation channel, which was explained by a slow homogeneous dissociation of bound vibrational levels of the final ionic state $A^2\Pi_{1/2}$ into vibrational continua of the lower lying states $X\ ^2\Sigma_{1/2}{}^+$ and $a^2\Pi_{3/2}$.

Later, *ab initio* calculations, performed by Mhamdi and co-workers, predicted a substantial scattering of the low-energy ICD electron wave on the density of the excited spectator electron in neon dimers.[192] As a consequence, the MFADs of the ICD electrons obtained for $5p\sigma$ and $5p\pi$ spectator electrons differ dramatically. As Figure 24a shows, the low-energy ICD electron wave tries to avoid the spectator electron when escaping the dimer-ion (see inset in Figure 24 for orientation). Therefore, $5p\sigma$ and $5p\pi$ excitations result in a suppression of the electron emission along and perpendicular to the dimer axis, respectively. The results from a coincidence experiment reported in the same work confirmed these theoretical predictions; the corresponding measured distributions are shown in Figure 24b and c. It was concluded that this effect should occur in general if low energy electrons are emitted in the presence of an excited spectator electron.

5.1.5. Superexchange ICD and the Influence of a Dielectric Continuum. In 2017, Miteva et al. demonstrated in theoretical work a further aspect of ICD.[364] In analogy to superexchange mediated coupling in FRET of extended systems[68] they observed that the efficiency of ICD can be drastically increased when a bridge atom is added to the decaying compound, that is, the lifetime of an ICD active state was drastically decreased due to a further (ICD-inactive) atom in the chemical neighborhood of atoms involved in ICD. As a model system the authors employed a NeHeNe trimer in which one of the neon atom has been inner-valence ionized. The calculations show, that the lifetime of the $Ne^+(2s^{-1})$ state decreases by a factor of 6 if, in addition to the second neon atom involved in the ICD, a helium atom is present. A corresponding diagram from ref 364 is shown in Figure 25. It turned out that this increase of the decay width occurs due to a coupling of virtual bridge states with an intermediate ionic configuration $Ne^+(2p^{-1})He^-Ne^+(2p^{-1})$. As soon as there is sufficient orbital overlap between these states and the bound states of the neon dimer, the superexchange mechanism becomes active and ICD may occur across the bridging atom. In followup work by Votavová et al. more detailed investigation on superexchange ICD were performed by analyzing the decay width of several superexchange ICD channels.[365] They found that only some ICD channels are enhanced due to the presence of the bridge atom. Similar analysis of superexchange ICD in NeHeAr showed that in this system the decay width is only doubled due to the superexchange contribution. This reduced enhancement was attributed to less favorable energy levels of NeHeAr.

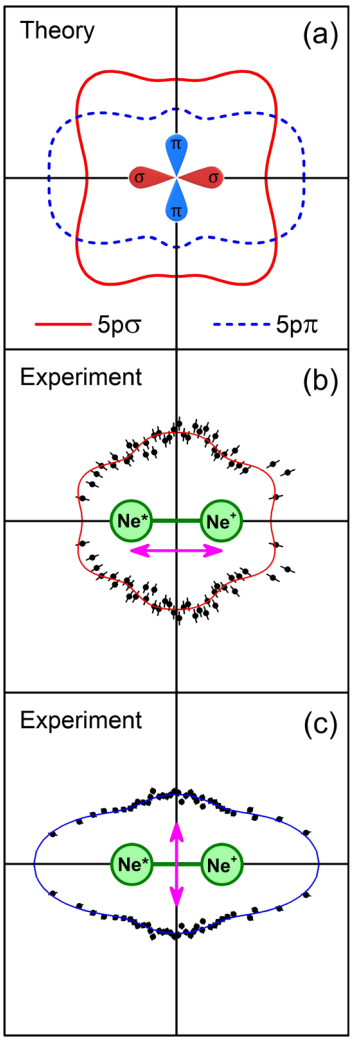

Figure 24. Reprinted in part with permission from ref 192. Copyright 2018 APS. Theoretical and experimental MFADs of sRICD electrons from neon dimers. (a) Predicted distributions for the $5p\sigma$ and $5p\pi$ spectator electrons. (b, c) Measured distributions in case the dimer is oriented in parallel or perpendicularly to the polarization direction of the linearly polarized light.

In 2018, Hemmerich et al. developed an approach to model ICD and its related phenomena based on macroscopic quantum electrodynamics,[121] which allows for a general description of ICD including retardation effects (i.e., due to the finite speed of light) and the influence of a macroscopic dielectric environment. They found, in particular, that the efficiency of ICD is greatly enhanced at large internuclear separations of the decaying partners when retardation effects are considered in the modeling. Furthermore, effects on the ICD rates caused by a surrounding medium and a nearby macroscopic body have been investigated in great detail. Their importance, when dealing with nonidealized real life-conditions, was emphasized by the authors. Building on this approach, a generalization of superexchange ICD has been presented very recently by Bennett and co-workers.[366] They developed the analog to the virtual photon approximation[9] (see eq 12) for the case of three-body ICD, incorporating an ICD donor, a mediator (i.e., the bridge atom in superexchange

https://dx.doi.org/10.1021/acs.chemrev.0c00106
Chem. Rev. 2020, 120, 11295−11369

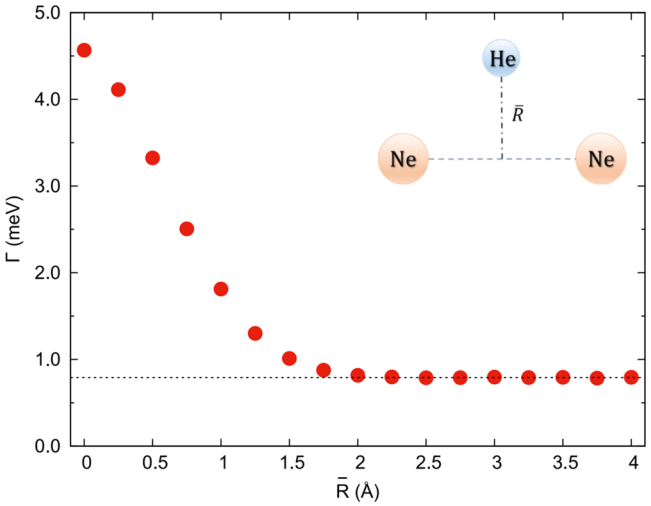

Figure 25. Total decay width of the $Ne^+(2s^{-1})HeNe\ ^2\Sigma^+_g$ state as a function of the distance R between the He atom and the center of mass of neon dimer. The distance between the two neon atoms R is fixed to 4 Å. The total decay width of the corresponding state of Ne_2 is shown as a black dotted line. Reprinted with permission from ref 364. Copyright 2017 APS.

ICD), and an acceptor. Their work highlighted the striking role of neighboring ICD-passive entities on the efficiency of ICD. In the retarded regime, these objects are able to substantially enhance or, as well, suppress ICD depending on their location with respect to the IC-decaying units.

5.1.6. On the Different Ways to Populate IC-Decaying States. The prototypical example for ICD shown in Figure 1 and several of the studies referred to above feature ICD from single-hole inner-valence vacancy states in some system. The single-hole nature of the excited state is not a necessary criterion for ICD, nor is the ionization of an inner-valence shell. Despite it seeming natural that the exact process which populates a IC-decaying state is only of minor importance, early work on ICD demonstrated in a first step that, indeed, ICD occurs independent of the way the decaying state was created. First, it has been predicted by theory that ICD will happen as a terminal step after core−shell ionization and subsequent Auger decay,[1,153] and follow up experiments have confirmed this prediction employing Ar_2,[296,297] Ar_3,[299] and Ne_2.[29] Later, similar decay routes have been identified in heterodimers.[300,301] The experimental studies then triggered further detailed theoretical investigations on the decay pathways in the corresponding dimer species[101,367,368] and calculations of corresponding ICD electron spectra.[195] Further synchrotron work on argon dimers by Keshavarz and co-workers presented a detailed overview of the decay routes occurring after irradiation of the dimers with photons in an energy range of 255 eV < $h\nu$ < 340 eV.[369] The investigations of the cascade decay channels in the Ne_2 and NeAr dimers after Ne(1s)-ionization was completed by Ouchi et al.[317] They observed ICD of triply ionized states populated in an atomic double Auger decay of Ne by investigating electron/ion-energy coincidence maps of different charge states and breakup channels of the dimers.

Another, different route of populating a state that can undergo ICD has been found by Barth and co-workers[370] and about the same time by Aoto et al.[256] Both investigations showed, that ICD occurs not only after inner-valence ionization but also after resonant excitation of the clusters. By scanning the energy of the exciting photons in the range of inner-valence excitation of neon clusters, distinct features have been observed, which have been attributed to resonant ICD (since then termend "RICD").[370] The corresponding plot is shown in Figure 26. The full series of Ne($2s^{-1}$)np-resonances

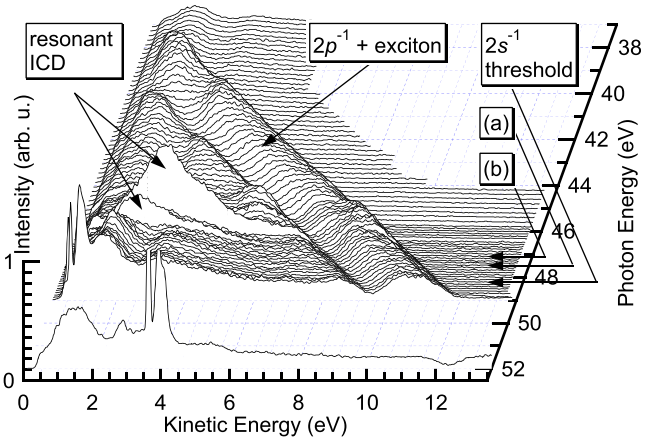

Figure 26. Low kinetic-energy electron spectra of Ne clusters excited with photon energies around the Ne 2s threshold. Resonantly enhanced ICD-like features can be identified at two photon energies below the 2s threshold. Moreover, two lines related to inelastic energy loss of 2p photoelectrons by intracluster creation of excitonic states can be seen at all photon energies. The latter occur at fixed binding energy, while the ICD-like features appear at fixed kinetic energy. Spectra in this graph are smoothed binomially over 10 points corresponding to an energy region of 120 meV for better clarity. Reprinted with permission from ref 370. Copyright 2005 AIP.

and their RICD in neon dimers has been observed by Aoto et al.[256] These studies triggered, as well, more detailed theoretical work on RICD.[81,82] Resonant ICD can also be observed via detection of fluorescence, as explained in Section 5.2.2.

As pointed out already in the last part of Section 5.1.1, ICD may occur, as well, after shakeup ionization (termed "SICD"). Experiments on systems in which the inner-valence states are too low in energy to decay by ICD nevertheless showed that type of decay for other states lying higher in energy, for example, satellite states of 2h1p-character. Particularly notable is an overview study of excited states in a series of homonuclear rare gas dimers[257] and a detailed investigation of ICD from Ar^+ $3p^{-2}nd$-states in the Ar dimer excited by electron impact.[202,313,314] The occurrence of energetic ion pairs was used as evidence for ICD in the latter series of works, and other studies of the same system.[59,371] Rist and co-workers performed corresponding investigations employing synchrotron radiation.[201] It is interesting that in ref 257 single energetic ions were seen even below the ICD threshold. Already before the experimental discovery of ICD, this process was observed in Ar clusters, and was assigned to Ar 3s ionization followed by relaxation plus energy transfer to a neighboring Ar site.[372] Different than in ICD, the energy transfer is not sufficient for ionization, however. The resulting Ar^+ $(3p^{-1})$ Ar* dimer subsequently dissociates, which explains the observation of energetic ions.[257,372] Patanen et al. observed a broadening of the satellite-lines in studies on xenon clusters, which they interpreted as the occurrence of ICD.[373]

Particle impact mechanisms for the excitation of ICD have been studied less intensively than photon absorption, which

https://dx.doi.org/10.1021/acs.chemrev.0c00106
Chem. Rev. 2020, 120, 11295−11369

might be because of additional experimental difficulties. As the energy transfer in a particle collision may have any value afforded by the primary beam, the discrimination of ICD against other mechanisms might be more difficult. Nevertheless, several teams were able to present results on ICD in the Ne dimer by impact with α-particles,[245] and in (satellite states of) the Ar dimer using fast (3 keV) or slow (37−67 eV) electrons.[59,314] A recent theoretical treatment of ICD after electron impact can be found in ref 374. More work on these processes will be presented below.

A peculiarity, however, is strong field ionization. To our knowledge, there has been, despite theoretical work on the topic (with respect to loosely bound matter),[375,376] no experimental observation of ICD in this research field (see, e.g., refs 303 and 377 for work on argon dimers). The intensity needed to generate states decaying by ICD in loosely bound matter by strong fs-lasers is typically very high. It is therefore assumed that these states are already depopulated shortly after their creation during the exciting laser pulse and prior to ICD. An exception in this respect is, however, the formation of Rydberg atoms in nanoplasmas in the ionization of clusters by very intense infrared laser fields.[219] More detail on theoretical work about ICD excited by two- and multiphoton processes will be given in section 5.7.1.

5.1.7. The Quest for Absolute Cross-Sections. Experimentally determined absolute probabilities of photon-induced processes are indispensable for quantitative validations of theoretical models. Moreover, the family of fundamental electron transfer and decay processes in weakly bound matter relevant for this review will certainly play a major role in astrophysical and, chemical processes occurring for example on interstellar dust particles subjected to high-energy radiation or in the understanding of the impact of ionizing radiation on biological entities. For a quantitative modeling in such areas, quantitative laboratory data are necessary. Whereas there is a manifold of methods for the determination of absolute absorption, photoexcitation, and photoionization cross-sections for isolated atoms or photodissociation cross-sections for isolated molecules, the determination of absolute cross-sections for photon-induced processes and possible subsequent decays for weakly bound systems such as rare gas clusters remains a big challenge. The major experimental difficulty is based on the typically used cluster beams. These are mainly created by supersonic expansions where monomers coexist with clusters of different sizes. For such beams, their composition is not very well-defined (see Section 5.2.1), and information on their consistence is of course needed to determine absolute cross-sections for photon-induced processes and their consequences in clusters. Therefore, only few data are available on cross-sections.[378,379] A recently developed strategy to determine absolute cross-sections for resonant ICD in rare gas clusters is based on the combination of time-resolved fluorescence spectrometry and photoelectron spectrometry,[329] which will briefly be summarized below. This combination of two methods can be used for absolute cluster cross-section determination when three conditions are fulfilled. (1) In a mixed cluster beam, the detector signals of clusters and monomers are separable. (2) For monomers, absolute cross-sections are known. (3) The number of condensed clusters in the mixed beam can be determined. As shown by Knie et al.,[280] the average emission time of fluorescence from clusters is considerably longer as the emission time of fluorescence from atoms. Therefore, gating the fluorescence detection window on short emission times (in the range of ns) will cut off the fluorescence signal from the clusters, gating on long emission times will cut off the monomer signal. This time characteristic enables the *in situ* comparison of the spectral features of the monomer signal versus cluster signal, that is, apart from spectral shifts between cluster and monomer signal the emission time can be used to distinguish unequivocally the fluorescence emission signal from clusters from the one of the monomers such that condition 1 is fulfilled. For rare gas atoms a variety of absolute values of fluorescence and electron emission cross-sections are known (see review by Sukhorukov et al.[380]) such that for studies on rare gas clusters or mixed clusters with rare gas contributions also condition 2 is fulfilled. To fulfill condition 3, the number of clusters with respect to the number of unclustered monomers has been determined by electron spectrometry using a magnetic bottle spectrometer. The total amount of atoms in a mixed cluster beam is the sum of the number of atoms condensed into clusters and the remaining free monomers.

We may define the degree of condensation K ($[0, 1]$) as the ratio between the number of cluster atoms and the total number of atoms in the jet. When expansion parameters are changed, K will change, as well. Moreover, K will be also different in different parts of the beam even for one set of expansion parameters. Therefore, different acceptance solid angles of the spectrometer will lead to different averaged K values. In the experiments described in ref 329, K has been determined using features in the electron spectra, which have been identified to belong to monomer or cluster processes by their different binding energies. If K is known for every 100 condensed atoms $(100-100 \cdot K)$ individual uncondensed atoms are present and $(100 \cdot K)/\langle N\rangle$ clusters with a given average number of monomers $\langle N\rangle$. Then absolute cross-sections σ_{clus} for clusters can be determined from the emission intensity ratio I_{clus}/I_{at} between clusters and monomers at known monomer cross-section σ_{at} by

$$\sigma_{clus} = \sigma_{at} \times \frac{I_{clus}}{I_{at}} \times \frac{(1-K) \times \langle N\rangle}{K} \tag{28}$$

Introducing a correction for the different solid angles the electron spectrometer and the fluorescence spectrometer is operating in and a correction for the varying quantum efficiencies of the photon detection systems at different emission wavelengths it is possible to determine (or at least estimate) cluster emission cross-sections. An example for the determination of absolute cluster specific cross-sections for a resonant ICD process is displayed in Figure 27. Still uncertainties are large, but a start has been made and a further strive to determine more accurate absolute cross-sections is certainly worthwhile.

5.1.8. Universality of ICD. As briefly mentioned already in the Introduction of this review, after the first decade of research on ICD, it has been clear that ICD is, rather than being an exotic exception, a very general phenomenon in nature. No evidence has been observed that there are any species of loosely bound matter or certain chemical elements in which ICD is conceptually prohibited (for example, ICD has been observed experimentally even in molecular anions, as well[382]). As explained in the preceding section, ICD occurs independent of the exact excitation route employed for creating the IC-decaying state. As soon as energetically compatible states are present in loosely bound matter, ICD

https://dx.doi.org/10.1021/acs.chemrev.0c00106
Chem. Rev. 2020, 120, 11295−11369

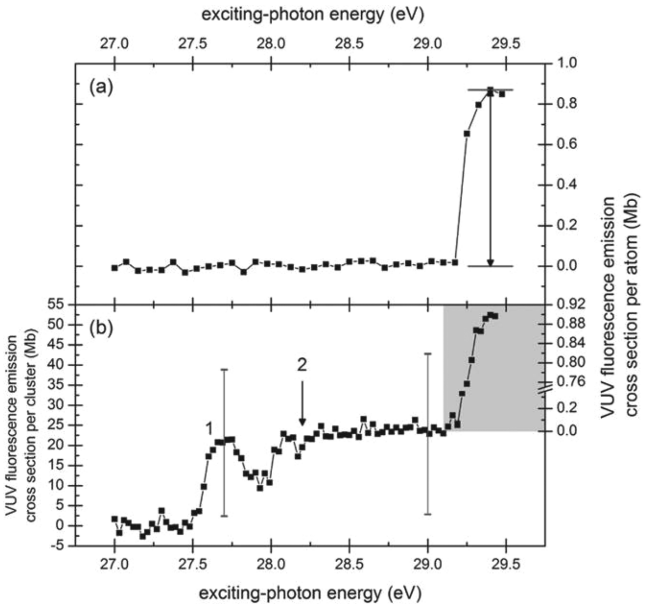

Figure 27. (a) Photon-induced VUV fluorescence (λ_{fl} < 130 nm) from an atomic Ar jet versus excitation energy. The absolute cross-section scale was calibrated to the data of ref 381 at 29.4 eV. (b) Analogous data for a partially condensed jet with a mean cluster size of <*N*> = 36. The right-hand side ordinate is valid for the shaded region and corresponds to the 3s-photoionization cross-section of isolated atoms ((a)[381]). The left-hand side ordinate (white region) indicates the VUV fluorescence emission cross-sections for clusters with the given mean size. Figure and caption reprinted from ref 329, with permission from IOP publishing.

is possible and will occur unless there is a (more efficient) competing process quenching it. This finding has been nicely summarized in the introduction of their paper by Ouchi et al. with the statement "It is now well-known that ICD appears everywhere and transfers the energy and the charge from the species with the vacancy to the environment surrounding it.".[23] The same publication demonstrated experimentally a further missing piece of the overall picture of ICD as the authors observed a "3*e*-ICD", as they identified a decay from Ne/$Ar^{2+}(3s^{-2})$ to $Ne^{+}(2p^{-1})/Ar^{2+}(3p^{-2})$. Accordingly, in this decay channel, two electrons from the Ar 3*p*-shell fill up two vacancies in the Ar 3*s*-shell and their combined excess energy is employed to emit a 2*p* electron from the neighboring neon atom. Theoretically, the possibility of such a decay route has been pointed out by Stoychev et al. in work on ICD after core-ionzation and Auger decay of neon dimers.[368] Later theoretical work by Demekhin and co-workers[124] and Averbukh and Kolorenč[383] showed according decay channels in NeAr and krypton heterotrimers. A single atom (i.e., local) analog has been reported in work by Žitnik et al. in 2016, where a two-electron one-electron (TEOE) transition has been observed in Auger spectra of Ar atoms.[384]

More recently, a corresponding process was observed where, instead of a two-electron transition providing the excitation energy for the emission of a third electron, the de-excitation of a single electron caused the simultaneous emission of two electrons. This process, which is the nonlocal equivalent to a double Auger decay, has been termed double-ICD (dICD) and was observed by LaForge and co-workers in mixed alkali dimers[269] (see Section 5.7.2). A corresponding decay pathway with respect to ETMD has been predicted in 2006 by Averbukh and Cederbaum to occur in Ne@C_{60} endohedral fullerenes[80] (see Section 5.2.4).

Cederbaum demonstrated recently a further extension of the scope of ICD.[385] He predicted, that vibrational energy from a molecule in the electronic ground state can be used to ionize a loosely bound neighbor. This ICD pathway should be feasible in loosely bound compounds of molecules and anions (as the latter have a very low electronic binding energy) or (long-living) electronically excited neutral species. Cederbaum predicted that (even though the vibrational lifetime of isolated molecules is typically in the seconds to milliseconds regime) a neighboring anion may decrease this lifetime down to nanoseconds or picoseconds.

The restriction that ICD occurs between two loosely bound entities, which is a key notion to the process, has been relaxed already in rather early work by Thomas et al.[386] (where the process was referred to as an interatomic Auger process) and later by Feifel and co-workers.[277] They pointed out that in an extended system, orbitals involved in a decay can still be strongly localized to certain sites of the system. Feifel et al. showed in their investigation of photoionization of SF_6 that an intramolecular Interatomic Coulombic Decay occurs after inner-valence ionization of a fluorine atom. Similar findings with respect to ETMD have been made very recently.[387] Further examples and details are provided in Section 5.7.4.

5.2. ICD and ETMD in Atomic and Molecular Clusters

The first evidence for the existence of ICD has been shown in pioneering experiments by Marburger and co-workers,[3] as they detected a surplus of low energy electrons after photon-induced excitation of large neon clusters above the neon 2*s*-threshold. Figure 28 shows the corresponding spectra published in ref 3. This section provides an overview on ICD and ETMD in clusters. It begins with a brief description of cluster generation techniques. After that, work on (rare gas) clusters in general is reviewed, followed by a short subsection on fullerenes. As a bridge to the subsequent section on ICD and ETMD in liquids, a subsection focusing on ICD in hydrogen-bonded systems is provided.

5.2.1. Cluster Generation Techniques. The generation of clusters for experimental investigations is routinely done using supersonic jet setups.[238] As gas flows through a small orifice from a high pressure region into a domain of substantially lower pressure, an adiabatic supersonic expansion occurs. During the expansion the enthalpy of the gas converts into a directed motion of its particles. As (in an ideal case) all gas particles move with equal energy after the expansion, the generated gas beam becomes intrinsically cold. In a real environment, conditions close to the idealized case only exist within a small volume behind the orifice, which is termed the zone-of-silence. At larger distances, perturbations emerge stemming, for example, from the interaction with residual gas in the low pressure domain. Therefore, a so-called skimmer (a funnel-shaped aperture) is introduced into the zone-of-silence extracting a thin, spatially localized, and cold gas beam into a further vacuum chamber. This supersonic jet is either skimmed further employing one or more additional skimmer stages or directly used in crossed beam experiments. Figure 29 shows a sketch of a corresponding arrangement.

The conditions occurring during the supersonic expansion and afterward inside the zone-of-silence are ideally suited for the generation of loosely bound clusters. For a condensation into larger aggregates, the gas particles need to be sufficiently

https://dx.doi.org/10.1021/acs.chemrev.0c00106
Chem. Rev. 2020, 120, 11295−11369

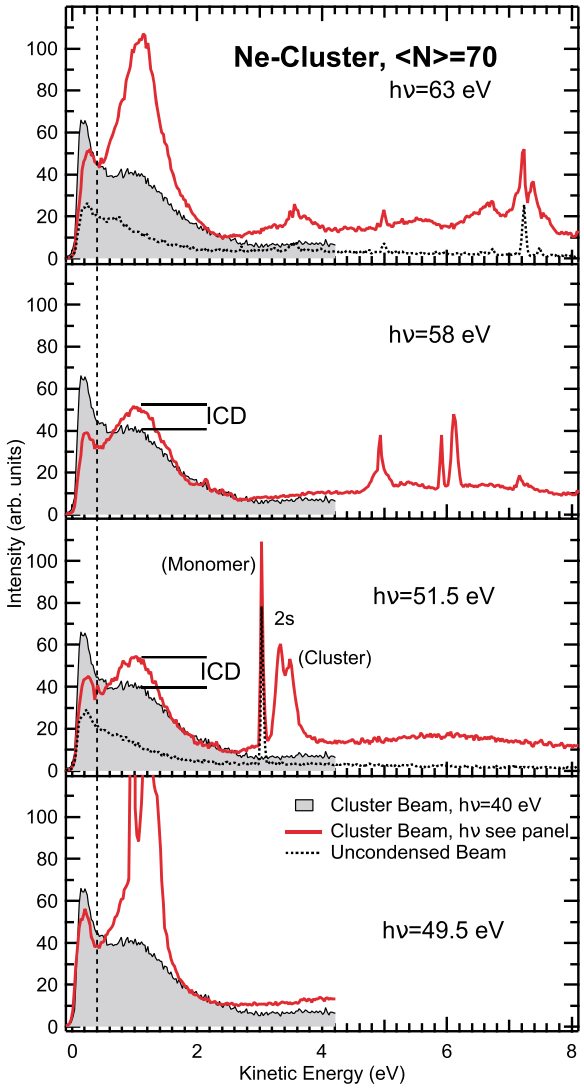

Figure 28. Electron spectra of neon clusters with an average size of $\langle N \rangle = 70$ atoms and neon monomers (i.e., uncondensed beam). As a reference, the electron spectrum recorded at $h\nu = 40$ eV is repeated as a shaded area in every panel. Spectra recorded above the cluster 2s ionization threshold (solid, red traces) show a surplus of low energy electrons occurring in the cluster spectra (see horizontal bars). This depicted the first evidence of the existence of ICD. Spectra of an atomic beam are shown for comparison in two panels (dotted lines). Reprinted with permission from ref 3. Copyright 2003 APS.

cold, and their excess energy is removed in three-body collisions. During the beginning of the supersonic expansion, the gas pressure is still high, allowing for three-body collisions, and as the pressure drops rapidly during the expansion, clusters formed by condensation are not subject to further collisions, which may break them before reaching the skimmer. Large clusters are generated by collisions of smaller ones (or by breakup of an even larger cluster) and supersonic jets consist typically of a broad distribution of cluster sizes. The physics of the process has been reviewed, for example, in ref 388. The mean cluster size is determined by the properties of the supersonic expansion. Available parameters are the backing pressure inside the gas nozzle, its temperature, its diameter, and its detailed shape. Similar expansion conditions occur for cases where the nozzle diameter d_0 and the backing pressure p_0 fulfill the relation $p_0 d_0^q = \text{const.}$, with the empirical parameter q

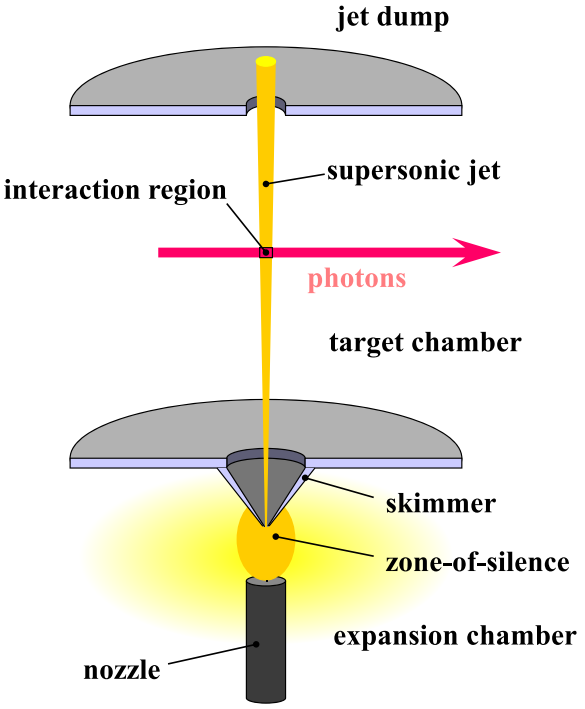

Figure 29. Scheme of a supersonic jet setup for cluster generation. The setup consists of three vacuum chambers. Bottom to top: Expansion chamber: gas is expanded from a small nozzle into a vacuum. A skimmer is used to extract a thin gas beam from the zone-of-silence. Target chamber: the supersonic jet is crossed with a projectile beam, for example, light from a synchrotron, triggering the cluster reaction under investigation. Jet dump: the part of the supersonic jet which did not react is discarded after leaving the target chamber through a small aperture.

varying for different gases (e.g., $q = 0.85$ for noble gases, and $q = 0.6$ for molecular gases as N_2 or CO).[389] A semiempirical relation between the expansion parameters and the mean cluster size was introduced during the late 70s and early 80s by Hagena.[390] Nowadays, cluster size distributions are typically assessed by referring to his later work[391] or work by Buck and Krohne.[392] Ref 393 provides further helpful insight and, for example, generation of water clusters is nicely covered in ref 394. An example of a supersonic jet setup (including electron detection capabilities) used in the study of electron spectra from rare gas and water clusters is shown in Figure 9.

5.2.2. Inner-Valence ICD and ETMD in Rare Gas Clusters. As pointed out before, large Ne clusters were the first system in which experimental evidence for ICD was found.[3] In these pioneering experiments, the ICD electron, e_{ICD}^- from the decay of Ne 2*s* inner-valence vacancy states was directly detected using a hemispherical electron analyzer. The process, in a cluster of *N* Ne atoms, is analogous to the one sketched in Figure 1:

$$\begin{aligned} Ne_N + h\nu &\rightarrow Ne_{N-1}Ne^+(2s^{-1}) + e_{ph}^- \\ &\rightarrow Ne_{N-2}(Ne^+(2p^{-1}))_2 + e_{ph}^- + e_{ICD}^- \end{aligned} \quad (29)$$

Both e_{ph}^- and e_{ICD}^- can be seen in Figure 30 with an about matching area, which was interpreted as an early indication of the efficiency of ICD.[255]

The profile of the 2*s* photoline from large Ne clusters was analyzed shortly after the discovery of ICD electrons, and a significant Lorentzian tail was found, indicating lifetime

https://dx.doi.org/10.1021/acs.chemrev.0c00106
Chem. Rev. 2020, 120, 11295−11369

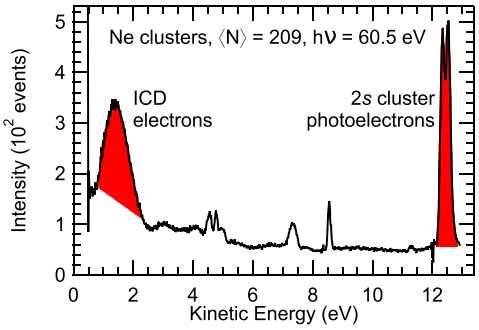

Figure 30. Electron spectrum of large Ne clusters excited at a photon energy above the 2*s* ionization threshold. The spectrum was corrected for the detection efficiency of the hemispherical electron analyzer, and a contribution of uncondensed atomic Ne was subtracted. Primary 2*s* photoelectrons, split into a bulk and a surface component, the latter at higher kinetic energy, and electrons due to ICD of the $2s^{-1}$ vacancy are clearly seen. Reprinted from ref 255, with permission from Elsevier.

broadening of the singly ionized state due to ICD (see above).[4] In the first experiments reported in refs 3 and 255, the correspondence of the 1.6 eV spectral ICD feature to the 2*s* photoline was made plausible from its disappearance when the photon energy was tuned below the Ne 2*s* ionization threshold. In a more careful study of this energy region, a resonant ICD process according to the reaction equation

$$\mathrm{Ne_N} + h\nu \rightarrow \mathrm{Ne_{N-1}Ne(2s^{-1}3p)} \rightarrow \mathrm{Ne_{N-2}Ne(2p^{-1}3p)Ne^{+}(2p^{-1})} + \mathrm{e_{ICD}}^{-} \quad (30)$$

was found by electron spectroscopy (see Section 5.1.6).[370] Here, $\mathrm{Ne}(2s^{-1}3p)$ is only one of several excited states that can undergo this decay; in a larger Ne aggregate, the appropriateness of quantum numbers *nl* to describe excited single electron states can be questioned.[395] This resonant ICD process was investigated in more detail by fluorescence decay of the spectator electron (3*p* in eq 30), see below and Section 4.5 for details.

Richer ICD spectra can be expected in heterogeneous systems. A variety of mixed rare gas systems can be produced by supersonic coexpansion of two rare gases. The first such system to be studied were large NeAr clusters, in which after Ne 2*s* photoionization two ICD channels are open:

$$\mathrm{Ar}_M\mathrm{Ne}_{N-1}\mathrm{Ne^{+}(2s^{-1})} \rightarrow \mathrm{Ar}_M\mathrm{Ne}_{N-2}(\mathrm{Ne^{+}(2p^{-1})})_2 + \mathrm{e_{ICD}}^{-} \quad (31)$$

$$\rightarrow \mathrm{Ar}_{M-1}\mathrm{Ne}_{N-1}\mathrm{Ar^{+}(3p^{-1})Ne^{+}(2p^{-1})} + e_{\mathrm{ICD}}{}'^{-} \quad (32)$$

The photoelectron has been omitted for clarity. Using approximate figures from atomic ionization potentials and the Coulomb repulsion at the respective Ne−Ne and Ne−Ar equilibrium distances, it can be estimated that ICD to Ne^+Ar^+ final states should have a kinetic energy of 7 eV.[356] On the other hand, ICD to Ne^+Ne^+ final states should be at about the same energy as in pure Ne clusters. Experimentally, the ICD to mixed final states (electron $e_{ICD}{}'^{-}$) is found at a somewhat larger kinetic energy (Figure 31) than estimated, possibly due to the absence of final state polarization in the simplified estimate. To first order, the relative contribution of ICD to Ne^+Ar^+ final states increases with the Ar content in the cluster.

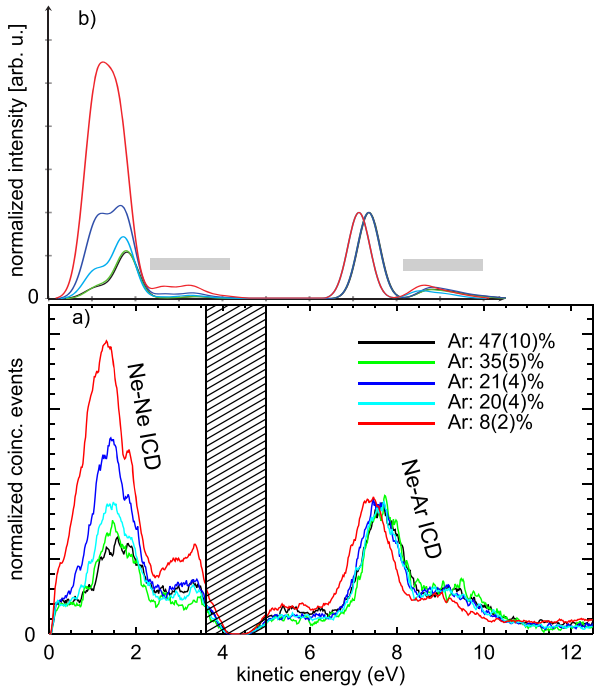

Figure 31. Electron spectra of large, photoionized NeAr clusters produced at different mixing Ne/Ar ratios. (a) Electrons that were detected in coincidence with a primary Ne 2*s* photoelectron, at a kinetic energy of approximately 4 eV (shaded region). Spectra were recorded at a photon energy of 52.1 eV. The fraction of Ar in the respective cluster set is indicated in the figure legend. ICD of Ne $2s^{-1}$ to both Ne^+Ne^+ and Ne^+Ar^+ final states is observed. (b) Calculated Ne $2s^{-1}$ ICD spectrum. All curves were normalized to equal height of the Ne^+Ar^+-ICD feature. Gray bars highlight ICD to final states that are separated by more than the Ne−Ne distance between neighboring shells. See text for details. Figure adapted from ref 281, used under CC BY.

The appearance of the Ne^+Ar^+-ICD peak was used in two studies as an indicator for the formation of mixed systems in a coexpansion of Ne and Ar.[356,396] In a combined study of valence- and core-level photoelectron spectra with ICD, it could be seen that mixed NeAr clusters assume a structure composed of an Ar core with one or several Ne outer layers.[396] The set of ICD spectra shown in Figure 31 was recorded after these initial studies and was compared to extensive theoretical calculations using a cluster model capable of treating extended systems. Experimentally, the cluster composition was varied by changing the initial gas mixture and the expansion conditions.[281] In the theoretical approach, first IC decay widths as a function of *R* were calculated for Ne_2 and NeAr dimers over a range of distances. In a second step, larger clusters were constructed using icosahedral Ar cores covered by different variants of Ne layers, with interatomic distances fixed according to the van der Waals-radii of Ne and Ar. All energies were calibrated to observed single particle ionization potentials for the Ne and Ar states in play. Thus, a computationally feasible and consistent treatment of clusters with more than 10 000 constituents became possible.[223] ICD spectra were then calculated by a sum over all combinatorially possible final states in which the ICD channel was open. Agreement of this comparatively simple approach with experiments is excellent (Figure 31). It is noteworthy that the calculated curves shown in Figure 31b have been selected from a large set of simulated structures according to best

https://dx.doi.org/10.1021/acs.chemrev.0c00106
Chem. Rev. 2020, 120, 11295−11369

agreement of the simulated data with the observed Ar fraction and the observed fraction of Ne^+Ar^+-ICD to total ICD, that is, ICD spectroscopy has been used as a tool to narrow down on the structure of the clusters that were investigated. Further details are provided in Section 5.6.3.

Another noteworthy feature appearing in all calculated and experimental spectra has been marked by gray bars in Figure 31b. These shoulders at the high kinetic energy sides of both ICD peaks have already been observed in ref 356 (for the Ne^+Ar^+ final state). The calculations allowed to interpret them as the signature of ICD involving states in the second coordination shell of the initially excited site.[281] This aspect has been explained in great detail in ref 346. The change in kinetic energy between the different contributions can be explained from the $1/R$-behavior of the Coulomb repulsion energy. Final state polarization will also have an influence in practice, but was not taken into account in the model. The detailed analysis of the calculations in ref 346 allowed a decomposition of the Ne^+Ne^+-ICD peak in contributions of atom pairs within the same shell, neighboring pairs within adjacent shells, and pairs at a larger distance. The same principal explanation also holds for the Ne^+Ar^+-peak. In summary, these studies showed for the first time that ICD between non-neighboring sites can have a significant intensity. Another comparison of Ar-rich to Ar-poor NeAr-clusters has been shown in ref 10 and showed that the relative importance of decays to the second coordination shell increases in clusters with a small Ar admixture.

The ICD spectra of medium sized and large clusters of other rare gas mixtures have also been investigated. NeKr clusters show a particularly high kinetic energy of the ICD peak, namely a broad feature between 10 and 12 eV.[278] This system was therefore suggested for time-dependent experiments on ICD via streaking of the decay electron (see Section 4.6.4). Results on ArKr and ArXe clusters will be detailed next.

Mixed rare gas clusters also may serve as prototypes to investigate ETMD (see Section 2.1). In the first predictions of this decay mode, its decay rate was found orders of magnitude lower than the one of ICD.[24] This may change, however, in situations were many more final states are accessible to ETMD compared to ICD,[25,34] if the ICD channel is energetically closed, but the ETMD channel open, or if the ICD channel is forbidden by selection rules. In the two latter cases, ETMD has meanwhile been identified experimentally,[26,28] after a report of strong hints for the observation of a charge transfer in ArXe clusters.[397]

We first turn to results on the Ar $3s^{-1}$ decay in ArKr, for which the available final state energies only support ETMD.[27] By electron−electron coincidence spectroscopy after photoionization, pertaining e_{ph}, e_{ETMD}-pairs were indeed found.[26] Experimental results on this decay process are shown in Figure 32. A rather structureless ETMD spectrum has been found, which is smoothly descending from a maximum at zero eV of kinetic energy (Figure 32a). This shape has been observed for both inner-valence ICD and ETMD in a number of systems (e.g., ArXe,[223] water[263,284]) and can be explained as resulting from a dense band of two-hole final states, the larger fraction of which is energetically not accessible. Therefore, the spectral intensity of the decay spectrum rises up to the lowest permitted energy. The theoretical formalism used for analysis of the NeAr ICD spectra (Figure 31) was extended to also cover ETMD, and its application to the ArKr decay led to a good agreement with experiment.[283]

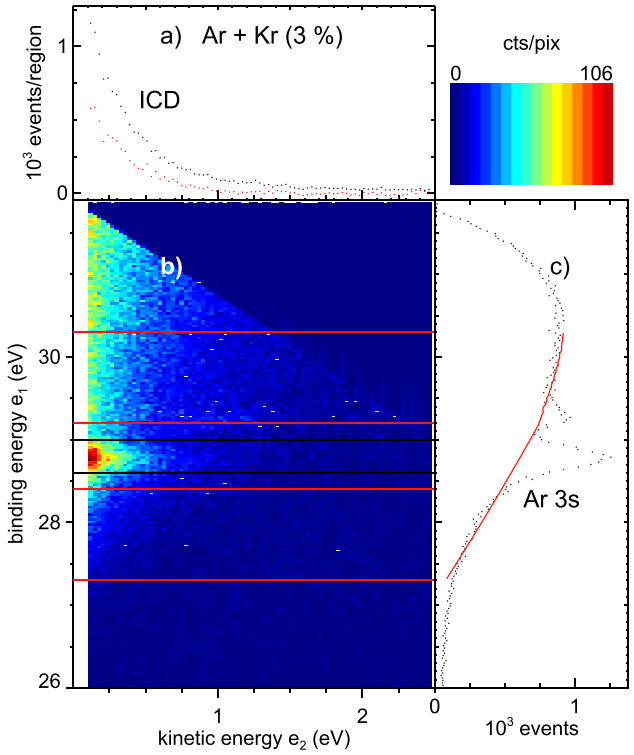

Figure 32. Electron−electron coincidence spectrum of mixed Ar−Kr clusters (3% Kr in the initial gas mixture), recorded with $h\nu$ = 32 eV photons. The first of the two electrons that were recorded, e_1, pertains to the Ar inner-valence region, the second one, e_2, is of low energy and identified as the ETMD electron. (a) Energy spectrum of all secondary (ETMD) electrons e_2, before (black symbols) and after (red symbols) background subtraction. (b) Number of coincident electron pairs on a linear color scale. The region between the two black bars was summed up to produce the ETMD signal in panel a. (c) Energy spectrum of primary electrons e_1, irrespective of the energy of the secondary electron (summation of the coincidence map along horizontal lines). Regions marked by red bars in panel b were used for background determination. Estimated background intensity is also shown by a red trace in panel c. Intensity is expressed (b) as coincident events/pixel of 30 meV^2 or (a, c) as coincident events per interval of 30 meV. A cluster size around 100 was estimated (order of magnitude). In total, approximately 1.2×10^5 events are shown. See text for details. Figure adapted from ref 283, with permission from Elsevier.

The other pioneering study on ETMD, ref 28, investigated the decay of triply charged states in the Ar dimer after $2p$-ionization and Auger decay. It was found that some $Ar^{3+}Ar$ states, notably satellite states with an inner-valence hole ($Ar(3s^1 3p^4)$), may only decay by ETMD to Ar^{2+}, Ar^{2+} ion pairs, which were detected experimentally, or via exchange ICD, which is not more effective than ETMD.

We return to investigations of larger clusters now. A detailed experimental and theoretical study was carried out on the decay of $Ar(3s^{-1})$ in ArXe clusters.[223] In large mixed clusters of these two species, both ETMD and ICD are energetically allowed. A decay via ICD, however, is possible only by energy transfer from Ar to a Xe site separated by at least one intermediate layer. Experimentally, several compositions of the clusters were probed. Spectra were interpreted by comparison to calculations for numerous model structures. Generally, a dominance of ICD to non-nearest neighbors over ETMD was found. The structural motifes that can best be reconciled with

https://dx.doi.org/10.1021/acs.chemrev.0c00106
Chem. Rev. 2020, 120, 11295−11369

this result are small clusters with few Xe atoms spread out over the whole structure, and Xe core, Ar shell systems. A high efficiency for decay by ICD or ETMD, summarized in α_{ICD} (see eq 28) was found: $\alpha_{ICD} > 0.62$ for systems with very low Xe content, $\alpha_{ICD} > 0.9$ everywhere else.

Electron−electron coincidence spectroscopy also allows to separate ICD from impact ionization by intracluster inelastic scattering. In principle, both processes produce a two-electron signature pertaining to two distinct positive charges in the final state. It turns out, however, that in Ne clusters they nevertheless can be separated in the e_1, e_2-plane, or in a diagram showing coincident intensity versus two-hole final state energy $h\nu - (e_1 + e_2)$, where e designates the kinetic energy of the respective electron. This representation of the coincident intensity can be calculated from the coincident intensity diagram (e.g., Figure 32b) by summing up along diagonals of constant total energy ($e_1 + e_2$ = const.). Results of this exercise for electron, electron coincidences from pure Ne clusters are shown in Figure 33. Intercluster inelastic scattering

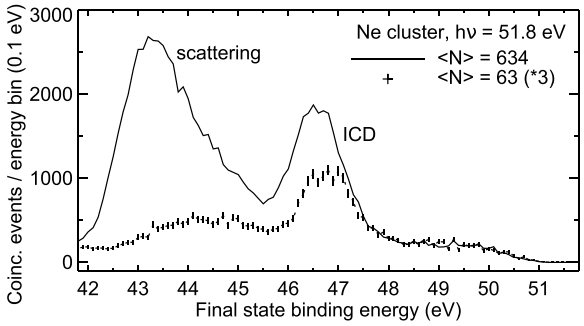

Figure 33. Energy of the two-hole final states after photodouble-ionization of Ne clusters, recorded by electron−electron coincidence spectroscopy. Two different cluster sizes were probed. The feature at approximately 46.5 eV binding energy is produced by ICD to $(Ne^+(2p^{-1}))_2$ final states. In larger clusters, at lower binding energy, final states populated by intracluster inelastic scattering are seen. Figure adapted from ref 276, with permission from Elsevier.

could also contribute, but was ruled out from an estimate of the density of the cluster beam.[276] For large clusters, more doubly ionized states are produced by intracluster scattering than by ICD. This is plausible because the scattering signal is fed by Ne 2*p* photoelectrons, which have a much higher cross-section than the 2*s* ionization processes preceding ICD.[398] Some contribution of ICD to non-nearest neighbors can also be expected in the same region of two-hole energies (see above), but scattering at least for the large cluster set is assumed the dominating factor. While in Ne clusters contributions from inelastic scattering and from ICD are spectroscopically distinct, for molecular clusters and liquid water, separation of the scattering signal from ICD is a major complication of any quantitative analysis.

From a fundamental physics point of view, the spectroscopy of electrons and ions is the logical experimental approach to investigate ICD. However, to unravel whether those processes also play a role in bulk solid or liquid matter a method must be used to track them that is independent of the ultrahigh vacuum conditions needed for ion or electron detection. The main obstacle for charged particle detection in dense media is the mean free path, that is, escape depth, of only a few nm. Photons, in contrast, have orders of magnitude larger mean free paths in dense media; depending on the wavelength up to millimeters. First investigations showed indications that ICD may be observed by photon emission.[327,328] In ref 280, it was shown unambiguously that the resonant ICD in neon clusters, one of the best studied ICD prototype systems (see Figure 26) is detectable by vacuum ultraviolet (VUV) photons. Figure 34

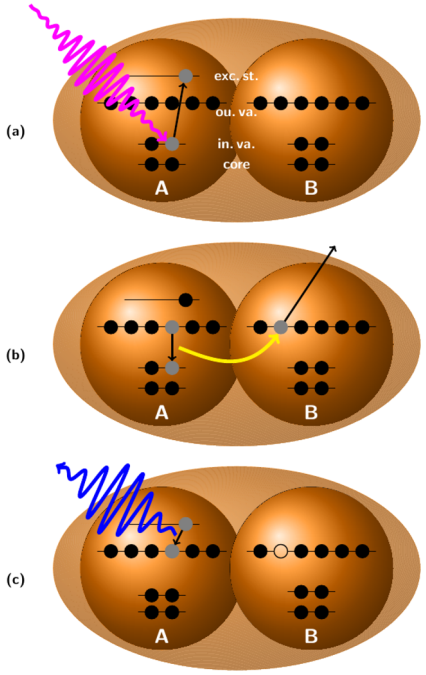

Figure 34. Schematic of fluorescence following ICD after resonant excitation in Ne clusters. (a) In the first step, an inner-valence electron of atom A is resonantly excited. For an isolated atom or molecule, this excitation would result in fast relaxation of site A via its autoionization, which totally suppresses possible radiation emission. In the cluster, due to environment the energy can be alternatively transferred to a neighbor B via ICD, (b) which results in the emission of a low-energy electron. The efficiency of ICD grows with the size of the cluster[4,399] and may even dominate over autoionization on site A. (c) Finally, the still excited atom A releases its energy by emission of a photon, which now becomes possible owing to the preceding ICD. Please note that, despite the atomic picture, the (outer) energy levels in the cluster might have changed dramatically, therefore, no atomic state notation is used in the figure. The caption has been taken from ref 280. Reprinted from ref 280, with permission from IOP publishing.

sketches the according process. In addition to the first direct observation of ICD by photon detection, Knie and co-workers were able to show that time-resolved measurements allow for a complete discrimination between cluster and monomer signal.[280]

Shortly after the initial observation of ICD by photon detection, Hans et al. succeeded to determine absolute cross-sections for specific ICD processes.[329] It is possible to use the condensation rate, determined by electron spectroscopy, to calibrate the absolute scale of the cluster signal by the known cross-sections of atoms in the jet. Hans et al. showed that, if one can measure the condensation rate of a given jet this method is applicable to any mixed sample.[329] Please refer to Section 5.1.7 for details. In follow-up experiments, the detection scheme was extended from the vacuum ultraviolet (VUV) region to the visible.[282] Thereby it was shown that more commonly used photon spectroscopy methods can be deployed to investigate ICD. Other investigations revealed the

https://dx.doi.org/10.1021/acs.chemrev.0c00106
Chem. Rev. 2020, 120, 11295−11369

cluster size dependent photon emission of the RICD process in Ne.[400]

Photon spectra recorded at inner-shell excitation energies showed a distinct new feature at the higher wavelength side of the VUV emission feature.[61] It was identified as resonant charge transfer (RCT, see Section 2.4). The mechanism is sketched in Figure 35: upon double ionization of a neon atom,

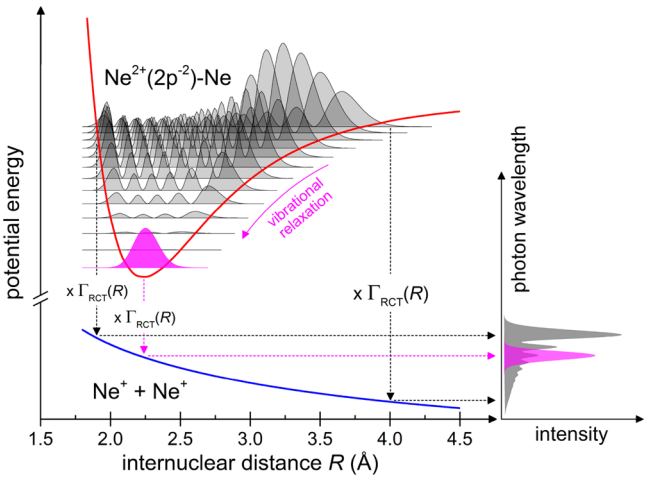

Figure 35. Sketch of the theoretical model used to compute the RCT spectra. In a free dimer, vibrational levels of the $Ne^{2+}(2p^{-2})$-Ne state are populated according to the corresponding excitation Franck–Condon factors. The respective densities are visualized by the gray shaded functions. Thereafter, each density is multiplied by the R-dependent decay widths $\Gamma_{RCT}(R)$ and mapped onto the RCT final state Ne^+–Ne^+. The observed photon spectrum (gray spectrum in right panel) is obtained by incoherent summation of contributions from all vibrational states. If the dimer is embedded in a cluster, it first relaxes vibrationally during the RCT lifetime. Therefore, only the vibrational ground state (visualized by the magenta shadowed functions) does contribute to the photon emission spectrum (magenta spectrum in right panel). The caption has been taken from ref 61. Reprinted from ref 61, with permission from IOP publishing.

a dimer of the dication and a neutral neighbor forms within the cluster. The vibrational energy of this dimer is dissipated ultrafast to the bath of weakly bound neighbors. Thereby, the vibrational ground state, and with it smaller internuclear distances, is reached very quickly. At the equilibrium distance of the Ne^{2+}–Ne dimer, it is energetically favorable for the system to transfer a 2*p* electron from the neutral atom to the 2*p* hole of the dication. The mismatch of the 2*p* levels amounts to the energy the system can emit by radiation and the process is termed, accordingly, radiative charge transfer. The initial production of the dication within the cluster can be achieved differently, for example, by electron scattering,[314] ion impact excitation,[401] or by local Auger decay.[29] The former, being more common in nature, especially in the radiation damage context, is a very unspecific process, whereas Auger decay can be addressed species- and very often site- and state-specific. Hence, the radiation detected in ref 61 was the prototypical example for RCT. Intriguing was the formation and ultrafast vibrational relaxation of a dimer in the cluster. This explains on a very fundamental level why no vibrational structure in the fluorescence emission of the clusters was observed before and why the emission spectra seem not to change with the size of the clusters from few tens to few thousands of atoms.

Resonant ICD and RCT are examples for ultrafast interatomic processes within dense media that can be directly tracked by photon detection. Certainly, all processes leading to residual energy in a system will finally relax via photon emission. Not all ICD processes, however, are detectable by photon spectroscopy. The first example ever measured for ICD, 2*s* ionization of a neon cluster, results in two singly ionized ground state ions. This effect quenches the monomer fluorescence very efficiently. If, nevertheless, a fluorescing channel is quenched efficiently also this vanishing of photon emission can be used to follow the progression of an excited system. In pure neon, this effect was already visible in the results of ref 280. There the quenching was masked by the omnipresence of monomers in the supersonic expansion. A much more compelling and at the same time more realistic system consists of heterogeneous clusters. In an exemplary study, it was shown that in a mixed neon argon cluster, valence excitation of neon atoms is followed by the release of a free electron on a neighboring argon atom.[285] The process follows the reaction equation

$$h\nu + Ne_N Ar_m \rightarrow Ne_{N-1}Ne^*Ar_m \rightarrow Ne_N Ar_{m-1}Ar^+(3p^{-1}) + e^- \quad (33)$$

It thus can be observed as resonant enhancement of the Ar 3*p* photoionization cross-section. Only a few percent of admixed argon quench the Ne fluorescence completely, indicating the nearly 100% efficiency of the process illustrated in Figure 36. The mechanism was proven by simultaneous

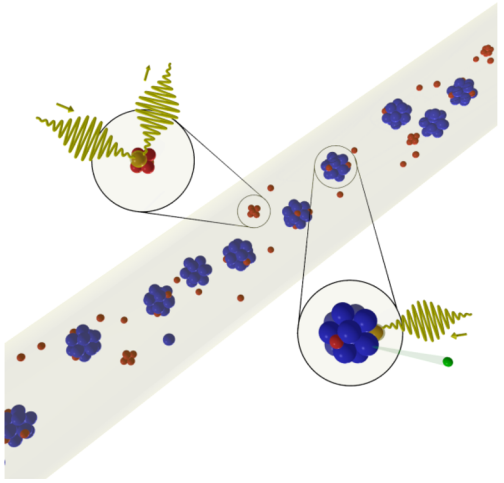

Figure 36. Sketch of the process under investigation. In a pure Ne cluster, resonant outer-valence excitation is followed by fluorescence emission (upper left magnification). Contrary, in heterogeneous Ne–Ar clusters, the energy is transferred to ionize a neighboring Ar atom (lower right magnification), leading to a resonantly enhanced ionization cross-section of Ar. Caption from ref 285. Reprinted with permission from ref 285. Copyright 2019 American Chemical Society.

electron and photon spectroscopy. The experimental results show that an admixture of 5% Ar quenches the fluorescence and simultaneously a strong Fano-shaped resonance appears for the Ar electrons. This Fano shape is a clear indication of the resonantly enhanced ionization, where Ne is primarily excited but decays by emission of an electron from a neighboring atom.

https://dx.doi.org/10.1021/acs.chemrev.0c00106
Chem. Rev. 2020, 120, 11295–11369

The underlying process was predicted theoretically, and was called two-center resonant photoionization.[230] It can be seen as the inverse of two-center dielectronic recombination (eq 4). More theoretical[33,52,154,231,233,402] and experimental[305,403,404] work has appeared.

5.2.3. ICD and ETMD in Core-Ionized Rare Gas Clusters. Auger decay or Auger decay cascades of core vacancies in isolated atoms and molecules result in multiply charged ions. These ions are mostly in the ground state or in low lying excited electronic states. Nevertheless, the excitation energy may be sufficient to enable ICD as the second step of a radiationless decay cascade (Figure 37). In pioneering work on

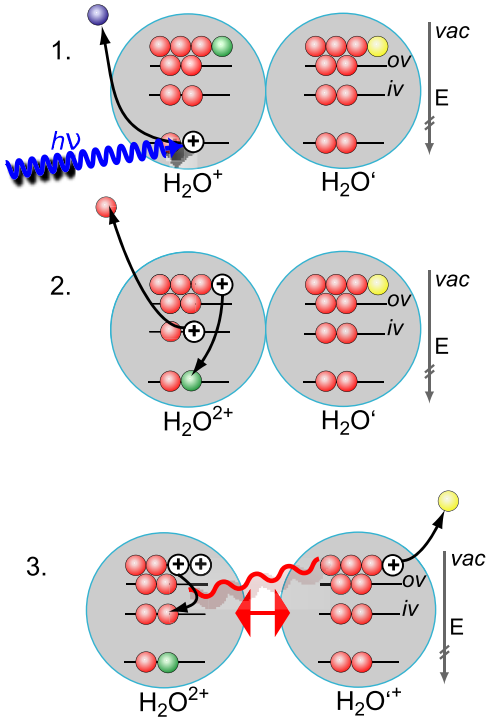

Figure 37. Sketch of a core level photoionization process (1) in a dimer (using an H_2O-dimer as an example), followed by Auger decay into an excited two-hole state (2) and ICD (3). Alternatively, the dicationic state after step (2) may decay by ETMD. Figure reprinted from ref 11, with permission from Taylor and Francis Ltd.

this scheme, ICD of Ar dimers after 2*p* photoionization followed by Auger decay of the $2p^{-1}$ vacancy was demonstrated.[296] Final states of the Auger decay with a sufficient residual energy budget were identified as $3s3p^5$-states, strongly mixed with the $3s^23p^33d$-satellite configuration.[367] Several subsequent experiments investigated analogous decay cascades in other rare gas dimers, see Section 5.1.6. While ICD as the second step of a decay cascade was found to be significant, nevertheless in a homonuclear dimer only for some Auger final states another decay is energetically feasible. The overall energy of these states relative to the environment however is still high since multiple holes reside on the same species. Small molecules usually release this Coulomb energy by dissociation,[405,406] while atomic cations distribute the charge over the surrounding species in electron transfer processes. Considering these processes in a heterogeneous medium (with two different atomic or molecular species M, M′ in Figure 37) shows that the Coulombic two-hole repulsion might enable ETMD in that situation. Whenever the electron attachment energy of the atomic cation exceeds the double ionization potential of the surrounding chemical medium, ETMD becomes energetically allowed. It causes efficient neutralization of the cation and ionization of the neighboring species.

Taking the Ne atom as a representative system one observes that the Auger decay of the 1*s* vacancy mostly populates low lying $Ne^{2+}(2p^{-2}\ ^1D,^1S)$ states (66%). The electron attachment, which leads to the formation of $Ne^+(2p^{-1})$, releases between 44 and 48 eV of energy. This energy lies above the double ionization threshold of NeXe, which renders the ETMD(2) process summed up in eq 34 energetically allowed:

$$\begin{aligned} Ne^{2+}(2p^{-2})Xe &\rightarrow Ne^+(2p^{-1})Xe^{2+}(5p^{-2}) + e_{ETMD}{}^- \\ &\rightarrow Ne^+(2p^{-1}) + Xe^{2+}(5p^{-2}) + e_{ETMD}{}^- \end{aligned} \quad (34)$$

This process was theoretically investigated by Stumpf et al.[103]

The results in NeXe show that ETMD lifetimes at the Franck−Condon geometries lie between 2 and 15.5 ps; they are one to two orders of magnitude larger than ICD lifetimes in the Ne dimer. As a result, while the Auger decay that populates an ETMD initial state proceeds at fixed nuclei, the following ETMD step is accompanied by nuclear dynamics. The decay tends to occur mostly either at the inner turning point of the respective potential energy curve or at the final states' thresholds. The corresponding interatomic distances become imprinted onto the KER spectra, where they appear as peaks at specific energies. Another important observation is that the nuclear dynamics in the repulsive final state leads to the population of triply ionized $NeXe^{3+}$ states, which are inaccessible in ETMD. That becomes possible because the $NeXe^{3+}$ states lie in the same energy range as the Ne^+Xe^{2+} ETMD final states; which is a common situation with sufficiently large neighbors. The impact of nuclear dynamics on the overall rate of the ETMD step in Auger−ETMD cascade was studied by Stumpf et al. in $NeKr_2$.[32] Sudden creation of the Ne^{2+} ion in the Auger decay leads to the shortening of the average Ne^{2+}−Kr distance in the following nuclear dynamics. Since the ETMD width grows sharply with decreasing distance, the overall effect of the dynamics was estimated to be an order of magnitude increase in the average ETMD rate.

The Auger−ETMD cascades were experimentally verified in large NeKr clusters by You et al.[54] Since in mixed noble gas clusters the heavier element usually forms the core and the lighter element the outer shell,[281] the ETMD step of the cascade can occur only in the interface region where Ne and Kr atoms are the nearest neighbors. Irradiating the clusters by X-rays with energy above the 1*s* ionization threshold of Ne led to the coincident observation of the Ne^+, two Kr^+ ions, and a slow electron with energy below 5 eV, which is the signature of ETMD(3) between $Ne^{2+}(2p^{-2}\ ^1D,^1S)$ and Kr. Moreover, electrons with energies above 5 eV, as well as multiple ion coincidences other than between Ne^+ and two Kr^+ indicated the presence of more complicated decay cascades. Indeed, the Auger decay also populates a minority of energetic Ne^{2+} ions capable of decaying by ICD with Kr. Therefore, the experimental observations can be explained in their entirety if one assumes that, in addition to the Auger−ETMD cascade, the Auger step might be followed by interatomic cascades comprising one or two ICD steps and culminating in ETMD. The specific order of the interatomic steps is determined by

https://dx.doi.org/10.1021/acs.chemrev.0c00106
Chem. Rev. 2020, 120, 11295−11369

their relative efficiency, and defines a scheme of a general electronic decay cascade (Auger−ICD−ETMD), whereby localized electronic energy is dissipated in medium.

5.2.4. ICD-Related Work on Fullerenes. Endohedral fullerenes[407] provide a class of systems other than weakly bound clusters that comprise atoms embedded in chemical environment. The large spherical molecular cage of a C_n fullerene can serve as a host for atoms or complexes that reside within. The presence of the cage modifies the electronic structure of the guest atoms and introduces interactions between the electrons of the atom and the fullerene.[408] The effects of this interaction should impact the photoionization of the embedded atoms and be visible in the corresponding photoelectron spectra.[409] Averbukh and Cederbaum[80] were first to observe in 2006 that interatomic decay processes would play an important role in photoionization of endohedral fullerenes. Choosing Ne@C_{60} as a representative system for their theoretical studies they found that ionizing the Ne atom would create highly excited ionic states of the combined system. The energetics considerations showed that the 2*s* vacancy of Ne can relax by ICD with C_{60}, while the 2*p* vacancy can undergo ETMD. Since the energy of the 2*s* vacancy exceeds the lowest triple ionization potential of Ne@C_{60}, an ICD-ETMD cascade becomes energetically allowed. Thus, endohedral fullerenes should exhibit upon ionization of the guest atom interatomic decay cascades, similar to the ones described for microsolvated metal ions[410] or observed in mixed rare gas clusters.[54] In addition, the authors predicted novel types of ICD and ETMD processes which involve simultaneous emission of two electrons from the fullerene molecule (double ICD and double ETMD). The dICD process has been recently observed in doped He nanodroplets.[269] As is pointed out in Section 5.1.1, the lifetime of an ICD state depends strongly on the number of open interatomic decay channels (and thus typically is proportional to the number of neighboring atoms). Accordingly, ICD in endohedral fullerenes is expected to be ultrafast on a time-scale where it can outpace even local Auger decays. Indeed, *ab initio* calculations in Ne@C_{60} produced 2 fs for the mean lifetime of a $Ne^+(2s^{-1})$ state. Thus, the decay rate of the excited Ne ion embedded in C_{60} is approximately 5 orders of magnitude larger than the decay rate in an isolated neon ion.

General theoretical consideration of ICD in endohedral fullerenes also confirmed that its rate exceeds the rate of radiative relaxation by orders of magnitude.[411] Moreover, calculations by Korol and Solov'yov showed[412] that, due to the polarization of the carbon cage, the ICD rate can increase further when the guest atom is located off-center inside the cage. This situation is realized in ionization of embedded clusters such as Sc_3N. Resonant ICD of inner-valence excited states was investigated by means of *ab initio* calculations in Ar@C_{60} and Kr@C_{60}.[413−415] These calculations demonstrated that the overlap of the outer-valence orbitals of the guest atom and the cage leads to the increase in the efficiency of ICD and ETMD processes and to the efficient ionization of the carbon cage.

While all studies discussed above were done theoretically, Müller et al. carried out first experiments on the topic. They performed, in a merged-beam experiment on ionic Ce@C_{82}^+, a detailed comparison of the photoionization of free versus encaged cerium atoms. The authors concluded that a dramatic redistribution of ionization contribution of the Ce 4*d* photoabsorption occurs, and more than half of the Ce 4*d* oscillator strength is diverted to decay channels involving the fullerene carbon cage.[416] In other words, Auger cascade decays that are seen in the photoion yield of the isolated atom most likely are quenched by ICD involving a Ce vacancy and the fullerene cage. Further experimental work on Sc_3N@C_{80} endohedral fullerene ions reported on ICD being a possible decay after ionization of the Sc *L*-shell.[417]

5.2.5. ICD in Hydrogen-Bonded Clusters. Hydrogen-bonded clusters were the first systems for which ICD was theoretically predicted.[1] This early paper covered ICD of inner-valence vacancy states in $(HF)_3$ and ICD of doubly ionized states populated by Auger decay in $(H_2O)_3$. Surprisingly, neither of these suggestions has been investigated experimentally, to the best of our knowledge. Nevertheless, ICD after inner-valence ionization (the first example in ref 1) became a major direction of research on this process in hydrogen bonded complexes. Results on the efficiency of this process in water clusters were already detailed in Section 5.1.3. Auger, ICD cascades (the second example in ref 1) were further investigated theoretically, but are still awaiting experimental scrutiny in hydrogen bonded systems. (In rare gas clusters, such cascade processes were seen in numerous studies described above in detail.) A third type of ICD in hydrogen bonded systems was not recognized to be of relevance initially. Namely, ICD processes occurring in competition with local core level relaxation (Auger decay). In fact, these processes can become highly significant and have amply been studied in liquid systems (see Section 5.3).

Here, we will first focus on experimental studies of hydrogen bonded clusters. Both water clusters[215,263,284] and water−organic complexes[250,319] were investigated. The ICD spectra of the $2a_1^{-1}$ state in water clusters of different size are shown in Figure 38. The broad, featureless appearance of the spectra is

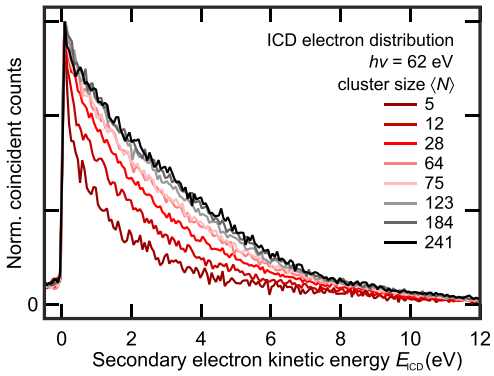

Figure 38. Experimental energy distribution of ICD electrons from decay of the $2a_1$ state in water clusters of different mean size, measured in an electron−electron coincidence experiment. All curves are shown normalized to the same height and without background subtraction. Coincident counts were summed up between 26 and 35 eV photoelectron kinetic energy. Figure adapted from ref 284, used under CC BY.

one reason why this ICD process, despite the obvious importance of water in chemistry and biochemisty, was demonstrated a number of years after the first successful experiments on Ne clusters.[215,263] While ICD of the Ne $2s^{-1}$ state can be straight-forwardly identified in an electron spectrum, for water, the use of coincidence methods proved to be indispensible for the separation of ICD and inelastic electron scattering, which generally also produces an

https://dx.doi.org/10.1021/acs.chemrev.0c00106
Chem. Rev. 2020, 120, 11295−11369

unstructured energy spectrum with highest intensity at unequal energy sharing, that is, including one slow electron. Using electron−electron coincidence spectroscopy on medium sized water clusters[263] or a COLTRIMS experiment on a jet containing water dimers,[215] decay spectra of the $2a_1^{-1}$ state could nevertheless be singled out. The size-dependent series of spectra shown in Figure 38 is in good agreement with the dimer results measured by Jahnke et al.[215] and has been explained as a result of changes in the polarization screening (averaged over all sites in the cluster) (see also Section 5.1.3).[284] An ICD kinetic energy spectrum calculated for the water tetramer also is in qualitative agreement with the experiment findings.[418]

It is interesting that an unusually large KER of approximately 4.1 eV with a sharp distribution of approximately 1 eV (fwhm) has been found in the dimer experiments. In view of the findings on proton dynamics in the inner-valence ionized state (Section 5.1.3) this is additional evidence that ICD occurs only from a narrow interval of distances along the nuclear potential curve for proton transfer. The large value of the KER has prompted further theoretical investigations of the nuclear dynamics in the decay process.[214,220] In a semiclassical simulation of the kinetic energy acquired by the two separating cations, the experimental results for the KER could be reproduced.[214] About 0.6 eV of Coulomb energy is converted into rotational energy of the fragments, which can be seen in the experiment only from the mismatch of the experimental KER maximum to the energy expected from the Coulomb repulsion of two positive charges at the equilibrium distance of the water dimer. A more detailed study of the energies of singly and doubly ionized state and of the potential curves as a function of O−O distance is reported in ref 220.

The study of clusters mixed from water and some organic molecule (also called microsolvated molecules) is interesting, as these may serve as prototypes for the effects of ICD in a biochemical or biological context. A theoretical calculation of the energy levels of dimers from water and either formaldehyde (H_2CO) or ammonia (NH_3), formaldimine (CH_2NH), hydrogen sulfide (H_2S), or another water molecule (Figure 39) showed that in most of these systems ICD after inner-valence ionization is energetically viable.[221] Both ICD after inner-valence ionization of the microsolvated molecule and of the H_2O $2a^1$ orbital was considered. As an example for the ICD spectrum of a water−organic complex, we use the water−formaldehyde dimer ($H_2O\cdots O{=}CH_2$) in the upper left of Figure 39. The calculated ICD spectrum of this dimer is shown in Figure 40. Focusing on the final states of ICD (blue) in panel b of this figure, we see that an inner-valence hole in the carbon of formaldehyde is stable, the O inner-valence vacancy in water may decay by ICD and the O inner-valence vacancy in formaldehyde may decay by ICD or into a local (Auger) channel.

Experiments targeted water bound to a slightly more complex molecule, namely $H_2O\cdots$THF (THF: tetrahydrofuran, C_4H_8O).[319] Calculations of the equilibrium structure of this dimer again find the O of the furan ring bridge bonded to water. Also, the calculated ICD spectrum features the same traits as the prototypical example in Figure 40.[319] Akin to work on the Ar dimer reported above, the authors used (e^-, 2 ion)-coincidences recorded in a COLTRIMS setup to identify the ICD channel from the occurrence of H_2O^+, THF^+ pairs. Excitation by an electron beam with a rather low energy of 66 eV was used to simulate radiation damage by the tail of the

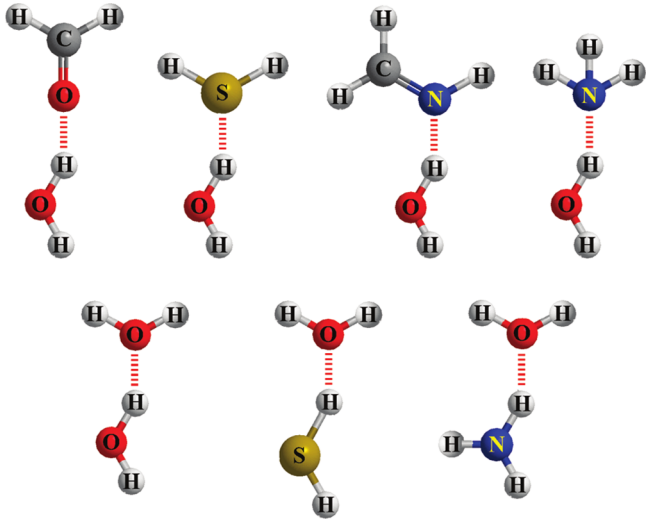

Figure 39. Set of prototypical bimolecular species that contain the types of hydrogen bonds common in biochemically relevant molecules. Inner-valence ionization in most of these systems initiates ICD. Figure adapted from ref 221.

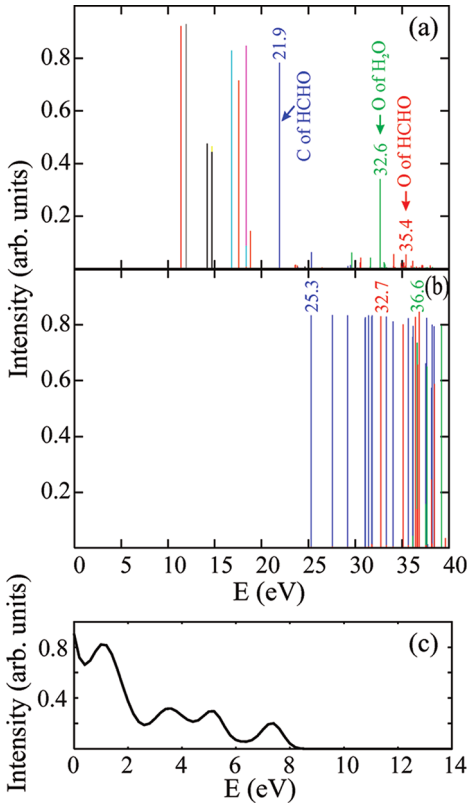

Figure 40. Calculated energy levels and calculated ICD spectrum of the water, formaldehyde ($H_2O\cdots O{=}CH_2$) dimer in its ground state equilibrium geometry. (a, b) Energy levels of the singly and doubly ionized states. Colors in panel a indicate the atom, at which the vacancy is mainly localized. Colors in panel b indicate the type of localization, with red: both vacancies on the OCH_2, green: both vacancies on the H_2O and blue: delocalized. Intermolecular Coulombic decay may proceed from any singly ionized state (top panel) to a doubly ionized state (middle panel) that is lower in energy (further to the left on the *x*-axis). The calculated ICD spectrum, by convoluting all viable transitions with a fixed width Gaussian, is in the bottom panel. See text for details. Figure adapted from ref 221.

https://dx.doi.org/10.1021/acs.chemrev.0c00106
Chem. Rev. 2020, 120, 11295−11369

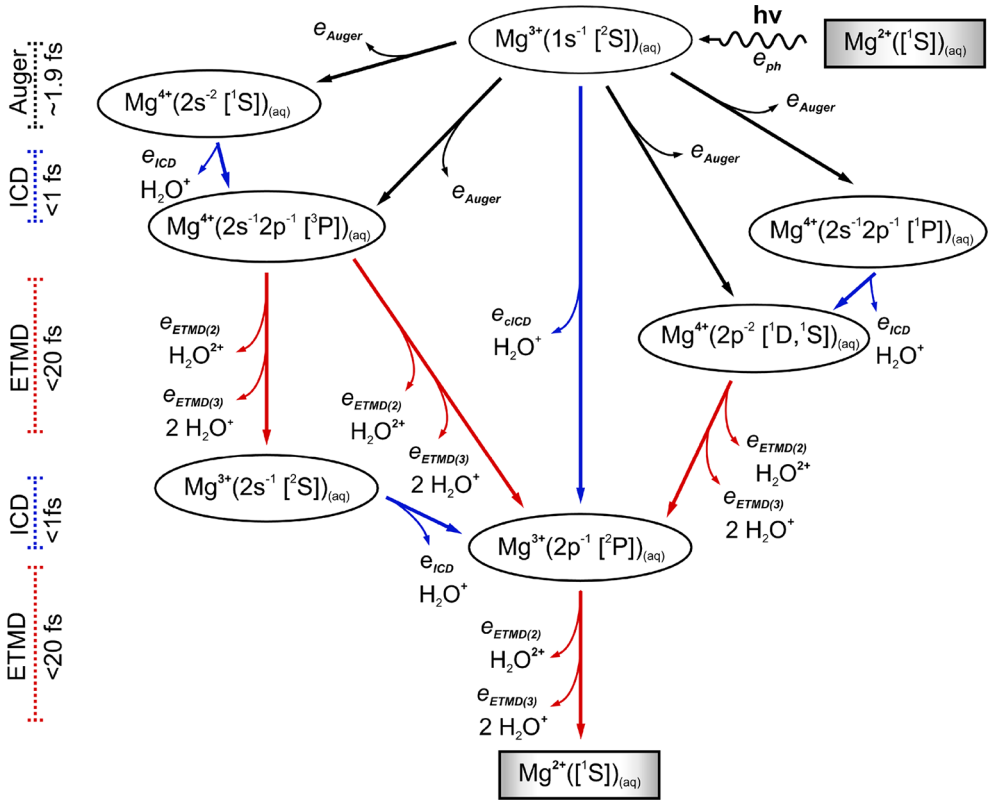

Figure 41. Schematic representation of the electronic decay cascade in a microsolvated Mg^{2+} dication. Auger, ICD, and ETMD steps are shown by black, blue, and red arrows, respectively. The time scale on the left shows the estimated lifetimes of different processes. Figure reprinted from ref 410.

secondary electron cloud produced after absorption of relativistic ions.[419] Such ion pairs, at equal but oppositely directed momenta, could clearly be identified; also numerous pairs including an $C_4H_7O^+$ ion (THF^+ after hydrogen loss) were seen. The latter were attributed to an α-cleavage of the THF^+ in the ICD final state. Energetically, ICD is viable after O 2*s* ionization of either the water or the THF center. However, as the O $2s^{-1}$ state of THF^+ may also undergo a local Auger decay to THF^{2+}, it was assumed that it quenches the THF-initiated ICD.[319] The observed ICD events were therefore fully attributed as being initiated by water ionization. Qualitatively, the measured spectrum resembles the one in Figure 40c. In the context of radiation chemistry this is an important result, as ICD may mediate damage to biomolecules, notably DNA, in a similar way. This aspect is further discussed in Section 5.6.4.

Theoretical study by Kryzhevoi and Cederbaum suggested an ingenious way of controlling ICD in hydrogen bonded systems.[420] They considered ICD in small ammonia clusters, which is initiated by the removal of a 2s electron from one of the nitrogen atoms. Since adding or removing a proton to a molecular cluster results in large shifts in ionization energies,[421] they were able to demonstrate that protonating of an ammonia cluster inhibits ICD and can even lead to the closing of all ICD channels. Alternatively, deprotonating the cluster increases the number of ICD channels and, correspondingly, the ICD efficiency. The immediate conclusion is that in solutions the efficiency of ICD can be controlled by modifying their pH-value.

Owing to its universality, ICD was also observed in a hydrogen bonded systems not containing water:[250] In an interesting experiment, these authors ionized the acethylene-dimer ($C_2H_2\cdots C_2H_2$) by impact of 50 keV/u α-particles. In this energy range, charge-transfer ionization by the projectiles has a high branching ratio. The detection of a He^+ fragment could therefore be used as a trigger in a COLTRIMS measurement, in which both $C_2H_2^+$, $C_2H_2^+$ and C_2H^+, $C_2H_3^+$ pairs were detected at a ratio of 1/0.4 ± 20%. This is an interesting observation, as acethylene possesses no O- or N-derived inner-valence states, and C-derived inner-valence states typically are not sufficient in energy to initiate ICD. However, due to breakdown of the single-particle picture in the inner-valence region some two hole-one particle satellite states can borrow intensity from the C $2\sigma_g^{-1}$ vacancy, and it is the former that may act as the initial state of ICD. The appearance of C_2H^+, $C_2H_3^+$ pairs suggests an importance of proton transfer. Different than in the water example, however, here this does not occur in competition to ICD, as the pertaining potential curves of the singly ionized dimer states do not support proton transfer. Still, the authors found calculational evidence that this final state of the dimer is reached after double ionization of a single site. For this excited state, radiative charge transfer, discussed in Section 2.4 and Figure 35, is a conceivable competing decay channel, but was found to disagree with the observed KER spectrum.

Core ionization of metal cations inside microsolvated clusters was shown to initiate multistep electronic decay cascades analogous to the cascades observed in large NeKr clusters.[54] Detailed theoretical investigation of such cascades was done for the $Mg^{2+}(H_2O)_6$ cluster by Stumpf et al.[410] Creating a 1*s* vacancy in the Mg ion triggers the Auger decay, which populates both low lying (≈ 63%) and highly excited (≈

https://dx.doi.org/10.1021/acs.chemrev.0c00106
Chem. Rev. 2020, 120, 11295−11369

37%) Mg^{4+} states. The excess energy of the former states relative to the $Mg^{4+}(2p^{-2}\ ^3P)$ ground state is only 4 to 9 eV, which is below the ICD threshold. However, these states can undergo both ETMD(2) and ETMD(3), neutralizing one positive charge of the Mg^{4+} cation to yield $Mg^{3+}(2p^{-1}\ ^2P)$, and producing either H_2O^{2+} or two H_2O^+ cations. The highly excited Mg^{4+} ions were shown to relax via ICD, first producing $Mg^{4+}(2p^{-2})$ ions and one H_2O^+ cation. In the presence of intact water molecules the $Mg^{4+}(2p^{-2})$ ions continue to decay by ETMD, as described above. The $Mg^{3+}(2p^{-1}\ ^2P)$ ions can also undergo ETMD with water resulting in the stable Mg^{2+} ion.

Piecing together decay pathways of different ions results in the decay cascade shown in Figure 41. It consists of several branches which comprise interatomic decay cascades each consisting of up to four steps. Together, these steps enable fast dissipation of up to 170 eV in electronic energy retained by the Mg ion after the Auger step. This excess energy is spent in ionizing neighboring water molecules and initiating nuclear dynamics such as proton transfer and Coulomb explosion. Calculations show that ICD states have lifetimes of less than 1 fs, which are similar to the measured ICD lifetimes of solvated $Mg^{3+}(2s^{-1})$ ions (Section 5.1.1).[347] Such extraordinarily short lifetimes are explained by the large number of neighbors, relative proximity of the metal ion to the water ligands, and polarization of the water molecules by the multiply charged ion.[347,410] For the same reasons, the computed ETMD lifetime is 16 fs, much shorter than the picosecond lifetimes found in rare gas clusters. Together these lifetimes ensure that 90% of the 1*s* vacancies decay within 220 fs. As the eventual result of this decay cascade, the Mg cation reverts to its original state, the solvation shell which surrounds the metal ion is ionized on average 4.3-times, while 2.4 ICD and ETMD electrons are emitted in the kinetic energy range of 0 to 40 eV. Such cascades initiated by X-ray absorption through metal ions embedded in biomolecules cause radiation damage to the host via its direct ionization and the emission of low energy electrons. Recently, this work triggered, detailed investigations of high-pressure assisted X-ray induced damage.[422] In addition, the authors concluded that such processes can be a new route for he synthesis of novel materials and structures.

5.3. ICD and ETMD in Liquids

The study of ICD and ETMD in liquid water is intrinsically connected with the question how these processes manifest for the weak hydrogen-bonding interaction, either among water molecules in neat liquid water or between water molecules and atomic or molecular solutes. In addition to mere electronic relaxation of core-ionized states, also nuclear dynamics may contribute on a similarly fast time scale, and may affect the electronic processes. First such ICD experiments have explored the autoionization electron spectra from neat water and hydroxide aqueous solutions following oxygen O(1*s*) core-level ionization.[423,426] In the following, we will briefly mention methods for electron spectroscopy on liquid targets, then we will go on to detail results on neat water, ammonia solutions, and Li electrolyte aqueous solutions. Finally, we summarize a number of results that address general aspects of ICD involving positively or negatively charged solutes.

5.3.1. Liquid-Jet Electron Spectroscopy. The experimental investigation of electronic structure in the liquid-phase, especially from highly volatile aqueous solution, was greatly spurred by the liquid-microjet technique; a schematic of an experiment making use of it is shown in Figure 42. Only after its introduction, photoemission spectra could be recorded for highly volatile liquid-phase systems, also paving the way to the exploration of ultrafast relaxation processes in the aqueous phase,[253] such as ICD and ETMD.

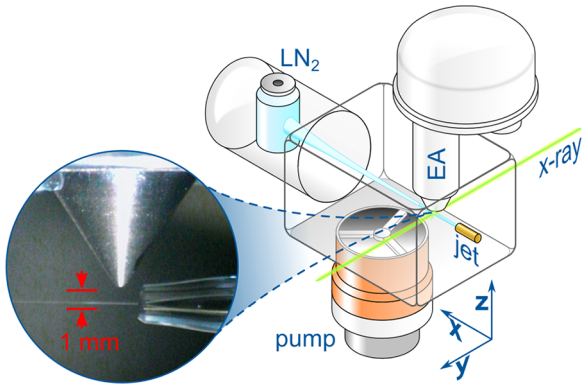

Figure 42. Sketch of a liquid jet vacuum chamber for PE spectroscopy measurements using soft X-ray photons from a synchrotron radiation facility. The photograph shows a magnified view on the conical entrance aperture of the hemispherical electron analyzer (EA) and the glass capillary, forming the jet. Pumping by a cold trap ("LN_2") and a turbomolecular pump together with the narrow entrance cone ensures a sufficiently low vacuum pressure for electron spectroscopy. Figure adapted from ref 424.

Briefly, the liquid-jet technique enables stabilization of a free-flowing liquid water surface in vacuum.[253,425] Because of its small diameter, the water vapor density quickly reduces with distance from the jet, which results in a considerable increase of the electron mean free path, large enough that electrons ejected from the liquid phase can reach the entrance into a differentially pumped electron energy detector at a few millimeters distance from the jet, without losing energy in collisions (Figure 42). The jet velocity is approximately 80 ms^{-1}, and the temperature is typically 4−6 °C. Solute concentrations are up to a few moles to obtain sufficient contrast in the electron signal. Liquid jet ICD and ETMD experiments that will be presented here have used soft X-rays from the synchrotron-radiation facilities BESSY at Helmholtz-Zentrum Berlin (HZB) and the Swedish National Synchrotron Facility MAX-lab for ionization of the liquid jet. Electrons emitted from the liquid jet are typically detected using a hemispherical electron analyzer (see Section 4.2), and in some cases, electron time-of-flight detection has been used. The latter is suitable for electron−electron coincidence measurements, by which inelastically scattered electrons can be separated from the simultaneously emitted ICD and ETMD electrons.

5.3.2. Liquid Water. ICD in liquid water was found to be a very efficient relaxation pathway, scaling with the hydrogen bond strength.[34,426,427] Core-ionization-induced ICD is thus well competitive with local Auger electron decay and can spectroscopically be identified by a unique high-energy shoulder in the leading Auger peak. This is quite remarkable since the photon energy in a core-level ionization experiment by far exceeds the energy required for producing a doubly charged entity. In contrast, for inner-valence ionization this is not the case. There, the initial photon energy is insufficient to create a double (2+) charge locally, that is, the Auger channel

https://dx.doi.org/10.1021/acs.chemrev.0c00106
Chem. Rev. 2020, 120, 11295−11369

is energetically closed. Electronic relaxation involving the immediate neighbors is thus the only viable pathway.

From a chemical point of view, and particularly in context of radiation chemistry, ICD in liquid water leads to the formation of reactive short-lived (few femtoseconds) species that could not be accessed in previous experiments using conventional short pulse time-resolved pump−probe spectroscopies.[426,428] In fact, the impact of nonlocal decay modes and proton transfer upon core ionization significantly diversifies the manifold of the molecular species produced in X-ray irradiated liquid water. Moreover, given the short core-hole lifetime, approximately 4 fs in the case of the O(1*s*) core hole, the experiment provides an internal clock (often referred to as the "core-hole clock"),[429,430] which allows tracking ultrafast coupled electron and nuclear dynamics in liquid water. Specifically, relaxation of core-ionized liquid water involves simultaneous autoionization and proton transfer from the ionized site to an adjacent molecule. This coordinated process has been termed proton transfer mediated charge separation (PTM-CS).[426] Within PTM-CS, transient conformations with a partially transferred proton are formed within a few femtoseconds after the core-level ionization event. Subsequent nonradiative decay of the highly nonequilibrium transients (with an excess energy of nearly 540 eV in the H_2O^{+}* state; the ionization energy of liquid water is 538 eV[431]) leads to a series of reactive species which have not been considered in any high-energy radiation process in water. The respective ultrafast reactions can be inferred from the characteristic shapes of the O(1*s*) Auger electron spectra from liquid water, which are found to exhibit larger ICD signal contributions when the experiment is carried out in light liquid water than for heavy (isotopically substituted) water.

A schematic illustration of coupled electronic and nuclear relaxations in liquid water within PTM-CS is presented in Figure 43, depicting the potential energy curves of the ground state H_2O(aq), the core-ionized state H_2O^{+}(aq), and final states H_2O^{2+}(aq). In the H_2O^{+}(aq) state, proton transfer leads to the formation of a continuum of nonequilibrium structures, a Zundel-type intermediate [HO*··· H···H_2O] being one of them. This particular state further ionizes to form a doubly charged species with the two positive charges located on different water units, creating an [H_2O^{+}···H_2O^{+}](aq) complex; compare also Figure 45. The relaxation into two-hole final states is taken to be monoexponential (the time constant is the core-hole lifetime). The Auger-electron spectra of water thus contain temporal information about changes in the electronic structure induced by ultrafast proton transfer in the core-ionized state. In the proton-transfer mediated Auger (PTM-Auger) process, core-excited HO* emits an Auger electron. In the proton-transfer mediated ICD process (PTM-ICD), energy released in the core refill of HO* is, instead, used to ionize the H_2O of the Zundel-type species; all processes are summarized in Figure 44. Experimentally, the delocalized dicationic (denoted 1*h*1*h*) states can be distinguished from the localized dicationic (2*h*) states by a high-energy shoulder in the Auger electron spectra. The actual occurrence of PTM charge-separation (PTM-CS) effects is reflected in the larger intensities of this Auger feature in H_2O(aq) compared to D_2O(aq), as demonstrated below.

The theoretical assignment of the species that occur upon PTM-ICD in liquid water comes from electronic structure calculations using methods of quantum chemistry and molecular dynamics.[34,426] Proton dynamics is discussed in

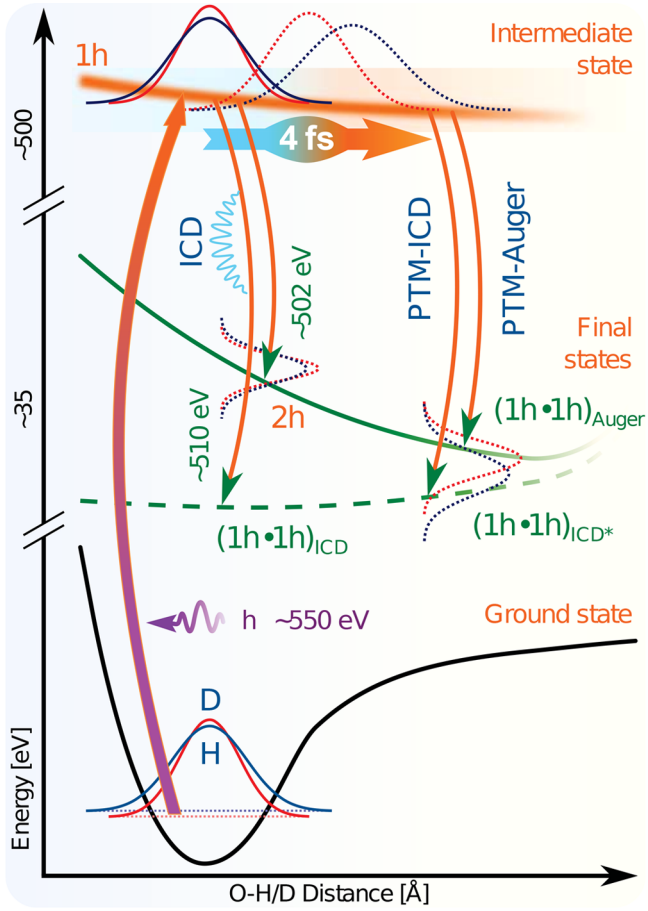

Figure 43. Schematic of the electronic and nuclear relaxation pathways in water with the help of potential energy curves. The respective curve for ground-state water is shown in black, for the dissociative core-ionized state in orange, and for the final doubly charged states in green. Also shown are the wave packets for both cases, H_2O and D_2O, in the ground state, and the ones in the excited states, that is, following photoionization. For the latter, the temporal evolution of the wave packets is depicted as well, reflecting the proton motion along the hydrogen (deuteron)-bond axis on the 4 fs-time scale of the core-hole lifetime. The wave packet for light water is seen to reach out further, which corresponds to a larger distance traveled. Autoionization occurs at any point on the core-excited potential energy curve which at small O−H/D distance leads to formation of local dicationic states and at larger distance to charge-separated dicationic states (illustrated by thin orange arrows turning green, labeled 2*h* and 1*h*1*h*, respectively). Figure reprinted from ref 426.

terms of the temporal evolution of the respective nuclear wave packets on the core-excited-state (cationic) potential energy curves. As illustrated at the top of Figure 43, orange-shaded area, the downhill curve implies that proton transfer along the hydrogen-bond axis (between oxygen atom of the ionized water molecule and a neighboring water molecule) is energetically possible. In contrast, ionization of gas-phase water is not dissociative.[432] How fast the proton is being transferred can be adjusted by isotope substitution. In the case of light water, the wave packet disperses stronger than for heavy water. As a result, the lighter proton travels larger distance than its heavier counterpart, and within the 4 fs lifetime of the core hole it intrudes into a neighboring water molecule: this is supported by calculations.[426] This behavior can be exploited to probe the occurrence as well as relative probability of PTM-CS processes. Here the key is that the

https://dx.doi.org/10.1021/acs.chemrev.0c00106
Chem. Rev. 2020, 120, 11295−11369

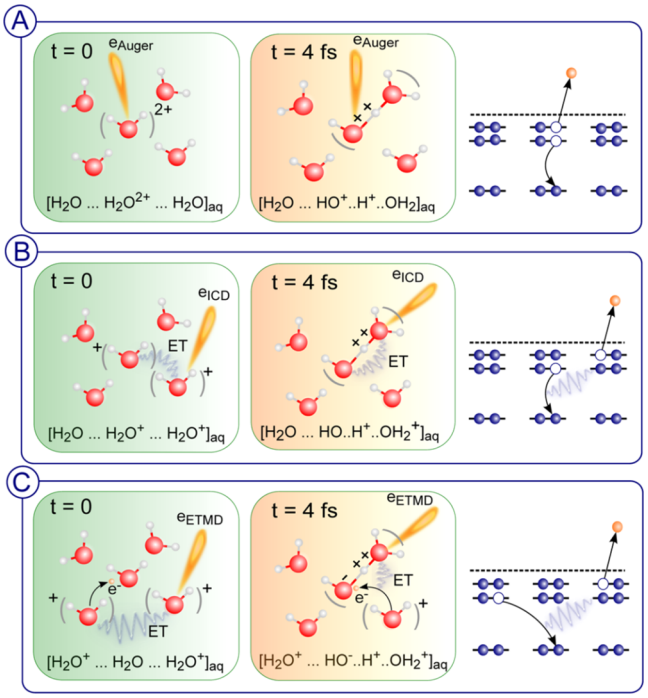

Figure 44. (A) Auger decay, ICD, and ETMD processes in liquid water after O 1*s* core-level ionization, illustrated for a water pentamer. The left (green) column shows the processes in the ground-state water structure, and the center (orange) column shows the processes for a proton-transferred Zundel-type cationic structure. This is illustrated for all three processes: PTM-Auger, PTM-ICD, and PTM-ETMD; molecules participating in the decay processes are enclosed in brackets. The decay outcomes are shown below each structure. ET denotes energy transfer. The right-hand column depicts the schematic energy diagrams of the (A) Auger decay, (B) ICD, and (C) ETMD processes generated by core-level ionization. Starting point is a molecule with a core-level hole. Different hole-refill routes are indicated by a black arrow. The respective resulting electron−hole in the valence level of either molecule, and the subsequently emitted autoionization electron are shown by white and yellow circles, respectively. Figure adapted from ref 34.

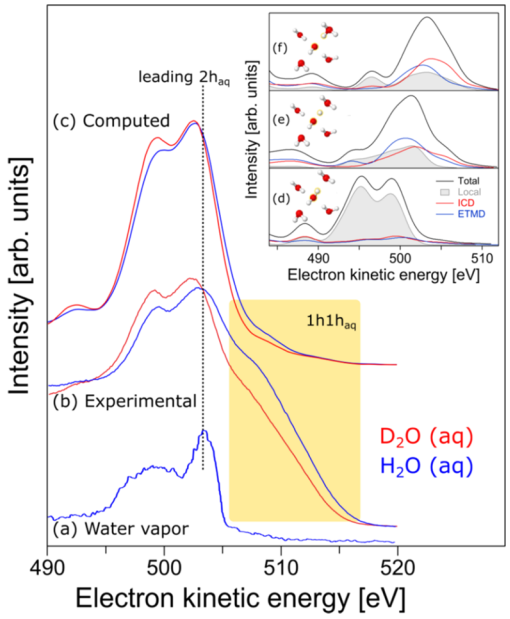

Figure 45. Main figure: Experimental (tier (b)) and computed (tier (c)) oxygen 1*s* Auger electron spectra from light (in blue) and heavy (red) liquid water. The experimental spectra were measured at 600 eV photon energy. Simulations were performed for a water pentamer. The theoretical spectra are shifted to larger energies by 3.4 eV to account for long-range polarization effects that are apparently missing in the finite size pentameric system. Tier (a) is the experimental Auger spectrum of water vapor exhibiting no high-kinetic energy shoulder associated with the 1*h*1*h* states (yellow-shaded region). The spectrum is shifted by the gas−liquid phase shift, as explained in the text. Inset: Simulated Auger-electron spectra (black curves) for three explicit geometries of the water pentamer (as depicted), representing structure changes upon proton dynamics. Results are shown for the proton-transfer coordinates 0.95 Å (ground-state geometry, tier (d)), 1.40 Å (Zundel-like structure, tier (e)), and 1.85 Å (water-hydronium complex, tier (f)). The areas under the gray (shaded area), red, and blue curves reflect the contributions of the Auger, ICD, and ETMD processes, respectively, to the total spectral intensity. Figure adapted from refs 34 and 427.

potential energy of the final state corresponding to the dicationic species following autoionization decreases with the distance traveled by the proton (deuteron); this is illustrated by the green solid curve. The main conclusion from Figure 43 is that any population of final states with large spatial separation between the two positive charges (the 1*h*1*h* delocalized states) can be identified by an electron signal at higher kinetic energy compared to the regular 2*h* Auger states (the final states in the absence of nuclear dynamics). The figure also shows that the 1*h*1*h* states can be populated from the various transient, Zundel-like structures evolving in time, via both Auger decay and ICD. Note that ICD in the ground-state geometry and in proton-transferred configurations leads to 1*h*1*h* states of comparable energies.

We now further elaborate on the qualitative picture of Figure 43, present experimental results, and more explicitly include also the PTM-ETMD channel. Experimental autoionization spectra from neat liquid water along with theoretical calculations to aid their interpretation are presented in Figure 45. One observes aforementioned occurrence of signal intensity in the kinetic energy region of the Auger electron spectra, at approximately 505−518 eV (tiers b). No signal in this range exists for gas-phase water (tier a) which implies that it must originate from the aqueous-phase surrounding. Another striking finding is that the ICD signal contribution is much stronger for light water, H_2O, than for D_2O, identifying the involvement of ultrafast nuclear dynamics.

Nonlocal electronic decay processes are surprisingly accelerated upon proton dynamics. Such strong coupling of electronic and nuclear dynamics is a common motif in the investigation of ICD; however, here its probability correlates strongly with hydration geometry.[34] Results for neat liquid water are presented in Figure 46. The figure shows that the probability for ICD and ETMD increases as time increases, that is, for the transient proton-shared structures. Analysis is based on computing the respective relative populations of the total autoionization spectral intensities for a model water pentamer. The dominating process at short times, that is, close to the ground-state structure, is Auger decay. However, this contribution amounts to only about 60%, implying that the nonlocal decays are quite efficient even in the case of little proton dynamics. At later times, the decay probability via ICD and ETMD increases to approximately 70%, after 10 fs (which is somewhat longer than the O 1s core-hole lifetime). Fractions in Figure 46 refer to the signal in the whole autoionization spectral range. For the decay only into dicationic states that

https://dx.doi.org/10.1021/acs.chemrev.0c00106
Chem. Rev. 2020, 120, 11295−11369

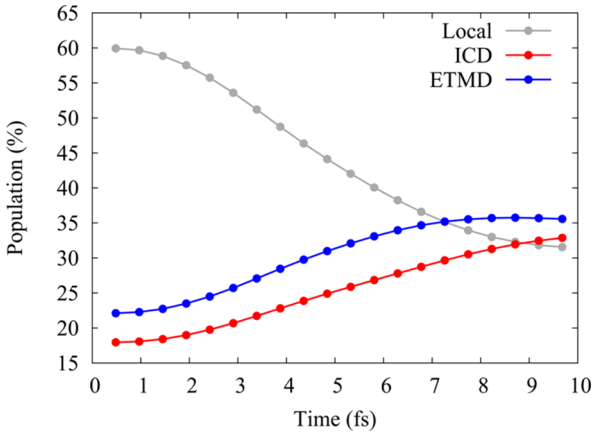

Figure 46. Populations of the final states populated by different, competing electronic relaxation processes in a model water pentamer computed as a function of time after core-level ionization. Reprinted from ref 34.

correspond to the signal intensity in the high-kinetic energy tail, the contribution of ICD and ETMD is about 75%, with little time dependence.[34] Different than in the case of $2a_1$ ionization, treated in Section 5.1.3, here the radiation-less decay channels always add up to 100%, because they are energetically allowed in the entire parameter space of the proton transfer. The small contribution of soft X-ray fluorescence has been neglected.

5.3.3. NH_3 and NH_4^+ Aqueous Solutions. Given the strong electronic and nuclear coupling in the core-level autoionization relaxation processes observed for neat liquid water, one expects ICD to be a rather general phenomenon in hydrogen-bonded aqueous solutes. This has indeed been demonstrated for aqueous solutions of hydrogen peroxide, glycine, ammonia (NH_3), and ammonium (NH_4^+).[433−435] These systems exhibit considerably different hydration patterns, thus allowing for the identification of important mechanistic details of the relaxation processes. Here we restrict ourselves to review the main findings from ammonia and ammonium aqueous solutions. Pure ammonia clusters are considered by theory in ref 226.

The N 1*s*-autoionization electron spectra from 2.6 M NH_3 in light water (blue curve) and from 2.6 M ND_3 in heavy water (red curve) are shown in Figure 47 (top traces). These measurements are fully analogous to the ones presented for water O 1*s*-ionization in Figure 45b, but now we consider the relaxation of core-ionized ammonia, NH_3^+* (aq), and the participation of its first hydration shell. Here again, the ICD signal is identified by the high-energy Auger spectral tail, approximately 375−385 eV KE range (inside the gray-shaded area), which has no gas-phase analogue. Because of its large Henry's law volatility constant, describing the propensity of solvated molecules to transfer into the gas phase, ammonia strongly evaporates from the solution, which leads to a large signal contribution from gas-phase ammonia. This contribution is responsible for the strong Auger peaks between 350 and 370 eV kinetic energy. The important observation is, however, that the ICD signal is stronger for NH_3 in H_2O than for ND_3 in D_2O, indicative of proton dynamics, analogous to water. Specifically, within the core-hole lifetime NH_3^+* (aq) turns into a manifold of transient molecular structures evolving upon proton motion along the hydrogen bond, of the type H_2N*···H^+···OH_2. Depending on the particular subsequent auto-

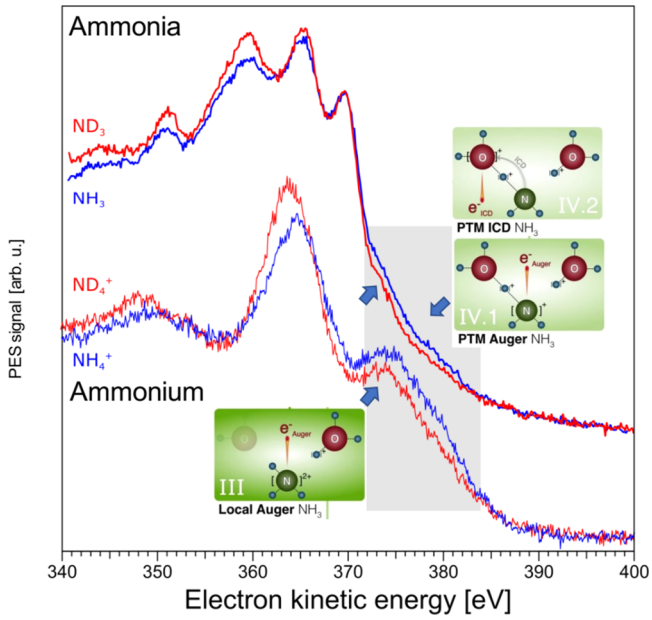

Figure 47. Top traces: Nitrogen 1*s* Auger/autoionization spectra from 2.6 M NH_3 in light water (in blue) and 2.6 M ND_3 in heavy water (in red). Bottom traces: N 1*s*-autoionization spectra from 2 M NH_4Cl (blue curve) and 2 M ND_4Cl (red circles) aqueous solution. All spectra were measured at 500 eV photon energy. Note that the N 1*s* binding energy of ammonia in water is approximately 405 eV. Cartoon (III) depicts the complete transfer of the first proton from (NH_4^{2+})* (aq) to a neighbor water molecule forming (NH_3^+)*-(aq)+H_3O^+ (aq) within 7 fs, followed by local Auger decay. Cartoons (IV): (NH_3^+)* also releases a proton which travels only half way to another water molecule, forming a Zundel-analogue complex where the proton is shared between the remaining NH_2* (aq) and a water molecule. The subsequent autoionization processes of the transient structures by Auger decay (IV.1) and ICD and PTM-Auger (IV.2) are shown. These latter processes are the same as for NH_3 aqueous solution. Gray shading highlights the spectral region sensitive to these processes, labels A and B are explained in the text. Figure adapted from ref 436, used under CC BY.

ionization channel different species form. ICD would lead to the NH_3^+···H_2O^+ cationic pair, while relaxation via regular Auger decay leads to NH_2^+···H_3O^+.[434] One finds from Figure 47 top that the ICD-like decays are less pronounced in the deuterated case but that the isotope effect is smaller than for water; compare Figure 45b.

Yet, the overall signal from 1*h*1*h* final states is seen to be rather large even for the deuterated system, either suggesting that even in the absence of proton dynamics such states can be populated, or PTM-CS processes do not lead to an isotope spectral shift. Molecular dynamics simulations of the evolution of the proton transfer transient structures in $NH_3(H_2O)_3$ and $ND_3(D_2O)_3$ clusters support the former scenario, finding that some nuclear dynamics does occur within the approximately 6.4 fs lifetime of the N 1s core hole, for both light and deuterated ammonia.[434] However, the direct proton transfer is less efficient than in water, due to unfavorable hydration configurations (less directional hydrogen bonds compared to water), and the difference between H- and D-transfer is less pronounced. Nonetheless, the small isotope effect in the high-kinetic energy region seen in Figure 47 would be consistent with weaker hydrogen-bonding ammonia.

The results from neat liquid water and ammonia (aq) show that the probability of PTM-CS is a sensitive spectral probe of

https://dx.doi.org/10.1021/acs.chemrev.0c00106
Chem. Rev. 2020, 120, 11295−11369

hydration structure, and this has led to explore how PTM-CS manifests in a much stronger hydrogen-bonded system. A well suited test case is ammonium (NH_4^+) in water since hydrogen bonding is stronger for this cation,[437] largely stabilized by strong ion−dipole interaction. The probability of PTM-CS in NH_4^+ (aq) has been predicted based on theoretical computations, and the effect of an extra charge on the structure of the transient species has been investigated.[436] The computational analysis has particularly addressed the role of the additional hydrogen atom as compared to water, as well as the fact that the direct core ionization leads to a dicationic species (resulting in a strong Coulomb repulsion between the parent molecule and a proton, furthermore leading to increased attraction between a water oxygen and a proton). Another unique aspect is that not only we expect favorable conditions for PTM-CS processes to take place, there is even a possibility for double-proton transfer giving rise to novel spectral features.

To explore the possibility of single and double proton transfer in NH_4^+ (aq), the energetics of the proton transfer are considered. Figure 48 shows the computed potential energy

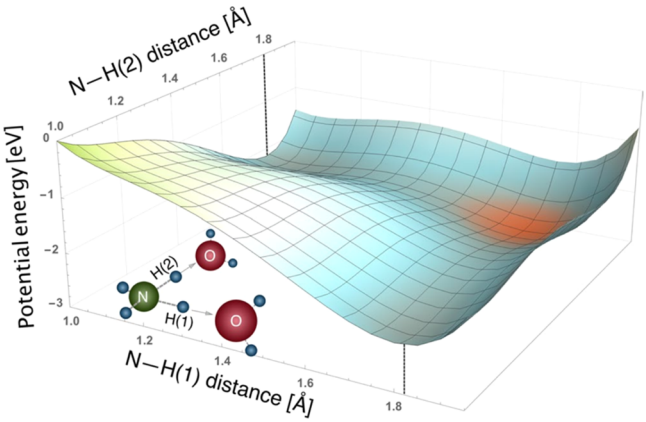

Figure 48. Unrelaxed two-dimensional cut through the potential-energy surface of a core-ionized NH_4^+ $(H_2O)_3$ cluster showing the electronic energy as a function of the N−H distances along the direction of two hydrogen bonds. The N−H ground state distance is 1.1 Å. The minimum energy corresponding to the fully transferred proton is at ∼1.8 Å, marked by black dashed lines. The third water molecule in the molecular sketch is omitted for clarity. Figure reprinted from ref 436, used under CC BY.

surface of microsolvated NH_4^+ $(H_2O)_3$ for two protons which independently move from the nitrogen atom toward the oxygen atoms of adjacent water molecules. Three hydrating water molecules are chosen to mimic the average coordination number obtained from MD simulations.[436] The observed steep energy decrease along both proton-transfer coordinates implies that core-ionization-induced proton transfer is energetically favorable, even if two protons move simultaneously. Note that the minimum energy at ∼1.8 Å N−H distance in Figure 48 corresponds to the proton being fully transferred, forming H_3O^+ (aq). However, dynamical calculations are required to determine that these processes actually occur during the ultrashort 6.4 fs nitrogen core-hole lifetime. Indeed, dynamical calculations on the N 1*s* core-ionized state for a larger number of hydration water molecules, $NH_4^+(H_2O)_{20}$ clusters, find that a complete proton-transfer reaction, $(NH_4^{2+})^*\cdots H_2O \rightarrow (NH_3^+)^* + H_3O^+$, occurs during this ultrashort time. That is, a new H^+-O chemical bond forms before the autoionization event. In addition, the simulations predict considerable motion of the second strongest bonding proton, reaching a mean N−H distance which is halfway toward its coordinated water oxygen. Although the dynamics is slowed down for the ND_4^{2+} $(D_2O)_{20}$ cluster, it is still remarkably fast for the strongest bonding deuteron. Both processes are indeed found experimentally.

Figure 47 (bottom traces) presents the N 1s Auger/autoionization spectra from a 2 M NH_4Cl (in H_2O) and 2 M ND_4Cl (in D_2O) aqueous solution measured at 500 eV photon energy, that is, approximately 100 eV above the N 1s-ionization energy.[438] Unlike their NH_3/ND_3 (or even H_2O and H_2O_2) counterpart spectra, one observes two broad peaks, near 362.5 eV KE and 373 eV KE, respectively. Both features exhibit a sizable isotope effect, which can be attributed to different species, one arising from single- and the other from double-proton transfer. As discussed in ref 436, the 362.5 eV peak results from the (local) Auger decay of core-ionized NH_4^+, yielding NH_4^{2+} (aq). The respective isotope effect arises from PTM-Auger and PTM-ICD processes. Important to note is that at longer times, corresponding to larger $(NH_3^+)^*\cdots H^+$ distance, less of these transient structures form, and autoionization continuously diminishes the population. The 373 eV peak, on the other hand, is a signature of a new relaxation channel becoming available at later time, yet within the N 1s core-hole lifetime. This peak is identified as the Auger peak of core-ionized ammonia, NH_3^+, formed upon a complete proton transfer which is an ultrafast chemical reaction (the other product being H_3O^+) induced upon the core ionization of NH_4^+ (aq). This is corroborated by the fact that the 373 eV peak almost quantitatively coincides with the spectral positions of the local 2*h* (373 eV; Figure 47 top) and delocalized 1*h*1*h* states (374−387 eV) found for NH_3 (aq). In other words, the relaxation processes of the NH_3^+ formed in this ultrafast reaction are almost the same (perhaps slightly affected by the presence of a nearby H_3O^+) as for core-ionized NH_3 in aqueous solution; PTM-Auger decay and PTM-ICD occur from incomplete proton-transfer structures. The situation is partially depicted with an illustration (cartoon III of Figure 47) of the Auger decay of the NH_3^+ reaction product, in the absence of nuclear dynamics. In contrast, cartoon IV presents the respective PTM-Auger (IV.1) and PTM-ICD (IV.2) processes from the evolving proton-transferred transient species. These are the processes responsible for the high-kinetic energy shoulder and the observed isotope effect.

For now we close the discussion of proton dynamics during core hole de-excitation. Investigations of the use of the spectral signature of proton transfer mediated ICD in liquids as a measure for hydrogen bond strength will be explained in Section 5.6.5.

5.3.4. Li^+ Aqueous Solutions. This section discusses electron transfer mediated decay (ETMD) in aqueous solution. In this process, discussed here for the simple case of Li^+ (aq), the 1s-core-ionized cation has to relax with the assistance of hydrating water. This is because this Li^{2+} ion has no valence electrons to refill the core hole, and the refilling electron will thus be provided by water; that is, the system cannot autoionize via Auger decay or ICD.[439] It is the first experimental demonstration of ETMD in aqueous phase, after it has been predicted also for hydrogen-bonded complexes.[34,410,440] In fact, two liquid-jet experiments on LiCl aqueous solution[31,441] have been conducted, challenged

https://dx.doi.org/10.1021/acs.chemrev.0c00106
Chem. Rev. 2020, 120, 11295−11369

by observing the small ETMD signal on a large background of inelastically scattered electrons. In the first reported work[441] long acquisition times were required, using conventional hemispherical electron analyzer for detecting the low-kinetic-energy ETMD electrons, whereas the subsequent measurements[31] used electron−electron coincidence detection, which delivered spectra with better signal-to-noise ratio.

Figure 49 is an energy-level diagram which illustrates the three most relevant ETMD processes that can be expected

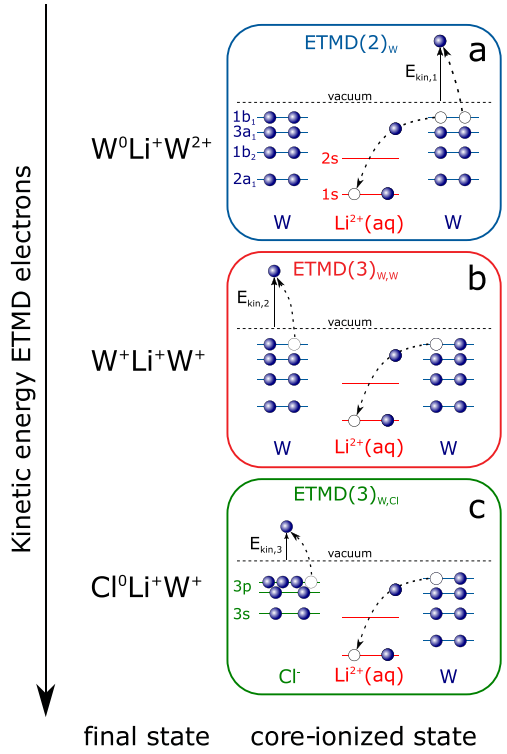

Figure 49. Sketch of the most relevant ETMD processes in LiCl aqueous solution. (a) $ETMD(2)_W$. (b) $ETMD(3)_{W,W}$. (c) $ETMD(3)_{W,Cl}$. The subscripts *W* and *Cl* refer to the species ionized in the final state (water molecules and a chloride anion), and (2) and (3) refer to the numbers of monomers involved in the ETMD process, including the core-ionized Li^+. The initial step in each case is the 1*s*-core-level ionization of $Li^+(aq)$, forming $Li^{2+}(aq)$. E_{kin} denotes the kinetic energies of electrons emitted in ETMD processes (briefly ETMD electrons), which are measured in the experiment. The respective final ETMD states and the relative kinetic energies of the ETMD electrons are indicated on the left-hand side. Figure reprinted from ref 441.

upon 1s-ionization of Li^+ (aq). They are denoted $ETMD(2)_W$, $ETMD(3)_{W,W}$, and $ETMD(3)_{W,Cl}$. Here the subscripts indicate the species that are ionized in the final state, and the number in parentheses shows the total number of species involved in the ETMD process. For example, $ETMD(2)_W$ (Figure 49a) refers to a process where a valence electron from a water molecule (*W*) refills the Li^{2+} (aq) core hole. The released energy is used to eject another valence electron from this same water molecule, which is detected in the experiment. In an ETMD(3) process, the energy released in the core-hole refill is used to either ionize a different water molecule ($ETMD(3)_{W,W}$ in Figure 49b) or detach an electron from the counteranion ($ETMD(3)_{W,Cl}$ in Figure 49c). Given the characteristic orbital energies of water and Cl^-, we can expect that the different ETMD processes result in different spectra, that is, the respective ETMD electrons will have different kinetic energies. Hence, one of the challenges is to assign the spectral distribution to specific ETMD channels, with an important goal to exploit ETMD spectroscopy for probing ion pairing. Measurements were conducted on 3 and 4.5 M LiCl aqueous solutions, applying 171 and 175 eV photon energies, respectively, which is well above the Li^+ (aq) ionization threshold (60.4 eV)[442] in water.

Results are presented in Figure 50. When analyzing the experimental spectra, the signal distribution as a function of electron kinetic energy, it is useful to translate the kinetic energy into double-ionization energies. Both energy scales are displayed, the former on the top and the latter on the bottom axis. The spectra exhibit a broad and rather structureless peak, ranging from approximately 45−20 eV, with a miximum near 28.5 eV; here and in the following, we refer to the double-ionization-energy axis. From a simple estimate based on the energies of the water valence orbitals and assuming perfect electronic screening, this maximum can be assigned to a very specific $ETMD(3)_{W,W}$ process with a final state of two $3a_1$-ionized water molecules. Indeed, twice the binding energy of H_2O $3a_1$ ($2 \cdot 13.5$ eV[443]) yields 27.5 eV, which is close to the experimental position.

The experimental spectra can be quantitatively assigned to solvent-separated ion pairs, solvent-shared ion pairs and contact ion pairs[441] with the help of cluster models, which are not detailed here. Simulated ETMD spectra are shown in the tiers c, d, and e of Figure 50, respectively. The solvent-shared structure yields a broad peak near 28.5 eV, similar to the experimental spectrum, but there is considerable additional intensity near 22 and 35−40 eV (Figure 50c) not found in the measurement. The main difference for the solvent-separated structure is the missing signal contribution near 22 eV, instead a shoulder near 33 eV is found. As indicated in the figure the main peak is due to $ETMD(3)_{W,W}$, and the 38 and 22 eV contributions arise from $ETMD(2)_W$ and $ETMD(3)_{W,Cl}$ processes, respectively. The calculations indeed corroborate our above suggestion based on a qualitative consideration that the most probable $ETMD(3)_{W,W}$ process is the one in which both water molecules are $3a_1$-ionized (denoted $ETMD(3)_{3a_1,3a_1}$, and the others analogously). Surprisingly little signal occurs with other water orbitals involved; this is also true for $ETMD(2)_W$ processes. The calculated double-ionization energy for $ETMD(3)_{3a_1,3a_1}$ processes is near 26 eV, where spectral intensity is small, and $ETMD(3)_{3a_1,1b_2}$ would contribute near 33 eV, that is, in the region of the high-energy shoulder of the main peak. At this latter energy also $ETMD(2)_W$ processes are found to contribute in the simulations. This dominant role played by the $3a_1$ orbital can be explained in terms of the favorable orientation of hydrating water molecules around Li^+. With their oxygen atom pointing toward the metal cation the respective orbitals in play, H_2O $3a_1$ and Li 1*s*, will strongly overlap. It is interesting to note that the dominance of $3a_1$-involving $ETMD(3)_{W,W}$ over $ETMD(2)_W$ processes can be attributed to the number of suitable water molecules nearby the Li center. The efficiency of $ETMD(2)_W$ largely scales with the number of hydration water molecules, but in the case of $ETMD(3)_{W,W}$, the much larger number of water final state pair configurations is crucial. The ETMD spectrum from the solvent-shared structure (Figure 50d) also exhibits a sizable signal from $ETMD(3)_{W,Cl}$ processes (this is the main origin of the peak near 22 eV), whereas such

https://dx.doi.org/10.1021/acs.chemrev.0c00106
Chem. Rev. 2020, 120, 11295−11369

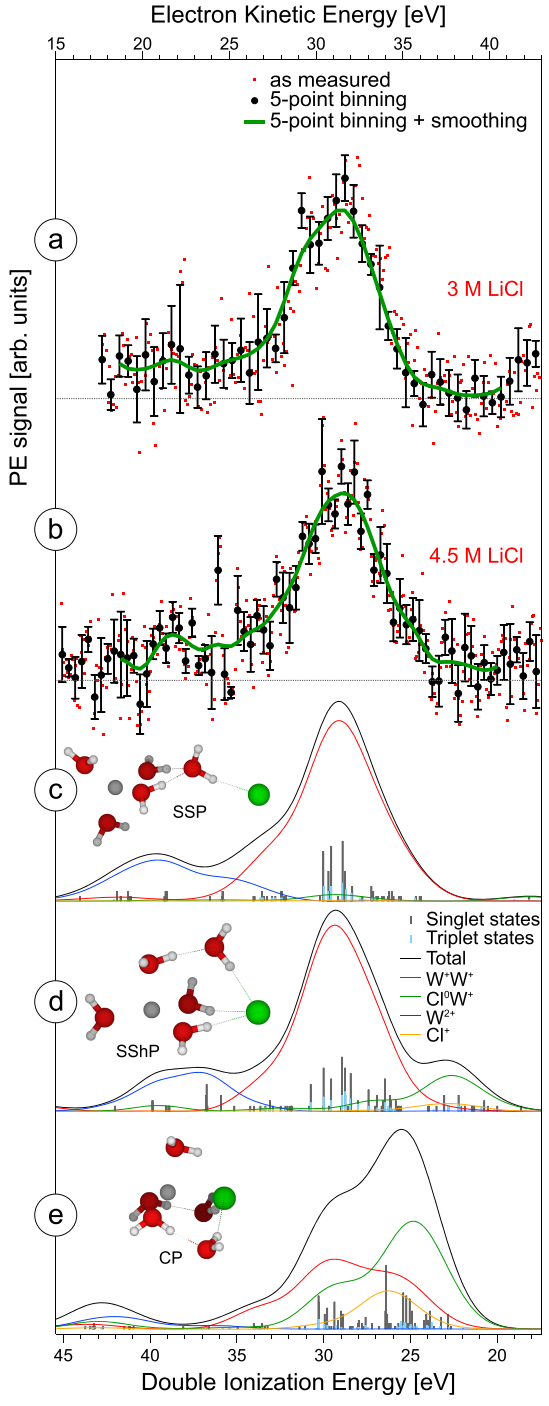

Figure 50. Experimental and simulated ETMD spectra of LiCl aqueous solutions, shown as a function of kinetic energy (top) and versus double-ionization energy (bottom). (a) Experimental ETMD spectra from 3.0 M LiCl solution, resulting from core ionization of Li^+ (aq) at 171 eV photon energy (red dots). A reference spectrum from neat liquid water has been subtracted. Black symbols result from five-point-binning of the red dots, and the green line results from additional smoothing. (b) Analogous data as in panel a but for 4.5 M concentration, and a photon energy of 175 eV. Error bars in panels a and b represent the standard deviation from five-point-binning. (c–e) Theoretical ETMD spectra (black solid curves) computed for the solvent-separated (SSP), solvent-shared (SShP), and contact (CP) ion pair cluster models, respectively. Energies and intensities of individual transitions are shown also as sticks. Each stick has been convoluted by a Gaussian with full width at half-maximum of 3.6 eV. The geometries of the cluster models are depicted in the insets (red, oxygen; green, Cl^-; gray, Li^+; white, hydrogen). The theoretical ETMD spectra are decomposed into various contributions corresponding to different ETMD processes (colored solid curves, see the key). Figure adapted from ref 441.

Figure 50. continued

contribution is missing in the case of the solvent-separated configuration (Figure 50c). This difference is due to the large separation between the metal cation and the chloride anion, located within the third solvation shell. The respective distance is considerably shorter for the solvent-shared structure (compare cartoons in Figure 50c,d). Not surprisingly, $ETMD(2)_{Cl}$ processes are not observed for these two solvation configurations but will become important for contact pairs which are considered next.

Upon substitution of a first-shell water molecule by Cl^-, which corresponds to forming a contact ion pair, a very different ETMD spectrum is obtained, shown in Figure 50e. Now, the largest signal occurs at approximately 26 eV, containing contributions from mainly $ETMD(3)_{W,Cl}$ processes, followed by $ETMD(3)_{W,W}$ processes (these are not the $ETMD(3)_{3a_1,3a_1}$ processes). There is also a very small contribution from $ETMD(2)_{Cl}$ processes (producing Cl^+ cations), which was not found for the solvent-separated and solvent-shared configurations. The strong intensity decrease near 28 eV implies that the particularly favorable $ETMD(3)_{3a_1,3a_1}$ process for these latter configurations plays a considerably lesser role for the contact pair, which is due to different orientation of the water molecules, now maximizing the overlap between Li^+ 1*s* and water 1_b1 orbitals.

In conclusion, the main spectral features in the experimental ETMD spectra can be well interpreted with the help of theoretical simulations. Yet, the signature of ion pairing, at least in the higher concentration spectrum needs to be identified. One expectation would have been to observe some contribution from $ETMD(3)_{W,Cl}$ processes, at an approximate energy near 23 eV; arguably, the 4.5 M LiCl aqueous solution spectrum does indeed exhibit increased intensity at that energy compared to the 3 M-concentration solution.

In a subsequent study, Li electrolyte solutions were investigated by electron–electron coincidence spectroscopy.[31] In the first application of this technique to a liquid jet, a magnetic bottle spectrometer adapted to the vacuum requirements of a liquid environment was used. Electrons resulting from the ETMD processes described above were separated from the background of inelastically scattered electrons from bulk water ionization by coincidence detection of the Li 1*s* photoelectron. Measurements were conducted at 4.5, 6, and 8 M concentration of LiCl and using photon energies of 110 and 130 eV. No significant differences between pairs of spectra recorded at different photon energies were found, and the shape of the ETMD spectrum shown in Figure 50a and b was confirmed.

To test whether the ETMD spectrum can be used as a novel probe for the presence of ion pairing in solutions, LiCl solution was compared to lithium acetate aqueous solution (CH_3COOLi, short: LiOAc)(Figure 51). For LiOAc(aq), evidence to form close contact pairs was seen in earlier studies (see discussion in ref 31). A clear excess in intensity is seen for LiOAc in kinetic energy regions that were earlier attributed to ETMD(3) involving a water site and the Cl^- counterion. The

https://dx.doi.org/10.1021/acs.chemrev.0c00106
Chem. Rev. 2020, 120, 11295–11369

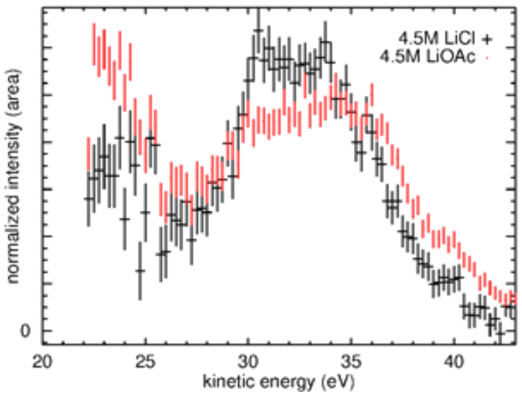

Figure 51. Electron spectrum from ETMD of Li^+ core ionized states in 4.5 M solutions of LiCl ('+' symbols) and Li acetate (LiOAc, dots). The spectra were normalized to equal total area.

signal involving the acetate anion instead of the chlorine is expected in that same range. The observed spectral change is therefore in line with expectations. The use of ETMD as a novel probe for solvation geometries is demonstrated by these results.

5.3.5. Other Aspects of ICD in Liquids. This section discusses the effect of solute charge, polarizability and solvation radius on core-level-induced ICD. Core-hole photoionization and subsequent radiation-less decay in aqueous electrolytes lead to a number of different possible scenarios, depending on which species (solute of a given charge state, or water) the initial core-hole is located at, and on the composition of the first coordination sphere of that species.[444,445] To begin with, let us consider the case of ICD following either ionization of an atomic cation or anion in water. The most relevant processes and species are sketched in Figure 52a and b, respectively. At the top of Figure 52a, we show the initial ground-state situation, C−W, which corresponds to a cation, C, and W is a water molecule in the first hydration shell. The '+' shown inside the blue circle is the single charge of the cation. The left branch depicts the core-level ionization of the cation which produces the intermediate core-excited state C^{c-1}−W where $c - 1$ indicates the missing core-level electron; this leads to C^{2+}, a dication. This highly excited intermediate can relax either via a localized or a nonlocal decay pathway. As shown, the former leads to a final state C^{v-2}−W, and the latter relaxation mechanism forms C^{v-1}−W^{v-1} ($v - 1$ and $v - 2$ refer to one and two missing valence electrons), that is, the respective solute charge states are C^{3+} and C^{2+}. Considering the right-hand branch in Figure 52a, illustrating the initial O 1*s* ionization of a hydration-shell water molecule, very different intermediates, C−W^{c-1}, and final states, C−W^{v-2} (via Auger decay) and C^{v-1}−W^{v-1} (via nonlocal decay) are created. Note though that the latter state is also formed upon initial cation ionization. The solute charge states are C^+ and C^{2+}, respectively.

We can identify analogous relaxation processes for the anion (A)−water system. All relevant steps and species are shown in Figure 52b. Most noticeable is the fact that the intermediate state after solute core ionization contains an overall neutral solute molecule, A^{c-1}−W. Such differences in the charge state, compared to the C^{c-1}−W state after ionization of a cationic solute, suggest to affect the efficiency of nonlocal ICD-type processes when going from cation (aq) to anion (aq). In other

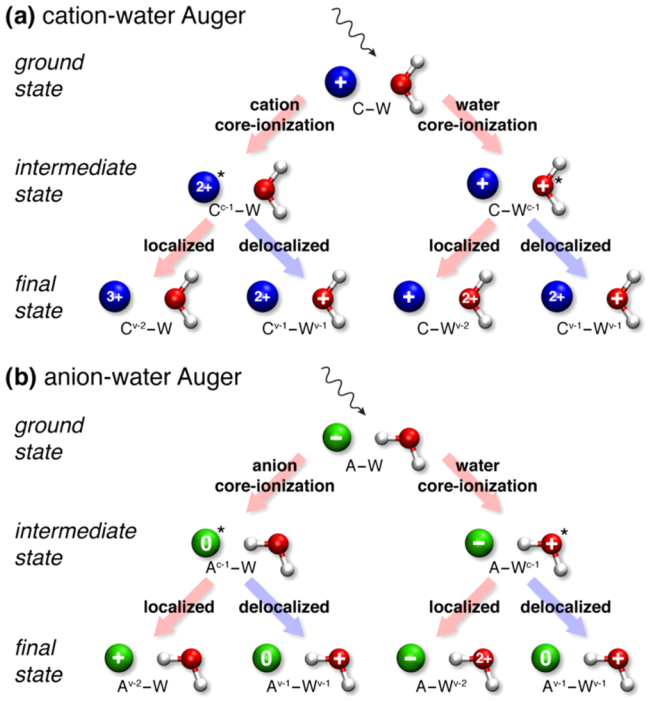

Figure 52. Flow diagram of initial, intermediate, and final state in the Auger process following absorption of ionizing X-rays in aqueous electrolytes. (a) Ionization of a cation or its solvation shell; (b) corresponding situation for an anion. In the intermediate state, either a core−hole on the ion or on one of its solvating water molecules has been formed, leading to varying sorts of interactions between the two species (see main text for details). In the Auger decay, a two-hole final state is produced in which either both valence holes remain localized on the species ionized initially (localized decay), or in which one of the holes has migrated to a neighbor (delocalized decay, ICD). Figure reprinted from ref 444, with permission from Elsevier.

words, the charge state of the solute is a means to control ICD (compare also to ref 420, see Section 5.2.5).

Considering on the other hand the highly excited intermediate state of the water−ionization case of the A−W system, namely A−W^{c-1}, cationic water will polarize the singly negatively charged anion. Qualitatively, via maximization of the overlap between the respective valence electrons and the core hole, the probability of the subsequent nonlocal autoionization pathway, which requires participation of the anion, increases. Such polarization effects will be considerably smaller for the intermediate state, C−W^{c-1} (with C^+ and W^+), in case of the C−W system since the cation's valence electrons are stronger bound.

Core-level ionization of the solute ions leads to a different situation. As seen in Figure 52b, the intermediate state for the A−W system is that of a neutral solute and neutral water molecule, and any strong polarization interactions between the two species are absent. One expects little effect on ICD probability. For the C−W system, the intermediate state is that of a dication and a neutral water molecule, the former polarizing the latter, and we expect a larger probability for nonlocal decay. In the following, we will discuss several experimental examples.

We first turn to results from a 4 M KCl aqueous solution, representative of a cation, and from 1 M $CaCl_2$ aqueous, representative of dicationic hydration. Measured K^+ 2*p* and Ca^{2+} Auger-electron spectra are presented in Figure 53a. Here,

https://dx.doi.org/10.1021/acs.chemrev.0c00106
Chem. Rev. 2020, 120, 11295−11369

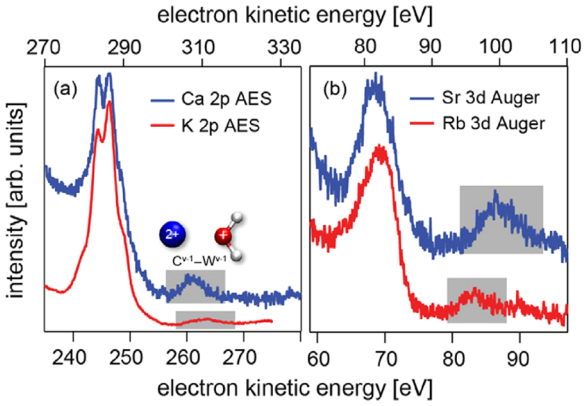

Figure 53. Auger spectra recorded from cations in aqueous solution. (a) $L_{2,3}M_{2,3}M_{2,3}$ Auger spectra of K^+ (red) and Ca^{2+} (blue) in a 4.0 M KCl and a 1.0 M $CaCl_2$ solution, respectively. The top energy scale refers to the Ca^{2+} spectrum, and the lower scale to the K^+ spectrum. (b) $M_{4,5}N_{2,3}N_{2,3}$ spectra of Rb^+ (red) and Sr^{2+} (blue) measured from a 1.0 M RbCl and a 0.5 M $SrCl_2$ solution. The top energy scale refers to the Sr^{2+} spectrum, and the lower one to the Rb^+ spectrum. Figure reprinted from ref 444, with permission from Elsevier.

we use two kinetic energy scales to present the data on top of each other; see comment in the figure caption. In both cases the large signal on the left part of the spectra arises from (local) Auger decay. The interesting aspect for the current discussion is the occurrence of extra rather broad peaks of lower intensity at higher kinetic energy, near 263 eV for K^+, and near 306 eV for Ca^{2+}. The relative signal intensity is larger in the latter case. Corroborated by high-level *ab initio* calculations,[446,447] these emissions correspond to final states in which at least one vacancy is not in the 3p shell of the parent solute ion. Also, relative signal intensities of the main Auger signal and the nonlocal autoionization signal agree with calculated transition rates. The experimental intensities have been used to estimate the time scales for these decays, yielding 195 ± 10 and 33 ± 1 fs for K^+ and Ca^{2+} 2*p* core ionization, respectively. Calculations have also addressed nonlocal relaxation involving counterions but probabilities are negligibly small,[446] and from an experimental point, ion pairs might not form at the concentrations studied. Furthermore, Auger spectra from different counterions (F^-, Cl^-, Br^-) of the same concentration were shown to exhibit no differences in the spectral features corresponding to the delocalized states.[444] This led to the conclusion that ion pairs are uncommon at the concentrations used, and hence, observed nonlocal spectral contributions solely involve water neighbors in this case. A remaining question is why the signal from delocalized final state is considerably larger for the dication. This is due to several effects, the smaller radius of Ca^{2+}, the double charge, and a more ordered water network. Combined, this leads to a shorter ion−water distance and stronger ion−water bonding, making ICD more favorable in Ca^{2+} than in K^+ aqueous solutions.

To further test the efficiency of ICD upon ionization of cations, experiments were conducted on 1.0 M RbCl and 0.5 M $SrCl_2$ aqueous solutions. The crucial difference is that Auger spectra were measured at the Rb^+ and Sr^{2+} 3d edges, which are at much lower energy than the 2p edges discussed above. Both autoionization spectra are presented in Figure 53b, and again with the respective kinetic energy axes shifted such that the spectra reasonably overlap. As in Figure 53a, the spectra exhibit a main Auger signal at lower kinetic energy, and a smaller peak at higher energy arising from delocalized final states (involving water valence ionization). This time, though, the ratio of Auger-to-ICD signal intensity is much smaller (particularly for Sr^{2+}), implying that ICD is more probable than for K^+ (aq) and Ca^{2+} (aq). This observation would seem inconsistent with the above finding that smaller ionic radii tend to increase the ICD efficiency; the radius of Rb^+ is larger than for K^+, and the one for Sr^{2+} is larger than for Ca^{2+}, and furthermore the respective ion−water distances are larger.[448,449] Apparently, there are other important parameters that determine the ICD probability. In the absence of assisting theoretical computations for these systems one can speculate that the core-level energy plays a considerable role, with lower energies favoring ICD. Possibly, also the coordination number of the hydration shell matters, in which case ICD could be a novel tool for coordination chemistry.

We next discuss the nonlocal relaxation processes occurring upon O 1s ionization of a hydration-shell water molecule. Referring back to ICD in neat water (compare Figure 45) a major question is how the presence of a solute will affect the efficiency of the water autoionization channel. It was found that the fraction of W^{v-1}−W^{v-1} states (here we have adopted the nomenclature introduced at the beginning of the current section) relative to the W^{v-2} produced via the (local) Auger channel is considerably smaller.[445] Qualitatively, this reduction largely arises from the fewer neighboring water molecules surrounding a given water molecule, where one or more first-shell H_2O are replaced by an (atomic) solute. The argument is similar to that given for ETMD, namely that the efficiency of the water−water ICD channel scales with the number of available surrounding water molecules. In the literature, this aspect has been termed a passive role played by the solute. However, solute ions can be also much more actively involved regarding the efficiency of nonlocal decay. For instance, anionic solute final states, we will consider halides, of the type A^{v-1}−W^{v-1} have been found upon water O 1s ionization. One may expect that the probability for populating such states scales with the hydration strength of the halides, that is, decreasing when going from F^- to I^-. However, measurements from NH_4X (X = F, Cl, Br, I) aqueous solutions reveal the opposite trend. The respective spectra are presented in Figure 54, which highlights the high-kinetic energy region of the water Auger spectra. Intensity decreases from I^- to F^- aqueous solutions. It thus appears that the ground-state charge transfer is rather irrelevant and instead the anions' polarizabilities matter. The behavior in Figure 54 must hence be attributed to an effect occurring during the ultrashort lifetime of the excited state. It is argued that electron density will flow from the anion toward the core-ionized water cation. Analogous transitions involving cations, that is, O 1s ionized transient states decaying into the C^{v-1} − W^{v-1} final states (compare Figure 52), have not been observed experimentally.[445] Instead, the respective spectra solely reflect aforementioned passive effect. Unlike in the anionic case, the electron-poor cations prevent a flow of electrons to neighboring water molecules.

We close this section by briefly considering O 1s resonant excitation from aqueous solutions, with a focus on changes of delocalization times of excited electrons upon solute addition. As a starting point it is useful to consider the X-ray absorption spectrum (XAS) from neat liquid water[450,451] which is shown in blue in the inset of Figure 55. It is noted that the obtained XAS spectrum is essentially identical to an XAS spectrum

https://dx.doi.org/10.1021/acs.chemrev.0c00106
Chem. Rev. 2020, 120, 11295−11369

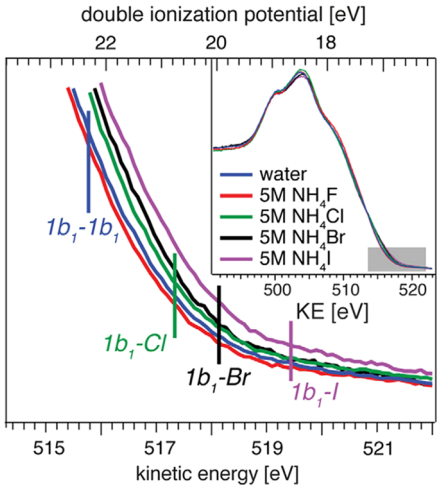

Figure 54. Oxygen 1s Auger spectra of 5 M ammonium halide salts in water. The inset shows the full spectrum while the main figure shows merely the high kinetic energy tail, as indicated by the gray box in the inset. Figure reprinted from ref 444, with permission from Elsevier.

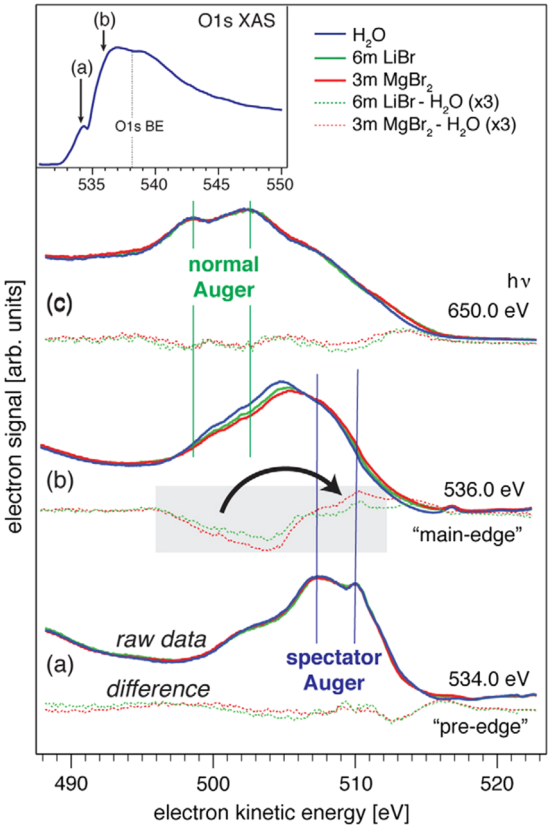

Figure 55. Oxygen 1*s* resonant and off-resonant Auger spectra of liquid water (blue trace) as well as 6 m LiBr (green trace) and 3 m $MgBr_2$ (red trace) aqueous solutions. The inset shows an X-ray absorption spectrum of water where the excitation energies used for producing the Auger spectra in traces (a) and (b) are indicated. Difference spectra of the respective solution minus water for each trace are shown as dotted lines. The gray boxes shown in the difference spectra of trace (b) highlight a characteristic spectral redistribution at the main and post edges discussed in the main text. Figure reprinted from ref 444, with permission from Elsevier.

measured by detection of emitted X-ray photons, or by X-ray transmission. The argument is that the absorption is proportional to the electronic relaxation quantified by the emitted Auger electron yield. Depending on the excitation photon energy the shape of the underlying Auger spectrum will change; individual Auger-electron spectra measured at photon energies corresponding to two positions (a, "pre-edge") and (b, "main-edge") are shown in the main Figure 55, in bottom and center traces, respectively, in blue color. In addition, an off-resonant Auger spectrum, measured at 650 eV, is presented in the top tier. The characteristic absorption pre-edge near 535 eV (labeled (a)) is due to a strong excitonic character in which the excited electron remains nearly fully localized on the parental molecule during the core-hole lifetime.[452] At higher excitation energies, spatially more diffuse states are populated, allowing delocalization of the excited electron into the hydrogen-bonded surroundings. Green and purple vertical lines mark the position of normal and spectator Auger emission, with the latter being a measure of electron localization (i.e., the excited electron has not delocalized within the ultrashort lifetime of the water core-hole).

All spectra in different color were measured under the same experimental conditions but using LiBr and $MgBr_2$ (equimolar in Br concentrations) aqueous solutions.[453] As expected, solutes have negligibly small effect on the spectral shape for pre-edge excitation (bottom tier) due the strong localization of the excited electron. Moving to main-edge excitation one observes considerable changes, manifested in some depopulation of the water (2*h*) states resulting from normal Auger decay, and an accompanying increasing population of the states corresponding to the spectator Auger channel (implying localization). From the differential spectra (dotted curves; shown in each tier) one notices a quantitative redistribution from one state to the other which can be attributed to a slowing-down of the electron delocalization dynamics as compared to neat water. Quantitatively, the effect is seen to be smaller for Li^+ than for Mg^{2+}, and can be explained in terms of a smaller electron-hopping time in the former system. On the basis of a core-hole clock analysis electron delocalization times were estimated to be 1.9 and 1.5 fs for the Mg^{2+} and Li^+ aqueous solutions, respectively. This can be compared with a much faster delocalization in neat water, estimated to be less than 500 attoseconds.[451]

5.4. ICD in Biological Systems

In the previous section (5.1.8), ICD has been argued to be everywhere and to be present in all molecules in condensed phases when an IC-decay is energetically feasible. ICD is thus an ubiquitous process in nature. Most fundamental studies on atomic dimers and clusters, van der Waals complexes of small molecules, have, however, been performed at rather high initial photon energies, preparing initial states of high energy, sufficient to initiate ICD processes. Most dominantly, these initial states were inner-valence ionized states. Under natural conditions, that is, solar irradiation, the available photons possess much less energy, only a few eV, and thus ICD triggered via inner-shell ionization is very unlikely to be a very common mechanism in nature. Therefore, two question naturally arise. (i) Can ICD occur in natural systems, and can the effect possibly be exploited? (ii) Can ICD also occur under natural conditions in biological systems, i.e under sun light-irradiation? These questions have been addressed in the works reviewed in the next subsections.

5.4.1. Small Molecules with Biological Relevance. Theoretical studies on small molecules representing either

https://dx.doi.org/10.1021/acs.chemrev.0c00106
Chem. Rev. 2020, 120, 11295−11369

molecular classes with biological relevance or building blocks of biological macromolecules, like protein or DNA, reveal whether ICD is generally possible in these biological systems.

Stoychev et al. investigated the possibility of ICD upon inner-shell ionizaion in hydrogen bound dimers of a whole set of small representative molecules comprising: H_2O, H_2S, NH_3, formaldehyde and formamide, which contain seven types of hydrogen bonds typical for biochemistry.[221] Within their theoretical investigation, algebraic diagrammatic construction schemes were employed for the calculation of accurate ionization and double ionization potentials. Furthermore, the energy range of the emitted ICD electrons, as well as the kinetic energy of the dissociating ions produced by ICD, is also reported. Indeed, ICD has been shown to take place in all of the selected species because, in particular, inner-valence ionization of the water molecule is followed by very fast and efficient ICD. These results provide insight into possible ICD processes in living tissues and allow for estimates of ICD in biosystems interacting with water.

A related study combining experiment and theory has been performed by Mondal et al.,[454] who investigated binary complexes of 2,6-difluorophenylacetylene (DFPHA) with methylamine, dimethylamine, trimethylamine, or triethylamine, respectively. Using one color resonant two photon ionization (1C-R2PI) and infrared-optical double resonance spectroscopic techniques combined with high level ab initio calculations, all four amines have been shown to form hydrogen bonds between their lone pairs and the acetylenic hydrogen of DFPHA. In addition, while isolated DFPHA and its methylamine complex can not be ionized with the photon energy available in the 1C-R2PI experiment, its complexes with the other amines break up into a positive amine fragment. Since the initial resonant two-photon excitation is localized at the DFPHA molecule, the authors conlcude the excitation energy must have been transferred to the amines eventually ionizing them. This corresponds to an indirect observation of an intermolecular Coulombic decay process.

5.4.2. ICD in Photolyases. Photolyases are remarkable enzymes utilizing near UV light to repair UV photolesions of DNA.[455,456] They contain a light-harvesting photoantenna pigment and a reduced flavin adenine dinucleotide ($FADH^-$). Upon binding of photolyases to a DNA lesion, the antenna pigment absorbs light and the excitation energy is transferred to $FADH^-$, which emits an electron (Figure 56) . The electron eventually catalyzes the repair of the DNA photolesion.[457,458]

The question of whether the initial generation of the catalytic electron corresponds to an ICD mechanism has been clarified by Harbach et al.[120] The crystal structure of the DNA photolyase of *Thermus thermophilus*[459] served as starting point for their theoretical investigations. Using the stabilization method[159,160] as has been described in Section 3.2, the initial excitation energy of the 8-hydroxy-5-deazaflavin (HDF) as well as the one of $FADH^-$ could be shown to be higher than the electron detachment energy of $FADH^-$. Thus, the latter state formally lies in the electronic continuum and the energy transfer process occurs between a bound and an unbound state, a prerequisite for ICD. In addition, the subsequent transfer of the electron to the photolesion occurs over a large distance and hence, on its way, the electron can indeed be seen as free. Therefore, the mechanism triggered by natural sunlight that is active in photolyases to create the required catalytic electron is undoubtedly an ICD process.

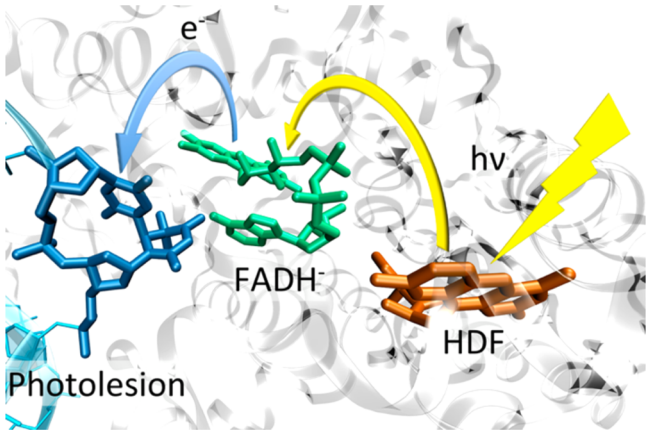

Figure 56. Sketch of the generation mechanism of the catalytic free electron responsible for DNA photolesion repair acting in DNA-photolyases. The excitation energy of the initially excited HDF (orange) is transferred to $FADH^-$ (green) and an electron is emitted, here in the deoxyribodipyrimidine photolyase of *Thermus thermophilus*. The figure is taken from ref 120.

Since the distance between the antenna pigment HDF and $FADH^-$ is as large as 16 Å, the mechanism of the transfer of the excitation energy proceeds via direct ICD, which obeys the same long-range behavior as FRET. Hence, the ICD rate can be estimated via Fermi's Golden rule as

$$k_{ICD} = \sum_n 2\pi f(D_{S_1}) f(A_{S_n}) |V_n^{long}|^2 \delta(\omega(D_{S_1}) - \omega(A_{S_n})) \tag{35}$$

Here f denotes the probability of electronic transition of the donor and acceptor. Because the excitation-energy transfer rate between a bound and unbound electronic states is computed, and the outgoing electron can always take up the appropriate amount of kinetic energy to ensure the resonance condition given by the δ-function. The summation runs over all possible open ICD channels n. Utilizing the transition densities ${\rho_D}^T$ and ${\rho_A}^T$ of the donor and acceptor states, the long-range coupling V_n^{long} element is then simply given as

$$V_n^{long} = \int dr \int dr' \frac{{\rho_{D_{S_1}}}^T(r) {\rho_{A_{S_n}}}^T(r')}{|r - r'|} \tag{36}$$

using the transition density cube method.[460] The estimated ICD rate amounts to $1.4-1.7 \times 10^9$ s^{-1} and is in excellent agreement with the experimentally observed rates of 1.9×10^{10} s^{-1} and 4.6×10^9 s^{-1} for the energy transfer from HDF to $FADH_2$ in *Anacystis nidulans* photolyase and from 10-methenyltetrahydrofolate (MTHF) to $FADH_2$ in *Escherichia coli* photolyase.[461,462] Summarizing, the initial steps in the repair mechanism of DNA lesions via photolyases corresponds to an ICD process, which is the first one shown to occur in a natural enzyme and natural conditions.

5.5. ICD in Quantum Dots

In a most general picture, ICD arises when two localized electronic moieties, with no or little spatial overlap, are coupled via the Coulomb interaction such that energy transfer leading to electron emission from one of the moieties can take place. Coupling between bound electrons of two different rare gas atoms in a cluster offers one possible realization of this idealized situation. Less conventionally, the interacting electrons might be localized not on two atomic nuclei, but in

https://dx.doi.org/10.1021/acs.chemrev.0c00106
Chem. Rev. 2020, 120, 11295−11369

semiconductor nanostructures such as quantum wells, wires and dots.[463,464] A quantum well (QW) is produced when a layer made of semiconductor A is sandwiched between layers of semiconductor B. If the band gap in the material A is smaller than in B, the electrons in the conduction band can be confined to the layer A, where they move freely in two dimensions. This structure can be replicated so that a double well or multiple quantum wells are obtained. While quantum wells can be described as two-dimensional semiconductor heterostructures, quantum dots (QDs) are the zero-dimensional ones. Quantum dots with sizes ranging from a few nanometers to a few tens of nanometers can be produced by a variety of techniques.[465] Similarly to the case of quantum wells, quantum dots can be organized in arrays with varying degree of interdot coupling.[466−468]

The energy levels of a single electron in a semiconductor heterostructure can be obtained by solving a one-particle Schrödinger equation derived in envelope function approximation. In this approach, the effects of crystal structure appear as an effective mass tensor in the kinetic energy term, while the effects of confinement appear as the potential energy.[463,464] In the case of quantum dots, the introduction of the confining potential leads to the appearance of atomic-like discrete energy levels in place of the continuous conduction band. Moreover, one observes narrow lines in the photon absorption or emission spectra of quantum dots, similar to atomic spectra.[469] These properties earned quantum dots the name of "artificial atoms".[469] Importantly, unlike for real atoms, the size and composition of QDs together with their electronic structure and optical properties can be varied in the production process. This offers additional means of controlling the efficiency of electronic processes unavailable in atomic and molecular clusters.

Spatial localization of electrons, atomic-like level structure, and the possibility of constructing coupled arrays suggest that ICD can be realized in quantum dots. The first theoretical investigation of this idea was done in refs 162 and 470, where the focus was on the computation of ICD rates in a representative QD array. As for ICD in atomic and molecular aggregates, the knowledge of its rate is crucial in view of other efficient relaxation processes, such as radiative decay or the relaxation due to coupling to phonons. The authors considered two coupled QDs, each containing an electron in the conduction band, such that a resonant electronic excitation in one dot leads to the electron emission from the other. Computations, which use electron effective masses and dielectric constant of GaAs, showed that for the dots with characteristic sizes of 20−30 nm at a distance of 80 nm from each other the ICD lifetime can be between 7 ps[470] and 140 ps[162]. The difference in the reported widths arises from different structure of electronic continua in the confining potentials used to model the QD array in the respective publications. While in the model of ref 470 the ICD electron is free to move in three dimensions, it is constrained to move along only one dimension in the model of ref 162 (see also ref 471 and discussion below). Even within this wide range, the ICD rate is orders of magnitude larger than the rate of radiative decay[162] and is comparable to the decay rates due to coupling to phonons.[472,473] Therefore, these calculations established the feasibility of the ICD process in quantum dots. Similar to the resonant ICD process in atomic clusters, the process in dots is initiated by resonant absorption of light. The excitation and the following electronic decay involves transitions between levels which originate from the conduction band, such that the transition energies are less than 10 meV. The high efficiency of resonant ICD to absorb light and convert it into electric current led to the conjecture that ICD in QD arrays can be used for detecting weak infrared light.[470]

The follow-up work on ICD in quantum dots focused on two topics. First, detailed description of their interaction with intense laser light prior to and during ICD. Second, optimization of the individual QD structure and the array geometry with the goal of enhancing the ICD efficiency. The ICD rate increases when the average distance between the interacting electron moieties becomes smaller, which can be achieved by placing the dots closer to each other. The calculations[162,470] reproduce the expected behavior of the rate with the interdot distance. Interestingly, the ICD width was found to oscillate about the expected $1/R^6$ asymptote, which indicates that for particular confining potentials the electron continuum strongly depends on the array's geometry.[162] Alternatively, the ICD width can be increased by manipulating the confining potential.[235] Understanding the effects these parameters have on the efficiency of the ICD process allows for constructing of optimized two-dot arrays.[474] Increasing the number of QDs in an array leads to the proportional increase in the ICD decay rate similar to the situation in atomic or molecular clusters.[79,475] Thus, in the three-dot array, the computed ICD rate is twice the rate of the two-dot array.[476]

Theoretical calculations also demonstrated that ICD in quantum dots can be controlled by applying specifically tailored laser pulses. Investigating electron dynamics in the coupled QD system irradiated by strong laser light established that preparing the ICD state by inverting population in one dot through applying a π-pulse leads to faster overall decay than when the QD array is subjected to the continuous action of the laser.[234] The π-pulse was also shown to be more efficient than the nπ-pulses and the effects of direct and multiphoton ionization were investigated in refs 236 and 237. In ref 471, the ICD rate in the case of quantum dots embedded in a wire was compared with the ICD rate in QDs embedded in thin semiconductor films. Expanding electronic continuum from one dimension to two dimensions leads to the increase in ICD rate. It also allows to control the decay rate and angular distribution of the emitted electrons by using different polarization of exciting photons.

Better control over the geometric parameters in the production process of quantum wells compared to quantum dots has led to the theoretical investigation of ICD in semiconductor double well structures. The ICD state is produced by exciting electrons from the valence band to the conduction band in each well. Intraband relaxation of the electron in one well then leads to the emission of the electron from the second well into the surrounding substrate.[477] Although, unlike in QDs, the electrons in QWs are free to move in two dimensions, electronic excitation followed by ICD is still possible provided that in preparing the decaying state the bottom of each respective conduction subband is populated. Moreover, under an additional condition of large separation between the wells, it was shown that the electron emission in ICD occurs mostly in the direction of layer growth.[478] Similarly to the case of QDs, one can optimize the efficiency of ICD by modifying the QW geometry. Investigation of the ICD rate when varying the geometry of the QW array in InGaAs/InAlAs wells produced non-monotonic behavior of the rate as a function of the distance

https://dx.doi.org/10.1021/acs.chemrev.0c00106
Chem. Rev. 2020, 120, 11295−11369

between the wells. Strikingly, this function exhibited a sharp peak, which corresponded to an order of magnitude increase in the ICD rate. The peak was attributed to the appearance of a shape resonance at a particular geometry (distance of the two QWs).[477] It was also shown that by devising QW structures, which contain shape resonances, one might control the direction at which the ICD electron is predominantly emitted and thus improve its detection.[479] This ability to tweak ICD via controlled modification of the heterostructure's geometry makes the study of ICD in semiconductor materials a promising avenue of research.

5.6. ICD as a Tool

Several publications showed that, due to its unique properties, ICD can be employed as a tool for either performing detailed investigations of other processes in the field of AMO-physics (atomic. molecular and optical physics) or in future applications not related to fundamental research. This section presents some examples of corresponding studies.

5.6.1. Impact of Electron Recoil on Nuclear Dynamics. The details of how ICD proceeds are intimately linked to many intriguing effects in photoionization, ion impact ionization, and cluster physics, which are known from other contexts. We briefly review the so-called recoil effect[171] and the effect of post collision interaction between photoelectrons and ICD electrons.[335] Cederbaum and Domcke[171] were the first to point out that the ejection of a photoelectron from a molecule transfers a recoil momentum to the parent ion. This induces internal dynamics of the molecular ion such as excitation of rotational or vibrational motion, which, in turn, modifies the photoelectron energy distribution,[480] leading to rotational Doppler shift on emitted Auger electrons[481] and to a loss of coherence in the emission from indistinguishable centers in a molecule.[482] A translational recoil effect on Auger spectra has been observed, for example, by Simon and co-workers in 2014.[483] The details of ICD can be influenced rather strongly by the photoelectron and Auger electron recoil, as well. This is because of the typically shallow potential energy surfaces on which the nuclear motion during ICD proceeds (see Section 3.3). For example, after $Ne_2(1s)$-ionization Kreidi and co-workers demonstrated that the kinetic energy release of the ions and the ICD energy spectrum is substantially altered by the photoelectron and the Auger electron recoil. This is a result of the initial velocity with which the nuclear wave packet starts the contraction of the system before ICD finally leads to a Coulomb explosion. The intuitive picture behind the process is the following: After the irradiation of the dimer with high energy synchrotron light ($h\nu$ = 880 eV), either a Ne(1s) electron is emitted yielding a high energy Auger electron (E_{kin} ≈ 870 eV), or (with less probability) a Ne(2s)-electron with an energy of approximately 830 eV is ejected. Being emitted locally from one of the two atoms of the dimer, this fast electron imparts a recoil onto the emitting atom, which, depending on the electron emission direction, causes a compression or stretching of the dimer's bond. In total, a recoil energy of about 22 meV is introduced to the nuclear motion, which is not negligible as compared to the dissociation energy of about 250 meV of the initial decaying states. Accordingly, the corresponding studies[197,198] report an enormous effect of that recoil on the underlying nuclear dynamics and on the ICD electron and KER spectra. The recoil effect leads obviously to a breakdown of the two-step model of photoionization and the subsequent decay processes[484] such as Auger decay or ICD. From Auger decay, it has been known for decades that there is yet another mechanism by which the two steps are intertwined. It is termed post collision interaction (PCI) in the literature.[335] As outlined in Section 4.6, this effect has been used, for example, for time-resolved measurements of ICD. PCI can, however, also lead to a recapture of the photoelectron to bound states.[311]

5.6.2. Core Hole Localization. Another intriguing phenomenon, which has been investigated with the help of ICD is the localization of core holes. In molecules consisting of identical atoms such as homonuclear diatomics or larger molecules with high symmetry (e.g., CO_2 or CF_4), hole states are often approximated by symmetry-adapted single particle wave functions which implies a physical picture of the hole being delocalized over the equivalent sites. Domcke and Cederbaum[485] have argued that asymmetric vibrational modes can lead to a localization of the holes. This has been confirmed later by photoelectron diffraction experiments.[486,487] For homonuclear diatomics, however, no such asymmetric vibrational modes exist, and as a consequence, it has been believed for a long time, that, for example, core holes in simple molecules as N_2 or O_2 are delocalized. Coincidence studies of Auger electron and photoelectrons on N_2[488,489] have shown that the question of the parity of the holes is quantum mechanically ill defined as it ignores the essential role of entanglement in many electron systems (see also ref 315). Because the holes are not stable, their creation and decay leads to entanglement between the fragments such as the photoelectron, Auger electron and ionic fragments. The hole itself is not an observable, and thus, the quantum mechanical prediction on the correlation of the electrons and ions may correspond, depending on the experimental arrangement, to localized or, as well, delocalized holes. This is an analog to Bell states of entangled photons where the polarization of the photons is not defined prior to its measurement.[489,490]

ICD in Ne_2 following K-shell ionization illustrates such apparent localization in a coincidence experiment.[58,491] Figure 57 shows the angular distribution of an 11 eV photoelectron emitted from the Ne K-shell in Ne_2 in coincidence with a Ne^+/Ne^{2+} pair. The photoionization step is followed by Auger decay

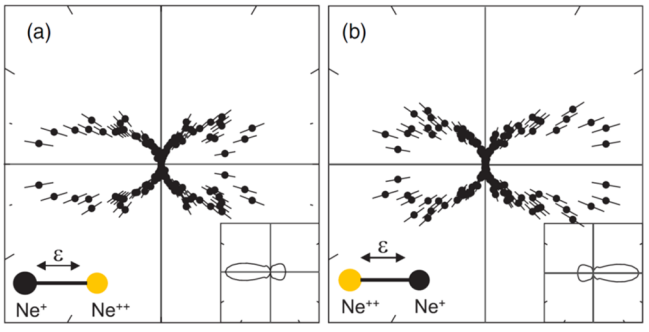

Figure 57. Angular distribution of the 1s photoelectron in dependence of the orientation of the dimer axis and the direction of the polarization vector ε (horizontal). The dimer is aligned in parallel to the polarization vector but with the doubly charged fragment is located in (a) on the right and in (b) on the left side. The asymmetry, being a result of core hole localization, is clearly visible in the experimental data (circles). Insets, solid line: frozen core Hartree−Fock calculation assuming a localized photoelectron emission. Figure adapted with permission from ref 58. Copyright 2008 IOP.

https://dx.doi.org/10.1021/acs.chemrev.0c00106
Chem. Rev. 2020, 120, 11295−11369

into Ne_2^{2+} decaying by ICD to Ne_2^{3+}. The broken symmetry of the photoelectron angular distribution shows that the Ne^{2+} fragment is entangled with the photoelectron. Similar asymmetries are observed also for the ICD electron angular distribution.[58,302,316] These distributions showed furthermore a switch of the preferred emission direction when investigating ICD routes dominated by the exchange contribution or the direct contribution, which is in line with the intuitive picture of the ICD process (see Figure 2).

5.6.3. ICD as a Tool for Observation of Cluster Structure and Breakup and Neutralization Dynamics. Noble gas clusters in the gas phase are typically generated by means of a supersonic expansion of the gas into a vacuum. During the expansion the gas cools down rapidly allowing for a condensation of the atoms to form larger aggregates or even small droplets. While this concept is rather straightforward, the exact details of the cluster formation are still subject to ongoing research, in particular in case of mixed species clusters. Lundwall and co-workers performed a detailed study of clusters generated in a coexpansion of neon and argon atoms. Part of their study employed ICD as a tool to gather information on the arrangement of the neon and argon atoms inside the cluster.[396] By changing the percentage of an argon admixture to the neon gas, they investigated the dependence of the electron energy spectrum to the composition of the expanded gas. For low fractions of argon, a distinct feature belonging to ICD between neon and argon atoms appeared, which vanished again when the argon abundance exceeded 50%. This behavior has been interpreted such, that if only a small fraction of argon is available, only few neon atoms have an argon neighbor (and accordingly the NeAr-ICD signal is weak). Upon increase of the argon percentage, more NeAr neighbors occur. However, even larger fractions of argon yield a generation of heterogeneous argon/neon clusters (the argon forms typically a core, which is surround by shells or islands of neon atoms) and the amount of atoms at the neon/argon interface decreases on a relative level. More recently, Fasshauer et al. reported on a more detailed approach on the same topic.[281] In this experimental/theoretical co-study, detailed information on the arrangement of the different atomic species inside the cluster was obtained from comparison of measured electron spectra to results from a complete theoretical modeling of the different possible ICD processes. Furthermore, this work provided evidence for ICD to the second coordination shell of the initially excited site.

Shcherbinin and co-workers demonstrated that ICD in helium nanodroplets occurs in a similar manner as in free helium dimers and the emitted ICD electrons are only weakly perturbed.[258] They performed a detailed investigation of the breakup dynamics of the helium nanodroplet after initiation of ICD, by measuring emitted He ions in coincidence and comparing the results to a classical model of the intradroplet dynamics. A main finding was that a large fraction of He ions undergoes inelastic collisions with surrounding He atoms causing a drastic energy loss of the ions. Subsequent work by Wiegandt et al. showed that the main energy loss mechanism is a single hard binary collision with another atom of the cluster.[259] The momentum resolving ion data showed, furthermore, a direct fingerprint of elastic scattering events between the ions and the surrounding atoms.

A further process happening inside large clusters and nanodroplets has been identified by means of ICD by Kazandjian et al. in 2018.[320] Other than suggested in ref 258, this work points out that a main energy loss inside the cluster occurs due to a frustrated Coulomb explosion. As the two ions generated by primary ionization and subsequent ICD perform a Coulomb explosion inside the cluster, they may pass other atoms at distances where they do not exchange large amount of momentum but (instead) exchange charge. This charge hopping from an initially neutral to the ionized atom yields an energetic neutral atom (which has the kinetic energy obtained initially from the Coulomb explosion) and a low-energy ion. The corresponding temporal evolution of the process is shown in Figure 58.

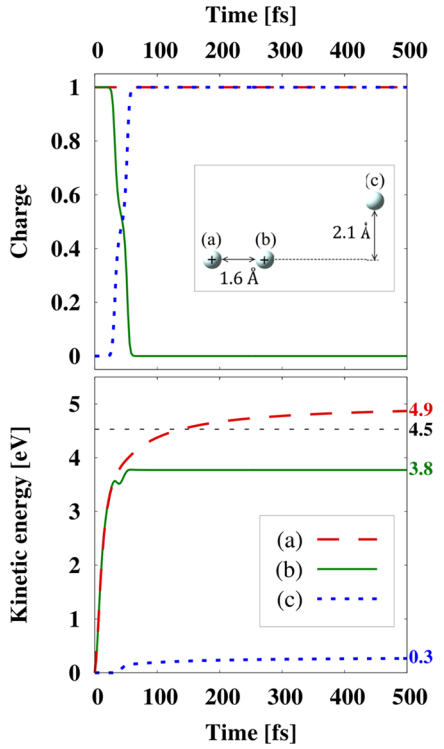

Figure 58. Upper panel: temporal evolution of the charges during a Coulomb explosion between the ions (a) and (b), with (b) transferring its charge to a neutral atom (c). Lower panel: kinetic energies of the three involved particles. The horizontal line at a kinetic energy of 4.5 eV corresponds to the asymptotic energy of the ions after a two-body Coulomb explosion. The figure and caption were taken from ref 320. Reprinted with permission from ref 320. Copyright 2018 APS.

Theoretical studies of ICD in molecular clusters showed that the ion and electron spectra contain information on the neutral cluster geometries or the fragmentation dynamics which follows the electronic decay. Sisourat et al. considered electronic decay in the benzene dimer which follows inner-shell ionization of one monomer.[222] The resulting vacancies can decay both via ICD and Auger decay. The authors showed that intensities and energies of the ICD and Auger peaks in the electron spectra differ for different dimer conformers. As the result the structure of the neutral benzene dimers can be deduced from the photoelectron, secondary electron coincidence spectra. Deleuze et al. predicted that ICD in benzene dimers can lead not only to the Coulomb explosion of the cluster, but also to the fusion of the two cations.[492] In the latter process a covalent bond is formed between two benzene rings,

https://dx.doi.org/10.1021/acs.chemrev.0c00106
Chem. Rev. 2020, 120, 11295−11369

while proton migrations inside the dimer contribute to the reduction of Coulomb repulsion.

5.6.4. Radiation Damage Induced by ICD. Already in early studies on ICD it has been speculated that the process might have an impact on radiation damage in living tissue. The rationale behind this assumption have been several studies in the early 2000s that demonstrated the vulnerability of DNA to low energy electrons.[493] For example, work by Bouddaifa et al.[494] showed the occurrence of DNA double strand breaks and Hanel et al.[495] the decomposition of Uracil molecules by collisions with low energy electrons. As ICD electrons are in most cases of low kinetic energy (E_{kin} < 15 eV), and as ICD occurs even after high energy ionization/excitation at some point during or after de-excitation cascades, it was suggested that ICD in biological systems might be to some extent responsible for radiation damage by secondary electrons.[496,497]

First experimental studies toward the role of ICD on damage of biological matter were conducted by demonstrating the occurrence of ICD in water clusters and dimers (see Section 5.2.5) after inner-valence ionization employing synchrotron radiation.[215,263,498] Studies on the dose enhancement due to high-Z-containing nanoparticles were performed, for example, by Seo et al. in 2015.[499] They investigated the production of reactive oxygen species in a gadolinium oxide nanoparticle solution irradiated with 50 keV X-rays and high energy protons. Later work by Ren et al. (see also Section 5.2.5) investigated electron impact ionization of hydrogen-bonded complexes that consist of tetrahydrofuran (THF) molecules loosely bound to a water molecule as a model system for more complex biological matter:[319]

$$e^- + H_2O\cdots C_4H_8O \rightarrow 2e^- + H_2O^+(2s^{-1})\cdots C_4H_8O \quad (37)$$

After the inner-valence ionization the system undergoes ICD:

$$H_2O^+(2s^{-1})\cdots C_4H_8O \rightarrow H_2O^+\cdots C_4H_8O^+ + e^-_{ICD} \quad (38)$$

As a final step, the dimer fragments in Coulomb explosion generating two energetic ions. A sketch of the overall process is shown in Figure 59. Ren et al. were able to identify the overall process by measuring the ionic fragments and the involved emitted electrons in coincidence. Their analysis displayed, as expected, in addition the occurrence of a surplus of genotoxic low energy electrons.

Of further interest with respect to radiation damage has been the identification of ICD in ion/cluster collisions. Pioneering work by Titze and co-workers showed that ICD is a substantial channel after bombardment of helium dimers with fast α-particles (150 keV/u)[247] and Kim et al. observed ICD in Ne_2 and Ar_2 after collision with different projectiles of several energies.[248] Complementary studies on neon dimers at very low projectile energies have been performed in 2015 by Iskandar et al.[312] Just as in the recent studies,[319] it has been shown already in 2011 that a large surplus of low-energy electrons can be found in ion/cluster collision which directly originate from ICD. Kim et al. observed an increase of the abundance of such electrons by a factor of 14.[245] An experiment involving α-particle-irradiated acetylene dimers confirmed furthermore ICD after ion collisions with a molecular system.[250]

A different twist to the topic came up with the suggestion that resonant Auger decay[500] is able to trigger ICD as the second step of a decay cascade.[125] It has been argued to thus use ICD as a means for targeted creation of low-energy electrons, with a potential for radiation therapy. Gokhberg and co-workers suggested, that after an initial resonant excitation of a high-Z (i.e., heavy) element inside a molecule, a large fraction of ICD-enabled states are generated as a final step of spectator Auger decay cascades. Accordingly, if such molecules can be used as a marker for cancerous cells, a low-energy electron emission can be resonantly initiated in the close vicinity of a tumor. Because of the resonant character of the initial excitation it occurs site-selectively and can be performed with a very narrow bandwidth, drastically reducing the irradiation dose. In addition, the inner-shell resonance energies of heavy elements are located in a regime in which typical biological tissue is transparent to the radiation. The predictions for the overall process included, in addition, an example showing that by detuning to an appropriate resonance the energy of the ICD electron can be adjusted.[125] Several experiments confirmed resonant Auger decay-induced ICD in atomic clusters[307,501] (and showed the ability to control the ICD electron energy)[308] and molecular systems.[309] Corresponding detailed theoretical studies on resonant Auger-induced ICD have been performed by Miteva and co-workers.[199,200] Schwartz et al. demonstrated a computationally inexpensive approach for the prediction of core-excited ICD in solutions, which they believe allows for a rational design of a therapeutic protocol employing ICD after resonant core-excitation of heavy elements containing drugs.[502] In this context, ongoing efforts to use decay cascades initiated by high kinetic energy Auger electrons from radioactive nuclei, for example, ^{125}I, for therapeutic processes are also of relevance.[503]

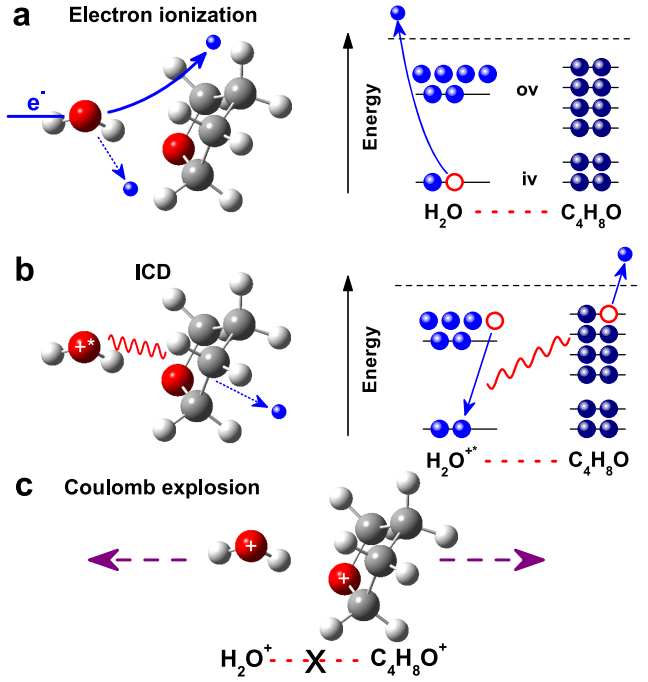

Figure 59. Schematic representation of ICD of an inner-valence vacancy in a hydrogen-bonded THF−water dimer. (a) Starting point of this intermolecular process is the creation of an inner-valence (*iv*) vacancy by direct electron-impact ionization of the water molecule. (b) Energy released by de-excitation of an outer-valence (*ov*) electron at the same molecule is transferred to the neighboring THF molecule, which consequently emits a low-energy electron. (c) Back-to-back emission of the fragment ions after Coulomb explosion of the dimer. Figure and caption reprinted from ref 319.

https://dx.doi.org/10.1021/acs.chemrev.0c00106
Chem. Rev. 2020, 120, 11295−11369

5.6.5. ICD and Hydrogen Bond Strength. Studies on PTM-ICD in liquids, presented in Sections 5.3.2 and 5.3.3, clearly show a mutual dependence between hydrogen bonding and proton transfer during the lifetime of an oxygen core-hole. The spectroscopical fingerprint of the proton transfer in the ICD spectrum has been explained (see Figure 45). One may ask whether this signature is sufficiently robust to be used as an indicator for hydrogen bonding, thus reversing the arguments made in the initial study. In investigations on clusters of water and heavy water, the spectral feature due to PTM-ICD could be seen in analogy to liquid water.[504] Differences between the two respective traces were more pronounced in larger clusters. A quantitative metric for the spectral difference was established by the authors, according to which the H-bonding related PTM-ICD signature is in large clusters as strong as in liquid water, within the accuracy of the experiment. Less pronounced effects in small clusters could be due to differences in the hydrogen bond network, but also to a larger propensity for surface sites with dangling bonds.

It is interesting to study the relation between H-bonding and PTM-ICD and liquids other than water. Liquid methanol (CH_3OH) is a suitable candidate, as it contains two core orbitals of different Z (C 1s, O 1s) and at atoms, which interact differently with their neighbors. The OH group in a methanol network acts similar to water, with respect to hydrogen bonding, and has a tendency to bond with water in a water−methanol mixture (hydrophilic site). The methyl group does not undergo strong hydrogen bonding, and avoids contact with water in a mixture (hydrophobic). Liquid methanol is thus one of the simplest amphiphilic molecules. The decay spectra after ionization of each core hole were studied for both normal and fully deuterated (d_4)-methanol.[505] For oxygen core holes, a propensity of decay into the high energy flank of the local Auger spectrum is again seen for the normal methanol compared to the deuterated, in analogy to Figure 45. Visually, the effect appears to be less pronounced, which seems explicable as each oxygen center in methanol is only singly bonded, while in water it accepts two H-bonds. This is borne out by the quantitative analysis of the spectral difference, resulting in a value of 0.40(9) for bulk methanol relative to liquid water, and in slightly lower values for methanol clusters of different size.[504]

The spectral difference in PTM-ICD spectra between normal and deuterated species thus might become a useful measure for hydrogen bond strength in various liquids.

5.6.6. ICD as a New Ultrafast Clock. The observation of the electron dynamics of a quantum systems on its native time scale (atto- to femtoseconds) has become an area of intense research in the last two decades. A recent review, cited as one example of this prolific field, is in ref 506. Common to a number of experiments that were and are being carried out is the use of attosecond photon pulses to initiate processes and probe the response of the electronic charge cloud. In this spirit, a recent suggestion of a time-dependent two-color experiment employs resonant ICD to explore fundamental quantum dynamics.[376] An ultrafast XUV pulse excites an inner-valence state to a resonance, which may decay by resonant ICD. Within the decay time, the excited electron of the neutral resonant state might be ionized with a second, ultrafast IR pulse, which quenches the resonant decay but at the same time enables normal ICD. In the cited work, $2s \rightarrow 5p$ excitation in a Ne dimer is discussed as a computational example. A related scheme was recently used to observe the buildup of a Fano-shaped absorption profile from an atomic resonance.[507] The common denominator of both works is the excitation of a neutral resonance in the continuum, which is ionized by a second photon pulse within its natural lifetime. Using ICD, this idea could be used to experimentally show an oscillation in time of the decay amplitude of a resonant state, which so far has escaped detection.[376] Proposing ICD in this context is well suited because its long lifetime compared to Auger decay makes it easier to observe the predicted oscillation by recording the resonant ICD intensity up to the (variable) moment of ionization by the IR photon.

5.7. Collective Autoionization and Other Phenomena Related to ICD

This subsection covers processes related to ICD in greater detail. Those include ICD initiated by multiphoton processes, experiments highlighting the connection to Penning ionization, collective autoionization, and collective ICD. Furtheron, results on ICD-like amplitudes in extended molecules will be presented. The section closes with a subsection on ICD at surfaces of solids.

5.7.1. ICD Excited by Multiphoton Processes. Several possibilities to efficiently initiate ICD by multiphoton absorption were discussed in the literature. In the collective ICD,[383] it is proposed to ionize inner-valence electrons of two atoms. Systems can be found in which a single vacancy cannot trigger ICD, but in a simultaneous relaxation of two vacancies, they can pool the transition energy to ionize a third neighbor. It is interesting that an analogous process has recently been discussed in the realm of FRET (that is, applying to a discrete transition in the receiving center).[69]

Alternatively,[51,207,212] if several atoms or molecules inside an aggregate are excited, relaxation of one of them may cause ionization of the other. As both centers involved in this collective ICD are excited already in the ICD initial state, the transition energy required to effectuate the release of an electron is lower compared to the conventional ICD process. In the initial paper, the excitation and de-excitation process proceeds according to[51]

$$\begin{aligned} Ne_2 + 2h\nu &\rightarrow Ne^*(2p^5 3s^1)Ne^*(2p^5 3s^1) \\ &\rightarrow NeNe^+(2p^5) + e_{ICD}^- \end{aligned} \tag{39}$$

By its initial photon energy, its final state and the emitted electron, this pathway cannot be distinguished from two-photon photoionization of a Ne 2p-electron. Estimates on the expected rates of both processes show that nevertheless a regime of cluster size and photon intensity exists, in which collective ICD is strongly dominating.[51] The excitation of two identical, close-by atoms by two photons of the same energy, however, is strongly suppressed, owing to a mechanism termed "Coulomb blockade". In a dimer, the blockade energy is enormous. For instance, the vertical $2p \rightarrow 3s$ excitation of one of the Ne atoms in the neon dimer requires a photon energy of about 16.75 eV, while the subsequent $2p \rightarrow 3s$ excitation of the neighboring Ne atom proceeds at only 16.03 eV. Refs 207 and 212 suggest to efficiently overcome this blockade of about 0.7 eV by the two-photon resonant double-excitation of the dimer with intense laser pulses of the average carrier frequency (the energy of two photons fits to the energy of the doubly excited state). Interestingly, the same relaxation mechanism was proposed to operate in a pair of Rydberg atoms in an ultracold Rydberg gas,[508] where both the decay lifetimes and interatomic

https://dx.doi.org/10.1021/acs.chemrev.0c00106
Chem. Rev. 2020, 120, 11295−11369

distances are orders of magnitude larger than in van der Waals clusters.

Another scheme to initiate ICD by the absorption of two low energy photons, which is much more efficient than traditional single-photon absorption schemes, was proposed in ref 206. In this scheme, the first photon from an intense FEL pulse ionizes a 2*p* electron from one of the Ne atoms in a neon dimer, and the second photon resonantly couples 2*s*- and 2*p*-ionized states of the same Ne atom, leading to a $Ne^+(2s^{-1})Ne$ state decaying by ICD akin to Figure 1. This can be efficiently done at the resonant photon energy of around 26.89 eV and using moderate pulse intensities below 10^{12} W/cm^2. At higher peak intensities, a two site-two photon double-ionization of the neon dimer becomes comparable with ICD. This scenario was successfully realized at FERMI.[211] We will return to the topic of collective ICD below, discussing its occurrence in larger clusters (Section 5.7.3).

5.7.2. Penning ionization en route to ICD. Ionization of a target by a collision with a metastable, excited projectile (e.g., He* (^3S)) has been known for a long time, and is a process of some similarity to ICD. This analogy becomes particularly compelling in the field of so-called He droplets, large He clusters (<*N*> = 200 to 5 × 10^6) produced by supersonic gas expansion.[509] He droplets are an interesting subject of study in its own right, but since they easily can be doped, they can also act as an ultracold, fluid medium hosting other particles, and they may participate in charge and energy transfer processes to and from a dopant. Kryzhevoi et al. were the first to point out the potential importance of ICD for the relaxation of excited centers in a He droplet.[510] In a theoretical study, they considered ICD of Ne 2*s* and Ca 3*p*-ionized states in He droplets of different size. They obtained an interesting result which was the dependence of the decay width Γ on *N*. The authors found it to increase when going to larger droplets, a trend which only saturated above sizes of $N \approx 1000$. Directional anisotropy of ICD widths was also theoretically demonstrated to exist in mixed He^3/He^4 droplets doped with Ca atoms.[511] Practical experiments on these predicitions, however, face the difficulty to selectively create a vacancy in the dopant, at energies which are sufficient to also ionize the He matrix. Energy transfer from the droplet atoms to the dopant turned out to be more promising to study, and a fruitful series of de-excitation studies of this type of processes was carried out.

The elements of a typical experimental setup are described in ref 261, and consist of a cooled nozzle for He cluster formation by a continuous supersonic gas expansion, a skimmer, a zone to realize dopant take-up from a heated oven, the interaction region in which photoionization by synchrotron or FEL radiation occurs, and a VMI spectrometer capable of e^-, ion coincidence acquisition (Section 4.4.1). Photoionization of He droplets doped with a single alkaline metal atom was studied in the same work. Ion yield spectra as a function of photon energy showed the production of alkaline cations at the energies of the He 1*s* → *np* resonances ($h\nu$ = 21.6 eV) below the He ionization threshold. This was explained as the de-excitation of excited He atoms, leading to ionization of the alkaline metal *X* according to the reaction equation:

$$He^*He_N + X \rightarrow HeHe_N + X^+ + e^- \quad (40)$$

For Li as a dopant, the abundance of Li^+ as a function of cluster size proposed a production of the He* in the bulk of the droplet, while the alkaline atoms are known to prefer surface sites. Diffusion of the He* to the Li center must therefore take place before the de-excitation. A measurement of the electron spectra produced in the Penning ionization process for several alkaline dopants also showed that, besides diffusion, relaxation of the He 1*snp* excited states to metastable 1*s*2*s*, or further to metastable He_2* dimers must take place. For rare gas dopants, indirect evidence for radiative charge transfer after photoionization was also achieved.

In ref 261, the term Penning ionization was used for the de-excitation process. The analogy to ICD however is visible, and it becomes even more compelling when a cluster is immersed in the He droplet. This experiment was done a few years later: LaForge et al. studied the de-excitation of Mg clusters (<*N*> = 5−6) embedded in an <*N*> = 50000 He droplet.[273] Similar to their earlier work, Penning ionization of Mg is seen on the He below-threshold resonances. However, the yield of Mg charged fragments is also increasing above the He ionization threshold and is behaving almost in sync with the He_2^+ photoion yield (with the He dimer cation formed immediately, 60 to 80 fs, after ionization).[273] Different from that, Na doping also shows resonant Penning ionization but no increase at higher photon energies. Photoelectron spectra recorded in coincidence with some Mg fragment after ionizing the droplet with synchrotron radiation at $h\nu$ = 40 eV are shown in Figure 60. Low kinetic

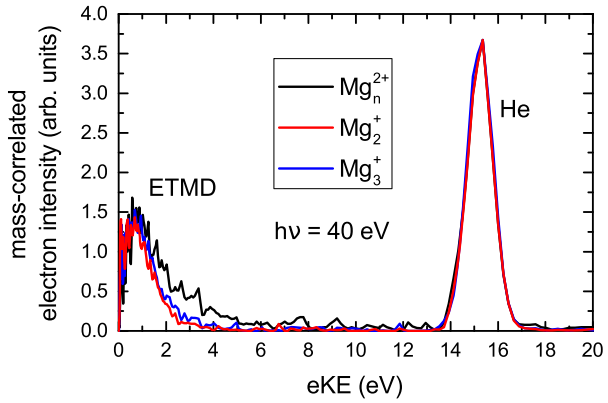

Figure 60. Electron spectra of He droplets doped with several Mg atoms, forming a cluster after condensation. Spectra were recorded in coincidence with charged Mg fragments with different *e*/*m* ratio. Low kinetic energy electrons received together with a doubly charged Mg fragment (all fragment sizes added to improve statistics) are interpreted as result of ETMD from an ionized He atom to the Mg cluster (black trace). Singly charged fragments result from breakup of a doubly charged Mg cluster after ETMD (red, blue trace). The 1*s* main line from He photoionization is also seen. Reprinted with permission from ref 273. Copyright 2016 APS.

energy electrons together with a doubly charged Mg cluster are clearly seen, besides He photoelectrons. As Mg charged fragment production depended on He ionization, it is convincing to identify this process with relaxation of a He photoion by ETMD, and not with direct photodouble-ionization of the Mg cluster. The experiment can be compared to a theoretical work of Stumpf et al.,[33] in which the authors predicted a far increased cross-section for double ionization via an indirect mechanism, such as ETMD, in a MgHe system. In detail, the observation differs however. While theory predicted the ETMD process to be active even for a single Mg atom inside He, this was not found experimentally, due to relaxation

https://dx.doi.org/10.1021/acs.chemrev.0c00106
Chem. Rev. 2020, 120, 11295−11369

energy lost to the He_2^+ formation.[273] As a prototype system for clusters inside a He droplet, ETMD of Li_2He was investigated theoretically.[512] The failure to observe increased double ionization for Na doping is in line with the above interpreation. While Mg has an outer-valence shell configuration of $3s^2$, Na with just a single 3*s* electron cannot decay by ETMD and therefore the amount of charged Na fragments is not increased by He ionization.

In a follow-up work, a two-electron ionization process in an alkaline metal cluster immersed in a He droplet was even seen after a resonant excitation.[269] It proceeds according to the reaction equation

$$h\nu + \mathrm{KRb@He_N} \rightarrow \mathrm{KRb@He_{N-1}He^*} \rightarrow (\mathrm{KRb})^{2+}@\mathrm{He_N} + 2e^-_{ICD} \rightarrow \mathrm{N(He) + K^+ + Rb^+ + 2e^-_{ICD}} \quad (41)$$

In words, a He droplet is excited at the He 1*s* → 2*p* resonance. He* cools down to metastable He* (1*s*2*s*), which diffuses until it neighbors a mixed alkaline metal dimer immersed in the droplet. The excitation then relaxes by energy transfer to the dimer, the double ionization potential of which is sufficiently low to allow the simultaneous ejection of two electrons into the continuum. In the experiment, the alkaline atom pair, with oppositely directed momenta, was observed in coincidence with an electron (one of the two ICD electrons that were ejected). The fate of the He droplet is not observed, but massive fragmentation due to the low interparticle binding energy can be surmised. A symmetric energy distribution of the electron, peaking at 0 eV and at (*E*(He*) − DIP) was observed, were DIP designates the double ionization potential of the cluster. This process was called (resonant) double ICD, dICD. General properties of resonant dICD processes were investigated in a recent theoretical work.[513] While this latest work and the original theoretical prediction of dICD in ref 80 consider the double ionization of a single site by the relaxation step in a neighboring partner, in the experiment described above a transition involving three sites has been observed. The rate for three site dICD was recently shown to vanish from an orbital overlap argument in a theoretical work about a triad of quantum dots.[476] To clarify the apparent contradiction to the experimental results is beyond the scope of this review; however, we would like to mention that atomic processes that are enabled by deviations from strict orbital orthogonality, so-called shake transitions, are observed in electron emission experiments in numerous settings. It is also interesting to compare collective ICD processes detailed above, and the three-electron ICD[23] (Section 5.1.8) to collective Auger processes in atoms and molecules, which were recently summarized.[514]

5.7.3. Details of Collective ICD. In a follow-up study to their work on alkaline doped He doplets,[261] the same team analyzed the photoionization of pure He droplets.[270] Somewhat unexpectedly, even in this situation free electrons from Penning ionization are seen if the photon energy is tuned to the He 1*s* → 2*p* resonance, with a kinetic energy slightly below $2h\nu$ − IP, with IP = 24.6 eV the ionization potential of He. This can only be explained if two metastable He* atoms react according to eq 40 with X = He* and can be seen as the first experimental evidence for collective ICD, as predicted in ref 51 (see Section 5.7.1). From estimating droplet size and photon flux, the authors suggested that the He droplet collects photons from subsequent synchrotron radiation bunches. As the He* excited states may convert to the long-lived 2*s* configuration by collisions, thus experiments on collective ICD-like decays are possible even with peak intensities far below those from an FEL.

Research on collective ICD picked up speed when FEL light sources became available for AMO research. The intensity dependence of ionization by multiple below-threshold excitations was measured by ion spectroscopy.[306,515] This information, however, was not sufficient to make definite conclusions on the underlying processes. A study on He droplets at FERMI[516] at the photon energy of the 1*s* → 2*p* absorption maximum in clusters, 21.4 eV, also presented the electron spectra.[53] They showed a clear signal of collective ICD, in full analogy to earlier synchrotron radiation results. However, this result could only be obtained for comparatively small droplets (<*N*> = 1000) at intensities of 8.7×10^{10} W/cm^2, far below of what is possible at FEL sources. For larger droplets (<N> = 50 000) at higher intensities (2.2×10^{12} W/cm^2 and above), electron spectra were found to descend in intensity from kinetic energies of zero eV and were otherwise rather structureless. This motivated the modeling of the decay path as collective autoionization, a blend of three- and more-center ICD processes that may also involve inelastic scattering of the ICD electron (Figure 6). Follow-up experiments on Li- and Xe-doped He droplets used the different site propensity of the dopants (Li: surface active, Xe: bulk sites) to confirm the formation of a nanoplasma inside the droplet, as a result of collective autoionization.[272]

Experiments on Ne clusters, at FEL intensities between 10^{13} and 10^{14} W/cm^2 tuned to the 2*p* → 3*d* excitation at 20.3 eV, also failed to see evidence for collective ICD at first.[271] Similar to the He droplet experiments it was found that at too high intensities, the ICD-like processes are masked by fast nanoplasma formation, discussed amply for other rare gas clusters ionized at FEL intensities.[517] It needed a suitable balance of cluster size and FEL intensity to arrive at an experimental demonstration of the original example for collective ICD in eq 39. Iablonskyi et al. used <*N*> = 5000 Ne clusters irradiated at intensities between $2 \times 10^{11} - 2 \times 10^{13}$ W/cm^2 to arrive at the electron spectra shown in Figure 61. The figure shows collective ICD at slightly lower energy than expected.[274] This was interpreted as an effect of relaxation of the Ne* 3*s*-excitation to an excitonic state at slightly lower energy. Spectra of surface Ne recorded at increasing intensity show an increasing tail of electrons at lower kinetic energy, caused by sequential multiple ionization of the Ne cluster to higher overall charge states. For bulk excited states, at the highest FEL intensity, the spectrum starts to assume the structureless shape seen for collective autoionization. Also for bulk excited states, inelastic losses of the ICD electron due to scattering at other Ne* centers, exciting the 3*s*-excited electron to higher Rydberg states ("knock-up") or into the continuum ("knockout") can be seen. Further detail on collective ICD in Ne clusters was added at about the same time, showing for the decay of multiple 2*p* → 3*d* excited states a series of collective ICD cascades, invoking a 3*d* → 3*s* de-excitation in one of the involved centers as the first step.[228]

Collective ICD was also shown in Xe clusters.[286] In these experiments, a medium-sized cluster beam (<*N*> = 5−40) from a pulsed jet source was excited by an optical laser (Ti:Sa). A two-photon absorption process, using the third laser harmonic (UV, λ = 263 nm, $h\nu$ = 4.71 eV), created excitonic states in the cluster. Recombination of two such excitons was

https://dx.doi.org/10.1021/acs.chemrev.0c00106
Chem. Rev. 2020, 120, 11295−11369

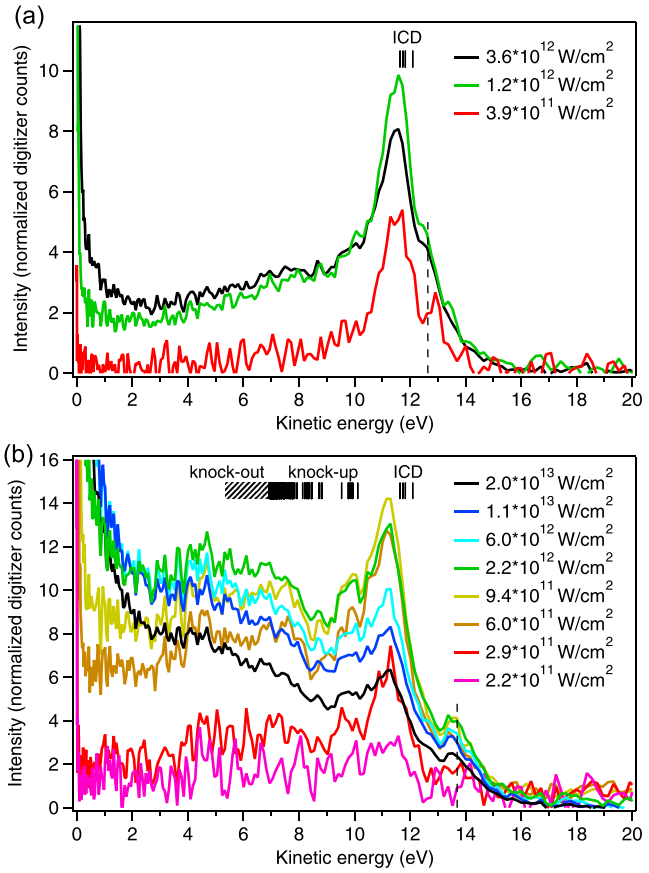

Figure 61. Electron spectra from Ne clusters excited by FEL radiation of $h\nu$ = 17.12 eV, corresponding to the Ne 2*p* → 3*s* excitation for surface sites (a), and of $h\nu$ = 17.65 eV, corresponding to bulk sites. All traces are normalized according to the FEL intensity, indicated in the legend. The dashed lines mark the energy corresponding to $2h\nu - IP$, at which a small amount of two photon direct photoionization can be seen. Continuum electrons corresponding to collective ICD between two excited Ne* centers are at somewhat lower energy (marked in the figure). See text for details. Reprinted with permission from ref 274. Copyright 2016 APS.

seen by emission of a band of electrons, about one eV broad. By adding a third laser photon in a pump−probe experiment, it was possible to quench the collective ICD by ionizing one or both of the excitons before the decay. By observing the reappearance of the collective ICD band as a function of pump−probe delay, the decay time could be measured as 6.5 ps.[286]

A collective ICD-like energy exchange between two highly excited neutral atoms was also used to explain a characteristic feature in the electron spectrum of Ar clusters heated by near-infrared laser pulses.[219]

5.7.4. Intramolecular ICD-like Decay Amplitudes in Molecules. By definition, ICD and ETMD are de-excitation processes in weakly bound systems. In covalently bonded systems, radiationless decay amplitudes are dominated by orbital overlap, and models like the virtual photon exchange shown in Figure 1 lose their meaning. It is appropriate then simply to speak of local Auger decay. The reader will have seen, however, at this point that real world cases of ICD often are not sharply either one or the other, one example being the O 1*s* decay in liquid water. For this system, in the inset of Figure 45, we have presented the decomposition of the radiationless decay amplitude into contributions from Auger decay, ICD and ETMD. Formally, the same type of analysis can be applied to molecular systems and is meaningful, for example, for molecules containing an ionized center with strongly electronegative ligands binding to it. Examples investigated experimentally are fluorine-containing molecules, such as SiF_4, XeF_2,[386,518] and the aforementioned SF_6[277] (see Section 5.1.8). For the Si L-shell decay of SiF_4, the lifetime was measured as the Lorentzian broadening of the Si 2*p* photoline and was compared to SiH_4. The figure found for SiF_4, 79 meV, exceeds the one found for SiH_4 by more than a factor of 2, and the expectation from a simple one-center model of Auger decay by more than a factor of 5. As the model was appropriate for SiH_4, a strong increase of the decay rate by nonlocal decay amplitudes was surmised.

A deeper theoretical investigation of these ideas was carried out for the Xe fluorides (XeF_2, XeF_4, XeF_6)[25] A summary of this work was given earlier:[10] A population analysis of the two-hole states showed the increasing importance of fluorine vacancies for dicationic states in $XeF_{4,6}$. In a second step the character of the Auger transition amplitudes after creation of a Xe 4*d*-vacancy was analyzed. All amplitudes were expanded into a set of atomic basis functions, and thus expressed as some "transition strength" (basically the square of the atomic decay matrix element) times the respective population numbers. Each term in this expansion can be grouped into one of the four categories, local decay, ICD, EMTD(2) and ETMD(3). Using the further assumption that the transition strengths are different between each category, but identical for all individual transitions within one category, it was possible to arrive at the relative importance of each type of transition. Owing to their local or nonlocal character, respectively, the transition strengths behaved as (local decay) > ICD > EMTD(2, 3). An impressive trend showed up when population numbers and transitions strengths were combined. Already in XeF_2, ICD-like amplitudes clearly dominate over the local ones, and are in XeF_4 and XeF_6 even superseded by ETMD(3).[25] A main ingredient underlying these findings is the nature of the strongly electronegative ligands; in most other molecules, Auger decay is a mainly local process as stated above.

One of these systems, XeF_2, was also investigated experimentally.[518] After exciting a K-shell electron of Xe into an antibonding orbital, the authors measured the total ionic charge of the fragments and found it to be higher than after K-shell ionization of isolated Xe. This was interpreted as an evidence for the presence of the ICD- and ETMD-like decay amplitudes discussed above.

An extended study of the 1*s*, 2*s*, and 2*p* core hole lifetime broadening in SiX_4 (X = F, Cl, Br, CH_3) was carried out recently.[387] The trend to an anomalously high lifetime broadening of SiF_4 prevailed for all core hole states that were measured. The authors also estimated the factors driving Auger, ICD, and ETMD in the model proposed by Buth et al., and concluded that ETMD-like amplitudes are indeed important in SiF_4.

Another fluorine containg molecule is SF_6, which was investigated in an electron−electron coincidence experiment.[277] These authors used a laboratory source based on emission of a He plasma. As they were thus limited in photon energy to 48.4 eV, only the outer-valence double ionization spectrum could be probed. By theoretical analysis the authors were able to show that it partly is produced by autoionization of F $2s^{-1}$, which are sufficiently high in energy to allow a

https://dx.doi.org/10.1021/acs.chemrev.0c00106
Chem. Rev. 2020, 120, 11295−11369

transition into a dicationic state with vacancies distributed over two different F atoms.

5.7.5. ICD at the Surface of a Solid. Quantum dots are one example of a system in the solid state of matter, in which ICD plays a role. Ice films are another interesting candidate for research on ICD, and probing the surface should give an opportunity to directly detect desorbed decay fragments. Grieves and Orlando described results of an experiment, in which they cryogenically adsorbed water layers either directly on the surface of highly ordered polycrystalline graphite (HOPG), or on a condensed rare gas film consisting of 10−20 monolayers of Ar, Kr or Xe, and acting as a spacer between water and the HOPG.[519] Water coverage was kept at half a monolayer, leading to formation of water islands. A pulsed electron gun with variable energy was used to excite the water film. Under this bombardment, protonated water clusters could be detected by mass spectroscopy. The onset of cluster desorption was measured as a function of electron beam energy, and varied slightly between the different rare gas species applied on the surface. In their study, the authors correlated the energy of the fragment onset with the estimated threshold energy for ICD between a center in the rare gas film and one in a water island. Desorption of a complete island after this process was assumed. All measured threshold values were lower than the $2a_1$-threshold in water; it was therefore concluded that ICD proceeded by creation of an inner-valence vacancy in the rare gas film, followed by outer-valence ionization of the condensed water island and Coulomb-driven desorption was observed.

For electron collisions with surfaces, ICD is mainly relevant as a de-excitation mechanism for excited states created by the exposure of the substrate to the electron beam. In contrast to that, in ion collision with surfaces the projectile itself can become a part of a relaxation process involving charge or energy transfer. Already in the 1950s, ejected electron spectra due to the neutralization of a rare gas ion on a bulk metal surface were measured and explained by a transition, in which a conduction band electron fills the ion's vacancy, and another electron is ejected from the metal by transfer of the relaxation energy.[520] The same author also described direct and exchange transition diagrams for de-excitation of a neutral excited ion at a metal surface, leading again to emission from the conduction band.[521] This technique was then termed 'Auger neutralization spectroscopy'. Similar to our comparison of Penning ionization to ICD in Section 2.5, these transitions take place in the same way as ICD or ETMD with respect to the excitation, de-excitation and ionization steps at the respective sites, but involve a collisional process and not a transition at an, initially, fixed geometry.

More recent work described impact of highly charged ions (HCI) on graphene.[47] Xe^{30+} was used as a projectile, for example. The experiments were carried out by extracting HCIs from an electron beam ion trap, and decelerating them to energies between 10 and 150 keV. The HCI beam was then guided onto a graphene film, stabilized by a metal grid with μm-sized holes, commonly used in transmission electron microscopy. Highly charged ions were neutralized by passage through the graphene, and the neutralization process was monitored by measuring the resulting charge states in an electrostatic analyzer. Depending on the HCI species, between 8 and 27 electrons are picked up during the passage. Several models have been tested by the authors to explain the neutralization rate. They concluded that in a first step a large number of electrons are captured into vacant Rydberg states of the HCI already when it approaches the surface (panel a in Figure 62). Those are de-excited within less than 10 fs by an

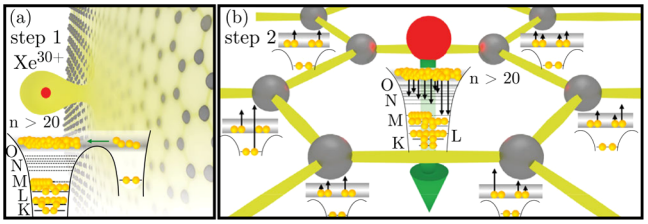

Figure 62. ICD-like de-excitation of a highly charged ion (red) via the passage through a graphene foil. Reprint with permission from ref 47. Copyright 2017 APS.

ICEC/ICD-like process, exchanging energy with the graphene substrate (panel b in Figure 62). A model to describe the de-excitation process with quantitative accuracy and predictive power toward materials research was presented recently.[48]

Another decay process in the solid state was discussed in several works starting in the 1970s.[522] These authors attempted to explain the Auger lifetime broadening in, for example, metal oxides, such as MgO. They surmised that oxygen orbitals can get involved in the decay of Mg 2p vacancies, and termed this hypothetical transition "interatomic Auger decay". To quantify their model they presented an analytical formula similar to eq 12, later rederived in the context of ICD research.[9] It contains for example the characteristic R^{-6} distance dependence of the decay rate.[522] How well it actually applies to the oxide systems in which the authors were originally interested, or to any solid, could not be fully clarified. Ionic crystals, for example, LiF, were explicitly mentioned, and due to the presence of the fluorine ligands here we see the closest analogy to ICD.

6. GENERAL INSIGHTS, OUTLOOK, AND FUTURE PERSPECTIVES

Many energy transfer processes are known to exist in matter; however, interatomic or intermolecular Coulombic decay (ICD) stands out in several aspects. ICD is a nonlocal deactivation process and occurs when the initial electronic excitation energy of an molecule is insufficient to ionize itself, but enough to ionize a loosely bound neighboring molecule. Therefore, ICD is the more efficient the more neighboring ionizable molecules are present. Further, ICD is ultrafast as it does not depend on nuclear motion and the energy is transferred via the electronic Coulomb interaction alone rather than in form of kinetic energy of massive particles. The energy is transferred via virtual photon exchange or, at short distances, also via an electron exchange contribution. ICD is extremely general because it is not limited to bound states or resonances of the system, but in most cases leads to continuum electrons with a continuous energy distribution. In general, when an ICD channel is open, the speed of ICD makes it the dominating process quenching all other radiative or non-radiative relaxation channels.

A further aspect adding to the generality and impact of ICD is its invariance with respect to the excitation step. In practice this is of great importance as it allows ICD to be present in diverse scenarios such as photon impact, charged particle impact or basically all other excitation processes in nature. These general aspects of ICD make it omnipresent in nature

https://dx.doi.org/10.1021/acs.chemrev.0c00106
Chem. Rev. 2020, 120, 11295−11369

across a large array of systems, ranging from rare gas clusters and water to hydrogen bonded complexes in general ranging to solid state systems and biology.

Where to go further? A number of topics have already been addressed briefly in this review, which indicate the large potential in studying ICD processes and which open new and promising avenues of research. Clearly, the investigation of more complex systems deserves to be intensified, in particular, of larger molecules, quantum dot, and quantum well arrays and nanoparticles. There is only a single example of ICD in fullerenes investigated so far and much more can be expected. Here, the impact of plasmons in strengthening ICD processes has been indicated, but has not been understood and quantified yet. ICD has been shown to quench other processes, for example, photodissociation. Hence, there is much room and need for further studying its role in the quenching, or in other words steering, of various popular processes. Intensifying and weakening ICD by varying the pH value of the environment is only one way of controlling ICD, and the search for further ways of control represents an interesting and relevant subject of research. Other examples of utilizing ICD are the development of ICD spectroscopy as tool to study the composition of local environments, and the development of sensors using quantum dots or well arrays.

A potential technological application of ICD in the realm of semiconductor physics has been outlined in Section 5.5. Long range energy transfer processes mediated by the Coulomb interaction are, however, present in devices already today. One example includes quantum dot solar cells, in which the tunable absorption properties of QDs are used to enhance the efficiency by which the solar radiation is used.[523] Ultrafast charge injection into a carrier is one way of producing a usable current in the device, but alternatively also energy transfer processes into a substrate have been discussed. Those are conventionally termed FRET,[524] but often occur into a broad band of electronic states, so that a practical distinction to ICD is difficult.

An important additional point concerns the chemistry which follows the ICD in matter after irradiation. ICD produces reactive radical species and low energy electrons, which are important species in causing radiation damage. Integrating ICD and the follow up chemistry into the description of radiation damage poses an outstanding problem. All of these call for future investment.

Since the ICD family including ETMD and ICEC is made up of processes abundant in nature, a major future perspective is the investigation of these processes *in situ*. This includes the development of experimental methods to identify and quantify the effects in various media present in nature. Of course, this goes hand in hand with the development of theoretical and computational tools indispensable for analyzing and simulating the experimental findings. We will not be surprised if during this endeavor new members of the ICD family will be discovered. It is by now apparent that nature uses the respective mechanisms to reduce or enhance the damage created by ionizing radiation. Of particular interest, therefore, is to exploit the accumulated knowledge, for instance, in designing strategies to manipulate and control these processes for medical and technological purposes.

AUTHOR INFORMATION

Corresponding Authors

Till Jahnke − *Institut für Kernphysik, Goethe Universität, 60438 Frankfurt, Germany*; Email: jahnke@atom.uni-frankfurt.de

Andreas Dreuw − *Interdisciplinary Center for Scientific Computing, Ruprecht-Karls University, 69120 Heidelberg, Germany*; orcid.org/0000-0002-5862-5113; Email: dreuw@uni-heidelberg.de

Authors

Uwe Hergenhahn − *Fritz-Haber-Institut der Max-Planck-Gesellschaft, 14195 Berlin, Germany; Max Planck Institute for Plasma Physics, 17491 Greifswald, Germany; Leibniz Institute of Surface Engineering (IOM), 04318 Leipzig, Germany*; orcid.org/0000-0003-3396-4511

Bernd Winter − *Fritz-Haber-Institut der Max-Planck-Gesellschaft, 14195 Berlin, Germany*; orcid.org/0000-0002-5597-8888

Reinhard Dörner − *Institut für Kernphysik, Goethe Universität, 60438 Frankfurt, Germany*

Ulrike Frühling − *Institut für Experimentalphysik and Center for Ultrafast Imaging, Universität Hamburg, 22761 Hamburg, Germany*

Philipp V. Demekhin − *Institut für Physik und CINSaT, Universität Kassel, 34132 Kassel, Germany*

Kirill Gokhberg − *Physical-Chemistry Institute, Ruprecht-Karls University, 69120 Heidelberg, Germany*

Lorenz S. Cederbaum − *Physical-Chemistry Institute, Ruprecht-Karls University, 69120 Heidelberg, Germany*; orcid.org/0000-0002-4598-0650

Arno Ehresmann − *Institut für Physik und CINSaT, Universität Kassel, 34132 Kassel, Germany*

André Knie − *Institut für Physik und CINSaT, Universität Kassel, 34132 Kassel, Germany*; orcid.org/0000-0002-2208-8838

Complete contact information is available at: https://pubs.acs.org/10.1021/acs.chemrev.0c00106

Notes

The authors declare no competing financial interest.

Biographies

Till Jahnke received his Ph.D. in Physics from the Goethe University Frankfurt in 2005. He became a Professor for experimental atomic physics in Frankfurt in 2017. His research interests cover the investigation of quantum dynamics in atoms and molecules employing synchrotron radiation, intense laser fields, and (X-ray) free-electron laser light.

Uwe Hergenhahn received his Ph.D. in Experimental Physics from the Technical University of Berlin in 1996. He worked at the Fritz-Haber-Institut before joining the Max Planck Institute for Plasma Physics in a staff scientist position. After a researcher position at Leibniz Institute of Surface Engineering (IOM), in 2020 he returned to the Fritz-Haber-Institut, Molecular Physics Department. His research interests are in the electron dynamics of clusters and liquids.

Bernd Winter received his Ph.D. in physics from the Freie Universität Berlin and the Fritz-Haber-Institut, Germany, and worked as a postdoc at Argonne National Laboratory, U.S.A., and at the Institut für Plasmaphysik in Garching, Germany. In the mid-1990s, he joined the Max-Born-Institut, Berlin for Nonlinear Optics, where he was a staff researcher until 2009, when he transferred to BESSY, now

https://dx.doi.org/10.1021/acs.chemrev.0c00106
Chem. Rev. 2020, 120, 11295−11369

Helmholtz-Zentrum Berlin. Currently, Winter is a Group Leader at the Fritz-Haber-Institut, Molecular Physics Department, and his research interests include liquid-jet photoelectron spectroscopy and the electronic structure of aqueous solutions.

Reinhard Dörner received his Ph.D. in Physics from Goethe University Frankfurt in 1991 in the group of Prof. Horst Schmidt-Böcking. He worked as a postdoc at the Lawrence Berkeley National Laboratory. Since 2002, he is a full Professor at the physics department of Goethe University Frankfurt. His research interest comprise multiparticles coincidence experiments and the development of the COLTRIMS Reaction Microscopes. With these tools, he studies ion collisions and light−matter interaction with femtosecond lasers, synchrotron radiation, and free-electron lasers.

Ulrike Frühling received her Ph.D. in Physics from the University of Hamburg in 2009. She became a Junior Professor for experimental physics in Hamburg in 2013. Her research interests cover the investigation of ultrafast dynamics in atoms and molecules employing free-electron lasers and laser-based light sources.

Philipp Demekhin received his Ph.D. in Physics in the Rostov State University in 2000 (now Southern Federal University in Russia). He made Habitation in Physics and worked as Assistant Professor in the Rostov State Transport University until 2008. After postdoctoral stays in the Universities of Kassel and Heidelberg, he joined the University of Kassel in 2013, first as a Junior-Professor and then as apl.-Professor for Theoretical Atomic and Molecular Physics. His research interests are spread over the wide range of fundamental aspects of light−matter interaction in the area of ultrafast electron and nuclear dynamics of correlated systems driven by electromagnetic pulses.

Kirill Gokhberg received his Ph.D. in Theoretical Chemistry in 2008 from Heidelberg University and completed his habilitation there in 2020. Since 2009, he is a group leader at the Institute of Theoretical Chemistry, Heidelberg University. His research interests comprise electronic processes in chemical media, theoretical electron spectroscopy, and the development of *ab initio* methods for computing electronic resonances.

Lorenz Cederbaum completed his doctoral studies in Chemistry in 1972 and completed his habilitation in Physics in 1976, both at the Technical University of Munich. In 1976, he joined the University of Freiburg as an Associate Professor of Physics, and in 1979, he moved to the University of Heidelberg as Professor of Theoretical Chemistry. Since 2017, he occupies the position of Senior Professor for Theoretical Chemistry at the University of Heidelberg. He is a member of the Leopoldina National Academy of Sciences and of the International Academy of Quantum Molecular Science and is Visiting Distinguished Professor at the Technion in Haifa, Israel. He received two ERC Advanced Investigators Grants (2008, 2016) towards the study of ICD, and ETMD and ICEC and other related interatomic processes. He was awarded honorary doctorates in 2009 from Sofia University (Bulgaria), in 2012 from the Technion, Israel Institute of Technology, and in 2016 from the University of Debrecen (Hungary). Among others, his research areas comprise the study of phenomena of electron correlation in molecules, clusters, and solids; multimode nuclear dynamics in molecules including conical intersections; atoms, and molecules in strong fields; Bose−Einstein condensation; and ultrafast electronic processes in chemical media.

Arno Ehresmann received his Ph.D. in Experimental Physics from Kaiserslautern University in 1994. After a 1.5-year postdoc at the Department of Chemistry, Tokyo Institute of Technology, he worked for two years in a management position for a private company. With a DFG scholarship for Habilitation, he returned to Kaiserslautern University in 1999. Since 2005, he holds a chair for Functional Thin Films and Physics with Synchrotron Radiation at the Institute of Physics, Kassel University. His research interests comprise research on magnetic patterning in magnetic thin film systems by light ions for sensing devices and lab-on-chip systems as well as research on electron correlations and quantum mechanical effects in atomic, molecular, cluster, and liquid systems with photon and electron spectroscopies.

André Knie received his Ph.D. in experimental physics in 2012 from Kassel University. He currently leads the group *physics with synchrotron radiation* at the Kassel University. Atoms, molecules, clusters, and liquids excited by interactions with synchrotron radiation, free-electron-lasers, electron, and heavy ion impact are his field of research. His primary tools are coincident angle resolved photon and photoelectron spectroscopy. Recently, he introduced machine learning as a new path for data evaluation in multiparameter studies and focuses on interactions of atoms and molecules with weakly bound environments.

Andreas Dreuw received his Ph.D. in Theoretical Chemistry from Heidelberg University in 2001. After a two-year postdoc at the UC Berkeley, he joined the Goethe University of Frankfurt first as an Emmy-Noether fellow and then as a Heisenberg-Professor for Theoretical Chemistry. Since 2011, Andreas Dreuw holds the chair for Theoretical and Computational Chemistry at the Interdisciplinary Center for Scientific Computing of Heidelberg University. His research interests comprise the development of electronic structure methods and their application in Photochemistry, Mechanochemistry, Biophysics, and Material Science.

ACKNOWLEDGMENTS

This work was supported by the Deutsche Forschungsgemeinschaft (DFG) as part of the DFG research unit 'Interatomic and Intermolecular Coulombic Decay' (FOR1789 and FOR1789/II). All authors acknowledge the valuable contributions made by our associate members and colleagues including Vitali Averbukh, Annika Bande, Olle Björneholm, Andreas Hans, Přemysl Kolorenč, Nikolai V. Kryzhevoi, Adrian L. Dempwolff, Alexander I. Kuleff, Melanie Mucke, Clemens Richter, Horst Schmidt-Böcking, Nicolas Sisourat, Petr Slavíček, Stephan Thürmer, Florian Trinter, Kiyoshi Ueda, Isaak Unger, and Joshua B. Williams. Some of the authors thank HZB for the allocation of synchrotron radiation beamtime. LSC is thankful for support by the European Research Council (Advanced Investigator Grant Nos. 227597 and 692657).

REFERENCES

(1) Cederbaum, L. S.; Zobeley, J.; Tarantelli, F. Giant InterMolecular Decay and Fragmentation of Clusters. *Phys. Rev. Lett.* **1997**, *79*, 4778−4781.
(2) Jahnke, T.; Czasch, A.; Schöffler, M. S.; Schössler, S.; Knapp, A.; Käsz, M.; Titze, J.; Wimmer, C.; Kreidi, K.; Grisenti, R. E.; et al. Experimental Observation of Interatomic Coulombic Decay in Neon Dimers. *Phys. Rev. Lett.* **2004**, *93*, 163401.
(3) Marburger, S.; Kugeler, O.; Hergenhahn, U.; Möller, T. Experimental Evidence for Interatomic Coulombic Decay in Ne Clusters. *Phys. Rev. Lett.* **2003**, *90*, 203401.
(4) Öhrwall, G.; Tchaplyguine, M.; Lundwall, M.; Feifel, R.; Bergersen, H.; Rander, T.; Lindblad, A.; Schulz, J.; Peredkov, S.; Barth, S.; et al. Femtosecond Interatomic Coulombic Decay in Free Neon Clusters: Large Lifetime Differences between Surface and Bulk. *Phys. Rev. Lett.* **2004**, *93*, 173401.
(5) Zobeley, J.; Cederbaum, L. S.; Tarantelli, F. InterMolecular Coulombic Decay of Molecular Clusters: Identification of the Decay

https://dx.doi.org/10.1021/acs.chemrev.0c00106
Chem. Rev. 2020, 120, 11295−11369

Mechanism Using a New Hole-Population Analysis. *J. Phys. Chem. A* **1999**, *103*, 11145−11160.
(6) Zobeley, J.; Cederbaum, L. S.; Tarantelli, F. Highly Excited Electronic States of Molecular Clusters and their Decay. *J. Chem. Phys.* **1998**, *108*, 9737−9750.
(7) Santra, R.; Cederbaum, L. S. Non-Hermitian Electronic Theory and Applications to Clusters. *Phys. Rep.* **2002**, *368*, 1−117.
(8) Jahnke, T.; Czasch, A.; Schöffler, M.; Schössler, S.; Käsz, M.; Titze, J.; Kreidi, K.; Grisenti, R. E.; Staudte, A.; Jagutzki, O.; et al. Experimental Separation of Virtual Photon Exchange and Electron Transfer in Interatomic Coulombic Decay of Neon Dimers. *Phys. Rev. Lett.* **2007**, *99*, 153401.
(9) Averbukh, V.; Müller, I. B.; Cederbaum, L. S. Mechanism of Interatomic Coulombic Decay in Clusters. *Phys. Rev. Lett.* **2004**, *93*, 263002.
(10) Hergenhahn, U. Interatomic and InterMolecular Coulombic Decay: The Early Years. *J. Electron Spectrosc. Relat. Phenom.* **2011**, *184*, 78−90.
(11) Hergenhahn, U. Production of Low Kinetic Energy Electrons and Energetic Ion Pairs by Intermolecular Coulombic Decay. *Int. J. Radiat. Biol.* **2012**, *88*, 871−883.
(12) Jahnke, T. Interatomic and Intermolecular Coulombic Decay: the Coming of Age Story. *J. Phys. B: At., Mol. Opt. Phys.* **2015**, *48*, 082001.
(13) Averbukh, V.; Demekhin, P. V.; Kolorenč, P.; Scheit, S.; Stoychev, S. D.; Kuleff, A. I.; Chiang, Y.-C.; Gokhberg, K.; Kopelke, S.; Sisourat, N.; et al. Interatomic Electronic Decay Processes in Singly and Multiply Ionized Clusters. *J. Electron Spectrosc. Relat. Phenom.* **2011**, *183*, 36−47.
(14) Dias, A. M. Interatomic Coulombic Decay: a Short Review. *Braz. J. Phys.* **2009**, *39*, 523−524.
(15) Saito, N.; Liu, X.-J.; Morishita, Y.; Suzuki, I. H.; Ueda, K. Electron-Ion Multiple Coincidence Spectroscopy for Small Molecules and Clusters. *J. Electron Spectrosc. Relat. Phenom.* **2007**, *156−158*, 68.
(16) Ueda, K. Photoemission and Coincidence Studies on Gas-phase Molecules. *Appl. Phys. A: Mater. Sci. Process.* **2008**, *92*, 487−494.
(17) Björneholm, O.; Öhrwall, G.; Tchaplyguine, M. Free Clusters Studied by Core-Level Spectroscopies. *Nucl. Instrum. Methods Phys. Res., Sect. A* **2009**, *601*, 161−181.
(18) Tchaplyguine, M.; Öhrwall, G.; Björneholm, O. In *Photoelectron Spectroscopy of Free Clusters*; Sattler, K. D., Ed.; CRC Press, 2011; pp 7−1.
(19) Frühling, U.; Trinter, F.; Karimi, F.; Williams, J. B.; Jahnke, T. Time-Resolved Studies of Interatomic Coulombic Decay. *J. Electron Spectrosc. Relat. Phenom.* **2015**, *204*, 237−244.
(20) Meitner, L. Über Die β-Strahl-Spektra und ihren Zusammenhang mit der γ-Strahlung. *Eur. Phys. J. A* **1922**, *11*, 35−54.
(21) Auger, P. Sur l'effet Photoélectrique Composé. *J. Phys. Radium* **1925**, *6*, 205−208.
(22) Averbukh, V.; Cederbaum, L. S. Calculation of Interatomic Decay Widths of Vacancy States Delocalized due to Inversion Symmetry. *J. Chem. Phys.* **2006**, *125*, 094107.
(23) Ouchi, T.; Sakai, K.; Fukuzawa, H.; Liu, X.-J.; Higuchi, I.; Tamenori, Y.; Nagaya, K.; Iwayama, H.; Yao, M.; Zhang, D.; et al. Three-Electron Interatomic Coulombic Decay from the Inner-Valence Double-Vacancy States in NeAr. *Phys. Rev. Lett.* **2011**, *107*, 053401.
(24) Zobeley, J.; Santra, R.; Cederbaum, L. S. Electronic Decay in Weakly Bound Heteroclusters: Energy Transfer versus Electron Transfer. *J. Chem. Phys.* **2001**, *115*, 5076−5088.
(25) Buth, C.; Santra, R.; Cederbaum, L. S. Impact of Interatomic Electronic Decay Processes on Xe 4d Hole Decay in the Xenon Fluorides. *J. Chem. Phys.* **2003**, *119*, 10575−10584.
(26) Förstel, M.; Mucke, M.; Arion, T.; Bradshaw, A. M.; Hergenhahn, U. Autoionization Mediated by Electron Transfer. *Phys. Rev. Lett.* **2011**, *106*, 033402.
(27) Pernpointner, M.; Kryzhevoi, N. V.; Urbaczek, S. Possible Electronic Decay Channels in the Ionization Spectra of Small Clusters Composed of Ar and Kr: A Four-Component Relativistic Treatment. *J. Chem. Phys.* **2008**, *129*, 024304.
(28) Sakai, K.; Stoychev, S.; Ouchi, T.; Higuchi, I.; Schöffler, M.; Mazza, T.; Fukuzawa, H.; Nagaya, K.; Yao, M.; Tamenori, Y.; et al. Electron-Transfer-Mediated Decay and Interatomic Coulombic Decay from the Triply Ionized States in Argon Dimers. *Phys. Rev. Lett.* **2011**, *106*, 033401.
(29) Kreidi, K.; Jahnke, T.; Weber, T.; Havermeier, T.; Liu, X.; Morisita, Y.; Schössler, S.; Schmidt, L.; Schöffler, M.; Odenweller, M.; et al. Relaxation Processes Following 1s Photoionization and Auger Decay in Ne_2. *Phys. Rev. A: At., Mol., Opt. Phys.* **2008**, *78*, 043422.
(30) Hoener, M.; Bostedt, C.; Schorb, S.; Thomas, H.; Foucar, L.; Jagutzki, O.; Schmidt-Böcking, H.; Dörner, R.; Möller, T. From Fission to Explosion: Momentum-Rresolved Survey over the Rayleigh Instability Barrier. *Phys. Rev. A: At., Mol., Opt. Phys.* **2008**, *78*, No. 021201(R).
(31) Pohl, M. N.; Richter, C.; Lugovoy, E.; Seidel, R.; Slavíček, P.; Aziz, E. F.; Abel, B.; Winter, B.; Hergenhahn, U. Sensitivity of Electron Transfer Mediated Decay to Ion Pairing. *J. Phys. Chem. B* **2017**, *121*, 7709−7715.
(32) Stumpf, V.; Kolorenč, P.; Gokhberg, K.; Cederbaum, L. S. Efficient Pathway to Neutralization of Multiply Charged Ions Produced in Auger Processes. *Phys. Rev. Lett.* **2013**, *110*, 258302.
(33) Stumpf, V.; Kryzhevoi, N. V.; Gokhberg, K.; Cederbaum, L. S. Enhanced One-Photon Double Ionization of Atoms and Molecules in an Environment of Different Species. *Phys. Rev. Lett.* **2014**, *112*, 193001.
(34) Slavíček, P.; Winter, B.; Cederbaum, L. S.; Kryzhevoi, N. V. Proton-Transfer Mediated Enhancement of Non-Local Electronic Relaxation Processes in X-ray Irradiated Liquid Water. *J. Am. Chem. Soc.* **2014**, *136*, 18170−18176.
(35) Gokhberg, K.; Cederbaum, L. S. Environment Assisted Electron Capture. *J. Phys. B: At., Mol. Opt. Phys.* **2009**, *42*, 231001.
(36) Gokhberg, K.; Cederbaum, L. S. Interatomic Coloumbic Electron Capture. *Phys. Rev. A: At., Mol., Opt. Phys.* **2010**, *82*, 052707.
(37) Sisourat, N.; Miteva, T.; Gorfinkiel, J. D.; Gokhberg, K.; Cederbaum, L. S. Interatomic Coulombic Electron Capture from First Principles. *Phys. Rev. A: At., Mol., Opt. Phys.* **2018**, *98*, No. 020701(R).
(38) Müller, C.; Voitkiv, A. B.; Crespo López-Urrutia, J. R.; Harman, Z. Strongly Enhanced Recombination via Two-Center Electronic Correlations. *Phys. Rev. Lett.* **2010**, *104*, 233202.
(39) Voitkiv, A. B.; Najjari, B. Two-Center Dielectronic Recombination and Resonant Photoionization. *Phys. Rev. A: At., Mol., Opt. Phys.* **2010**, *82*, 052708.
(40) Eckey, A.; Jacob, A.; Voitkiv, A. B.; Muller, C. Resonant Electron Scattering and Dielectronic Recombination in Two-Center Atomic Systems. *Phys. Rev. A: At., Mol., Opt. Phys.* **2018**, *98*, 012710.
(41) Jacob, A.; Müller, C.; Voitkiv, A. B. Two-Center Dielectronic Recombination in Slow Atomic Collisions. *Phys. Rev. A: At., Mol., Opt. Phys.* **2019**, *100*, 012706.
(42) Jacob, A.; Müller, C.; Voitkiv, A. B. Interatomic Coulombic Electron Capture in Slow Atomic Collisions. *J. Phys. B: At., Mol. Opt. Phys.* **2019**, *52*, 225201.
(43) Pont, F. M.; Bande, A.; Cederbaum, L. S. Controlled Energy-Selected Electron Capture and Release in Double Quantum Dots. *Phys. Rev. B: Condens. Matter Mater. Phys.* **2013**, *88*, 241304.
(44) Pont, F. M.; Bande, A.; Cederbaum, L. S. Electron-Correlation Driven Capture and Release in Double Quantum Dots. *J. Phys.: Condens. Matter* **2016**, *28*, 075301.
(45) Pont, F. M.; Molle, A.; Berikaa, E. R.; Bubeck, S.; Bande, A. Predicting the Performance of the Inter-Coulombic Electron Capture from Single-Electron Quantities. *J. Phys.: Condens. Matter* **2020**, *32*, 065302.
(46) Molle, A.; Berikaa, E. R.; Pont, F. M.; Bande, A. Quantum Size Effect Affecting Environment Assisted Electron Capture in Quantum Confinements. *J. Chem. Phys.* **2019**, *150*, 224105.
(47) Wilhelm, R. A.; Gruber, E.; Schwestka, J.; Kozubek, R.; Madeira, T. I.; Marques, J. P.; Kobus, J.; Krasheninnikov, A. V.; Schleberger, M.; et al. Interatomic Coulombic Decay: The

https://dx.doi.org/10.1021/acs.chemrev.0c00106
Chem. Rev. 2020, 120, 11295−11369

Mechanism for Rapid Deexcitation of Hollow Atoms. *Phys. Rev. Lett.* **2017**, *119*, 103401.
(48) Wilhelm, R. A.; Grande, P. L. Unraveling Energy Loss Processes of Low Energy Heavy Ions in 2D Materials. *Commun. Phys.* **2019**, *2*, 89−96.
(49) Schwestka, J.; Niggas, A.; Creutzburg, S.; Kozubek, R.; Heller, R.; Schleberger, M.; Wilhelm, R. A.; Aumayr, F. Charge-Exchange-Driven Low-Energy Electron Splash Induced by Heavy Ion Impact on Condensed Matter. *J. Phys. Chem. Lett.* **2019**, *10*, 4805−4811.
(50) Tiedtke, K.; Azima, A.; von Bargen, N.; Bittner, L.; Bonfigt, S.; Düsterer, S.; Faatz, B.; Frühling, U.; Gensch, M.; Gerth, C.; et al. The Soft X-ray Free-Electron Laser FLASH at DESY: Beamlines, Diagnostics and End-Stations. *New J. Phys.* **2009**, *11*, 023029.
(51) Kuleff, A. I.; Gokhberg, K.; Kopelke, S.; Cederbaum, L. S. Ultrafast Interatomic Electronic Decay in Multiply Excited Clusters. *Phys. Rev. Lett.* **2010**, *105*, 043004.
(52) Müller, C.; Voitkiv, A. B. Resonant Two-Photon Single Ionization of Two Identical Atoms. *Phys. Rev. Lett.* **2011**, *107*, 013001.
(53) Ovcharenko, Y.; Lyamayev, V.; Katzy, R.; Devetta, M.; LaForge, A.; O'Keeffe, P.; Plekan, O.; Finetti, P.; Di Fraia, M.; Mudrich, M.; et al. Novel Collective Autoionization Process Observed in Electron Spectra of He Clusters. *Phys. Rev. Lett.* **2014**, *112*, 073401.
(54) You, D.; Fukuzawa, H.; Sakakibara, Y.; Takanashi, T.; Ito, Y.; Maliyar, G. G.; Motomura, K.; Nagaya, K.; Nishiyama, T.; Asa, K.; et al. Charge Transfer to Ground-State Ions Produces Free Electrons. *Nat. Commun.* **2017**, *8*, 14277−14282.
(55) Johnsen, R.; Biondi, M. A. Measurements of Radiative Charge-Transfer Reactions of Doubly and Singly Charged Rare-Gas Ions with Rare-Gas Atoms at Thermal Energies. *Phys. Rev. A: At., Mol., Opt. Phys.* **1978**, *18*, 996.
(56) Cohen, J. S.; Bardsley, J. N. Calculation of Radiative Single-Charge-Transfer Cross Sections for Collisions of He^{2+} with He at Low Energy. *Phys. Rev. A: At., Mol., Opt. Phys.* **1978**, *18*, 1004.
(57) Saito, N.; Morishita, Y.; Suzuki, I. H.; Stoychev, S. D.; Kuleff, A. I.; Cederbaum, L. S.; Liu, X.-J.; Fukuzawa, H.; Prümper, G.; Ueda, K. Evidence of Radiative Charge Transfer in Argon Dimers. *Chem. Phys. Lett.* **2007**, *441*, 16−19.
(58) Kreidi, K.; Jahnke, T.; Weber, T.; Havermeier, T.; Grisenti, R. E.; Liu, X.-J.; Morisita, Y.; Schössler, S.; Schmidt, L.; Schöffler, M.; et al. Localization of Inner-Shell Photoelectron Emission and Interatomic Coulombic Decay in Ne_2. *J. Phys. B: At., Mol. Opt. Phys.* **2008**, *41*, 101002.
(59) Yan, S.; Zhang, P.; Ma, X.; Xu, S.; Li, B.; Zhu, X. L.; Feng, W. T.; Zhang, S. F.; Zhao, D. M.; Zhang, R.; et al. Observation of Interatomic Coulombic Decay and Electron-Transfer-Mediated Decay in High-Energy Electron-Impact Ionization of Ar_2. *Phys. Rev. A: At., Mol., Opt. Phys.* **2013**, *88*, 042712.
(60) Higuchi, I.; Ouchi, T.; Sakai, K.; Fukuzawa, H.; Liu, X.-J.; Ueda, K.; Iwayama, H.; Nagaya, K.; Yao, M.; Ding, D.; et al. Radiative Charge Transfer and Interatomic Coulombic Decay Following Direct Double Photoionization of Neon Dimers. *J. Phys.: Conf. Ser.* **2010**, *235*, 012015.
(61) Hans, A.; Stumpf, V.; Holzapfel, X.; Wiegandt, F.; Schmidt, P.; Ozga, C.; Reiß, P.; Ltaief, L. B.; Küstner-Wetekam, C.; Jahnke, T.; et al. Direct Evidence for Radiative Charge Transfer after Inner-Shell Excitation and Ionization of Large Clusters. *New J. Phys.* **2018**, *20*, 012001.
(62) Hans, A.; Miteva, T.; Holzapfel, X.; Ozga, C.; Schmidt, P.; Otto, H.; Hartmann, G.; Richter, C.; Sisourat, N.; Ehresmann, A.; et al. Electronic Decay of Singly Charged Ground-State Ions by Charge Transfer via van der Waals Bonds. *Phys. Rev. Lett.* **2019**, *123*, 213001.
(63) Förster, T. Zwischenmolekulare Energiewanderung und Fluoreszenz. *Ann. Phys.* **1948**, *437*, 55−75.
(64) Dexter, D. L. A. Theory of Sensitized Luminescence in Solids. *J. Chem. Phys.* **1953**, *21*, 836−850.
(65) Balzani, V. *Electron Transfer in Chemistry*; Wiley-VCH: Weinheim, Germany, 2001.
(66) Natali, M.; Campagna, S.; Scandola, F. Photoinduced Electron Transfer across Molecular Bridges: Electron- and Hole-Transfer Superexchange Pathways. *Chem. Soc. Rev.* **2014**, *43*, 4005−4018.
(67) Penning, F. M. Über Ionisation durch Metastabile Atome. *Naturwissenschaften* **1927**, *15*, 818.
(68) Scholes, G. D. Long-Range Resonance Energy Transfer in Molecular Systems. *Annu. Rev. Phys. Chem.* **2003**, *54*, 57−87.
(69) Jones, G. A.; Bradshaw, D. S. Resonance Energy Transfer: From Fundamental Theory to Recent Applications. *Front. Phys.* **2019**, *7*, 100−118.
(70) Siska, P. E. Molecular-Beam Studies of Penning Ionization. *Rev. Mod. Phys.* **1993**, *65*, 337−412.
(71) Fano, U. Effects of Configuration Interaction on Intensities and Phase Shifts. *Phys. Rev.* **1961**, *124*, 1866−1878.
(72) Åberg, T.; Howat, G. In *Encyclopedia of Physics*; Mehlhorn, W., Ed.; Springer: Berlin, 1982; Vol. *31*, pp 469−630.
(73) Bardsley, J. N.; Mandl, F. Resonant Scattering of Electrons by Molecules. *Rep. Prog. Phys.* **1968**, *31*, 471−531.
(74) Klaiman, S.; Cederbaum, L. S. Barrierless Single-Electron-Induced Cis−Trans Isomerization. *Angew. Chem., Int. Ed.* **2015**, *54*, 10470−10473.
(75) Klaiman, S.; Gilary, I. In *Adv. Quantum Chem.*; Nicolaides, C. A., Brändas, E., Sabin, J. R., Eds.; Academic Press, 2012; Vol. *63*, pp 1−31.
(76) Feshbach, H. Unified Theory of Nuclear Reactions. *Ann. Phys.* **1958**, *5*, 357−390.
(77) Feshbach, H. A Unified Theory of Nuclear Reactions. II. *Ann. Phys.* **1962**, *19*, 287−313.
(78) Wentzel, G. Über Strahlungslose Quantensprünge. *Eur. Phys. J. A* **1927**, *43*, 524−530.
(79) Santra, R.; Zobeley, J.; Cederbaum, L. S. Electronic Decay of Valence Holes in Clusters and Condensed Matter. *Phys. Rev. B: Condens. Matter Mater. Phys.* **2001**, *64*, 245104.
(80) Averbukh, V.; Cederbaum, L. S. Interatomic Electronic Decay in Endohedral Fullerenes. *Phys. Rev. Lett.* **2006**, *96*, 053401.
(81) Gokhberg, K.; Averbukh, V.; Cederbaum, L. S. Interatomic Decay of Inner-Valence-Excited States in Clusters. *J. Chem. Phys.* **2006**, *124*, 144315.
(82) Kopelke, S.; Gokhberg, K.; Cederbaum, L. S.; Averbukh, V. Calculation of Resonant Interatomic Coulombic Decay Widths of Inner-Valence-Excited States Delocalized due to Inversion Symmetry. *J. Chem. Phys.* **2009**, *130*, 144103.
(83) Miteva, T.; Kazandjian, S.; Sisourat, N. On the Computations of Decay Widths of Fano Resonances. *Chem. Phys.* **2017**, *482*, 208−215.
(84) Schirmer, J. Beyond the Random-Phase Approximation: A new Approximation Scheme for the Polarization Propagator. *Phys. Rev. A: At., Mol., Opt. Phys.* **1982**, *26*, 2395−2416.
(85) Wormit, M.; Dreuw, A. The Algebraic Diagrammatic Construction Scheme for the Polarization Propagator for the Calculation of Excited States. *WIREs Comput. Mol. Sci.* **2015**, *5*, 82−95.
(86) Schirmer, J.; Cederbaum, L. S.; Walter, O. New Approach to the One-Particle Green's Function for Finite Fermi Systems. *Phys. Rev. A: At., Mol., Opt. Phys.* **1983**, *28*, 1237−1259.
(87) Dempwolff, A. L.; Schneider, M.; Hodecker, M.; Dreuw, A. Efficient Implementation of the Non-Dyson Third-Order Algebraic Diagrammatic Construction Approximation for the Electron Propagator for Closed- and Open-Shell Molecules. *J. Chem. Phys.* **2019**, *150*, 064108.
(88) Schirmer, J.; Barth, A. Higher-Order Approximations for the Particle-Particle Propagator. *Z. Phys. A: At. Nucl.* **1984**, *317*, 267−279.
(89) Trofimov, A. B.; Stelter, G.; Schirmer, J. Electron Excitation Energies Using a Consistent Third-Order Propagator Approach: Comparison with Full Configuration Interaction and Coupled Cluster Results. *J. Chem. Phys.* **2002**, *117*, 6402−6410.
(90) Harbach, P. H. P.; Wormit, M.; Dreuw, A. The Third-Order Algebraic Diagrammatic Construction Method (ADC(3)) for the Polarization Propagator for Closed-Shell Molecules: Efficient

https://dx.doi.org/10.1021/acs.chemrev.0c00106
Chem. Rev. 2020, 120, 11295−11369

Implementation and Benchmarking. *J. Chem. Phys.* **2014**, *141*, 064113.
(91) Schirmer, J. Closed-Form Intermediate Representations of Many-Body Propagators and Resolvent Matrices. *Phys. Rev. A: At., Mol., Opt. Phys.* **1991**, *43*, 4647−4659.
(92) Mertins, F.; Schirmer, J. Algebraic Propagator Approaches and Intermediate-State Representations. I. The Biorthogonal and Unitary Coupled-Cluster Methods. *Phys. Rev. A: At., Mol., Opt. Phys.* **1996**, *53*, 2140−2152.
(93) Dempwolff, A. L.; Paul, A. C.; Belogolova, A. M.; Trofimov, A. B.; Dreuw, A. Intermediate State Representation Approach to Physical Properties of Molecular Electron-Detached States. I. Theory and Implementation. *J. Chem. Phys.* **2020**, *152*, 024113.
(94) Dempwolff, A. L.; Paul, A. C.; Belogolova, A. M.; Trofimov, A. B.; Dreuw, A. Intermediate State Representation Approach to Physical Properties of Molecular Electron-Detached States. II. Benchmarking. *J. Chem. Phys.* **2020**, *152*, 024125.
(95) Schirmer, J.; Trofimov, A. B. Intermediate State Representation Approach to Physical Properties of Electronically Excited Molecules. *J. Chem. Phys.* **2004**, *120*, 11449−11464.
(96) Wormit, M.; Rehn, D. R.; Harbach, P. H.; Wenzel, J.; Krauter, C. M.; Epifanovsky, E.; Dreuw, A. Investigating Excited Electronic States Using the Algebraic Diagrammatic Construction (ADC) Approach of the Polarisation Propagator. *Mol. Phys.* **2014**, *112*, 774−784.
(97) Gokhberg, K.; Averbukh, V.; Cederbaum, L. S. Decay Rates of Inner-Valence Excitations in Noble Gas Atoms. *J. Chem. Phys.* **2007**, *126*, 154107.
(98) Kopelke, S.; Gokhberg, K.; Cederbaum, L. S.; Tarantelli, F.; Averbukh, V. Autoionization Widths by Stieltjes Imaging Applied to Lanczos Pseudospectra. *J. Chem. Phys.* **2011**, *134*, 024106.
(99) Kopelke, S.; Gokhberg, K.; Averbukh, V.; Tarantelli, F.; Cederbaum, L. S. Ab Initio Interatomic Decay Widths of Excited States by Applying Stieltjes Imaging to Lanczos Pseudospectra. *J. Chem. Phys.* **2011**, *134*, 094107.
(100) Averbukh, V.; Cederbaum, L. S. Ab Initio Calculation of Interatomic Decay Rates by a Combination of the Fano Ansatz, Green's-Function Methods, and the Stieltjes Imaging Technique. *J. Chem. Phys.* **2005**, *123*, 204107.
(101) Kolorenč, P.; Averbukh, V.; Gokhberg, K.; Cederbaum, L. S. Ab Initio Calculation of Interatomic Decay Rates of Excited Doubly Ionized States in Clusters. *J. Chem. Phys.* **2008**, *129*, 244102.
(102) Kolorenč, P.; Sisourat, N. Interatomic Coulombic Decay Widths of Helium Trimer: Ab Initio Calculations. *J. Chem. Phys.* **2015**, *143*, 224310.
(103) Stumpf, V.; Scheit, S.; Kolorenč, P.; Gokhberg, K. Electron Transfer Mediated Decay in NeXe Triggered by K-LL Auger Decay of Ne. *Chem. Phys.* **2017**, *482*, 192−200.
(104) Jabbari, G.; Klaiman, S.; Chiang, Y.-C.; Trinter, F.; Jahnke, T.; Gokhberg, K. Ab Initio Calculation of ICD Widths in Photoexcited HeNe. *J. Chem. Phys.* **2014**, *140*, 224305.
(105) Howat, G.; Aberg, T.; Goscinski, O. Relaxation and Final-State Channel Mixing in the Auger Effect. *J. Phys. B: At. Mol. Phys.* **1978**, *11*, 1575−1573.
(106) Demekhin, P. V.; Ehresmann, A.; Sukhorukov, V. L. Single Center Method: A Computational Tool for Ionization and Electronic Excitation Studies of Molecules. *J. Chem. Phys.* **2011**, *134*, 024113.
(107) Mhamdi, A.; Trinter, F.; Rauch, C.; Weller, M.; Rist, J.; Waitz, M.; Siebert, J.; Metz, D.; Janke, C.; Kastirke, G.; et al. Resonant Interatomic Coulombic Decay in HeNe: Electron Angular Emission Distributions. *Phys. Rev. A: At., Mol., Opt. Phys.* **2018**, *97*, 053407.
(108) Reinhardt, W. P. L2 Discretization of Atomic and Molecular Electronic Continua: Moment, Quadrature and J-matrix Techniques. *Comput. Phys. Commun.* **1979**, *17*, 1−21.
(109) Langhoff, P. Stieltjes Imaging of Atomic and Molecular Photoabsorption Profiles. *Chem. Phys. Lett.* **1973**, *22*, 60−64.
(110) Müller-Plathe, F.; Diercksen, G. H. F. Perturbative-Polarization-Propagator Study of the Photoionization Cross Section of the Water Molecule. *Phys. Rev. A: At., Mol., Opt. Phys.* **1989**, *40*, 696−711.
(111) Hazi, A. U. A. Purely L2Method for Calculating Resonance Widths. *J. Phys. B: At. Mol. Phys.* **1978**, *11*, L259−L266.
(112) Hazi, A. U.; Orel, A. E.; Rescigno, T. N. Ab Initio Study of Dissociative Attachment of Low-Energy Electrons to F_2. *Phys. Rev. Lett.* **1981**, *46*, 918−922.
(113) Nesbet, R. K. Stieltjes Imaging Method for Computation of Oscillator-Strength Distributions for Complex Atoms. *Phys. Rev. A: At., Mol., Opt. Phys.* **1976**, *14*, 1065−1081.
(114) Whitten, B. L.; Hazi, A. U. Autoionization Widths of Doubly Excited States for Highly Ionized Systems: An Application of the Stieltjes Moment Theory. *Phys. Rev. A: At., Mol., Opt. Phys.* **1986**, *33*, 1039−1044.
(115) Meyer, H.; Pal, S. A BandLanczos Method for Computing Matrix Elements of a Resolvent. *J. Chem. Phys.* **1989**, *91*, 6195−6204.
(116) Sisourat, N.; Kazandjian, S.; Randimbiarisolo, A.; Kolorenč, P. Interatomic Coulombic Decay Widths of Helium Trimer: A Diatomics-in-Molecules Approach. *J. Chem. Phys.* **2016**, *144*, 084111.
(117) Sisourat, N.; Engin, S.; Gorfinkiel, J. D.; Kazandjian, S.; Kolorenč, P.; Miteva, T. On the Computations of Interatomic Coulombic Decay Widths with R-matrix Method. *J. Chem. Phys.* **2017**, *146*, 244109.
(118) Averbukh, V.; Saalmann, U.; Rost, J. M. Suppression of Exponential Electronic Decay in a Charged Environment. *Phys. Rev. Lett.* **2010**, *104*, 233002.
(119) Gokhberg, K.; Kopelke, S.; Kryzhevoi, N. V.; Kolorenč, P.; Cederbaum, L. S. Dependence of Interatomic Decay Widths on the Symmetry of the Decaying State: Analytical Expressions and Ab Initio Results. *Phys. Rev. A: At., Mol., Opt. Phys.* **2010**, *81*, 013417.
(120) Harbach, P. H. P.; Schneider, M.; Faraji, S.; Dreuw, A. Intermolecular Coulombic Decay in Biology: The Initial Electron Detachment from $FADH^-$ in DNA Photolyases. *J. Phys. Chem. Lett.* **2013**, *4*, 943−950.
(121) Hemmerich, J. L.; Bennett, R.; Buhmann, S. Y. The Influence of Retardation and Dielectric Environments on Interatomic Coulombic Decay. *Nat. Commun.* **2018**, *9*, 2934−2942.
(122) Bartlett, R. J. CoupledCluster Theory and its Equation-ofMotion Extensions. *Wiley Interdiscip. Rev.: Comput. Mol. Sci.* **2012**, *2*, 126−138.
(123) Koch, H.; Jorgensen, P. Coupled Cluster Response Functions. *J. Chem. Phys.* **1990**, *93*, 3333−3344.
(124) Demekhin, P. V.; Chiang, Y.-C.; Stoychev, S. D.; Kolorenč, P.; Scheit, S.; Kuleff, A. I.; Tarantelli, F.; Cederbaum, L. S. Interatomic Coulombic Decay and its Dynamics in NeAr Following K-LL Auger Transition in the Ne Atom. *J. Chem. Phys.* **2009**, *131*, 104303.
(125) Gokhberg, K.; Kolorenč, P.; Kuleff, A. I.; Cederbaum, L. S. Site- and Energy-Selective Slow-Electron Production Through Intermolecular Coulombic Decay. *Nature* **2014**, *505*, 661−663.
(126) Pernpointner, M.; Trofimov, A. B. The One-Particle Green's Function Method in the Dirac−Hartree−Fock Framework. I. Second-Order Valence Ionization Energies of Ne Through Xe. *J. Chem. Phys.* **2004**, *120*, 4098−4106.
(127) Pernpointner, M. The One-Particle Green's Function Method in the Dirac−Hartree−Fock Framework. II. Third-Order Valence Ionization Energies of the Noble Gases, CO and ICN. *J. Chem. Phys.* **2004**, *121*, 8782−8791.
(128) Pernpointner, M. The Four-Component Two-Particle Propagator for the Calculation of Double-Ionization Spectra of Heavy-Element Compounds: I. Method. *J. Phys. B: At., Mol. Opt. Phys.* **2010**, *43*, 205102.
(129) Pernpointner, M. The Relativistic Polarization Propagator for the Calculation of Electronic Excitations in Heavy Systems. *J. Chem. Phys.* **2014**, *140*, 084108.
(130) Fasshauer, E.; Kolorenč, P.; Pernpointner, M. Relativistic Decay Widths of Autoionization Processes: The Relativistic FanoADC-Stieltjes Method. *J. Chem. Phys.* **2015**, *142*, 144106.
(131) Pernpointner, M.; Knecht, S.; Cederbaum, L. S. Ionization Spectra and Electronic Decay in Small Iodide Clusters: Fully Relativistic Results. *J. Chem. Phys.* **2006**, *125*, 034309.

https://dx.doi.org/10.1021/acs.chemrev.0c00106
Chem. Rev. 2020, 120, 11295−11369

(132) Faßhauer, E.; Kryzhevoi, N. V.; Pernpointner, M. Possible Electronic Decay Channels in the Ionization Spectra of Small Clusters Composed of Ar and Xe: A Four-Component Relativistic Treatment. *J. Chem. Phys.* **2010**, *133*, 014303.
(133) Faßhauer, E.; Pernpointner, M.; Gokhberg, K. Interatomic Decay of Inner-Valence Ionized States in ArXe Clusters: Relativistic Approach. *J. Chem. Phys.* **2013**, *138*, 014305.
(134) Pernpointner, M.; Cederbaum, L. S. Pt F^{2-}_6 Dianion and its Detachment Spectrum: A Fully Relativistic Study. *J. Chem. Phys.* **2007**, *126*, 144310.
(135) Zobel, J. P.; Kryzhevoi, N. V.; Pernpointner, M. Communication: Electron Transfer Mediated Decay Enabled by Spin-Orbit Interaction in Small Krypton/Xenon Clusters. *J. Chem. Phys.* **2014**, *140*, 161103.
(136) Siegert, A. J. F. On the Derivation of the Dispersion Formula for Nuclear Reactions. *Phys. Rev.* **1939**, *56*, 750−752.
(137) Reinhardt, W. P. Complex Coordinates in the Theory of Atomic and Molecular Structure and Dynamics. *Annu. Rev. Phys. Chem.* **1982**, *33*, 223−255.
(138) Moiseyev, N. Quantum Theory of Resonances: Calculating Energies, Widths and Cross-Sections by Complex Scaling. *Phys. Rep.* **1998**, *302*, 212−293.
(139) White, A. F.; Epifanovsky, E.; McCurdy, C. W.; Head-Gordon, M. Second Order M−ller-Plesset and Coupled Cluster Singles and Doubles Methods with Complex Basis Functions for Resonances in Electron-Molecule Scattering. *J. Chem. Phys.* **2017**, *146*, 234107.
(140) Riss, U.; Meyer, H.-D. Calculation of Resonance Energies and Widths Using the Complex Absorbing Potential Method. *J. Phys. B: At., Mol. Opt. Phys.* **1993**, *26*, 4503−4535.
(141) Riss, U.; Meyer, H.-D. Reflection Free Complex Absorbing Potentials. *J. Phys. B: At., Mol. Opt. Phys.* **1995**, *28*, 1475−1493.
(142) Sommerfeld, T.; Ehara, M. Complex Absorbing Potentials with Voronoi Isosurfaces Wrapping Perfectly around Molecules. *J. Chem. Theory Comput.* **2015**, *11*, 4627−4633.
(143) Santra, R.; Cederbaum, L. S. An Efficient Combination of Computational Techniques for Investigating Electronic Resonance States in Molecules. *J. Chem. Phys.* **2001**, *115*, 6853−6861.
(144) Vaval, N.; Cederbaum, L. S. Ab Initio Lifetimes in the Interatomic Coulombic Decay of Neon Clusters Computed with Propagators. *J. Chem. Phys.* **2007**, *126*, 164110.
(145) Sajeev, Y.; Ghosh, A.; Vaval, N.; Pal, S. Coupled Cluster Methods for Autoionisation Resonances. *Int. Rev. Phys. Chem.* **2014**, *33*, 397−425.
(146) Jagau, T.-C.; Bravaya, K. B.; Krylov, A. I. Extending Quantum Chemistry of Bound States to Electronic Resonances. *Annu. Rev. Phys. Chem.* **2017**, *68*, 525−553.
(147) Sommerfeld, T.; Santra, R. Efficient Method to Perform CAP/CI Calculations for Temporary Anions. *Int. J. Quantum Chem.* **2001**, *82*, 218−226.
(148) Santra, R.; Breidbach, J.; Zobeley, J.; Cederbaum, L. S. Parallel Filter Diagonalization: A Novel Method to Resolve Quantum States in Dense Spectral Regions. *J. Chem. Phys.* **2000**, *112*, 9243−9252.
(149) Sommerfeld, T.; Tarantelli, F. Subspace iteration Techniques for the Calculation of Resonances Using Complex Symmetric Hamiltonians. *J. Chem. Phys.* **2000**, *112*, 2106−2110.
(150) Santra, R.; Cederbaum, L. S.; Meyer, H.-D. Electronic Decay of Molecular Clusters: Non-Stationary States Computed by Standard Quantum Chemistry Methods. *Chem. Phys. Lett.* **1999**, *303*, 413−419.
(151) Santra, R.; Zobeley, J.; Cederbaum, L. S.; Moiseyev, N. Interatomic Coulombic Decay in van der Waals Clusters and Impact of Nuclear Motion. *Phys. Rev. Lett.* **2000**, *85*, 4490−4493.
(152) Moiseyev, N.; Santra, R.; Zobeley, J.; Cederbaum, L. S. Fingerprints of the Nodal Structure of Autoionizing Vibrational Wave Functions in Clusters: Interatomic Coulombic Decay in Ne Dimer. *J. Chem. Phys.* **2001**, *114*, 7351−7360.
(153) Santra, R.; Cederbaum, L. S. Coulombic Energy Transfer and Triple Ionization in Clusters. *Phys. Rev. Lett.* **2003**, *90*, 153401.
(154) Gokhberg, K.; Trofimov, A. B.; Sommerfeld, T.; Cederbaum, L. S. Ionization of Metal Atoms Following Valence-Excitation of Neighbouring Molecules. *Europhys. Lett.* **2005**, *72*, 228−234.
(155) Ghosh, A.; Vaval, N. Geometry-Dependent Lifetime of Interatomic Coulombic Decay Using Equation-of-Motion Coupled Cluster Method. *J. Chem. Phys.* **2014**, *141*, 234108.
(156) Ghosh, A.; Pal, S.; Vaval, N. Study of Interatomic Coulombic Decay of $Ne(H_2O)_n$ (n = 1,3) Clusters Using Equation-of-Motion Coupled-Cluster Method. *J. Chem. Phys.* **2013**, *139*, 064112.
(157) Ghosh, A.; Pal, S.; Vaval, N. Interatomic Coulombic Decay in $(HF)_2$ (n = 2−3) Clusters Using CAP/EOM-CCSD Method. *Mol. Phys.* **2014**, *112*, 669−673.
(158) Hazi, A.; Taylor, H. Stabilization Method of Calculating Resonance Energies: Model Problem. *Phys. Rev. A: At., Mol., Opt. Phys.* **1970**, *170* (1), 1109−1120.
(159) Eliezer, I.; Taylor, H. S.; Williams, J. K. Resonant States of H_2^-. *J. Chem. Phys.* **1967**, *47*, 2165−2178.
(160) Volobuev, Y. L.; Truhlar, D. G. Strategy for Quantum Mechanical Reactive Scattering. *Comput. Phys. Commun.* **2000**, *128*, 516−526.
(161) Maier, C.; Cederbaum, L.; Domcke, W. A spherical-box approach to resonances. *J. Phys. B: At. Mol. Phys.* **1980**, *13*, L119−L124.
(162) Bande, A.; Gokhberg, K.; Cederbaum, L. S. Dynamics of Interatomic Coulombic Decay in Quantum Dots. *J. Chem. Phys.* **2011**, *135*, 144112.
(163) Landau, A.; Ben-Asher, A.; Gokhberg, K.; Cederbaum, L.; Moiseyev, N. Ab initio complex potential energy curves of the He*(1s2p ^{1}P)-Li dimer. *J. Chem. Phys.* **2020**, *152*, 184303.
(164) Bardsley, J. N. Configuration Interaction in the Continuum States of Molecules. *J. Phys. B: At. Mol. Phys.* **1968**, *1*, 349−351.
(165) Cederbaum, L. S.; Tarantelli, F. Nuclear Dynamics of Decaying States: A Time-Dependent Formulation. *J. Chem. Phys.* **1993**, *98*, 9691−9706.
(166) Cederbaum, L. S.; Tarantelli, F. Nuclear Dynamics of Several Decaying Overlapping Electronic States: A Time-Dependent Formulation. *J. Chem. Phys.* **1993**, *99*, 5871−58846.
(167) Pahl, E.; Meyer, H.-D.; Cederbaum, L. S. Competition between Excitation and Electronic Decay of Short-lived Molecular States. *Z. Phys. D: At., Mol. Clusters* **1996**, *38*, 215−232.
(168) Pahl, E.; Meyer, H.-D.; Cederbaum, L.; Minelli, D.; Tarantelli, F. Adiabatic and Nonadiabatic Effects of Nuclear Dynamics in Spectra of Decaying States: Auger Spectrum of HF. *J. Chem. Phys.* **1996**, *105*, 9175−9181.
(169) Pahl, E.; Cederbaum, L. S.; Tarantelli, F. Resonant Decay Spectra for Energetically Unselective Excitation Exemplified by the Broadband Resonant Auger Spectrum of HF. *Phys. Rev. A: At., Mol., Opt. Phys.* **1999**, *60*, 1070−1078.
(170) Pahl, E.; Brand, J.; Cederbaum, L. S.; Tarantelli, F. Impact of Narrow-Band Excitation on Resonant Decay Spectra. *Phys. Rev. A: At., Mol., Opt. Phys.* **1999**, *60*, 1079−1090.
(171) Cederbaum, L. S.; Domcke, W. Local against Non-Local Complex Potential in Resonant Electron-Molecule Scattering. *J. Phys. B: At. Mol. Phys.* **1981**, *14*, 4665−4689.
(172) Domcke, W. Theory of Resonance and Threshold Effects in Electron-Molecule Collisions: The Projection-Operator Approach. *Phys. Rep.* **1991**, *208*, 97−188.
(173) Chiang, Y.-C.; Otto, F.; Meyer, H.-D.; Cederbaum, L. S. Interrelation between the Distributions of Kinetic Energy Release and Emitted Electron Energy Following the Decay of Electronic States. *Phys. Rev. Lett.* **2011**, *107*, 173001.
(174) Chiang, Y.-C.; Otto, F.; Meyer, H.-D.; Cederbaum, L. S. Kinetic Energy Release in Fragmentation Processes Following Electron Emission: A Time-Dependent Approach. *J. Chem. Phys.* **2012**, *136*, 114111.
(175) Meyer, H.-D.; Manthe, U.; Cederbaum, L. S. The Multi-configurational Time-Dependent Hartree Approach. *Chem. Phys. Lett.* **1990**, *165*, 73−78.

https://dx.doi.org/10.1021/acs.chemrev.0c00106
Chem. Rev. 2020, 120, 11295−11369

(176) Manthe, U.; Meyer, H.-D.; Cederbaum, L. S. Wave-packet Dynamics within the Multiconfiguration Hartree Framework: General Aspects and Application to NOCl. *J. Chem. Phys.* **1992**, *97*, 3199−3213.
(177) Manthe, U.; Meyer, H.-D.; Cederbaum, L. S. Multiconfigurational Time-Dependent Hartree Study of Complex Dynamics: Photodissociation of NO_2. *J. Chem. Phys.* **1992**, *97*, 9062−9071.
(178) *Multidimensional Quantum Dynamics: MCTDH Theory and Applications*; Meyer, H.-D., Gatti, F., Worth, G. A., Eds.; Wiley-VCH, 2009.
(179) Moiseyev, N.; Scheit, S.; Cederbaum, L. Non-Hermitian Quantum Mechanics: Wave Packet Propagation on Autoionizing Potential. *J. Chem. Phys.* **2004**, *121*, 722−725.
(180) Sisourat, N.; Kryzhevoi, N. V.; Kolorenč, P.; Scheit, S.; Cederbaum, L. S. Impact of Nuclear Dynamics on Interatomic Coulombic Decay in a He Dimer. *Phys. Rev. A: At., Mol., Opt. Phys.* **2010**, *82*, 053401.
(181) Narevicius, E.; Moiseyev, N. Non-Hermitian Formulation of Interference Effect in Scattering Experiments. *J. Chem. Phys.* **2000**, *113*, 6088−6095.
(182) Moiseyev, N. Quantum Theory of Resonances: Calculating Energies, Widths and Cross-Sections by Complex Scaling. *Phys. Rep.* **1998**, *302*, 211−293.
(183) Scheit, S.; Cederbaum, L. S.; Meyer, H.-D. Time-Dependent Interplay between Electron Emission and Fragmentation in the Interatomic Coulombic Decay. *J. Chem. Phys.* **2003**, *118*, 2092−2107.
(184) Scheit, S.; Averbukh, V.; Meyer, H.-D.; Moiseyev, N.; Santra, R.; Sommerfeld, T.; Zobeley, J.; Cederbaum, L. S. On the Interatomic Coulombic Decay in the Ne Dimer. *J. Chem. Phys.* **2004**, *121*, 8393−8398.
(185) Scheit, S.; Averbukh, V.; Meyer, H.-D.; Zobeley, J.; Cederbaum, L. S. Interatomic Coulombic Decay in a Heteroatomic Rare Gas Cluster. *J. Chem. Phys.* **2006**, *124*, 154305.
(186) O'Keeffe, P.; Ciavardini, A.; Ripani, E.; Bolognesi, P.; Coreno, M.; Avaldi, L.; Devetta, M.; Di Fraia, M.; Callegari, C.; Prince, K. C.; et al. Experimental Investigation of the Interatomic Coulombic Decay in NeAr Dimers. *Phys. Rev. A: At., Mol., Opt. Phys.* **2014**, *90*, 042508.
(187) Havermeier, T.; Jahnke, T.; Kreidi, K.; Wallauer, R.; Voss, S.; Schöffler, M.; Schössler, S.; Foucar, L.; Neumann, N.; Titze, J.; et al. Interatomic Coulombic Decay Following Photoionization of the Helium Dimer: Observation of Vibrational Structure. *Phys. Rev. Lett.* **2010**, *104*, 133401.
(188) Havermeier, T.; Kreidi, K.; Wallauer, R.; Voss, S.; Schöffler, M.; Schössler, S.; Foucar, L.; Neumann, N.; Titze, J.; Sann, H.; et al. Angular Distributions of Photoelectrons and Interatomic-Coulombic-Decay Electrons from Helium Dimers: Strong Dependence on the Internuclear Distance. *Phys. Rev. A: At., Mol., Opt. Phys.* **2010**, *82*, 063405.
(189) Sisourat, N.; Kryzhevoi, N. V.; Kolorenč, P.; Scheit, S.; Jahnke, T.; Cederbaum, L. S. Ultralong-Range Energy Transfer by Interatomic Coulombic Decay in an Extreme Quantum System. *Nat. Phys.* **2010**, *6*, 508−511.
(190) Kolorenč, P.; Kryzhevoi, N. V.; Sisourat, N.; Cederbaum, L. S. Interatomic Coulombic Decay in a He Dimer: Ab Initio Potential Energy Curves and Decay Widths. *Phys. Rev. A: At., Mol., Opt. Phys.* **2010**, *82*, 013422.
(191) Sisourat, N.; Sann, H.; Kryzhevoi, N. V.; Kolorenč, P.; Havermeier, T.; Sturm, F.; Jahnke, T.; Kim, H.-K.; Dörner, R.; Cederbaum, L. S. Interatomic Electronic Decay Driven by Nuclear Motion. *Phys. Rev. Lett.* **2010**, *105*, 173401.
(192) Mhamdi, A.; Rist, J.; Aslitürk, D.; Weller, M.; Melzer, N.; Trabert, D.; Kircher, M.; Vela-Pérez, I.; Siebert, J.; Eckart, S.; et al. Breakdown of the Spectator Concept in Low-Electron-Energy Resonant Decay Processes. *Phys. Rev. Lett.* **2018**, *121*, 243002.
(193) Scheit, S. *Nuclear Dynamics in the Decay of Excited Electronic States: Theory Including Cascades and Multimechanism Decays and Applications to the Interatomic Coulombic Decay*. Ph.D. Thesis, Ruprecht-Karls-Universitat Heidelberg, 2007.
(194) Santra, R.; Cederbaum, L. S. Erratum: Coulombic Energy Transfer and Triple Ionization in Clusters [Phys. Rev. Lett. 90,153401(2003)]. *Phys. Rev. Lett.* **2005**, *94*, 199901.
(195) Demekhin, P. V.; Scheit, S.; Stoychev, S. D.; Cederbaum, L. S. Dynamics of Interatomic Coulombic Decay in a Ne Dimer Following the K-$L_1L_{2,3}(^1P)$ Auger Transition in the Ne Atom. *Phys. Rev. A: At., Mol., Opt. Phys.* **2008**, *78*, 043421.
(196) Ouchi, T.; Sakai, K.; Fukuzawa, H.; Higuchi, I.; Demekhin, P. V.; Chiang, Y.-C.; Stoychev, S. D.; Kuleff, A. I.; Mazza, T.; Schöffler, M.; et al. Interatomic Coulombic Decay Following Ne 1s Auger Decay in NeAr. *Phys. Rev. A: At., Mol., Opt. Phys.* **2011**, *83*, 053415.
(197) Demekhin, P. V.; Scheit, S.; Cederbaum, L. S. Recoil by Auger Electrons: Theory and Application. *J. Chem. Phys.* **2009**, *131*, 164301.
(198) Kreidi, K.; Demekhin, P. V.; Jahnke, T.; Weber, T.; Havermeier, T.; Liu, X.; Morisita, Y.; Schössler, S.; Schmidt, L.; Schöffler, M.; et al. Photo- and Auger-Electron Recoil Induced Dynamics of Interatomic Coulombic Decay. *Phys. Rev. Lett.* **2009**, *103*, 033001.
(199) Miteva, T.; Chiang, Y.-C.; Kolorenc, P.; Kuleff, A. I.; Gokhberg, K.; Cederbaum, L. S. Interatomic Coulombic Decay Following Resonant Core Excitation of Ar in Argon Dimer. *J. Chem. Phys.* **2014**, *141*, 064307.
(200) Miteva, T.; Chiang, Y.-C.; Kolorenc, P.; Kuleff, A. I.; Cederbaum, L. S.; Gokhberg, K. The Effect of the Partner Atom on the Spectra of Interatomic Coulombic Decay Triggered by Resonant Auger Processes. *J. Chem. Phys.* **2014**, *141*, 164303.
(201) Rist, J.; Miteva, T.; Gaire, B.; Sann, H.; Trinter, T.; Keiling, M.; Gehrken, N.; Moradmand, A.; Berry, B.; Zohrabi, M.; et al. A Comprehensive Study of Interatomic Coulombic Decay in Argon Dimers: Extracting R-Dependent Absolute Decay Rates from the Experiment. *Chem. Phys.* **2017**, *482*, 185−191.
(202) Ren, X.; Miteva, T.; Kolorenč, P.; Gokhberg, K.; Kuleff, A. I.; Cederbaum, L. S.; Dorn, A. Observation of Fast and Slow Interatomic Coulombic Decay in Argon Dimers Induced by Electron-Impact Ionization. *Phys. Rev. A: At., Mol., Opt. Phys.* **2017**, *96*, 032715.
(203) Schnorr, K.; Senftleben, A.; Kurka, M.; Rudenko, A.; Foucar, L.; Schmid, G.; Broska, A.; Pfeifer, T.; Meyer, K.; Anielski, D.; et al. Time-Resolved Measurement of Interatomic Coulombic Decay in Ne_2. *Phys. Rev. Lett.* **2013**, *111*, 093402.
(204) Schnorr, K.; Senftleben, A.; Schmid, G.; Augustin, S.; Kurka, M.; Rudenko, A.; Foucar, L.; Broska, A.; Meyer, K.; Anielski, D.; et al. Time-Resolved Study of ICD in Ne Dimers Using FEL Radiation. *J. Electron Spectrosc. Relat. Phenom.* **2015**, *204*, 245−256.
(205) Trinter, F.; Williams, J. B.; Weller, M.; Waitz, M.; Pitzer, M.; Voigtsberger, J.; Schober, C.; Kastirke, G.; Müller, C.; Goihl, C.; et al. Evolution of Interatomic Coulombic Decay in the Time Domain. *Phys. Rev. Lett.* **2013**, *111*, 093401.
(206) Demekhin, P. V.; Stoychev, S. D.; Kuleff, A. I.; Cederbaum, L. S. Exploring Interatomic Coulombic Decay by Free Electron Lasers. *Phys. Rev. Lett.* **2011**, *107*, 273002.
(207) Demekhin, P. V.; Gokhberg, K.; Jabbari, G.; Kopelke, S.; Kuleff, A. I.; Cederbaum, L. S. Overcoming Blockade in Producing Doubly Excited Dimers by a Single Intense Pulse and their Decay. *J. Phys. B: At., Mol. Opt. Phys.* **2013**, *46*, 021001.
(208) Cederbaum, L. S.; Chiang, Y.-C.; Demekhin, P.; Moiseyev, N. Resonant Auger Decay of Molecules in Intense X-Ray Laser Fields: Light-Induced Strong Nonadiabatic Effects. *Phys. Rev. Lett.* **2011**, *106*, 123001.
(209) Demekhin, P. V.; Chiang, Y.-C.; Cederbaum, L. S. Resonant Auger Decay of the Core-Excited C*O Molecule in Intense X-ray Laser Fields. *Phys. Rev. A: At., Mol., Opt. Phys.* **2011**, *84*, 033417.
(210) Demekhin, P. V.; Cederbaum, L. S. Resonant Auger Decay of Core-Excited CO Molecules in Intense X-ray Laser Pulses: the O(1*s* → π^*) Excitation. *J. Phys. B: At., Mol. Opt. Phys.* **2013**, *46*, 164008.
(211) Dubrouil, A.; Reduzzi, M.; Devetta, M.; Feng, C.; Hummert, J.; Finetti, P.; Plekan, O.; Grazioli, C.; Di Fraia, M.; Lyamayev, V.; et al. Two-Photon Resonant Excitation of Interatomic Coulombic Decay in Neon Dimers. *J. Phys. B: At., Mol. Opt. Phys.* **2015**, *48*, 204005.

https://dx.doi.org/10.1021/acs.chemrev.0c00106
Chem. Rev. 2020, 120, 11295−11369

(212) Takanashi, T.; Golubev, N. V.; Callegari, C.; Fukuzawa, H.; Motomura, K.; Iablonskyi, D.; Kumagai, Y.; Mondal, S.; Tachibana, T.; Nagaya, K.; et al. Time-Resolved Measurement of Interatomic Coulombic Decay Induced by Two-Photon Double Excitation of Ne_2. *Phys. Rev. Lett.* **2017**, *118*, 033202.
(213) Kopelke, S.; Chiang, Y. C.; Gokhberg, K.; Cederbaum, L. S. Quenching Molecular Photodissociation by Intermolecular Coulombic Decay. *J. Chem. Phys.* **2012**, *137*, 034302.
(214) Vendrell, O.; Stoychev, S. D.; Cederbaum, L. S. Generation of Highly Damaging H_2O^+ Radicals by Inner Valence Shell Ionization of Water. *ChemPhysChem* **2010**, *11*, 1006−1009.
(215) Jahnke, T.; Sann, H.; Havermeier, T.; Kreidi, K.; Stuck, C.; Meckel, M.; Schöffler, M.; Neumann, N.; Wallauer, R.; Voss, S.; et al. Ultrafast Energy Transfer between Water Molecules. *Nat. Phys.* **2010**, *6*, 139−142.
(216) Li, X.; Millam, J. M.; Schlegel, H. B. Ab Initio Molecular Dynamics Studies of the Photodissociation of Formaldehyde, $H_2CO \rightarrow H_2 + CO$: Direct Classical Trajectory Calculations by MP2 and Density Functional Theory. *J. Chem. Phys.* **2000**, *113*, 10062−10067.
(217) Frisch, M. J.; Trucks, G. W.; Schlegel, H. B.; Scuseria, G. E.; Robb, M. A.; Cheeseman, J. R.; Montgomery, J. A., Jr.; Vreven, T.; Kudin, K. N.; Burant, J. C.; Millam, J. M.; Iyengar, S. S.; Tomasi, J.; Barone, V.; Mennucci, B.; Cossi, M.; Scalmani, G.; Rega, N.; Petersson, G. A.; Nakatsuji, H.; Hada, M.; Ehara, M.; Toyota, K.; Fukuda, R.; Hasegawa, J.; Ishida, M.; Nakajima, T.; Honda, Y.; Kitao, O.; Nakai, H.; Klene, M.; Li, X.; Knox, J. E.; Hratchian, H. P.; Cross, J. B.; Bakken, V.; Adamo, C.; Jaramillo, J.; Gomperts, R.; Stratmann, R. E.; Yazyev, O.; Austin, A. J.; Cammi, R.; Pomelli, C.; Ochterski, J. W.; Ayala, P. Y.; Morokuma, K.; Voth, G. A.; Salvador, P.; Dannenberg, J. J.; Zakrzewski, V. G.; Dapprich, S.; Daniels, A. D.; Strain, M. C.; Farkas, O.; Malick, D. K.; Rabuck, A. D.; Raghavachari, K.; Foresman, J. B.; Ortiz, J. V.; Cui, Q.; Baboul, A. G.; Clifford, S.; Cioslowski, J.; Stefanov, B. B.; Liu, G.; Liashenko, A.; Piskorz, P.; Komaromi, I.; Martin, R. L.; Fox, D. J.; Keith, T.; Al-Laham, M. A.; Peng, C. Y.; Nanayakkara, A.; Challacombe, M.; Gill, P. M. W.; Johnson, B.; Chen, W.; Wong, M. W.; Gonzalez, C.; Pople, J. A. *Gaussian 03*, revision C.02; Gaussian, Inc.: Wallingford, CT, 2003.
(218) Sisourat, N. Nuclear Dynamics of Decaying States: A Semiclassical Approach. *J. Chem. Phys.* **2013**, *139*, 074111.
(219) Schütte, B.; Arbeiter, M.; Fennel, T.; Jabbari, G.; Kuleff, A. I.; Vrakking, M.; Rouzée, A. Observation of Correlated Electronic Decay in Expanding Clusters Triggered by Near-Infrared Fields. *Nat. Commun.* **2015**, *6*, 8596−8602.
(220) Stoychev, S. D.; Kuleff, A. I.; Cederbaum, L. S. On the Intermolecular Coulombic Decay of Singly and Doubly Ionized States of Water Dimer. *J. Chem. Phys.* **2010**, *133*, 154307.
(221) Stoychev, S. D.; Kuleff, A. I.; Cederbaum, L. S. Intermolecular Coulombic Decay in Small Biochemically Relevant Hydrogen-Bonded Systems. *J. Am. Chem. Soc.* **2011**, *133*, 6817−6824.
(222) Sisourat, N.; Kazandjian, S.; Miteva, T. Probing Conformers of Benzene Dimer with Intermolecular Coulombic Decay Spectroscopy. *J. Phys. Chem. A* **2017**, *121*, 45−50.
(223) Förstel, M.; Mucke, M.; Arion, T.; Lischke, T.; Pernpointner, M.; Hergenhahn, U.; Fasshauer, E. Long-Range Interatomic Coulombic Decay in ArXe Clusters: Experiment and Theory. *J. Phys. Chem. C* **2016**, *120*, 22957−22971.
(224) Kryzhevoi, N. V. Microhydration of LiOH: Insight from Electronic Decays of Core-Ionized States. *J. Chem. Phys.* **2016**, *144*, 244302.
(225) Kryzhevoi, N. V.; Cederbaum, L. S. Exploring Protonation and Deprotonation Effects with Auger Electron Spectroscopy. *J. Phys. Chem. Lett.* **2012**, *3*, 2733−2727.
(226) Kryzhevoi, N. V.; Cederbaum, L. S. Nonlocal Effects in the Core Ionization and Auger Spectra of Small Ammonia Clusters. *J. Phys. Chem. B* **2011**, *115*, 5441−5447.
(227) Kuleff, A. I.; Cederbaum, L. S. Tracing Ultrafast Interatomic Electronic Decay Processes in Real Time and Space. *Phys. Rev. Lett.* **2007**, *98*, 083201.
(228) Nagaya, K.; Iablonskyi, D.; Golubev, N. V.; Matsunami, K.; Fukuzawa, H.; Motomura, K.; Nishiyama, T.; Sakai, T.; Tachibana, T.; Mondal, S.; et al. Interatomic Coulombic Decay Cascades in Multiply Excited Neon Clusters. *Nat. Commun.* **2016**, *7*, 13477−13482.
(229) Kumagai, Y.; Fukuzawa, H.; Motomura, K.; Iablonskyi, D.; Nagaya, K.; Wada, S.; Ito, Y.; Takanashi, T.; Sakakibara, Y.; You, D.; et al. Following the Birth of a Nanoplasma Produced by an Ultrashort Hard-X-Ray Laser in Xenon Clusters. *Phys. Rev. X* **2018**, *8*, 031034.
(230) Najjari, B.; Voitkiv, A. B.; Müller, C. Two-Center Resonant Photoionization. *Phys. Rev. Lett.* **2010**, *105*, 153002.
(231) Voitkiv, A. B.; Najjari, B. Resonant Photoionization in a System of Two Nonidentical Atoms. *Phys. Rev. A: At., Mol., Opt. Phys.* **2011**, *84*, 013415.
(232) Müller, C.; Macovei, M. A.; Voitkiv, A. B. Collectively Enhanced Resonant Photoionization in a Multiatom Ensemble. *Phys. Rev. A: At., Mol., Opt. Phys.* **2011**, *84*, 055401.
(233) Najjari, B.; Müller, C.; Voitkiv, A. B. Resonantly Enhanced Photoionization in Correlated Three-Atomic Systems. *New J. Phys.* **2012**, *14*, 105028.
(234) Bande, A. Electron Dynamics of Interatomic Coulombic Decay in Quantum Dots Induced by a Laser Field. *J. Chem. Phys.* **2013**, *138*, 214104.
(235) Dolbundalchok, P.; Peláez, D.; Aziz, E. F.; Bande, A. Geometrical Control of the Interatomic Coulombic Decay Process in Quantum Dots for Infrared Photodetectors. *J. Comput. Chem.* **2016**, *37*, 2249−2259.
(236) Haller, A.; Chiang, Y.-C.; Menger, M.; Aziz, E. F.; Bande, A. Strong Field Control of the Interatomic Coulombic Decay Process in Quantum Dots. *Chem. Phys.* **2017**, *482*, 135−145.
(237) Haller, A.; Bande, A. Favoritism of Quantum Dot Inter-Coulombic Decay over Direct and Multi-Photon Ionization by Laser Strength and Focus. *J. Chem. Phys.* **2018**, *149*, 134102.
(238) Miller, D. R. In *Atomic and Molecular Beam Methods*; Scoles, G., Ed.; Oxford University Press, 1988.
(239) Santra, R.; Zobeley, J.; Cederbaum, L. S. Inner-Valence Ionization of Molecular Anions and Ultrafast Relaxation by Electron Emission. *Chem. Phys. Lett.* **2000**, *324*, 416−422.
(240) Dreuw, A.; Faraji, S. A Quantum Chemical Perspective on (6−4) Photolesion Repair by Photolyases. *Phys. Chem. Chem. Phys.* **2013**, *15*, 19957−19969.
(241) Wiedemann, H. *Synchrotron Radiation*; Springer: Berlin, Heidelberg, 2003.
(242) Holldack, K. V.; Hartrott, M.; Hoeft, F.; Neitzke, O.; Bauch, E.; Wahl, M. Bunch Fill Pattern at BESSY Monitored by Time-Correlated Single Photon Counting. *Proc. SPIE 6771, Advanced Photon Counting Techniques II*, 2007; pp 281−288, DOI: 10.1117/12.734226.
(243) Jahnke, T. *Interatomic Coulombic Decay − Experimentelle Untersuchung eines Neuartigen, Interatomaren Abregungsmechanismus*. Ph.D. Thesis, Goethe Universität Frankfurt, 2005.
(244) Schnorr, K. *XUV Pump-Probe Experiments on Electron Rearrangement and Interatomic Coulombic Decay in Diatomic Molecules*. Ph.D. Thesis, Ruprecht-Karls-Universität Heidelberg, 2014.
(245) Kim, H. K.; Titze, J.; Schöffler, M.; Trinter, F.; Waitz, M.; Voigtsberger, J.; Sann, H.; Meckel, M.; Stuck, C.; Lenz, U.; et al. Enhanced Production of Low Energy Electrons by Alpha Particle Impact. *Proc. Natl. Acad. Sci. U. S. A.* **2011**, *108*, 11821−11825.
(246) Xu, S.; Ma, X.; Ren, X.; Senftleben, A.; Pflüger, T.; Dorn, A.; Ullrich, J. Formation of Protons from Dissociative Ionization of Methane Induced by 54 eV Electrons. *Phys. Rev. A: At., Mol., Opt. Phys.* **2011**, *83*, 052702.
(247) Titze, J.; Schöffler, M.; Kim, H. K.; Trinter, F.; Waitz, M.; Voigtsberger, J.; Neumann, N.; Ulrich, B.; Kreidi, K.; Wallauer, R.; et al. Ionization Dynamics of Helium Dimers in Fast Collisions with He^{+2}. *Phys. Rev. Lett.* **2011**, *106*, 033201.
(248) Kim, H. K.; Gassert, H.; Schöffler, M. S.; Titze, J. N.; Waitz, M.; Voigtsberger, J.; Trinter, F.; Becht, J.; Kalinin, A.; Neumann, N.;

https://dx.doi.org/10.1021/acs.chemrev.0c00106
Chem. Rev. 2020, 120, 11295−11369

et al. Ion-Impact-Induced Interatomic Coulombic Decay in Neon and Argon Dimers. *Phys. Rev. A: At., Mol., Opt. Phys.* **2013**, *88*, 042707.
(249) Yan, S.; Zhang, P.; Stumpf, V.; Gokhberg, K.; Zhang, X. C.; Xu, S.; Li, B.; Shen, L. L.; Zhu, X. L.; Feng, W. T.; et al. Interatomic Relaxation Processes Induced in Neon Dimers by Electron-Impact Ionization. *Phys. Rev. A: At., Mol., Opt. Phys.* **2018**, *97*, No. 010701(R).
(250) Xu, S.; Guo, D.; Ma, X.; Zhu, X.; Feng, W.; Yan, S.; Zhao, D.; Gao, Y.; Zhang, S.; Ren, X.; et al. Damaging Intermolecular Energy and Proton Transfer Processes in Alpha-Particle-Irradiated Hydrogen-Bonded Systems. *Angew. Chem., Int. Ed.* **2018**, *57*, 17023−17027.
(251) Marburger, S. P.; Kugeler, O.; Hergenhahn, U. A Molecular Beam Source for Electron Spectroscopy of Clusters. *AIP Conf. Proc.* **2003**, *705*, 1114−1117.
(252) Granneman, E. H. A.; van der Wiel, M. J. In *Handbook on Synchrotron Radiation*; Koch, E. E., Ed.; North-Holland: Amsterdam, 1983; Vol. *1*, pp 367−462.
(253) Winter, B.; Faubel, M. PhotoEmission from Liquid Aqueous Solutions. *Chem. Rev.* **2006**, *106*, 1176−1211.
(254) Seidel, R.; Pohl, M. N.; Ali, H.; Winter, B.; Aziz, E. F. Advances in Liquid Phase Soft-X-ray Photoemission Spectroscopy: A new Experimental Setup at BESSY II. *Rev. Sci. Instrum.* **2017**, *88*, 073107.
(255) Barth, S.; Marburger, S.; Kugeler, O.; Ulrich, V.; Joshi, S.; Bradshaw, A. M.; Hergenhahn, U. The Efficiency of Interatomic Coulombic Decay in Ne Clusters. *Chem. Phys.* **2006**, *329*, 246−250.
(256) Aoto, T.; Ito, K.; Hikosaka, Y.; Shigemasa, E.; Penent, F.; Lablanquie, P. Properties of Resonant Interatomic Coulombic Decay in Ne Dimers. *Phys. Rev. Lett.* **2006**, *97*, 243401.
(257) Lablanquie, P.; Aoto, T.; Hikosaka, Y.; Morioka, Y.; Penent, F.; Ito, K. Appearance of Interatomic Coulombic Decay in Ar, Kr, and Xe Homonuclear Dimers. *J. Chem. Phys.* **2007**, *127*, 154323.
(258) Shcherbinin, M.; LaForge, A. C.; Sharma, V.; Devetta, M.; Richter, R.; Moshammer, R.; Pfeifer, T.; Mudrich, M. Interatomic Coulombic Decay in Helium Nanodroplets. *Phys. Rev. A: At., Mol., Opt. Phys.* **2017**, *96*, 013407.
(259) Wiegandt, F.; Trinter, F.; Henrichs, K.; Metz, D.; Pitzer, M.; Waitz, M.; Jabbour al Maalouf, E.; Janke, C.; Rist, J.; Wechselberger, N.; et al. Direct Observation of Interatomic Coulombic Decay and Subsequent Ion-Atom Scattering in Helium Nanodroplets. *Phys. Rev. A: At., Mol., Opt. Phys.* **2019**, *100*, 022707.
(260) Eppink, A. T. J. B.; Parker, D. H. Velocity Map Imaging of Ions and Electrons Using Electrostatic Lenses: Application in Photoelectron and Photofragment Ion Imaging of Molecular oxygen. *Rev. Sci. Instrum.* **1997**, *68*, 3477−3484.
(261) Buchta, D.; Krishnan, S. R.; Brauer, N. B.; Drabbels, M.; O'Keeffe, P.; Devetta, M.; Di Fraia, M.; Callegari, C.; Richter, R.; Coreno, M.; et al. Extreme Ultraviolet Ionization of Pure He Nanodroplets: Mass-Correlated Photoelectron Imaging, Penning Ionization, and Electron Energy-Loss Spectra. *J. Chem. Phys.* **2013**, *139*, 084301.
(262) Kruit, P.; Read, F. H. Magnetic Field Paralleliser for 2pi Electron-Spectrometer and Electron-Image Magnifier. *J. Phys. E: Sci. Instrum.* **1983**, *16*, 313−324.
(263) Mucke, M.; Braune, M.; Barth, S.; Förstel, M.; Lischke, T.; Ulrich, V.; Arion, T.; Becker, U.; Bradshaw, A.; Hergenhahn, U. A Hitherto Unrecognized Source of Low-Energy Electrons in Water. *Nat. Phys.* **2010**, *6*, 143.
(264) Dörner, R.; Mergel, V.; Jagutzki, O.; Spielberger, L.; Ullrich, J.; Moshammer, R.; Schmidt-Böcking, H. Cold Target Recoil Ion Momentum Spectroscopy: a 'Momentum Microscope' to View Atomic Collision Dynamics. *Phys. Rep.* **2000**, *330*, 95−192.
(265) Ullrich, J.; Moshammer, R.; Dorn, A.; Dörner, R.; Schmidt, L. P. H.; Schmidt-Böcking, H. Recoil-Ion and Electron Momentum Spectroscopy: Reaction-Microscopes. *Rep. Prog. Phys.* **2003**, *66*, 1463−1545.
(266) Jahnke, T.; Weber, T.; Osipov, T.; Landers, A. L.; Jagutzki, O.; Schmidt, a. L. P. H.; Cocke, C.; Prior, M.; Schmidt-Böcking, H.; Dörner, R. Multicoincidence Studies of Photo and Auger Electrons from Fixed-in-Space Molecules Using the COLTRIMS Technique. *J. Electron Spectrosc. Relat. Phenom.* **2004**, *141*, 229−238.
(267) Bordas, C.; Paulig, F.; Helm, H.; Huestis, D. L. Photoelectron Imaging Spectrometry: Principle and Inversion Method. *Rev. Sci. Instrum.* **1996**, *67*, 2257−2268.
(268) O'Keeffe, P.; Bolognesi, P.; Coreno, M.; Moise, A.; Richter, R.; Cautero, G.; Stebel, L.; Sergo, R.; Pravica, L.; Ovcharenko, Y.; et al. A Photoelectron Velocity Map Imaging Spectrometer for Experiments Combining Synchrotron and Laser Radiations. *Rev. Sci. Instrum.* **2011**, *82*, 033109.
(269) LaForge, A. C.; Shcherbinin, M.; Stienkemeier, F.; Richter, R.; Moshammer, R.; Pfeifer, T.; Mudrich, M. Highly Efficient Double Ionization of Mixed Alkali Dimers by Intermolecular Coulombic Decay. *Nat. Phys.* **2019**, *15*, 247−251.
(270) Buchta, D.; Krishnan, S. R.; Brauer, N. B.; Drabbels, M.; O'Keeffe, P.; Devetta, M.; Di Fraia, M.; Callegari, C.; Richter, R.; Coreno, M.; et al. Charge Transfer and Penning Ionization of Dopants in or on Helium Nanodroplets Exposed to EUV Radiation. *J. Phys. Chem. A* **2013**, *117*, 4394−4403.
(271) Yase, S.; Nagaya, K.; Mizoguchi, Y.; Yao, M.; Fukuzawa, H.; Motomura, K.; Yamada, A.; Ma, R.; Ueda, K.; Saito, N.; et al. Crossover in the Photoionization Processes of Neon Clusters with Increasing EUV Free-Electron-laser Intensity. *Phys. Rev. A: At., Mol., Opt. Phys.* **2013**, *88*, 043203.
(272) Katzy, R.; LaForge, A. C.; Ovcharenko, Y.; Coreno, M.; Devetta, M.; Di Fraia, M.; Drabbels, M.; Finetti, P.; Lyamayev, V.; Mazza, T.; et al. Migration of Surface Excitations in Highly-Excited Nanosystems Probed by Intense Resonant XUV Radiation. *J. Phys. B: At., Mol. Opt. Phys.* **2015**, *48*, 244011.
(273) LaForge, A. C.; Stumpf, V.; Gokhberg, K.; von Vangerow, J.; Stienkemeier, F.; Kryzhevoi, N. V.; O'Keeffe, P.; Ciavardini, A.; Krishnan, S. R.; Coreno, M.; et al. Enhanced Ionization of Embedded Clusters by Electron-Transfer-Mediated Decay in Helium Nanodroplets. *Phys. Rev. Lett.* **2016**, *116*, 203001.
(274) Iablonskyi, D.; Nagaya, K.; Fukuzawa, H.; Motomura, K.; Kumagai, Y.; Mondal, S.; Tachibana, T.; Takanashi, T.; Nishiyama, T.; Matsunami, K.; et al. Slow Interatomic Coulombic Decay of Multiply Excited Neon Clusters. *Phys. Rev. Lett.* **2016**, *117*, 276806.
(275) Mucke, M.; Förstel, M.; Lischke, T.; Arion, T.; Bradshaw, A. M.; Hergenhahn, U. Performance of a Short "Magnetic Bottle" Electron Spectrometer. *Rev. Sci. Instrum.* **2012**, *83*, 063106.
(276) Mucke, M.; Arion, T.; Förstel, M.; Lischke, T.; Hergenhahn, U. Competition of Inelastic Electron Scattering and Interatomic Coulombic Decay in Ne Clusters. *J. Electron Spectrosc. Relat. Phenom.* **2015**, *200*, 232−238.
(277) Feifel, R.; Eland, J.; Storchi, L.; Tarantelli, F. Complete Valence Double Photoionization of SF_6. *J. Chem. Phys.* **2005**, *122*, 144309.
(278) Arion, T.; Mucke, M.; Förstel, M.; Bradshaw, A. M.; Hergenhahn, U. Interatomic Coulombic Decay in Mixed NeKr Clusters. *J. Chem. Phys.* **2011**, *134*, 074306.
(279) Förstel, M.; Arion, T.; Hergenhahn, U. Measuring the Efficiency of Interatomic Coulombic Decay in Ne Clusters. *J. Electron Spectrosc. Relat. Phenom.* **2013**, *191*, 16−19.
(280) Knie, A.; Hans, A.; Förstel, M.; Hergenhahn, U.; Schmidt, P.; Ph, R.; Ozga, C.; Kambs, B.; Trinter, F.; Voigtsberger, J.; et al. Detecting Ultrafast Interatomic Electronic Processes in Media by Fluorescence. *New J. Phys.* **2014**, *16*, 102002.
(281) Fasshauer, E.; Förstel, M.; Pallmann, S.; Pernpointner, M.; Hergenhahn, U. Using ICD for Structural Analysis of Clusters: a Case Study on NeAr Clusters. *New J. Phys.* **2014**, *16*, 103026.
(282) Hans, A.; Ltaief, L. B.; Förstel, M.; Schmidt, P.; Ozga, C.; Reiß, P.; Holzapfel, X.; Küstner-Wetekam, C.; Wiegandt, F.; Trinter, F.; et al. Fluorescence Cascades Evoked by Resonant Interatomic Coulombic Decay of Inner-Valence Excited Neon Clusters. *Chem. Phys.* **2017**, *482*, 165−168.
(283) Fasshauer, E.; Förstel, M.; Mucke, M.; Arion, T.; Hergenhahn, U. Theoretical and Experimental Investigation of Electron Transfer Mediated Decay in ArKr Clusters. *Chem. Phys.* **2017**, *482*, 226−238.

https://dx.doi.org/10.1021/acs.chemrev.0c00106
Chem. Rev. 2020, 120, 11295−11369

(284) Richter, C.; Hollas, D.; Saak, C.-M.; Förstel, M.; Miteva, T.; Mucke, M.; Björneholm, O.; Sisourat, N.; Slavíček, P.; Hergenhahn, U. Competition between Proton Transfer and Intermolecular Coulombic Decay in Water. *Nat. Commun.* **2018**, *9*, 4988−4995.
(285) Hans, A.; Schmidt, P.; Ozga, C.; Richter, C.; Otto, H.; Holzapfel, X.; Hartmann, G.; Ehresmann, A.; Hergenhahn, U.; Knie, A. Efficient Fluorescence Quenching by Distant Production of a Free Electron. *J. Phys. Chem. Lett.* **2019**, *10*, 1078−1082.
(286) Serdobintsev, P. Y.; Melnikov, A. S.; Pastor, A. A.; Timofeev, N. A.; Khodorkovskiy, M. A. Relaxation Times Measurement in Single and Multiply Excited Xenon Clusters. *J. Chem. Phys.* **2018**, *148*, 194301.
(287) Lafosse, A.; Lebech, M.; Brenot, J. C.; Guyon, P. M.; Jagutzki, O.; Spielberger, L.; Vervloet, M.; Houver, J. C.; Dowek, D. Vector Correlations in Dissociative Photoionization of Diatomic Molecules in the VUV Range: Strong Anisotropies in Electron Emission from Spatially Oriented NO Molecules. *Phys. Rev. Lett.* **2000**, *84*, 5987−5990.
(288) Lebech, M.; Houver, J. C.; Dowek, D. Ion/Electron Velocity Vector Correlations in Dissociative Photoionization of Simple Molecules Using Electrostatic Lenses. *Rev. Sci. Instrum.* **2002**, *73*, 1866−1874.
(289) Jagutzki, O.; Cerezo, A.; Czasch, A.; Dörner, R.; Hattass, M.; Huang, M.; Mergel, V.; Spillmann, U.; Ullmann-Pfleger, K.; Weber, T.; et al. Multiple Hit Readout of a Microchannel Plate Detector with a Three-Layer Delay-Line Anode. *IEEE Trans. Nucl. Sci.* **2002**, *49*, 2477−2483.
(290) Jagutzki, O.; Mergel, V.; Ullmann-Pfleger, K.; Spielberger, L.; Spillmann, U.; Dörner, R.; Schmidt-Böcking, H. A Broad-Application Microchannel-Plate Detector System for Advanced Particle or Photon Detection Tasks: Large Area Imaging, Precise Multi-hit Timing Information and High Detection Rate. *Nucl. Instrum. Methods Phys. Res., Sect. A* **2002**, *A477*, 244−249.
(291) Moshammer, R.; Unverzagt, M.; Schmitt, W.; Ullrich, J.; Schmidt-Böcking, H. A 4π Recoil-Ion Electron Momentum Analyzer. *Nucl. Instrum. Methods Phys. Res., Sect. B* **1996**, *108*, 425−445.
(292) Schmidt, L.; Jahnke, T.; Czasch, A.; Schöffler, M.; Schmidt-Böcking, H.; Dörner, R. Spatial Imaging of the H_2^+Vibrational Wave Function at the Quantum Limit. *Phys. Rev. Lett.* **2012**, *108*, 073202.
(293) Zeller, S.; Kunitski, M.; Voigtsberger, J.; Kalinin, A.; Schottelius, A.; Schober, C.; Waitz, M.; Sann, H.; Hartung, A.; Bauer, T.; et al. Imaging the He_2 Quantum Halo State Using a Free Electron Laser. *Proc. Natl. Acad. Sci. U. S. A.* **2016**, *113*, 14651−14655.
(294) Pitzer, M.; Kunitski, M.; Johnson, A. S.; Jahnke, T.; Sann, H.; Sturm, F.; Schmidt, L. P. H.; Schmidt-Böcking, H.; Dörner, R.; Stohner, J.; et al. Direct Determination of Absolute Molecular Stereochemistry in Gas Phase by Coulomb Explosion Imaging. *Science* **2013**, *341*, 1096−1100.
(295) Weber, T.; Jagutzki, O.; Hattass, M.; Staudte, A.; Nauert, A.; Schmidt, L.; Prior, M.; Landers, A.; Bräuning-Demian, A.; Bräuning, H.; et al. K-Shell Photoionization of CO and N2: Is There a Link between the Photoelectron Angular Distribution and the Molecular Decay Dynamics? *J. Phys. B: At., Mol. Opt. Phys.* **2001**, *B34*, 3669−3678.
(296) Morishita, Y.; Liu, X.-J.; Saito, N.; Lischke, T.; Kato, M.; Prümper, G.; Oura, M.; Yamaoka, H.; Tamenori, Y.; Suzuki, I. H.; et al. Experimental Evidence of Interatomic Coulombic Decay from the Auger Final States in Argon Dimers. *Phys. Rev. Lett.* **2006**, *96*, 243402.
(297) Ueda, K.; Liu, X.-J.; Prümper, G.; Fukuzawa, H.; Morishita, Y.; Saito, N. Electron-Ion Coincidence Momentum Spectroscopy: Its Application to Ar Dimer Interatomic Decay. *J. Electron Spectrosc. Relat. Phenom.* **2007**, *155*, 113−118.
(298) Jahnke, T.; Czasch, A.; Schöffler, M.; Schössler, S.; Käsz, M.; Titze, J.; Kreidi, K.; Grisenti, R. E.; Staudte, A.; Jagutzki, O.; et al. Photoelectron and ICD Electron Angular Distributions from Fixed-in-Space Neon Dimers. *J. Phys. B: At., Mol. Opt. Phys.* **2007**, *40*, 2597−2606.
(299) Liu, X.-J.; Saito, N.; Fukuzawa, H.; Morishita, Y.; Stoychev, S.; Kuleff, A.; Suzuki, I. H.; Tamenori, Y.; Richter, R.; Prümper, G.; et al. Evidence of Sequential Interatomic Decay in Argon Trimers Obtained by Electron-Triple-Ion Coincidence Spectroscopy. *J. Phys. B: At., Mol. Opt. Phys.* **2007**, *40*, F1.
(300) Ueda, K.; Fukuzawa, H.; Liu, X.-J.; Sakai, K.; Prümper, G.; Morishita, Y.; Saito, N.; Suzuki, I. H.; Nagaya, K.; Iwayama, H.; et al. Interatomic Coulombic Decay Following the Auger Decay: Experimental Evidence in Rare-Gas Dimers. *J. Electron Spectrosc. Relat. Phenom.* **2008**, *166−167*, 3−10.
(301) Morishita, Y.; Saito, N.; Suzuki, I. H.; Fukuzawa, H.; Liu, X.-J.; Sakai, K.; Prümper, G.; Ueda, K.; Iwayama, H.; Nagaya, K.; et al. Evidence of Interatomic Coulombic Decay in ArKr after Ar 2*p* Auger Decay. *J. Phys. B: At., Mol. Opt. Phys.* **2008**, *41*, 025101.
(302) Kreidi, K.; Jahnke, T.; Weber, T. H.; Havermeier, T.; Grisenti, R. E.; Liu, X.; Morisita, Y.; Schössler, S.; Schmidt, L.; Schöffler, M.; et al. Localization of Inner Shell Photoelectron Emission and Interatomic Coulombic Decay in Neon Dimers. *J. Phys.: Conf. Ser.* **2010**, *212*, 012007.
(303) Ulrich, B.; Vredenborg, A.; Malakzadeh, A.; Meckel, M.; Cole, K.; Smolarski, M.; Chang, Z.; Jahnke, T.; Dörner, R. Double-Ionization Mechanisms of the Argon Dimer in Intense Laser Fields. *Phys. Rev. A: At., Mol., Opt. Phys.* **2010**, *82*, 013412.
(304) Semenov, S. K.; Kreidi, K.; Jahnke, T.; Weber, T.; Havermeier, T.; Grisenti, R. E.; Liu, X.; Morisita, Y.; Schmidt, L.; Schöffler, M.; et al. Interatomic Coulombic Decay of Fixed-in-Space Neon Dimers. *Phys. Rev. A: At., Mol., Opt. Phys.* **2012**, *85*, 043421.
(305) Trinter, F.; Williams, J. B.; Weller, M.; Waitz, M.; Pitzer, M.; Voigtsberger, J.; Schober, C.; Kastirke, G.; Müller, C.; Goihl, C.; et al. Vibrationally Resolved Decay Width of Interatomic Coulombic Decay in HeNe. *Phys. Rev. Lett.* **2013**, *111*, 233004.
(306) Nagaya, K.; Sugishima, A.; Iwayama, H.; Murakami, H.; Yao, M.; Fukuzawa, H.; Liu, X.-J.; Motomura, K.; Ueda, K.; Saito, N.; et al. Unusual Under-Threshold Ionization of Neon Clusters Studied by Ion Spectroscopy. *J. Phys. B: At., Mol. Opt. Phys.* **2013**, *46*, 164023.
(307) Kimura, K.; Fukuzawa, H.; Sakai, K.; Mondal, S.; Kukk, E.; Kono, Y.; Nagaoka, S.; Tamenori, Y.; Saito, N.; Ueda, K. Efficient Site-Specific Low-Energy Electron Production via Interatomic Coulombic Decay Following Resonant Auger Decay in Argon Dimers. *Phys. Rev. A: At., Mol., Opt. Phys.* **2013**, *87*, 043414.
(308) Kimura, K.; Fukuzawa, H.; Tachibana, T.; Ito, Y.; Mondal, S.; Okunishi, M.; Schöffler, M.; Williams, J.; Jiang, Y.; Tamenori, Y.; et al. Controlling Low-Energy Electron Emission via Resonant-Auger-Induced Interatomic Coulombic Decay. *J. Phys. Chem. Lett.* **2013**, *4*, 1838−1848.
(309) Trinter, F.; Schöffler, M. S.; Kim, H. K.; Sturm, F. P.; Cole, K.; Neumann, N.; Vredenborg, A.; Williams, J.; Bocharova, I.; Guillemin, R.; et al. Resonant Auger Decay Driving Intermolecular Coulombic Decay in Molecular Dimers. *Nature* **2014**, *505*, 664−666.
(310) Kim, H. K.; Gassert, H.; Titze, J. N.; Waitz, M.; Voigtsberger, J.; Trinter, F.; Becht, J.; Kalinin, A.; Neumann, N.; Zhou, C.; et al. Orientation Dependence in Multiple Ionization of He_2 and Ne_2 Induced by Fast, Highly Charged Ions: Probing the Impact-Parameter-Dependent Ionization Probability in 11.37-MeV/u S^{14+} Collisions with He and Ne. *Phys. Rev. A: At., Mol., Opt. Phys.* **2014**, *89*, 022704.
(311) Burzynski, P.; Trinter, F.; Williams, J. B.; Weller, M.; Waitz, M.; Pitzer, M.; Voigtsberger, J.; Schober, C.; Kastirke, G.; Müller, C.; et al. Interatomic-Coulombic-Decay-Induced Recapture of Photoelectrons in Helium Dimers. *Phys. Rev. A: At., Mol., Opt. Phys.* **2014**, *90*, 022515.
(312) Iskandar, W.; Matsumoto, J.; Leredde, A.; Fléchard, X.; Gervais, B.; Guillous, S.; Hennecart, D.; Méry, A.; Rangama, J.; Zhou, C. L.; et al. Interatomic Coulombic Decay as a New Source of Low Energy Electrons in Slow Ion-Dimer Collisions. *Phys. Rev. Lett.* **2015**, *114*, 033201.
(313) Pflüger, T.; Ren, X.; Dorn, A. Electron-Impact-Induced Dissociation of Small Argon Clusters. *Phys. Rev. A: At., Mol., Opt. Phys.* **2015**, *91*, 052701.

https://dx.doi.org/10.1021/acs.chemrev.0c00106
Chem. Rev. 2020, 120, 11295−11369

(314) Ren, X.; Al Maalouf, E. J.; Dorn, A.; Denifl, S. Direct Evidence of Two Interatomic Relaxation Mechanisms in Argon Dimers Ionized by Electron Impact. *Nat. Commun.* **2016**, *7*, 11093−11098.
(315) Sann, H.; Schober, C.; Mhamdi, A.; Trinter, F.; Müller, C.; Semenov, S. K.; Stener, M.; Waitz, M.; Bauer, T.; Wallauer, R.; et al. Delocalization of a Vacancy across Two Neon Atoms Bound by the van der Waals Force. *Phys. Rev. Lett.* **2016**, *117*, 263001.
(316) Sann, H.; Havermeier, T.; Kim, H.-K.; Sturm, F.; Trinter, F.; Waitz, M.; Zeller, S.; Ulrich, B.; Meckel, M.; Voss, S.; et al. Interatomic Coulombic Decay of HeNe Dimers after Ionization and Excitation of He and Ne. *Chem. Phys.* **2017**, *482*, 221−225.
(317) Ouchi, T.; Fukuzawa, H.; Sakai, K.; Mazza, T.; Schöffler, M.; Nagaya, K.; Tamenori, Y.; Saito, N.; Ueda, K. Interatomic Coulombic Decay and Electron-Transfer-Mediated Decay Following Triple Ionization of Ne_2 and NeAr. *Chem. Phys.* **2017**, *482*, 244−248.
(318) Ouchi, T.; Stumpf, V.; Miteva, T.; Fukuzawa, H.; Sakai, K.; Liu, X.-J.; Mazza, T.; Schöffler, M.; Iwayama, H.; Nagaya, K.; et al. Ion Pair Formation in the NeAr Dimer Irradiated by Monochromatic Soft X-rays. *Chem. Phys.* **2017**, *482*, 178−184.
(319) Ren, X.; Wang, E.; Skitnevskaya, A. D.; Trofimov, A. B.; Gokhberg, K.; Dorn, A. Experimental Evidence for Ultrafast Intermolecular Relaxation Processes in Hydrated Biomolecules. *Nat. Phys.* **2018**, *14*, 1062−1067.
(320) Kazandjian, S.; Rist, J.; Weller, M.; Wiegandt, F.; Aslitürk, D.; Grundmann, S.; Kircher, M.; Nalin, G.; Pitters, D.; Vela Pérez, I.; et al. Frustrated Coulomb Explosion of Small Helium Clusters. *Phys. Rev. A: At., Mol., Opt. Phys.* **2018**, *98*, No. 050701(R).
(321) Mhamdi, A.; Rist, J.; Havermeier, T.; Dörner, R.; Jahnke, T.; Demekhin, P. V. Theoretical Study of Molecular Frame Angular Emission Distributions of Electrons Emitted by Interatomic Coulombic Decay from Helium Dimers. *Phys. Rev. A: At., Mol., Opt. Phys.* **2020**, *101*, 023404.
(322) Fukuzawa, H.; Li, Y.; You, D.; Sakakibara, Y.; Yamada, S.; Ito, Y.; Takanashi, T.; Oura, M.; Saito, N.; Ueda, K. Low-Energy-Electron Production after 2p Ionization of Argon Clusters. *Phys. Rev. A: At., Mol., Opt. Phys.* **2019**, *99*, 042505.
(323) Iskandar, W.; Gatton, A. S.; Gaire, B.; Sturm, F. P.; Larsen, K. A.; Champenois, E. G.; Shivaram, N.; Moradmand, A.; Williams, J. B.; Berry, B.; et al. Tracing Intermolecular Coulombic Decay of Carbon-Dioxide Dimers and Oxygen Dimers after Valence Photoionization. *Phys. Rev. A: At., Mol., Opt. Phys.* **2019**, *99*, 043414.
(324) Schmid, G.; Schnorr, K.; Augustin, S.; Meister, S.; Lindenblatt, H.; Trost, F.; Liu, Y.; Miteva, T.; Gisselbrecht, M.; Düsterer, S.; et al. Tracing Charge Transfer in Argon Dimers by XUV-pump IR-probe Experiments at FLASH. *J. Chem. Phys.* **2019**, *151*, 084314.
(325) Hans, A.; Schmidt, P.; Ozga, C.; Hartmann, G.; Holzapfel, X.; Ehresmann, A.; Knie, A. Extreme Ultraviolet to Visible Dispersed Single Photon Detection for Highly Sensitive Sensing of Fundamental Processes in Diverse Samples. *Materials* **2018**, *11*, 869.
(326) Hans, A.; Ozga, C.; Schmidt, P.; Hartmann, G.; Nehls, A.; Wenzel, P.; Richter, C.; Lant, C.; Holzapfel, X.; Viehmann, J. H.; et al. Setup for Multicoincidence Experiments of Photons in the Extreme Ultraviolet to Visible Spectral Range and Charged Particles − The Solid Angle Maximization Approach. *Rev. Sci. Instrum.* **2019**, *90*, 093104.
(327) Bradeanu, I. L.; Flesch, R.; Meyer, M.; Jochims, H.-W.; Rühl, E. Radiative Relaxation in 2p-Excited Argon Clusters: Evidence for the Interatomic Coulombic Decay Mechanism. *Eur. Phys. J. D* **2005**, *36*, 173−178.
(328) Gejo, T.; Iseda, M.; Tamura, T.; Honma, K.; Harries, J. R.; Tamenori, Y. Investigation of the 2p Ionization Threshold Thresh of Ar Clusters by Observation of the Fluorescence Lifetime. *J. Electron Spectrosc. Relat. Phenom.* **2007**, *155*, 119−123.
(329) Hans, A.; Knie, A.; Förstel, M.; Schmidt, P.; Reiß, P.; Ozga, C.; Hergenhahn, U.; Ehresmann, A. Determination of Absolute Cross Sections for Cluster-Specific Decays. *J. Phys. B: At., Mol. Opt. Phys.* **2016**, *49*, 105101.
(330) Chen, J. C. Y. Interpretation of the Cross Section for Vibrational Excitation of Molecules by Electrons. *J. Chem. Phys.* **1966**, *45*, 2710−2712.
(331) Hasted, J. B.; Awan, A. M. Resonance Scattering of Electrons by Diatomic Molecules. *J. Phys. B: At. Mol. Phys.* **1969**, *2*, 367−380.
(332) Zewail, A. Femtochemistry. Past, Present, and Future. *Pure Appl. Chem.* **2009**, *72*, 2219−2231.
(333) Allaria, E.; Bencivenga, F.; Borghes, R.; Capotondi, F.; Castronovo, D.; Charalambous, P.; Cinquegrana, P.; Danailov, M.; De Ninno, G.; Demidovich, A.; et al. Two-Colour Pump−Probe Experiments with a Twin-Pulse-Seed Extreme Ultraviolet Free-Electron Laser. *Nat. Commun.* **2013**, *4*, 2476.
(334) Fukuzawa, H.; Takanashi, T.; Kukk, E.; Motomura, K.; Wada, S.; Nagaya, K.; Ito, Y.; Nishiyama, T.; Nicolas, C.; Kumagai, Y.; et al. Real-Time Observation of X-ray-Induced Intramolecular and Interatomic Electronic Decay in CH_2I_2. *Nat. Commun.* **2019**, *10*, 2186−2195.
(335) Niehaus, A. Analysis of Post-Collision Interactions in Auger Processes Following Near-Threshold Inner-Shell Photoionization. *J. Phys. B: At. Mol. Phys.* **1977**, *10*, 1845−1857.
(336) Schütte, B.; Bauch, S.; Frühling, U.; Wieland, M.; Gensch, M.; Plönjes, E.; Gaumnitz, T.; Azima, A.; Bonitz, M.; Drescher, M. Evidence for Chirped Auger-Electron Emission. *Phys. Rev. Lett.* **2012**, *108*, 253003.
(337) Guillemin, R.; Sheinerman, S.; Bomme, C.; Journel, L.; Marin, T.; Marchenko, T.; Kushawaha, R. K.; Trcera, N.; Piancastelli, M. N.; Simon, M. Ultrafast Dynamics in Postcollision Interaction after Multiple Auger Decays in Argon 1 s Photoionization. *Phys. Rev. Lett.* **2012**, *109*, 013001.
(338) Bauch, S.; Bonitz, M. Theoretical Description of Field-Assisted Postcollision Interaction in Auger Decay of Atoms. *Phys. Rev. A: At., Mol., Opt. Phys.* **2012**, *85*, 053416.
(339) Kienberger, R.; Goulielmakis, E.; Uiberacker, M.; Baltuska, A.; Yakovlev, V.; Bammer, F.; Scrinzi, A.; Westerwalbesloh, T.; Kleineberg, U.; Heinzmann, U.; et al. Atomic Transient Recorder. *Nature* **2004**, *427*, 817−821.
(340) Itatani, J.; Quéré, F.; Yudin, G. L.; Ivanov, M. Y.; Krausz, F.; Corkum, P. B. Attosecond Streak Camera. *Phys. Rev. Lett.* **2002**, *88*, 173903.
(341) Drescher, M.; Hentschel, M.; Kienberger, R.; Uiberacker, M.; Yakovlev, V.; Scrinzi, A.; Westerwalbesloh, T.; Kleineberg, U.; Heinzmann, U.; Krausz, F. Time-Resolved Atomic Inner-Shell Spectroscopy. *Nature* **2002**, *419*, 803−807.
(342) Cavalieri, A. L.; Müller, N.; Uphues, T.; Yakovlev, V. S.; Baltuška, A.; Horvath, B.; Schmidt, B.; Blümel, L.; Holzwarth, R.; Hendel, S.; et al. Attosecond Spectroscopy in Condensed Matter. *Nature* **2007**, *449*, 1029−1032.
(343) Schultze, M.; Fieß, M.; Karpowicz, N.; Gagnon, J.; Korbman, M.; Hofstetter, M.; Neppl, S.; Cavalieri, A. L.; Komninos, Y.; Mercouris, T.; et al. Delay in Photoemission. *Science* **2010**, *328*, 1658−1662.
(344) Frühling, U.; Wieland, M.; Gensch, M.; Gebert, T.; Schütte, B.; Krikunova, M.; Kalms, R.; Budzyn, F.; Grimm, O.; Rossbach, J.; et al. Single-Shot Terahertz-Field-Driven X-ray Streak Camera. *Nat. Photonics* **2009**, *3*, 523−528.
(345) Sansone, G.; Pfeifer, T.; Simeonidis, K.; Kuleff, A. I. Electron Correlation in Real Time. *ChemPhysChem* **2012**, *13*, 661−680.
(346) Fasshauer, E. Non-Nearest Neighbour ICD in Clusters. *New J. Phys.* **2016**, *18*, 043028.
(347) Öhrwall, G.; Ottosson, N.; Pokapanich, W.; Legendre, S.; Svensson, S.; Björneholm, O. Charge Dependence of Solvent-Mediated Intermolecular Coster-Kronig Decay Dynamics of Aqueous Ions. *J. Phys. Chem. B* **2010**, *114*, 17057−17061.
(348) Rander, T.; Schulz, J.; Huttula, M.; Mökinen, A.; Tchaplyguine, M.; Svensson, S.; Öhrwall, G.; Björneholm, O.; Aksela, S.; Aksela, H. Core-Level Electron Spectroscopy on the Sodium Dimer Na 2p Level. *Phys. Rev. A: At., Mol., Opt. Phys.* **2007**, *75*, 032510.

https://dx.doi.org/10.1021/acs.chemrev.0c00106
Chem. Rev. 2020, 120, 11295−11369

(349) Ågren, H.; Siegbahn, H. Semi-Internal Correlation in the Auger Electron Spectrum of H_2O. *Chem. Phys. Lett.* **1980**, *69*, 424−429.
(350) Ågren, H.; Siegbahn, H. Many-Electron Contributions in the Auger Spectrum of CO. *Chem. Phys. Lett.* **1980**, *72*, 498−503.
(351) Ågren, H. On the Interpretation of Molecular Valence Auger Spectra. *J. Chem. Phys.* **1981**, *75*, 1267−1283.
(352) Jing, Q.; Madsen, L. B. Dynamics of Interatomic Coulombic Decay in Neon Dimers by XUV-Pump-XUV-Probe Spectroscopy. *Phys. Rev. A: At., Mol., Opt. Phys.* **2019**, *99*, 013409.
(353) Yabashi, M.; Yabashi, M.; Tanaka, H.; Tanaka, T.; Tomizawa, H.; Togashi, T.; Nagasono, M.; Ishikawa, T.; Harries, J.; Hikosaka, A.; et al. Compact XFEL and AMO sciences: SACLA and SCSS. *J. Phys. B: At., Mol. Opt. Phys.* **2013**, *46*, 164001.
(354) Gislason, E. Series Expansions for Franck-Condon Factors. I. Linear Potential and the Reflection Approximation. *J. Chem. Phys.* **1973**, *58*, 3702−3707.
(355) Jabbari, G.; Sadri, K.; Cederbaum, L. S.; Gokhberg, K. Strong Enhancement of Cage Effects in Water Photolysis Caused by Interatomic Coulombic Decay. *J. Chem. Phys.* **2016**, *144*, 164307.
(356) Barth, S.; Marburger, S.; Joshi, S.; Ulrich, V.; Kugeler, O.; Hergenhahn, U. Interface Identification by Non-Local Autoionization Transitions. *Phys. Chem. Chem. Phys.* **2006**, *8*, 3218−3222.
(357) Barth, S.; Ončák, M.; Ulrich, V.; Mucke, M.; Lischke, T.; Slavíček, P.; Hergenhahn, U. Valence Ionization of Water Clusters: From Isolated Molecules to Bulk. *J. Phys. Chem. A* **2009**, *113*, 13519−13527.
(358) Svoboda, O.; Hollas, D.; Ončák, M.; Slavíček, P. Reaction Selectivity in Ionized Water Dimer: Nonadiabatic Ab Initio Dynamics Simulations. *Phys. Chem. Chem. Phys.* **2013**, *15*, 11531−11542.
(359) Buch, V.; Bauerecker, S.; Devlin, J. P.; Buck, U.; Kazimirski, J. K. Solid Water Clusters in the Size Range of Tens-Thousands of H2O: a Combined Computational/Spectroscopic Outlook. *Int. Rev. Phys. Chem.* **2004**, *23*, 375−433.
(360) Reid, K. L. Photoelectron Angular Distributions. *Annu. Rev. Phys. Chem.* **2003**, *54*, 397−424.
(361) Reid, K. L. Photoelectron Angular Distributions: Developments in Applications to Isolated Molecular Systems. *Mol. Phys.* **2012**, *110*, 131−147.
(362) Yagishita, A. Photoelectron Angular Distributions from Single Oriented Molecules: Past, Present and Future. *J. Electron Spectrosc. Relat. Phenom.* **2015**, *200*, 247−256.
(363) Stolow, A.; Underwood, J. G. Time-Resolved Photoelectron Spectroscopy of Nonadiabatic Dynamics in Polyatomic Molecules. *Adv. Chem. Phys.* **2008**, 497−584.
(364) Miteva, T.; Kazandjian, S.; Kolorenč, P.; Votavová, P.; Sisourat, N. Interatomic Coulombic Decay Mediated by Ultrafast Superexchange Energy Transfer. *Phys. Rev. Lett.* **2017**, *119*, 083403.
(365) Votavová, P.; Miteva, T.; Engin, S.; Kazandjian, S.; Kolorenč, P.; Sisourat, N. Mechanism of Superexchange Interatomic Coulombic Decay in Rare-Gas Clusters. *Phys. Rev. A: At., Mol., Opt. Phys.* **2019**, *100*, 022706.
(366) Bennett, R.; Votavová, P.; Kolorenč, P.; Miteva, T.; Sisourat, N.; Buhmann, S. Y. Virtual Photon Approximation for Three-Body Interatomic Coulombic Decay. *Phys. Rev. Lett.* **2019**, *122*, 153401.
(367) Stoychev, S. D.; Kuleff, A. I.; Tarantelli, F.; Cederbaum, L. S. On the Doubly Ionized States of Ar_2 and their Intra- and Interatomic Decay to Ar_2^{3+}. *J. Chem. Phys.* **2008**, *128*, 014307.
(368) Stoychev, S. D.; Kuleff, A. I.; Tarantelli, F.; Cederbaum, L. S. On the Interatomic Electronic Processes Following Auger Decay in Neon Dimer. *J. Chem. Phys.* **2008**, *129*, 074307.
(369) Keshavarz, E.; Farrokhpour, H.; Sabzyan, H.; Noorisafa, Z.; Kivimäki, A.; Richter, R. Core Photoionization of the Argon Dimer in the Photon-Energy Range of 255−340 eV Studied by a Photoelectron-Photoion-Photoion Coincidence Technique. *Phys. Rev. A: At., Mol., Opt. Phys.* **2014**, *89*, 053409.
(370) Barth, S.; Joshi, S.; Marburger, S.; Ulrich, V.; Lindblad, A.; Öhrwall, G.; Björneholm, O.; Hergenhahn, U. Observation of Resonant Interatomic Coulombic Decay in Ne Clusters. *J. Chem. Phys.* **2005**, *122*, 241102.
(371) Yan, S.; Zhang, P.; Ma, X.; Xu, S.; Tian, S. X.; Li, B.; Zhu, X. L.; Feng, W. T.; Zhao, D. M. Dissociation Mechanisms of the Ar Trimer Induced by a Third Atom in High-Energy Electron-Impact Ionization. *Phys. Rev. A: At., Mol., Opt. Phys.* **2014**, *89*, 062707.
(372) Thissen, R.; Lablanquie, P.; Hall, R. I.; Ukai, M.; Ito, K. Photoionization of Argon, Krypton and Xenon Clusters in the Inner Valence Shell Region. *Eur. Phys. J. D* **1998**, *4*, 335−332.
(373) Patanen, M.; Nicolas, C.; Liu, X.-J.; Travnikova, O.; Miron, C. Structural Characterization of Small Xe Clusters Using their 5s Correlation Satellite Electron Spectrum. *Phys. Chem. Chem. Phys.* **2013**, *15*, 10112−10117.
(374) Grüll, A.; Voitkiv, A. B.; Müller, C. Two-Center Electron-Impact Ionization via Collisional Excitation-autoionization. *Phys. Rev. A: At., Mol., Opt. Phys.* **2019**, *100*, 032702.
(375) Fedyk, J.; Voitkiv, A. B.; Müller, C. Strong-Field Photoionization in Two-Center Atomic Systems. *Phys. Rev. A: At., Mol., Opt. Phys.* **2018**, *98*, 033418.
(376) Fasshauer, E.; Madsen, L. B. Time-Resolved Spectroscopy of Interparticle Coulombic Decay Processes. *Phys. Rev. A* **2020**, *101*, 043414 DOI: 10.1103/PhysRevA.101.043414.
(377) Manschwetus, B.; Rottke, H.; Steinmeyer, G.; Foucar, L.; Czasch, A.; Schmidt-Böcking, H.; Sandner, W. Mechanisms Underlying Strong-Field Double Ionization of Argon Dimers. *Phys. Rev. A: At., Mol., Opt. Phys.* **2010**, *82*, 013413.
(378) Haberland, H.; von Issendorff, B.; Kolar, T.; Kornmeier, H.; Ludewigt, C.; Risch, A. Electronic and Geometric Structure of $Ar_n^+$and CXe_n^+lusters: The Solvation of Rare-Gas Ions by their Parent Atoms. *Phys. Rev. Lett.* **1991**, *67*, 3290−3293.
(379) Ayotte, P.; Weddle, G. H.; Bailey, C. G.; Johnson, M. A.; Vila, F.; Jordan, K. D. Infrared Spectroscopy of Negatively Charged Water Clusters: Evidence for a Linear Network. *J. Chem. Phys.* **1999**, *110*, 6268−6277.
(380) Sukhorukov, V.; Petrov, I.; Lagutin, B.; Ehresmann, A.; Schartner, K.-H.; Schmoranzer, H. Many-Electron Dynamics of Atomic Processes Studied by Photon-Induced Fluorescence Spectroscopy. *Phys. Rep.* **2019**, *786*, 1−60.
(381) Möbus, B.; Magel, B.; Schartner, K.-H.; Langer, B.; Becker, U.; Wildberger, M.; Schmoranzer, H. Measurements of Absolute Ar 3s Photoionization Cross Sections. *Phys. Rev. A: At., Mol., Opt. Phys.* **1993**, *47*, 3888−3893.
(382) Bilodeau, R. C.; Walter, C. W.; Dumitriu, I.; Gibson, N. D.; Ackerman, G. D.; Bozek, J. D.; Rude, B. S.; Santra, R.; Cederbaum, L. S.; Berrah, N. Photo Double Detachment of CN^-: Electronic Decay from an Inner-Valence Hole in Molecular Anions. *Chem. Phys. Lett.* **2006**, *426*, 237−241.
(383) Averbukh, V.; Kolorenč, P. Collective Interatomic Decay of Multiple Vacancies in Clusters. *Phys. Rev. Lett.* **2009**, *103*, 183001.
(384) Žitnik, M.; Püttner, R.; Goldsztejn, G.; Bučar, K.; Kavčič, M.; Mihelič, A.; Marchenko, T.; Guillemin, R.; Journel, L.; Travnikova, O.; et al. Two-to-one Auger decay of a double *L* vacancy in argon. *Phys. Rev. A: At., Mol., Opt. Phys.* **2016**, *93*, 021401.
(385) Cederbaum, L. S. Ultrafast Intermolecular Energy Transfer from Vibrations to Electronic Motion. *Phys. Rev. Lett.* **2018**, *121*, 223001.
(386) Thomas, T. D.; Miron, C.; Wiesner, K.; Morin, P.; Carroll, T. X.; Saethre, L. J. Anomalous Natural Linewidth in the 2*p* Photoelectron Spectrum of SiF_4. *Phys. Rev. Lett.* **2002**, *89*, 223001.
(387) Püttner, R.; Marchenko, T.; Guillemin, R.; Journel, L.; Goldsztejn, G.; Céolin, D.; Takahashi, O.; Ueda, K.; Lago, A. F.; Piancastelli, M. N.; et al. Si 1 s^{-1}, 2 s^{-1}, and $2p^{-1}$ Lifetime Broadening of SiX_4 (X = F,Cl,Br,CH_3) Molecules: SiF_4 Anomalous Behaviour Reassessed. *Phys. Chem. Chem. Phys.* **2019**, *21*, 8827−8836.
(388) Haberland, H. *Clusters of Atoms and Molecules*; Springer: Berlin Heidelberg New York, 1994.
(389) Hagena, O. F. Scaling laws for condensation in nozzle flows. *Phys. Fluids* **1974**, *17*, 894−896.

https://dx.doi.org/10.1021/acs.chemrev.0c00106
Chem. Rev. 2020, 120, 11295−11369

(390) Hagena, O. F. Nucleation and Growth of Clusters in Expanding Nozzle Flows. *Surf. Sci.* **1981**, *106*, 101−116.
(391) Hagena, O. F. Cluster Ion sources. *Rev. Sci. Instrum.* **1992**, *63*, 2374−2379.
(392) Buck, U.; Krohne, R. Cluster Size Determination from Diffractive He Atom Scattering. *J. Chem. Phys.* **1996**, *105*, 5408−5415.
(393) Karnbach, R.; Joppien, M.; Stapelfeldt, J.; Wörmer, J.; Möller, T. CLULU: An Experimental Setup for Luminescence Measurements on van der Waals Clusters with Synchrotron Radiation. *Rev. Sci. Instrum.* **1993**, *64*, 2838−2849.
(394) Bobbert, C.; Schütte, S.; Steinbach, C.; Buck, U. Fragmentation and reliable Size Distributions of large ammonia and Water Clusters. *Eur. Phys. J. D* **2002**, *19*, 183−192.
(395) Wiethoff, P.; Ehrke, H.-U.; Menzel, D.; Feulner, P. Doubly Excited Rydberg Series in Solid Neon Studied by Electron and Photodesorption Spectroscopies. *Phys. Rev. Lett.* **1995**, *74*, 3792−3795.
(396) Lundwall, M.; Pokapanich, W.; Bergersen, H.; Lindblad, A.; Rander, T.; Öhrwall, G.; Tchaplyguine, M.; Barth, S.; Hergenhahn, U.; Svensson, S.; et al. Self-Assembled Heterogeneous Argon/Neon Core-Shell Clusters Studied by Photoelectron Spectroscopy. *J. Chem. Phys.* **2007**, *126*, 214706.
(397) Hoener, M.; Rolles, D.; Aguilar, A.; Bilodeau, R. C.; Esteves, D.; Velasco, P.; Pešić, Z. D.; Red, E.; Berrah, N. Site-Selective Ionization and Relaxation Dynamics in Heterogeneous Nanosystems. *Phys. Rev. A: At., Mol., Opt. Phys.* **2010**, *81*, No. 021201(R).
(398) Yeh, J.; Lindau, I. Atomic Subshell Photoionization Cross Sections and Asymmetry Parameters: $1 \leq Z \leq 103$. *At. Data Nucl. Data Tables* **1985**, *32*, 1−155.
(399) Santra, R.; Zobeley, J.; Cederbaum, L. S.; Tarantelli, F. InterMolecular Coulombic Decay of Clusters. *J. Electron Spectrosc. Relat. Phenom.* **2001**, *114−116*, 41−47.
(400) Ltaief, L. B.; Hans, A.; Schmidt, P.; Holzapfel, X.; Wiegandt, F.; Reiss, P.; Küstner-Wetekam, C.; Jahnke, T.; Dörner, R.; Knie, A.; et al. VUV Photon Emission from Ne Clusters of Varying Sizes Following Photon and Photoelectron Excitations. *J. Phys. B: At., Mol. Opt. Phys.* **2018**, *51*, 065002.
(401) Matsumoto, J.; Leredde, A.; Flechard, X.; Hayakawa, K.; Shiromaru, H.; Rangama, J.; Zhou, C. L.; Guillous, S.; Hennecart, D.; Muranaka, T.; et al. Asymmetry in Multiple-Electron Capture Revealed by Radiative Charge Transfer in Ar Dimers. *Phys. Rev. Lett.* **2010**, *105*, 263202.
(402) Voitkiv, A. B.; Müller, C.; Zhang, S. F.; Ma, X. Dynamic Two-Center Resonant Photoionization in Slow Atomic Collisions. *New J. Phys.* **2019**, *21*, 103010.
(403) Golan, A.; Ahmed, M. Ionization of Water Clusters is Mediated by Exciton Energy Transfer from Argon Clusters. *J. Phys. Chem. Lett.* **2012**, *3*, 458−462.
(404) Kočišek, J.; Lengyel, J.; Fárník, M.; Slavíček, P. Energy and Charge Transfer in Ionized Argon Coated Water Clusters. *J. Chem. Phys.* **2013**, *139*, 214308.
(405) Pedersen, H. B.; Domesle, C.; Lammich, L.; Dziarzhytski, S.; Guerassimova, N.; Treusch, R.; Harbo, L. S.; Heber, O.; Jordon-Thaden, B.; Arion, T.; et al. Photolysis of Water-Radical Ions H_2O^+ in the XUV: Fragmentation through Dicationic States. *Phys. Rev. A: At., Mol., Opt. Phys.* **2013**, *87*, 013402.
(406) Tavernelli, I.; Gaigeot, M.; Vuilleumier, R.; Stia, C.; Hervé du Penhoat, M.; Politis, M. TimeDependent Density Functional Theory Molecular Dynamics Simulations of Liquid Water Radiolysis. *ChemPhysChem* **2008**, *9*, 2099−2103.
(407) Popov, A. A.; Yang, S.; Dunsch, L. Endohedral Fullerenes. *Chem. Rev.* **2013**, *113*, 5989−6113.
(408) Connerade, J.-P.; Dolmatov, V. K.; Manson, S. T. A Unique Situation for an Endohedral Metallofullerene. *J. Phys. B: At., Mol. Opt. Phys.* **1999**, *32*, L395−L403.
(409) Dolmatov, V. K.; Brewer, P.; Manson, S. T. Photoionization of Atoms Confined in Giant Single-Walled and Multi-Walled Fullerenes. *Phys. Rev. A: At., Mol., Opt. Phys.* **2008**, *78*, 013415.
(410) Stumpf, V.; Gokhberg, K.; Cederbaum, L. S. The Role of Metal Ions in X-ray-Induced Photochemistry. *Nat. Chem.* **2016**, *8*, 237−241.
(411) Amusia, M. Y.; Baltenkov, A. S. Vacancy Decay in Endohedral Atoms. *Phys. Rev. A: At., Mol., Opt. Phys.* **2006**, *73*, 063206.
(412) Korol, A. V.; Solov'yov, A. V. Vacancy Decay in Endohedral Atoms: the Role of an Atom's Non-Central Position. *J. Phys. B: At., Mol. Opt. Phys.* **2011**, *44*, 085001.
(413) Javani, M. H.; Wise, J. B.; De, R.; Madjet, M. E.; Manson, S. T.; Chakraborty, H. S. Resonant Auger-Intersite-Coulombic Hybridized Decay in the Photoionization of Endohedral Fullerenes. *Phys. Rev. A: At., Mol., Opt. Phys.* **2014**, *89*, 063420.
(414) Magrakvelidze, M.; De, R.; Javani, M. H.; Madjet, M. E.; Manson, S. T.; Chakraborty, H. S. Coherence of Auger and Inter-Coulombic Decay Processes in the Photoionization of $Ar@C_{60}$ versus $Kr@C_{60}$. *Eur. Phys. J. D* **2016**, *70*, 96−102.
(415) De, R.; Magrakvelidze, M.; Madjet, M. E; Manson, S. T; Chakraborty, H. S First Prediction of Inter-Coulombic Decay of C_{60} Inner Vacancies Through the Continuum of Confined Atoms. *J. Phys. B: At., Mol. Opt. Phys.* **2016**, *49*, 11LT01.
(416) Müller, A.; Schippers, S.; Habibi, M.; Esteves, D.; Wang, J. C.; Phaneuf, R. A.; Kilcoyne, A. L. D.; Aguilar, A.; Dunsch, L. Significant Redistribution of Ce 4*d* Oscillator Strength Observed in Photoionization of Endohedral $Ce@C_{82}^+$Ions. *Phys. Rev. Lett.* **2008**, *101*, 133001.
(417) Müller, A.; Martins, M.; Kilcoyne, A.; Phaneuf, R. A.; Hellhund, J.; Borovik, A., Jr.; Holste, K.; Bari, S.; Buhr, T.; Klumpp, S.; et al. Photoionization and Photofragmentation of Singly Charged Positive and Negative $Sc_3N@C_{80}$ Endohedral Fullerene Ions. *Phys. Rev. A: At., Mol., Opt. Phys.* **2019**, *99*, 063401.
(418) Müller, I. B.; Cederbaum, L. S. Ionization and Double Ionization of Small Water Clusters. *J. Chem. Phys.* **2006**, *125*, 204305.
(419) Pimblott, S. M.; LaVerne, J. A. Production of Low-Energy Electrons by Ionizing Radiation. *Radiat. Phys. Chem.* **2007**, *76*, 1244−1247.
(420) Kryzhevoi, N. V.; Cederbaum, L. S. Using pH Value To Control Intermolecular Electronic Decay. *Angew. Chem., Int. Ed.* **2011**, *50*, 1306−1309.
(421) Müller, I. B.; Zobeley, J.; Cederbaum, L. S. Comparison of Electronic Decay of Valence Ionized Fluorinated Carbanions and their Acids. *J. Chem. Phys.* **2002**, *117*, 1085−1097.
(422) Evlyukhin, E.; Kim, E.; Goldberger, D.; Cifligu, P.; Schyck, S.; Weck, P. F.; Pravica, M. High-Pressure-Assisted X-ray-Induced Damage as a New Route for Chemical and Structural Synthesis. *Phys. Chem. Chem. Phys.* **2018**, *20*, 18949−18956.
(423) Aziz, E. F.; Ottosson, N.; Faubel, M.; Hertel, I. V.; Winter, B. Interaction between Liquid Water and Hydroxide Revealed by Core-Hole De-Excitation. *Nature* **2008**, *455*, 89−91.
(424) Seidel, R.; Thürmer, S.; Winter, B. Photoelectron Spectroscopy Meets Aqueous Solution: Studies from a Vacuum Liquid Microjet. *J. Phys. Chem. Lett.* **2011**, *2*, 633−641.
(425) Winter, B. Liquid Microjet for Photoelectron Spectroscopy. *Nucl. Instrum. Methods Phys. Res., Sect. A* **2009**, *601*, 139−150.
(426) Thürmer, S.; Ončák, M.; Ottosson, N.; Seidel, R.; Hergenhahn, U.; Bradforth, S. E.; Slavíček, P.; Winter, B. On the Nature and Origin of Dicationic, Charge-Separated Species Formed in Liquid Water on X-ray Irradiation. *Nat. Chem.* **2013**, *5*, 590−596.
(427) Slavíček, P.; Kryzhevoi, N. V.; Aziz, E. F.; Winter, B. Relaxation Processes in Aqueous Systems upon X-ray Ionization: Entanglement of Electronic and Nuclear Dynamics. *J. Phys. Chem. Lett.* **2016**, *7*, 234−243.
(428) Pettersson, L. Radiation Chemistry: Radical Water. *Nat. Chem.* **2013**, *5*, 553−554.
(429) Björneholm, O.; Sundin, S.; Svensson, S.; Marinho, R. R. T.; Naves de Brito, A.; Gel'mukhanov, F.; Ågren, H. Femtosecond Dissociation of Core-Excited HCl Monitored by Frequency Detuning. *Phys. Rev. Lett.* **1997**, *79*, 3150−3153.

https://dx.doi.org/10.1021/acs.chemrev.0c00106
Chem. Rev. 2020, 120, 11295−11369

(430) Brühwiler, P. A.; Karis, O.; Mårtensson, N. Charge-transfer dynamics studied using resonant core spectroscopies. *Rev. Mod. Phys.* **2002**, *74*, 703−740.
(431) Winter, B.; Aziz, E. F.; Hergenhahn, U.; Faubel, M.; Hertel, I. V. Hydrogen Bonds in Liquid Water Studied by Photoelectron Spectroscopy. *J. Chem. Phys.* **2007**, *126*, 124504.
(432) Sankari, R.; Ehara, M.; Nakatsuji, H.; Senba, Y.; Hosokawa, K.; Yoshida, H.; De Fanis, A.; Tamenori, Y.; Aksela, S.; Ueda, K. Vibrationally resolved O 1s photoelectron spectrum of water. *Chem. Phys. Lett.* **2003**, *380*, 647−653.
(433) Unger, I.; Thürmer, S.; Hollas, D.; Aziz, E. F.; Winter, B.; Slavíček, P. Ultrafast Proton and Electron Dynamics in Core-Ionized Hydrated Hydrogen Peroxide: Photoemission Measurements with Isotopically Substituted Hydrogen Peroxide. *J. Phys. Chem. C* **2014**, *118*, 29142−29150.
(434) Unger, I.; Hollas, D.; Seidel, R.; Thürmer, S.; Aziz, E. F.; Slavíček, P.; Winter, B. Control of X-ray Induced Electron and Nuclear Dynamics in Ammonia and Glycine Aqueous Solution via Hydrogen Bonding. *J. Phys. Chem. B* **2015**, *119*, 10750−10759.
(435) Thürmer, S.; Unger, I.; Slavíček, P.; Winter, B. Relaxation of Electronically Excited Hydrogen Peroxide in Liquid Water: Insights from Auger-Electron Emission. *J. Phys. Chem. C* **2013**, *117*, 22268−22275.
(436) Hollas, D.; Pohl, M. N.; Seidel, R.; Aziz, E. F.; Slavíček, P.; Winter, B. Aqueous Solution Chemistry of Ammonium Cation in the Auger Time Window. *Sci. Rep.* **2017**, *7*, 756−855.
(437) Steiner, T. The Hydrogen Bond in the Solid State. *Angew. Chem., Int. Ed.* **2002**, *41*, 48−76.
(438) Lindblad, A.; Bergersen, H.; Pokapanich, W.; Tchaplyguine, M.; Öhrwall, G.; Björneholm, O. Charge Delocalization Dynamics of Ammonia in Different Hydrogen Bonding Environments: Free Clusters and in Liquid Water Solution. *Phys. Chem. Chem. Phys.* **2009**, *11*, 1758−1764.
(439) Muller, I. B.; Cederbaum, L. S.; Tarantelli, F. Microsolvation of Li+ in Water Analyzed by Ionization and Double Ionization. *J. Phys. Chem. A* **2004**, *108*, 5831−5844.
(440) Müller, I. B.; Cederbaum, L. S. Electronic Decay Following Ionization of Aqueous Li^+ Microsolvation Clusters. *J. Chem. Phys.* **2005**, *122*, 094305.
(441) Unger, I.; Seidel, R.; Thürmer, S.; Pohl, M. N.; Aziz, E. F.; Cederbaum, L. S.; Muchová, E.; Slavíček, P.; Winter, B.; Kryzhevoi, N. V. Observation of Electron-Transfer-Mediated Decay in Aqueous Solution. *Nat. Chem.* **2017**, *9*, 708−714.
(442) Weber, R.; Winter, B.; Schmidt, P. M.; Widdra, W.; Hertel, I. V.; Dittmar, M.; Faubel, M. Photoemission from Aqueous Alkali-Metal - Iodide Salt Solutions Using EUV Synchrotron Radiation. *J. Phys. Chem. B* **2004**, *108*, 4729−4736.
(443) Winter, B.; Weber, R.; Widdra, W.; Dittmar, M.; Faubel, M.; Hertel, I. V. Full Valence Band Photoemission from Liquid Water Using EUV Synchrotron Radiation. *J. Phys. Chem. A* **2004**, *108*, 2625−2632.
(444) Ottosson, N.; Öhrwall, G.; Björneholm, O. Ultrafast Charge Delocalization Dynamics in Aqueous Electrolytes: New Insights from Auger Electron Spectroscopy. *Chem. Phys. Lett.* **2012**, *543*, 1−11.
(445) Pokapanich, W.; Ottosson, N.; Svensson, S.; Öhrwall, G.; Winter, B.; Björneholm, O. Bond-Breaking, Electron-Pushing and Proton-Pulling: Active and Passive Roles in the Interaction between Aqueous Ions and Water as Manifested in the O1s Auger Decay. *J. Phys. Chem. B* **2012**, *116*, 3−8.
(446) Pokapanich, W.; Bergersen, H.; Bradeanu, I. L.; Marinho, R.; Lindblad, A.; Legendre, S.; Rosso, A.; Svensson, S.; Björneholm, O.; Tchaplyguine, M.; et al. Auger Electron Spectroscopy as a Probe of the Solution of Aqueous Ions. *J. Am. Chem. Soc.* **2009**, *131*, 7264−7271.
(447) Pokapanich, W.; Kryzhevoi, N. V.; Ottosson, N.; Svensson, S.; Cederbaum, L. S.; Öhrwall, G.; Björneholm, O. Ionic-Charge Dependence of the Intermolecular Coulombic Decay Time-scale for Aqueous Ions Probed by the Core-Hole Clock. *J. Am. Chem. Soc.* **2011**, *133*, 13430−13436.
(448) Ohtaki, H.; Radnai, T. Structure and Dynamics of Hydrated Ions. *Chem. Rev.* **1993**, *93*, 1157−1204.
(449) Marcus, Y. Effect of Ions on the Structure of Water: Structure Making and Breaking. *Chem. Rev.* **2009**, *109*, 1346−1370.
(450) Winter, B.; Hergenhahn, U.; Faubel, M.; Björneholm, O.; Hertel, I. V. Hydrogen Bonding in Liquid Water Probed by Resonant Auger-Electron Spectroscopy. *J. Chem. Phys.* **2007**, *127*, 094501.
(451) Nordlund, D.; Ogasawara, H.; Bluhm, H.; Takahashi, O.; Odelius, M.; Nagasono, M.; Pettersson, L. G. M.; Nilsson, A. Probing the Electron Delocalization in Liquid Water and Ice at Attosecond Time Scales. *Phys. Rev. Lett.* **2007**, *99*, 217406.
(452) Wernet, P.; Nordlund, D.; Bergmann, U.; Cavalleri, M.; Odelius, M.; Ogasawara, H.; Näslund, L. A.; Hirsch, T. K.; Ojamäe, L.; Glatzel, P.; et al. The Structure of the First Coordination Shell in Liquid Water. *Science* **2004**, *304*, 995−999.
(453) Ottosson, N.; Odelius, M.; Spangberg, D.; Pokapanich, W.; Svanqvist, M.; Öhrwall, G.; Winter, B.; Björneholm, O. Cations Strongly Reduce Electron-Hopping Rates in Aqueous Solutions. *J. Am. Chem. Soc.* **2011**, *133*, 13489−13495.
(454) Mondal, S. I.; Dey, A.; Sen, S.; Patwari, G. N.; Ghosh, D. Spectroscopic and Ab Initio Investigation of 2,6-Difluorophenylacetylene-Amine Complexes: Coexistence of C-H N and Lone-Pair pi Complexes and Intermolecular Coulombic Decay. *Phys. Chem. Chem. Phys.* **2015**, *17*, 434−443.
(455) Todo, T.; Takemori, H.; Ryo, H.; Ihara, M.; Matsunaga, T.; Nikaido, O.; Sato, K.; Nomura, T. A new Photoreactivating Enzyme that Specifically Repairs Ultraviolet LightInduced (64)Photoproducts. *Nature* **1993**, *361*, 371−374.
(456) Sancar, A. Structure and Function of DNA Photolyase and Cryptochrome BlueLight Photoreceptors. *Chem. Rev.* **2003**, *103*, 2203−2237.
(457) Faraji, S.; Dreuw, A. Physicochemical Mechanism of the Light-Driven DNA Repair by (6−4) Photolyases. *Annu. Rev. Phys. Chem.* **2014**, *65*, 275−292.
(458) Faraji, S.; Dreuw, A. Insights into Light-Driven DNA Repair by Photolyases: Challenges and Opportunities for Electronic Structure Theory. *Photochem. Photobiol.* **2017**, *93*, 37−50.
(459) Klar, T.; Kaiser, G.; Hennecke, U.; Carell, T.; Batschauer, A.; Essen, L.-O. Natural and Non-Natural Antenna Chromophores in the DNA Photolyase from Thermus Thermophilus. *ChemBioChem* **2006**, *7*, 1798−1806.
(460) Krueger, B. P.; ScHoles, G. D.; Fleming, G. R. Couplings and Energy Transfer Pathways between the Pigments of LH2 by the Ab Initio Transition Density Cube Method. *J. Phys. Chem. B* **1998**, *102*, 5378−5386.
(461) Kim, S. T.; Heelis, P. F.; Okamura, T.; Hirata, Y.; Mataga, N.; Sancar, A. Determination of Rates and Yields of Interchromophore (Folate → Flavin) Energy Transfer and Intermolecular (Flavin → DNA) Electron Transfer in *Escherichia coli* Photolyase by Time-Resolved Fluorescence and Absorption Spectroscopy. *Biochemistry* **1991**, *30*, 11262−11270.
(462) Kim, S. T.; Heelis, P. F.; Sancar, A. Energy Transfer (Deazaflavin → FADH2) and Electron Transfer (FADH2 → T < > T) Kinetics in *Anacystic Nidulans* Photolyase. *Biochemistry* **1992**, *31*, 11244−11248.
(463) Bastard, G. *Wave Mechanics Applied to Semiconductor Heterostructures*; Monographies de Physique; Les Éditions de Physique, 1988.
(464) Harrison, P.; Valavanis, A. *Quantum Wells, Wires and Dots*; John Wiley & Sons, Ltd, 2016.
(465) Bera, D.; Qian, L.; Tseng, T.-K.; Holloway, P. H. Quantum Dots and Their Multimodal Applications: A Review. *Materials* **2010**, *3*, 2260−2345.
(466) Waugh, F. R.; Berry, M. J.; Mar, D. J.; Westervelt, R. M.; Campman, K. L.; Gossard, A. C. Single-Electron Charging in Double and Triple Quantum Dots with Tunable Coupling. *Phys. Rev. Lett.* **1995**, *75*, 705−708.
(467) Salfi, J.; Roddaro, S.; Ercolani, D.; Sorba, L.; Savelyev, I.; Blumin, M.; Ruda, H. E.; Beltram, F. Electronic Properties of

https://dx.doi.org/10.1021/acs.chemrev.0c00106
Chem. Rev. 2020, 120, 11295−11369

Quantum Dot Systems Realized in Semiconductor Nanowires. *Semicond. Sci. Technol.* **2010**, *25*, 024007.
(468) van der Wiel, W. G.; De Franceschi, S.; Elzerman, J. M.; Fujisawa, T.; Tarucha, S.; Kouwenhoven, L. P. Electron Transport Through Double Quantum Dots. *Rev. Mod. Phys.* **2002**, *75*, 1−22.
(469) Alivisatos, A. P. Semiconductor Clusters, Nanocrystals, and Quantum Dots. *Science* **1996**, *271*, 933−937.
(470) Cherkes, I.; Moiseyev, N. Electron Relaxation in Quantum Dots by the Interatomic Coulombic Decay Mechanism. *Phys. Rev. B: Condens. Matter Mater. Phys.* **2011**, *83*, 113303.
(471) Haller, A.; Peláez, D.; Bande, A. Inter-Coulombic Decay in Laterally Arranged Quantum Dots Controlled by Polarized Lasers. *J. Phys. Chem. C* **2019**, *123*, 14754−14765.
(472) Donovan, K.; Harrison, P.; Kelsall, R. W. Stark Ladders as Tunable Far-Infrared Emitters. *J. Appl. Phys.* **1998**, *84*, 5175−5179.
(473) Bande, A. Acoustic Phonon Impact on the Inter-Coulombic Decay Process in Charged Quantum Dot Pairs. *Mol. Phys.* **2019**, *117*, 2014−2028.
(474) Weber, F.; Aziz, E. F.; Bande, A. Interdependence of ICD Rates in Paired Quantum Dots on Geometry. *J. Comput. Chem.* **2017**, *38*, 2141−2150.
(475) Stumpf, V.; Brunken, C.; Gokhberg, K. Impact of Metal Ion's Charge on the Interatomic Coulombic Decay Widths in Microsolvated Clusters. *J. Chem. Phys.* **2016**, *145*, 104306.
(476) Langkabel, F.; Lützner, M.; Bande, A. Interparticle Coulombic Decay Dynamics along Single- and Double-Ionization Pathways. *J. Phys. Chem. C* **2019**, *123*, 21757−21762.
(477) Goldzak, T.; Gantz, L.; Gilary, I.; Bahir, G.; Moiseyev, N. Interatomic Coulombic Decay in Two Coupled Quantum Wells. *Phys. Rev. B: Condens. Matter Mater. Phys.* **2015**, *91*, 165312.
(478) Goldzak, T.; Gantz, L.; Gilary, I.; Bahir, G.; Moiseyev, N. Vertical Currents due to Interatomic Coulombic Decay in Experiments with Two Coupled Quantum Wells. *Phys. Rev. B: Condens. Matter Mater. Phys.* **2016**, *93*, 045310.
(479) Goldzak, T. Partial Widths and Branching Ratios for the Emitted Electron Resulting from Interatomic Coulombic Decay in Quantum Wells Heterostructure. *Mol. Phys.* **2019**, *117*, 2179−2177.
(480) Thomas, T.; Kukk, E.; Ueda, K.; Ouchi, T.; Sakai, K.; Carroll, T. X.; Nicolas, C.; Travnikova, O.; Miron, C. Experimental Observation of Rotational Doppler Broadening in a Molecular System. *Phys. Rev. Lett.* **2011**, *106*, 193009.
(481) Céolin, D.; Liu, J.-C.; Vaz da Cruz, V.; Ågren, H.; Journel, L.; Guillemin, R.; Marchenko, T.; Kushawaha, R. K.; Piancastelli, M. N.; Püttner, R.; et al. Recoil-Induced Ultrafast Molecular Rotation Probed by Dynamical Rotational Doppler Effect. *Proc. Natl. Acad. Sci. U. S. A.* **2019**, *116*, 4877−4882.
(482) Liu, X.; Miao, Q.; Gel'mukhanov, F.; Patanen, M.; Travnikova, O.; Nicolas, C.; Ågren, H.; Ueda, K.; Miron, C. Einstein−Bohr Recoiling Double-slit Dedanken Experiment Performed at the Molecular Level. *Nat. Photonics* **2015**, *9*, 120−125.
(483) Simon, M.; Püttner, R.; Marchenko, T.; Guillemin, R.; Kushawaha, R. K.; Journel, L.; Goldsztejn, G.; Piancastelli, M. N.; Ablett, J. M.; Rueff, J.-P.; et al. Atomic Auger Doppler effects upon emission of fast photoelectrons. *Nat. Commun.* **2014**, *5*, 4069.
(484) Kuznetsov, V.; Cherepkov, N. Auger Decay of Fixed-in-Space Linear Molecules. *J. Electron Spectrosc. Relat. Phenom.* **1996**, *79*, 437−440.
(485) Domcke, W.; Cederbaum, L. Vibronic Coupling and Symmetry Breaking in Core Electron Ionization. *Chem. Phys.* **1977**, *25*, 189−196.
(486) Saito, N.; Ueda, K.; Fanis, A. D.; Kubozuka, K.; Machida, M.; Koyano, I.; Dörner, R.; Czasch, A.; Schmidt, L.; Cassimi, A.; et al. Molecular Frame Photoelectron Angular Distribution for Oxygen 1s Photoemission from CO2Molecules. *J. Phys. B: At., Mol. Opt. Phys.* **2005**, *38*, L277−L284.
(487) McCurdy, C. W.; Rescigno, T. N.; Trevisan, C. S.; Lucchese, R. R.; Gaire, B.; Menssen, A.; Schöffler, M. S.; Gatton, A.; Neff, J.; Stammer, P. M.; et al. Unambiguous Observation of F-Atom Core-Hole Localization in CF_4 through Body-Frame Photoelectron Angular Distributions. *Phys. Rev. A: At., Mol., Opt. Phys.* **2017**, *95*, 011401.
(488) Schöffler, M. S.; Titze, J.; Petridis, N.; Jahnke, T.; Cole, K.; Schmidt, L. P. H.; Czasch, A.; Akoury, D.; Jagutzki, O.; Williams, J. B.; et al. Ultrafast Probing of Core Hole Localization in N_2. *Science* **2008**, *320*, 920−923.
(489) Schöffler, M.; Jahnke, T.; Titze, J.; Petridis, N.; Cole, K.; Schmidt, L. P. H.; Czasch, A.; Jagutzki, O.; Williams, J. B.; C L Cocke, T. O. Matter Wave Optics Perspective at Molecular Photoionization: K-Shell Photoionization and Auger Decay of N2. *New J. Phys.* **2011**, *12*, 095013.
(490) Ruberti, M. Onset of Ionic Coherence and Ultrafast Charge Dynamics in Attosecond Molecular Ionisation. *Phys. Chem. Chem. Phys.* **2019**, *32*, 17584−17604.
(491) Yamazaki, M.; Adachi, J.; Kimura, Y.; Yagishita, A.; Stener, M.; Decleva, P.; Kosugi, N.; Iwayama, H.; Nagaya, K.; Yao, M. Decay Channel Dependence of the Photoelectron Angular Distributions in Core-Level Ionization of Ne Dimers. *Phys. Rev. Lett.* **2008**, *101*, 043004.
(492) Deleuze, M. S.; Francois, J.-P.; Kryachko, E. S. The Fate of Dicationic States in Molecular Clusters of Benzene and Related Compounds. *J. Am. Chem. Soc.* **2005**, *127*, 16824−16834.
(493) Alizadeh, E.; Orlando, T. M.; Sanche, L. Biomolecular Damage Induced by Ionizing Radiation: The Direct and Indirect Effects of Low-Energy Electrons on DNA. *Annu. Rev. Phys. Chem.* **2015**, *66*, 379−398.
(494) Boudaiffa, B.; Cloutier, P.; Hunting, D.; Huels, M. A.; Sanche, L. Resonant Formation of DNA Strand Breaks by Low-Energy (3 to 20 eV) Electrons. *Science* **2000**, *287*, 1658−1660.
(495) Hanel, G.; Gstir, B.; Denifl, S.; Scheier, P.; Probst, M.; Farizon, B.; Farizon, M.; Illenberger, E.; Mark, T. D. Electron Attachment to Uracil: Effective Destruction at Subexcitation Energies. *Phys. Rev. Lett.* **2003**, *90*, 188104.
(496) Howell, R. W. Auger Processes in the 21st Century. *Int. J. Radiat. Biol.* **2008**, *84*, 959−975.
(497) Surdutovich, E.; Solov'yov, A. V. Double Strand Breaks in DNA Resulting from Double Ionization Events. *Eur. Phys. J. D* **2012**, *66*, 206−210.
(498) Märk, T. D.; Scheier, P. Ionization Dynamics: Unexpected Electrons. *Nat. Phys.* **2010**, *6*, 82−83.
(499) Seo, S.-J.; Han, S.-M.; Cho, J.-H.; Hyodo, K.; Zaboronok, A.; You, H.; Peach, K.; Hill, M. A.; Kim, J.-K. Enhanced Production of Reactive Oxygen Species by Gadolinium Oxide Nanoparticles under Core-Inner-Shell Excitation by Proton or Monochromatic X-ray Irradiation: Implication of the Contribution from the Interatomic De-Excitation-Mediated Nanoradiator Effect to Dose Enhancement. *Radiat. Environ. Biophys.* **2015**, *54*, 423−431.
(500) Ueda, K. Core Excitation and De-Excitation Spectroscopies of Free Atoms and Molecules. *J. Phys. Soc. Jpn.* **2006**, *75*, 032001.
(501) O'Keeffe, P.; Ripani, E.; Bolognesi, P.; Coreno, M.; Devetta, M.; Callegari, C.; Di Fraia, M.; Prince, K. C.; Richter, R.; Alagia, M.; et al. The Role of the Partner Atom and Resonant Excitation Energy in Interatomic Coulombic Decay in Rare Gas Dimers. *J. Phys. Chem. Lett.* **2013**, *4*, 1797−1801.
(502) Schwartz, C. P.; Fatehi, S.; Saykally, R. J.; Prendergast, D. Importance of Electronic Relaxation for Inter-Coulombic Decay in Aqueous Systems. *Phys. Rev. Lett.* **2010**, *105*, 198102.
(503) Martin, R. F.; Feinendegen, L. E. The Quest to Exploit the Auger Effect in Cancer Radiotherapy - a Reflective Review. *Int. J. Radiat. Biol.* 2016, *92*, 617−632, DOI: 10.3109/09553002.2015.1136854.
(504) Saak, C.-M.; Richter, C.; Unger, I.; Mucke, M.; Nicolas, C.; Hergenhahn, U.; Caleman, C.; Huttula, M.; Patanen, M.; Björneholm, O. Proton Dynamics in Molecular Solvent Clusters as an Indicator for Hydrogen Bond Network Strength in Confined Geometries. *Phys. Chem. Chem. Phys.* **2020**, *22*, 3264−3272.
(505) Saak, C.-M.; Unger, I.; Brena, B.; Caleman, C.; Björneholm, O. Site-Specific X-ray Induced Dynamics in Liquid Methanol. *Phys. Chem. Chem. Phys.* **2019**, *21*, 15478−15486.

https://dx.doi.org/10.1021/acs.chemrev.0c00106
Chem. Rev. 2020, 120, 11295−11369

(506) Palacios, A.; Martín, F. The Quantum Chemistry of Attosecond Molecular Science. *Wiley Interdiscip. Rev.: Comput. Mol. Sci.* **2020**, *10*, No. e1430.
(507) Kaldun, A.; Blättermann, A.; Stooß, V.; Donsa, S.; Wei, H.; Pazourek, R.; Nagele, S.; Ott, C.; Lin, C. D.; Burgdörfer, J.; et al. Observing the Ultrafast Buildup of a Fano Resonance in the Time Domain. *Science* **2016**, *354*, 738−741.
(508) Amthor, T.; Denskat, J.; Giese, C.; Bezuglov, N. N.; Ekers, A.; Cederbaum, L. S.; Weidemüller, M. Autoionization of an Ultracold Rydberg Gas Through Resonant Dipole Coupling. *Eur. Phys. J. D* **2009**, *53*, 329−336.
(509) Stienkemeier, F.; Lehmann, K. K. Spectroscopy and Dynamics in Helium Nanodroplets. *J. Phys. B: At., Mol. Opt. Phys.* **2006**, *39*, R127−R166.
(510) Kryzhevoi, N. V.; Averbukh, V.; Cederbaum, L. S. High Activity of Helium Droplets Following Ionization of Systems inside those Droplets. *Phys. Rev. B: Condens. Matter Mater. Phys.* **2007**, *76*, 094513.
(511) Kryzhevoi, N. V.; Mateo, D.; Pi, M.; Barranco, M.; Cederbaum, L. S. Probing the Interface of Doped Isotopically Mixed Helium Droplets by the Directional Anisotropy of Interatomic Coulombic Decay. *Phys. Chem. Chem. Phys.* **2013**, *15*, 18167−18173.
(512) Ghosh, A.; Cederbaum, L. S.; Gokhberg, K. Electron Transfer Mediated Decay in $HeLi_2$ Cluster: Potential Energy Surfaces and Decay Widths. *J. Chem. Phys.* **2019**, *150*, 164309.
(513) Eckey, A.; Voitkiv, A. B.; Müller, C. Resonant Single-Photon Double Ionization Driven by Combined Intra- and Interatomic Electron Correlations. *J. Phys. B: At., Mol. Opt. Phys.* **2020**, *53*, 055001.
(514) Kolorenč, P.; Averbukh, V.; Feifel, R.; Eland, J. Collective Relaxation Processes in Atoms, Molecules and Clusters. *J. Phys. B: At., Mol. Opt. Phys.* **2016**, *49*, 082001.
(515) LaForge, A. C.; Drabbels, M.; Brauer, N. B.; Coreno, M.; Devetta, M.; Di Fraia, M.; Finetti, P.; Grazioli, C.; Katzy, R.; Lyamayev, V.; et al. Collective Autoionization in Multiply-Excited Systems: A Novel Ionization Process Observed in Helium Nanodroplets. *Sci. Rep.* **2015**, *4*, 3621−3624.
(516) Lyamayev, V.; Ovcharenko, Y.; Katzy, R.; Devetta, M.; Bruder, L.; LaForge, A.; Mudrich, M.; Person, U.; Stienkemeier, F.; Krikunova, M.; et al. A Modular End-Station for Atomic, Molecular, and Cluster Science at the Low Density Matter Beamline of FERMI@Elettra. *J. Phys. B: At., Mol. Opt. Phys.* **2013**, *46*, 164007.
(517) Laarmann, T.; Rusek, M.; Wabnitz, H.; Schulz, J.; de Castro, A. R. B.; Gürtler, P.; Laasch, W.; Möller, T. Emission of Thermally Activated Electrons from Rare Gas Clusters Irradiated with Intense VUV Light Pulses from a Free Electron Laser. *Phys. Rev. Lett.* **2005**, *95*, 063402.
(518) Dunford, R. W.; Southworth, S. H.; Ray, D.; Kanter, E. P.; Krässig, B.; Young, L.; Arms, D. A.; Dufresne, E. M.; Walko, D. A.; Vendrell, O.; et al. Evidence for Interatomic Coulombic Decay in Xe K-Shell-Vacancy Decay of XeF_2. *Phys. Rev. A: At., Mol., Opt. Phys.* **2012**, *86*, 033401.
(519) Grieves, G. A.; Orlando, T. M. Intermolecular Coulomb Decay at Weakly Coupled Heterogeneous Interfaces. *Phys. Rev. Lett.* **2011**, *107*, 016104.
(520) Hagstrum, H. D. Auger Ejection of Electrons from Tungsten by Noble Gas Ions. *Phys. Rev.* **1954**, *96*, 325−335.
(521) Hagstrum, H. D. Theory of Auger Ejection of Electrons from Metals by Ions. *Phys. Rev.* **1954**, *96*, 336−365.
(522) Matthew, J. A. D.; Komninos, Y. Transition Rates for Interatomic Auger Processes. *Surf. Sci.* **1975**, *53*, 716−725.
(523) Kamat, P. V. Quantum Dot Solar Cells. The Next Big Thing in Photovoltaics. *J. Phys. Chem. Lett.* **2013**, *4*, 908−918.
(524) Algar, W. R.; Kim, H.; Medintz, I. L.; Hildebrandt, N. Emerging Non-Traditional Förster Resonance Energy Transfer Configurations with Semiconductor Quantum Dots: Investigations and Applications. *Coord. Chem. Rev.* **2014**, *263*−*264*, 65−85.

https://dx.doi.org/10.1021/acs.chemrev.0c00106
Chem. Rev. 2020, 120, 11295−11369